UAB
Universitat Autònoma de Barcelona

Optomechanical transduction in the near infrared range: coupling optical nanoantennas to micro and nanoelectromechanical systems

Daniyal Khoshmaram

ADVERTIMENT. L'accés als continguts d'aquesta tesi queda condicionat a l'acceptació de les condicions d'ús establertes per la següent llicència Creative Commons: https://creativecommons.org/licenses/?lang=ca

ADVERTENCIA. El acceso a los contenidos de esta tesis queda condicionado a la aceptación de las condiciones de uso establecidas por la siguiente licencia Creative Commons: https://creativecommons.org/licenses/?lang=es

WARNING. The access to the contents of this doctoral thesis it is limited to the acceptance of the use conditions set by the following Creative Commons license: https://creativecommons.org/licenses/?lang=en

PhD Thesis

Optomechanical transduction in the near infrared range: coupling optical nanoantennas to micro and nanoelectromechanical systems

Thesis by compendium of publications

Author:

Daniyal Khoshmaram

Thesis Directors and Academic Tutors:

Gabriel Abadal Berini and Xavier Cartoixà Soler

PhD in Electronic and Telecommunication Engineering

Department of Electronic Engineering

UAB
Universitat Autònoma
de Barcelona

Universitat Autònoma de Barcelona, Bellaterra, 2025

Certificate

Doctor Gabriel Abadal Berini, associate professor at the Department of Electronic Engineering of the Universitat Autònoma de Barcelona and
Doctor Xavier Cartoixà Soler, associate professor at the Department of Electronic Engineering of the Universitat Autònoma de Barcelona

HEREBY CERTIFY THAT

The thesis entitled ”Optomechanical transduction in the near infrared range: coupling optical nanoantennas to micro and nanoelectromechanical systems” submitted by Daniyal Khoshmaram to fulfill part of the requirements to achieve the degree of Doctor of Philosophy in Electronic Engineering, has been performed under their supervision.

Bellaterra, October 2025

Gabriel Abadal Berini and **Xavier Cartoixà Soler**

Quote

> “Research is to see what everybody else has seen, and to think what nobody else has thought.”
>
> **– Albert Szent-Györgyi**

Abstract

This thesis presents the design, simulation, fabrication, and experimental analysis of optomechanical nanoantennas for near-infrared (NIR) radiation detection and translation into mechanical motion. Three antenna structures were developed, corresponding to the fundamental $\lambda/2$ and higher-order $3\lambda/2$ and $5\lambda/2$ resonant modes. Each design integrates a plasmonic gold nanodipole at the tip of Si_3N_4 microcantilevers, forming a NEMSTENNA (nano-electromechanical antenna) device. In the working principle two transduction pathways are present: the desired *opto-electromechanical (OEM)* effect, where the induced feed-gap voltage generates an electrostatic force that deflects the cantilevers, and the parasitic *opto-thermomechanical (OTM)* effect, where laser-induced heating produces bimetallic bending.

Fabrication of prototypes was achieved by focused ion beam (FIB) milling on commercial AFM cantilevers. Electromagnetic simulations confirmed strong resonances at 1.55 μm, with induced voltages in the tens of millivolts and OEM deflections in the tens-of-picometer range per mW of optical input. OTM deflections, however, were several nanometers under the same conditions, making them the dominant static contribution. A figure of merit was defined as the ratio between OEM and OTM displacements, and both simulations and experiments validated the predominance of the parasitic thermal response.

To overcome these limitations, a new *tuning-fork optomechanical antenna* with an integrated optical transmission line was proposed and analyzed. This monolithic configuration eliminates the effect of out-of-plane OTM bending, and significantly enhances OEM responsivity, with predicted deflections in the 10 nm range for a few milliwatts of input power. This corresponds to responsivities above 1 nm/mW, surpassing earlier prototypes and approaching or exceeding other reported optomechanical detectors.

This work demonstrates the feasibility of direct light-to-mechanical transduc-

tion using plasmonic nanoantennas, provides a quantitative assessment of parasitic photothermal effects, and introduces optimized designs that pave the way for faster, more sensitive NIR optomechanical transducers. The results benchmark the NEMSTENNA concept against state-of-the-art detectors and highlight design strategies to enhance performance for future integrated photonic–NEMS systems.

Acknowledgements

I would like to express my heartfelt gratitude to all those who have supported me throughout this thesis journey.

To my family — Baba, Maman, Hongxin, Benyamin, and everyone close to me — thank you for always standing by my side, despite the distances, whether inevitable or chosen. Your love and support have been a constant source of strength.

To my dear friends, both near and far, who have encouraged me through this long academic adventure— your companionship has meant more than words can say. Special thanks to those who made even the most stressful days lighter through their presence. To my colleagues, advisors, and everyone I have had the privilege to work with during this research: your insights, encouragement, and knowledge have been invaluable. Thank you for being generous with your time, your feedback, and your collaboration.

To the *Ministerio de Ciencia e Innovación* under Grant No. PID2021-127840NB-I00 (MICINN/AEI/FEDER, UE), and the *Ministerio de Ciencia, Innovación y Universidades* under Grant No. PID2024-161603NB-I00 (MICIU/AEI/10./13039/501100011033/FEDER, UE) for the financial support of the research activities presented in this thesis.

To those involved in the experimental work, simulation support — I deeply appreciate your contributions, which made this work possible.

To my mentors, Gabriel and Xavier, thank you for inspiring me to look beyond what is visible and strive for what is meaningful. Your guidance has shaped not only my thesis but also the way I approach science.

Thank you all, sincerely.

Contents

Abstract **5**

7

List of Acronyms **21**

1 Introduction **23**
1.1 Limitations of traditional THz/NIR detectors 24
1.2 MEMS/NEMS as an alternative detection paradigm 25
1.3 Terahertz optomechanical detectors 27
1.4 Optomechanical transduction mechanisms 29
1.4.1 Electrostatic transduction 29
1.4.2 Radiation pressure transduction 30
1.4.3 Optothermal transduction 31
1.5 Other detection alternatives 32
1.6 The NEMSTENNA solution 34
1.7 Application contexts: biomedical diagnostics, communication, and passive sensing 36
1.8 Thesis objectives 38
1.9 Summary of thesis publications 38

2 Methods **41**
2.1 Computational methods and modeling techniques 41
2.1.1 Electromagnetic modeling 45

2.1.1.1 Boundary Conditions . . . 46
2.1.1.2 Structure Excitation . . . 49
2.1.2 Thermal Modeling . . . 51
2.1.2.1 Thermal Boundary Conditions . . . 52
2.1.3 Optothermal coupling equations . . . 54
2.1.4 Mechanical modeling . . . 55
2.1.4.1 Thermomechanical . . . 55
2.1.4.2 Electromechanical . . . 55
2.2 Fabrication methods . . . 58
2.2.1 FIB-SEM nanofabrication system and imaging . . . 59
2.2.2 Library of FIB milling procedures . . . 60

3 Results 63
3.1 Designed structures . . . 63
3.2 Working principle . . . 67
3.3 Fabricated prototypes . . . 73
3.4 Nanoantenna response . . . 79
3.4.1 S_{11} versus V_{gap} as optimization variables . . . 79
3.4.2 Nanoantenna resonant mode selection . . . 83
3.5 OTM response: parasitic optothermomechanical effect . . . 84
3.6 OEM response: opto-electromechanical effect . . . 91
3.7 OEM versus OTM comparison optomechanical transducers . . . 95
3.8 Comparison with state of the art . . . 97

4 Conclusions and Future Work 101
4.1 Conclusions . . . 101
4.2 Future Work . . . 103
4.3 Scientific contributions of the author . . . 104
4.3.1 Publications . . . 104
4.3.1.1 Journal publications . . . 104
4.3.1.2 Conference proceedings publications . . . 105

4.3.2 Conference contributions 105
4.3.3 Publications not directly related to the thesis 107

A Compendium Papers **123**
A.1 Design and fabrication of an opto-mechanical antenna in the NIR range 125
A.2 Impact of the parasitic photothermal effect on the performance of an optomechanical nanoantenna for NIR radiation detection 135

B Non-Compendium Papers **145**
B.1 Analysis of the Photothermal Parasitic Effect on an Optomechanical Antenna 147
B.2 Plasmomechanical actuation at the nanoscale activated by NIR radiation 153
B.3 Tuning fork optomechanical NIR antenna with integrated optical transmission line 169

C Library of FIB milling procedures **183**
C.1 Nanodipole coupled to a micro or nanocantilever (Papers 1 and 3) (A.1)(B.2) 185
C.2 Tuning fork NEMSTENNA with integrated optical transmission line (Paper 4)(B.3) 187

D Measurement setup **191**
D.1 Measurement setup 193
D.2 Experimental setup elements 194

List of Figures

1.1 MEMSTENNA: dipole antenna arms as cantilevers deflected by incoming RF radiation [32]. 26

2.1 Operating frequency–object size domain map indicating the applicable physics modules in COMSOL MULTIPHYSICS. The NIR regime (highlighted in this work) lies in the transition between the RF and Wave Optics modules, where full-wave electromagnetic solutions are required (Wave Regime). In this study, the RF, Electrostatics, Solid Mechanics, and Heat Transfer in Solids modules were combined to evaluate the opto-electromechanical (OEM) and opto-thermo-mechanical (OTM) effects in the NEMSTENNA device [73]. 42

2.2 Geometry of the NEMSTENNA device Paper 1 (A.1) showing the excitation applied through a lumped port. The lumped port (indicated by the red and blue arrows) was used to excite the antenna structure and evaluate its optical and electromagnetic response in the near-infrared (NIR) regime. 47

2.3 Comparison of different PML (Perfectly Matched Layer) geometries used for electromagnetic simulations: (left) spherical PML enclosing a hemispherical scatterer, (center) cuboidal PML surrounding a block-shaped domain, and (right) cylindrical PML adapted to a rotationally symmetric model. PMLs are employed to absorb outgoing waves and prevent artificial reflections at the boundaries of finite simulation domains [73]. 48

2.4 Background electric field, x component (V/m), of a laser Gaussian beam focused on the gap of a nanoantenna structure. 50
2.5 Schematic top (a) and side (b) views of the proposed gold–silicon nitride bilayer cantilever system. The free ends of the cantilever form a dipole nanoantenna separated by a narrow gap. The structure parameters are labeled as L_{Arm1}, L_{Arm2}, L_1, L_2, W_1, and W_2. The gold and Si_3N_4 layers have thicknesses of 35 nm and 140 nm, respectively. 56
2.6 Focused Ion Beam–Scanning Electron Microscope (FIB-SEM) system used for nanoantenna fabrication and structural characterization. The dual-beam setup enables high-resolution SEM imaging and site-specific milling with ion beams, which is essential for preparing and analyzing nanoscale structures. This system was instrumental in prototyping and inspecting the critical dimensions of the fabricated NEMSTENNA devices. 59

3.1 Schematic top and side views of the proposed first structure, including nano-antenna and microcantilever (Paper 1)(A.1). 65
3.2 Lateral (a) and top (b) views of the second plasmomechanical antenna (Paper 3)(B.2). 66
3.3 Top and lateral view of the third optomechanical antenna (Paper 4)(B.3). 66
3.4 Maps of the current density (a-c) and z-component of the electric field (d-f), for the first three detectable resonance modes observed when dipole length is 300 nm (a,d), 810 nm (b,e) and 1361 nm (c,f) (Paper 2)(A.2). 67
3.5 Comparison of opto-thermo-mechanical (OTM) (a) and opto-electro-mechanical (OEM) (b) transduction mechanisms. Both pathways convert incident light into mechanical displacement, but rely on different intermediate physical effects. 69
3.6 Actuation principle of the optomechanical antenna (Paper 3)(B.2). 72

3.7 FIB based fabrication process steps of the proposed structure: (a) Initial AFM microcantilever structure, (b) microcantilever flipping, (c) local FIB milling thickness reduction, (d) local FIB milling half nanoantenna definition and (e) NEMSTENNA final build-up (Paper 1)(A.1). 74
3.8 SEM images of a fabricated NEMSTENNA prototype after (a) step c (see figure 3.7c) and (b) step d (see figure 3.7d) of the fabrication process. 75
3.9 NEMSTENNA fabrication process: (a) Unprocessed microcantilever structure, (b) microcantilever flipping, (c) thickness reduction in the nanocantilever and nanodipole area, (d) nanocantilever and one arm nanodipole definition and (e) NEMSTENNA final build-up (Paper 3)(B.2). 76
3.10 SEM images from top (a) and lateral (b) perspectives of a NEMSTENNA nanocantilever in the residual stress limit of slenderness (Paper 3)(B.2). 76
3.11 Fabrication steps for tuning fork optomechanical antenna (Paper 4)(B.3). 77
3.12 SEM images of a tuning fork optomechanical antenna (Paper 4)(B.3). 77
3.13 The frequency response of S_{11} (a) and V_{gap} (b) obtained from COMSOL simulation is shown for 8 different values of L_1 and L_2 around the optimum case. The laser power is set to 500 mW, and the gap distance is $g_0 = 10$ nm (Paper 1)(A.1). 80
3.14 V_{gap} and E_z vs. frequency and wavelength for different spot radius (SR) for second proposed optomechanical antenna (Paper 3)(B.2). 82

3.15 Laser-induced mechanical responses of the NEMSTENNA cantilever. (a) Measured static deflection vs. time in the OFF–ON–OFF transients for 5.8 mW, 4.7 mW, and 3.7 mW IR laser powers [93]. (b) Measured dynamic oscillation amplitude (Z_{dynamic}) vs. laser modulated frequency for different IR laser powers (1.33 mW to 6 mW). 87
3.16 Experimental and COMSOL simulated steady-state displacement of the cantilever free-end in the out-of-plane direction, z, after laser power OFF-ON switching transient for different laser powers ranging from 1 to 7.5 mW. Spot radius is SR = 27.5 μm and gap distance is g_0 = 10 nm (Paper 2)(A.2) [89]. 88
3.17 Thermal response of the microcantilever under IR illumination. (a) Simulated temperature and static displacement at the cantilever free end as a function of IR laser power, with spatial maps of temperature and displacement shown for the 5.8 mW case. (b) Time-resolved temperature evolution at the cantilever tip for various laser powers, showing faster saturation and higher steady-state temperatures at increased IR power. 90
3.18 Lateral displacement in the x-direction, δ_x, vs. laser power. All simulations have been performed for a laser beam excitation with λ = 1.55 μm and spot radius, SR = 8 μm (Paper 4)(B.3) [91]. . . . 94
3.19 OEM and OTM displacements and their corresponding OEM/OTM ratio as defined by the FoM as a function of the laser spot radii, ranging from 8 to 27.5 μm. Laser power is P_{in} = 7.5 mW and gap distance is g_0 = 10 nm (Paper 2)(A.2) [89]. 96
3.20 OTM and OEM responses (left axis) together with the figure of merit FoM = $z_{\text{OEM}}/z_{\text{OTM}}$ (right axis), as a function of spot radius SR. Nanocantilever dimensions are l_n = 50 μm, t_n = 600 nm, $t_{\text{Au},n}$ = 70 nm; and the laser power is 1 mW in all cases (Paper 3)(B.2) [90]. 97

D.1 Schematic of the NEMSTENNA characterization setup. Key components include infrared laser (IRL), 4-quadrant photodetector (4QPD), CCD camera (CCD), White light source (WLS), microscope objective (MO), red diode laser (RL), collimator (C), optical fiber, (OF), and beam splitters (BS1/BS2). The Tektronix MDO3024 oscilloscope handles analysis. 193

List of Tables

3.1 Comparison of three different optomechanical antenna structures. . 64
3.2 Geometry dimensions of the NEMSTENNA device corresponding to Figure 3.1 used in COMSOL simulations (Paper 1)(A.1). 68
3.3 Dimensions of the optimal NEMSTENNA design corresponding to Figure 3.2 (Paper 3)(B.2). 68
3.4 Geometry characteristics of tuning fork optomechanical device corresponding to Figure 3.3 (Paper 4)(B.3). 69
3.5 Definition of parameters used in the electrostatic force and capacitance equations. 71
3.6 Responsivity values of some of the state-of-the-art optomechanical transducers [90, 91]. 98

D.1 Experimental setup elements used for NEMSTENNA characterization. 194

List of Acronyms

Acronym	Definition
AC	Alternating Current
AFM	Atomic Force Microscope / Microscopy
COMSOL®	COMSOL Multiphysics Simulation Software
CTE	Coefficient of Thermal Expansion
DC	Direct Current
EM	Electromagnetic
EMW	Electromagnetic Waves
FDTD	Finite-Difference Time-Domain
FEA	Finite Element Analysis
FEM	Finite Element Method
FIB	Focused Ion Beam
IR	Infrared
MEMS	Micro-Electro-Mechanical System
NEMS	Nano-Electro-Mechanical System
NEMSTENNA	Nano-Electro-Mechanical System Antenna
NIR	Near-Infrared
OEM	Opto-Electro-Mechanical
OTL	Optical Transmission Line
OTM	Opto-Thermo-Mechanical
PML	Perfectly Matched Layer
RF	Radio Frequency
SEM	Scanning Electron Microscope / Microscopy
TBR	Thermal Boundary Resistance
VNA	Vector Network Analyzer

Chapter 1

Introduction

Modern society's growing demand for sensitive detection across a broad swath of the electromagnetic spectrum [1, 2] has pushed the development of innovative sensing technologies. In particular, the terahertz (THz, 10^{12} Hz) and near-infrared (NIR, wavelengths 0.75–2.5 μm) ranges have attracted intense interest [1, 3] due to their unique application domains. The THz band, spanning roughly 1–20 THz, offers myriad uses in spectroscopy, biomedical imaging, environmental monitoring (e.g. gas sensing), security screening [4, 5], and is even envisioned as a frontier for next-generation ultra-high-speed wireless communications [6, 7]. Likewise, NIR optical frequencies underlie crucial technologies in telecommunications (fiber-optic and free-space optical links around 1.3–1.5 μm) [8, 9], advanced imaging and diagnostics in medicine, for example, NIR fluorescence and spectroscopy for minimally invasive tissue analysis, [10–13], as well as remote sensing of chemicals and pollutants [14–16]. Achieving efficient, fast, and low-noise detection in these frequency ranges is therefore of great scientific and practical importance [17, 18], enabling applications from real-time molecular spectroscopy to high-bandwidth wireless data transfer. However, detecting THz or NIR radiation with high speed and sensitivity at room temperature remains a notorious challenge [19]. Most conventional detectors in these bands are thermal-based [20, 21]: they rely on the heating of a material by incident radiation, and transduce this temperature rise into an electrical signal. Examples include microbolometers, pyroelectric sensors, and Golay cells. These devices typically suffer from slow response times (limited by thermal time constants on the order of milliseconds) [22, 23], significant power draw (requiring bias currents or chopping for readout) [24, 25], and often cryogenic

cooling for an acceptable signal-to-noise ratio in the THz range. Indeed, the need to average over relatively long thermal response times means traditional THz detectors trade off speed for sensitivity: room-temperature operation is generally incompatible with simultaneously achieving high speed and high sensitivity using these technologies [24, 25]. These performance limitations of conventional THz and NIR detectors are reported in the next section.

1.1 Limitations of traditional THz/NIR detectors

The traditional infrared detectors (e.g. semiconductor photodiodes for the near-infrared, 0.7–1.7 μm) can achieve high speed, but they require specialized materials (InGaAs, Ge) and active power, and their performance may degrade at longer wavelengths or high temperatures. Thermal infrared detectors (microbolometers) operate uncooled but suffer from slow response (millisecond-scale) due to thermal time constants. These limitations motivate the exploration of novel detection paradigms that bypass thermal or purely semiconductor-based conversion mechanisms, aiming for higher bandwidth and room-temperature operation [26].

For instance, a Golay cell [27, 28] , a broadband THz/IR pneumatic detector, has a response time on the order of 10 ms [29, 30], and even optimized semiconductor bolometers or pyroelectrics have cut-off frequencies only in the kilohertz range [26].

Thus, widespread THz detection techniques are “slow” by the standards of modern electronics, precluding their use in fast modulation or imaging beyond video frame-rates. At the same time, many of these sensors are bulky, require mechanical chopping or lock-in techniques, and cannot be easily integrated on-chip. There is therefore a strong motivation to explore alternative detection paradigms that can provide faster, more energy-efficient, and miniaturizable detection of THz and NIR signals at ambient conditions.

1.2 MEMS/NEMS as an alternative detection paradigm

One promising route involves leveraging micro- and nano-electromechanical systems (MEMS/NEMS) to directly transduce electromagnetic waves into mechanical motion, which can then be read out electrically or optically. MEMS/NEMS-based detectors offer several inherent advantages over purely thermal or electronic sensors. First, they can be extremely fast: a miniature mechanical resonator can respond on microsecond to sub-microsecond timescales (with resonance frequencies in the kHz–MHz or even GHz range) [31], far outpacing the thermal RC constants of bolometric detectors [26]. In such devices, the energy of the incident radiation is converted to a mechanical response (displacement or vibration) without needing to appreciably heat a bulk mass, thereby bypassing the bottleneck of heat diffusion. Second, MEMS/NEMS transducers can be highly energy-efficient and even passive. By designing the structure to be driven directly by the incident field (for example, via an embedded charge or piezoelectric element), one can eliminate the need for power-hungry amplifiers or bias circuits at the sensor node – the incoming radiation itself powers the mechanical response [32]. This is especially attractive for battery-powered or remote sensors (e.g. distributed environmental or IoT sensors), where energy autonomy is paramount [33, 34]. Third, MEMS/NEMS fabrication is largely CMOS-compatible [35–38]. These detectors can be realized using microfabrication techniques on silicon or other substrates, allowing potential monolithic integration with readout electronics and large-scale array deployment [37, 39]. The small form factor and compatibility with integrated circuit technology open the door to sensor arrays and pixellated cameras operating in frequency bands (like THz) that are currently served by much bulkier instrumentation. These advantages have inspired the development of a new class of opto-electro-mechanical antenna detectors, sometimes referred to as “mechanical antennas” or MEMSTENNA devices (from MEMS-antenna) in the radiofrequency community [32, 40, 41]. In a pioneering work, Ruiz et al. introduced the MEMSTENNA concept at RF/microwave frequencies: they demonstrated a flexible half-wavelength dipole antenna

in which the antenna's two arms are free-standing microcantilever beams that bend in response to incoming radio waves [32], as shown in Figure 1.1.

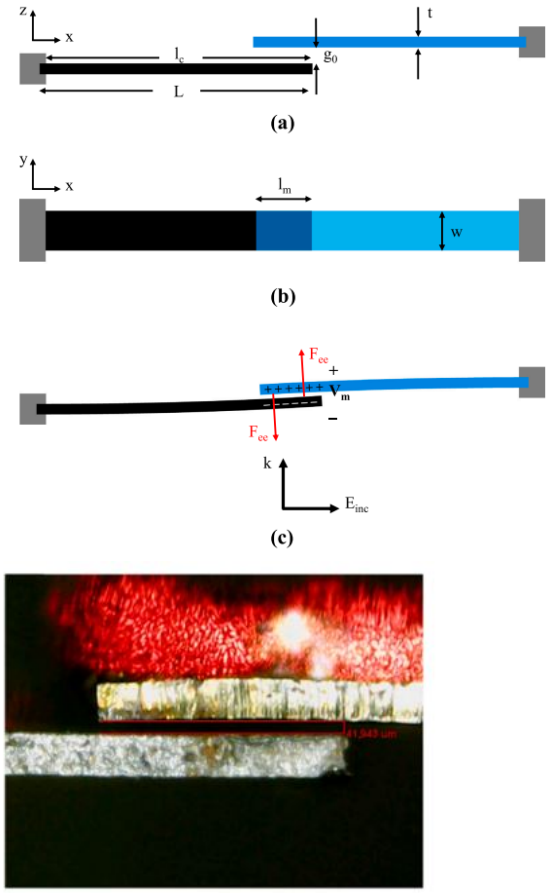

Figure 1.1: MEMSTENNA: dipole antenna arms as cantilevers deflected by incoming RF radiation [32].

In that device, the capacitive coupling between the antenna and the cantilever produces a mechanical deflection (static or dynamic) when the antenna intercepts an RF signal, effectively performing envelope detection of amplitude-modulated microwaves in a fully passive manner. Their prototype was capable of directly converting an 0.8 GHz wireless signal into a DC nanomechanical deflection, without any intermediate electronics [40].

Beyond radio and microwave implementations, optomechanical detection concepts have been extended into the terahertz regime, as described below.

1.3 Terahertz optomechanical detectors

The THz optomechanical detection approaches have been explored. Zhu *et al.* developed an uncooled THz detector using an array of bi-material microcantilevers coupled to a THz metasurface absorber [42]. Incoming THz radiation heats the metasurface, causing the bi-material cantilevers (e.g. gold on SiN_x) to bend via the photothermal expansion effect. An optical readout measures the deflection of the cantilevers as a proxy for the THz intensity. The device demonstrated a mechanical responsivity of about 24.8 μm/μW in deflection per absorbed power, showing good agreement between design and experiment. This optomechanical responsivity is high enough that even sub-microwatt THz powers produce tens of micrometers of deflection, a large signal that can be readily detected. Such a detector can be used as a pixel in a THz focal-plane array for imaging. Because it relies on photothermal actuation, its response time is bounded by thermal diffusion (typically on the order of milliseconds), but by microfabricating the cantilevers at microscale dimensions, response times can be pushed into the sub-millisecond regime.

In another advancement, Li *et al.* demonstrated an ultrafast THz optomechanical detector by using a miniaturized mechanical resonator driven by a dielectric (electrostatic) force [43]. Their device forgoes any deliberate thermal effect; instead, the THz electric field directly polarizes a tiny high-permittivity mechanical element, exerting an electrostatic force at the frequency of the THz field. By designing the mechanical resonator to have a high natural frequency and by operating in a regime dominated by this instantaneous dielectric force, they achieved detection bandwidths in the MHz range– orders of magnitude faster than bolometers. This miniaturized optomechanical resonator was able to detect THz pulses on sub-microsecond timescales, representing a significant step toward high-speed THz instrumentation. Notably, Li *et al.*'s approach is also compatible with room

temperature operation and does not require any optical pumping or local oscillator, making it a passive, chip-scale THz detector. Recent reviews have catalogued these and other emerging MEMS/NEMS-based THz detectors that leverage micromechanical motion, indicating growing interest in marrying microfabrication with THz sensing [43]. The general trend is that by introducing mechanical degrees of freedom into THz detector design, one can in principle circumvent the "terahertz gap" limitations of purely electronic or thermal detectors, achieving decent sensitivity with dramatically improved speed at ambient conditions.

The key advantage of electrostatic transduction is speed: the force follows the electromagnetic field almost instantaneously (limited only by the RC times of the structure, which at THz/NIR are negligible), allowing detector response times down to the nanosecond scale. Li *et al.*'s ultrafast THz detector [43] is an example that relies on such a dielectric force (polarization of a nanoresonator by the THz field) to attain MHz–GHz mechanical bandwidth.

Belacel et al. reported an optomechanical meta-atom detector for the THz range, wherein a sub-wavelength metal metamaterial resonator (specifically, an asymmetric split-ring resonator) was integrated with a nanoscale cantilever element [26].

In their device, the free end of the split-ring acted as a flexible mechanical oscillator, so that incident THz photons induced currents and charges in the resonator which coupled to the cantilever's motion [26]. By optically reading out the cantilever displacement (via a laser probe), they demonstrated THz detection at room temperature with dramatically improved speed compared to conventional thermal detectors: the mechanical response bandwidth exceeded 10 MHz, far beyond the cut-off frequencies of Golay cells, pyroelectrics, or even cryogenically-cooled bolometers [26]. The detection mechanism was shown to be extremely fast (non-thermal), arising from a nanoscale Coulomb force between oscillating charges – a form of direct electromechanical transduction of THz radiation [26]. Optomechanical antennas have now been extended all the way to optical frequencies. In this thesis, we propose a nano-optomechanical antenna operating in the NIR range

[44]. Our device consists of a plasmonic optical nanoantenna patterned onto a microcantilever. The plasmonic nanoantenna (with dimensions on the order of the light wavelength) serves to concentrate and absorb the incoming NIR electromagnetic radiation, while the cantilever transduces this optical energy into mechanical deflection. The result is a NEMSTENNA (Nano-Electro-Mechanical System Antenna) device: an antenna that directly converts free-space optical radiation into a mechanical motion signal.

1.4 Optomechanical transduction mechanisms

Understanding the physics of such NEMSTENNA transducers requires a grasp of several light–matter interaction mechanisms. In general, three main transduction pathways can contribute to optomechanical coupling in these systems: electrostatic forces, radiation pressure, and photothermal forces. Notably, these mechanisms are not mutually exclusive. In some detectors, more than one may occur simultaneously. Belacel *et al.* found that both a fast electrostatic force and a slower photothermal bending were present in their THz meta-atom detector; the photothermal effect provided a phase reference but the primary signal at resonance was due to the instantaneous Coulomb force. Careful device design can tailor which mechanism dominates. The MEMSTENNA approach intentionally avoids thermal intermediaries, favoring electrostatic transduction for speed [32, 40], whereas a bolometric microcantilever like Zhu's maximizes photothermal bending for sensitivity [42]. Understanding these forces is crucial for optimizing detector performance for different applications.

1.4.1 Electrostatic transduction

The electrostatic mechanism (sometimes termed Coulomb or capacitive coupling) occurs when the incident electromagnetic wave drives oscillating charges or currents in a structure, leading to time-varying electric fields that exert forces on charged or polarizable mechanical elements. In the THz meta-atom example [26],

the intense field in the split-ring's capacitive gap produced a periodic attraction between the cantilever and the opposite side of the gap, effectively pulling the cantilever with the THz field envelope. Because this force results directly from the electric field interaction (with no thermal intermediary), its response can be extremely fast – limited essentially by the inertia of the mechanical element and the timescale of the driving field modulation, rather than by heat diffusion [45–47].

1.4.2 Radiation pressure transduction

The radiation pressure mechanism is another non-thermal coupling. Light carries momentum, and when it is reflected or absorbed by a surface, a tiny mechanical force is exerted (the pressure $P = I/c$ for intensity I). At optical frequencies, radiation pressure is the basis for laser trapping and manipulation of particles (as first demonstrated by Ashkin in 1978) [48] and for cavity optomechanics laser light in a resonant cavity can drive mechanical oscillations or cool the motion of mirrors [49]. In principle, radiation pressure could transduce electromagnetic energy to mechanics without any material absorption (unlike photothermal) and without requiring an electrical charge (unlike Coulomb force). However, the force is typically very small. For instance, even a laser with intensity $I = 1\ \mathrm{kW/cm^2}$ exerts a pressure of about $3.3 \times 10^{-5}\ \mathrm{N/m^2}$. In macroscopic cavity optomechanical systems, multiple reflections or high optical power build-up can amplify this effect, enabling significant mechanical coupling. In cavity optomechanics experiments [49], for instance, laser light circulating in an optical cavity can exert sufficient radiation pressure on a mirror or membrane to measurably shift its position or vibrational frequency [50]. This effect has enabled quantum optomechanics demonstrations such as laser cooling of a mechanical resonator's motion to its ground state and observation of radiation-pressure shot noise [26, 50]. However, radiation pressure typically requires a high-Q optical cavity (to build up intracavity photon number) or high-power lasers to be effective, which can be impractical for a simple sensing device. In the context of THz/NIR nano-detectors, pure radiation pressure is generally a secondary effect – the surface area of microcantilevers is small and

the available intensities limited, so photothermal or electrostatic forces dominate. Nonetheless, the principle of radiation pressure is relevant for understanding optomechanical interactions and is actively used in precision measurement systems (e.g. optical levitation, cavity cooling of MEMS) [51–53]. Future NEMS detectors might conceivably exploit radiation pressure in specially designed photonic resonator structures, but so far most demonstrations [26, 41–43] rely on the former two mechanisms, or a combination thereof.

1.4.3 Optothermal transduction

Finally, the photothermal mechanism (also called bolometric or thermoelastic forcing) comes into play when the structure absorbs incident photons and heats up unevenly, causing thermal expansion that in turn drives mechanical motion [54–57]. Photothermal forces have been known to produce significant optomechanical coupling, especially in devices where one part of the resonator is illuminated and undergoes a temperature rise relative to another (creating differential stress or bending) [26]. In fact, early optomechanical systems often observed photothermal effects alongside radiation pressure, as heating usually accompanies absorption. Photothermal actuation is generally slower than pure radiation pressure or electrostatic forces, being limited by the thermal relaxation time of the structure (often micro- to milliseconds). Nonetheless, it can still reach MHz-scale bandwidth in micro/nano structures with tiny thermal masses [26], and can augment the overall responsivity of a detector. In a well-designed NEMSTENNA, one or more of these mechanisms may be engineered to dominate. For example, a plasmonic nanoantenna on a cantilever can leverage electrostatic forces (via charge displacement across a gap) and radiation pressure (from light reflection), while minimizing photothermal lag by using materials and geometries with fast thermal dissipation. A thorough understanding of all three transduction modes is essential for optimizing the device performance.

1.5 Other detection alternatives

It is instructive to compare the NEMSTENNA approach against other contemporary strategies for optical/THz detection, to highlight the advantages of our proposed platform. One competing concept is the microwave rectenna – a direct analog of a radio-frequency rectifying antenna, which aims to convert light to DC electricity using a nanoscale antenna coupled to an ultrafast diode [58]. In theory, a rectenna could harvest or detect optical waves with very high speed (limited only by the diode's tunneling time) and without cooling [59–62]. However, in practice, optical rectennas face formidable challenges. The extremely high frequency of NIR/visible light (~200–400 THz) means that conventional semiconductor diodes cannot respond – their junction capacitances and transit times impose cut-offs in the few-THz range. Specialized nano-diodes such as metal-insulator-metal (MIM) tunnel junctions have been explored to overcome this, but even these suffer from impedance mismatches with the optical antenna and intrinsically low conversion efficiency. To date, reported optical rectennas have achieved only minuscule power conversion efficiencies (on the order of 10^{-3}) at NIR wavelengths [63, 64]. For example, a recent plasmonic rectenna operating at 1.06 μm demonstrated 0.001% efficiency, whereas practical applications would demand efficiencies well above 1% [65]. The shortfall is attributed to several factors: impedance and mode mismatch between the nanoantenna and the diode, significant resistive losses in nanoscale metals (due to the skin effect at optical frequencies), and sensitivity of the antenna resonance to polarization and incidence angle. Overcoming these would likely require complex nanofabrication (e.g. incorporating optical metasurfaces for matching) and has proven very challenging.

Another approach, more traditional in the infrared regime, is the microbolometer or thermoresistive detector. Uncooled microbolometer focal plane arrays are widely used in thermal cameras for the mid-IR (8–12μm) and can operate at room temperature by measuring the change in resistance of a heated element (typically a semiconductor or metal film on a membrane) [66–68]. While bolometers offer

broad spectral response and high sensitivity (especially when thermal isolation is maximized), they are fundamentally slow and power-intensive [67, 69, 70]. A microbolometer pixel usually has a response time in the few-millisecond range or worse, since it must reach a new thermal equilibrium when irradiance changes [26]. Fast modulation or pulsed signals in the kHz–MHz range are essentially invisible to such a detector. Moreover, bolometers require constant bias current and produce a small analog resistance change, necessitating active readout circuits (often with noise performance limited by $1/f$ noise). For THz detection in particular, the highest sensitivity bolometric detectors (e.g. superconducting bolometers or transition-edge sensors) still require cryogenic operation to reduce thermal noise, which is impractical outside laboratory settings [71]. There have been experimental demonstrations of metamaterial bolometers – placing lithographically patterned resonant absorbers on a thermal-isolation membrane to enhance absorption at THz or IR frequencies – but these devices, too, have typical response times on the order of milliseconds [26] and do not solve the speed limitation. In summary, conventional photodetection approaches at THz–optical frequencies either suffer in speed (thermal detectors) or suffer in efficiency/interface (rectennas), and often lack the ability to be truly power-autonomous.

Cavity optomechanics offers another perspective on light detection, one that shares some conceptual similarity to NEMSTENNA in that it marries photonics with mechanics [49]. Over the past decade, cavity optomechanical systems – wherein a mechanical element (like a micro-mirror or membrane) is embedded in a high-finesse optical cavity – have achieved spectacular feats such as quantum-coherent coupling between phonons and photons, laser cooling of mechanical motion to near the quantum ground state, and even entanglement between mechanical oscillators and light [26, 49]. These research breakthroughs, while scientifically important, typically require elaborate setups: high-Q optical cavities aligned with precision, low-noise lasers, and often cryogenic temperatures to suppress thermal noise and achieve quantum regimes. For instance, laser cooling a micromechanical resonator to its ground state has been demonstrated only in cryostat environments

(dilution refrigerators or liquid helium temperatures) in combination with active feedback or dynamical back-action from intense laser drive [50]. The necessity of these conditions means that cavity optomechanical detectors are not yet practical for real-world sensing applications that demand room-temperature operation and simple, robust integration. Moreover, most cavity optomechanics experiments thus far focus on narrowband interactions (tuned to a specific cavity resonance), rather than broadband free-space detection. Integrating an optical cavity on-chip with a mechanical sensor and bringing it to the level of a turnkey device remains an ongoing engineering challenge, with issues such as optical alignment, temperature stabilization, and fabrication complexity to contend with.

1.6 The NEMSTENNA solution

The NEMSTENNA approach intentionally forgoes cavity enhancement and instead uses a nanoantenna to concentrate electromagnetic energy directly onto a mechanical transducer. This cavity-free design sacrifices the ultra-high sensitivity of a resonant optical cavity, but gains in simplicity, bandwidth, and the ability to work passively at room temperature. Essentially, NEMSTENNA aims to harness the light–matter coupling intrinsic to the antenna itself (via near-field forces and absorption) to drive a mechanical response, thereby combining some of the strengths of optomechanics (e.g. precision displacement sensing, high-speed capability) with the practicality of antenna-based detection (broadband operation, direct free-space coupling). The considerations above underscore the need for a detector that can unify the desirable features of speed, sensitivity, room-temperature operation, and low power, which current technologies struggle to provide simultaneously. The proposed NEMSTENNA platform is precisely motivated by this gap. By integrating a plasmonic nanoantenna with a compliant N/MEMS structure (a microcantilever), we create a one-to-one link between the electromagnetic field and a mechanical degree of freedom. The opto-electro-mechanical (OEM) transduction in NEMSTENNA is direct: incident photons are converted

to a force and displacement, without intermediate electronic conversion (as in photodiodes/rectennas) and without relying on heat accumulation (as in bolometers). This confers several key advantages. Speed: The detection is limited by the mechanical resonator's response time, which can be in the microsecond regime or faster – orders of magnitude quicker than thermal detectors [26]. In fact, the interaction can be quasi-instantaneous at the timescale of the optical field envelope, as demonstrated by the Coulomb-force-driven THz meta-atom achieving > 10 MHz bandwidth [26]. Room-temperature, ambient operation: No cryogenic cooling or vacuum environment is required – the NEMSTENNA uses materials and designs compatible with ambient conditions, yet still attains high sensitivity by concentrating field energy at the nanoscale and efficiently coupling it to motion. Non-thermal mechanism: Because it does not hinge on a temperature change, the device is immune to thermal inertia; moreover, it inherently circumvents thermal noise sources that limit bolometer SNR at high frequencies. The principal noise floor in an OEM detector is set by the Brownian (thermomechanical) noise of the mechanical resonator and the readout noise, which at room temperature can still be very low for high-Q microcantilevers (especially when observed over a narrow detection bandwidth). Techniques from cavity optomechanics (like displacement noise measurement near the standard quantum limit) can be leveraged to optimize the readout sensitivity if needed, without fundamentally altering the passive nature of the sensor. In summary, the NEMSTENNA platform represents a novel convergence of nanophotonics, MEMS/NEMS, and optomechanics, aiming to provide fast, sensitive, room-temperature detection of electromagnetic waves.

Having established the operating principles and advantages of NEMSTENNA-type detectors, it is instructive to consider the broad application contexts that motivate their development.

1.7 Application contexts: biomedical diagnostics, communication, and passive sensing

The ability to transduce THz and NIR radiation into mechanical signals opens up a wide range of applications, many of which motivate the development of NEMSTENNA-type devices. Terahertz waves, for instance, have myriad uses in imaging and spectroscopy. The THz band can penetrate certain non-metals and reveal spectral signatures of molecules, making it attractive for chemical sensing, security scanning, and medical imaging. However, the lack of fast, room-temperature THz detectors has historically impeded THz technology deployment. The advent of room-temperature optomechanical THz detectors [26, 42, 43] could enable real-time THz imaging (e.g. for cancerous tissue differentiation or concealed object detection) without cryogenics. For example, an array of THz MEMS meta-atom pixels could form a passive camera to detect terahertz reflections/emissions from a target, potentially useful in biomedical diagnostics (such as skin lesion analysis or dental cavity detection where THz can discriminate water content). Similarly, THz wireless communication is an emerging frontier for beyond-5G networks, promising extremely high data rates. Such systems will require detectors and receivers operating at tens of GHz to sub-THz frequencies. Optomechanical detectors with MHz–GHz bandwidth [43] might be integrated into receivers for short-range THz links, especially if combined with on-chip optical readout. In the near-infrared realm, applications in biomedicine and sensing are abundant. The NIR tissue transparency window (approximately 700–1300 nm) is optimal for deep tissue imaging because absorption and scattering in tissue are minimized. This has led to the rise of NIR optical diagnostic techniques, including fluorescence imaging, photoacoustic imaging, and optical coherence tomography, which can probe centimeters into biological tissue. An NIR-responsive NEMS detector could be used as a biosensor or imaging pixel that is activated by NIR light. For instance, Huang *et al.* [72] demonstrated a biomimetic NIR photoacoustic nanoprobe for cancer diagnosis, in which indocyanine-green-loaded nanoparticles accumulate in tumors

and provide enhanced photoacoustic imaging contrast. This illustrates the power of NIR in biomedical diagnostics: by using NIR illumination, one can achieve deeper, high-contrast imaging of pathological sites. A NEMSTENNA device could potentially serve as a miniaturized photoacoustic sensor or an implantable optical sensor that reacts mechanically to specific NIR illumination (for example, detecting the presence of a particular dye or molecular marker that absorbs NIR).

Another context is wireless communication and remote sensing. Free-space optical communication (FSO) often uses near-infrared lasers (e.g. 1550 nm) for point-to-point links. Conventional photodiodes easily handle such signals, but in scenarios where one desires a completely passive receiver (no electrical power at the receiving end), a NIR NEMSTENNA could be intriguing. It could convert the received optical communication signal into a mechanical vibration that can be sensed without powering a diode. Such a passive optical receiver might find use in environments with high electromagnetic interference or where electronics cannot be used (for example, inside an MRI machine or in space applications with high radiation). Additionally, the concept of remotely powering and reading sensors via optical beams is attractive for the Internet of Things (IoT). A network of tiny MEMS sensors spread in an environment could be interrogated by a scanning laser that simultaneously powers them and reads their mechanical response, analogous to how RFID tags are read by radio waves. Because NIR light can carry high power density with eye-safe operation (at 1550 nm), one can envision delivering milliwatt-level power to a MEMS device to actuate it, then monitoring its response optically. A particularly promising application area is in biomedical implants and microrobotics. As noted, a NEMSTENNA device can be configured as a wireless nanoswitch or actuator controlled by light. For example, an implanted microstimulator in the body could incorporate a NIR-driven MEMS switch that turns on in response to an external NIR light (transcutaneously delivered), eliminating the need for batteries or transcutaneous wires.

1.8 Thesis objectives

This thesis is devoted to the design, modeling, and experimental validation of such a platform operating in the NIR range. The main goals of the work include: (1) Design optimization of the nanoantenna-cantilever structure, in terms of geometry, to maximize the optomechanical coupling (i.e. maximize mechanical deflection per incident optical power) while maintaining mechanical resonance characteristics suitable for high-speed operation. We explore different antenna designs and cantilever dimensions, taking into account plasmonic resonance behavior, impedance matching, and mechanical stiffness/mass trade-offs. (2) Theoretical modeling and simulation of the coupled electro-opto-mechanical behavior, primarily using finite-element multiphysics simulations (COMSOL) to predict electromagnetic field distributions, photothermal effects, and the resultant mechanical deformation. Both frequency-domain and time-domain analyses are employed to understand the steady-state responsivity and the transient dynamics of the device. Analytical models are also developed to capture the essence of the transduction mechanism and to provide intuition for scaling laws. (3) Fabrication of prototype NEMSTENNA devices. A relatively simple nanofabrication process is utilized, starting from commercially available silicon nitride microcantilevers (like those used in atomic force microscopy) and nano-patterning plasmonic structures onto them via focused ion beam (FIB) milling [44].

1.9 Summary of thesis publications

This doctoral work has been carried out within the framework of four main research papers, which together trace the development of an optomechanical antenna operating in the near-infrared (NIR) range. The chronological progression of these studies reflects the conceptual, experimental, and theoretical advances achieved during the thesis.

- **Paper 1:** *Design and fabrication of an opto-mechanical antenna in the*

NIR range (section A.1) — This paper presents the initial design concept and nanofabrication methodology of the optomechanical antenna. The work establishes the foundational principles for coupling optical and mechanical modes in the NIR regime.

- **Paper 2:** *Impact of the parasitic photothermal effect on the performance of an optomechanical nanoantenna for NIR radiation detection* (section A.2) — This study investigates the influence of parasitic photothermal effects on device sensitivity, combining experimental observations with theoretical modeling.

- **Paper 3:** *Plasmomechanical actuation at the nanoscale activated by NIR radiation* (section B.2) — This publication explores the actuation mechanisms of an improved design of optomechanical antenna when excited by near-infrared radiation, demonstrating the enhancement of responsivity.

- **Paper 4:** *Tuning fork optomechanical NIR antenna with integrated optical transmission line* (section B.3) — The final paper presents an integrated antenna system featuring an optical transmission line for efficient signal extraction, representing the culmination of the thesis development.

These four publications form the research journey, from design and modeling to fabrication, and characterization.

Chapter 2

Methods

This chapter outlines the multiphysics framework used to design and analyze the proposed optomechanical antennas (NEMSTENNA). We employ the Finite Element Method in COMSOL Multiphysics® to model four tightly coupled domains—electromagnetic, electrical, thermal, and mechanical—chosen for their relevance to resonance, absorption, heating, and deformation. Frequency-domain Maxwell solutions (with PMLs and lumped ports) provide field distributions and gap voltages; these drive heat generation used in steady/transient thermal analyses with thin-film properties and interface resistances. The resulting temperature fields and electrostatic forces are the input variables for mechanical simulations.

In this chapter, methods related to nanofabrication, FIB milling process are also described.

2.1 Computational methods and modeling techniques

This section provides a comprehensive overview of the computational techniques and numerical methods employed in this thesis to perform the analyses required for evaluating the proposed NEMSTENNA devices.

Modelling was carried out in the near-infrared (NIR) spectral region, where the free-space wavelength is on the order of one micrometer. According to the frequency–size domain map (Figure 2.1), this regime lies at the transition between the RF and Wave Optics modules (Wave Regime) in COMSOL Multiphysics, which justifies the use of numerical solvers that fully account for Maxwell's equations in this wavelength range. The modeling covers four main physical domains:

electromagnetic, electrical, thermal, and mechanical. Each domain presents unique challenges in terms of simulation strategy, numerical accuracy, and computational efficiency.

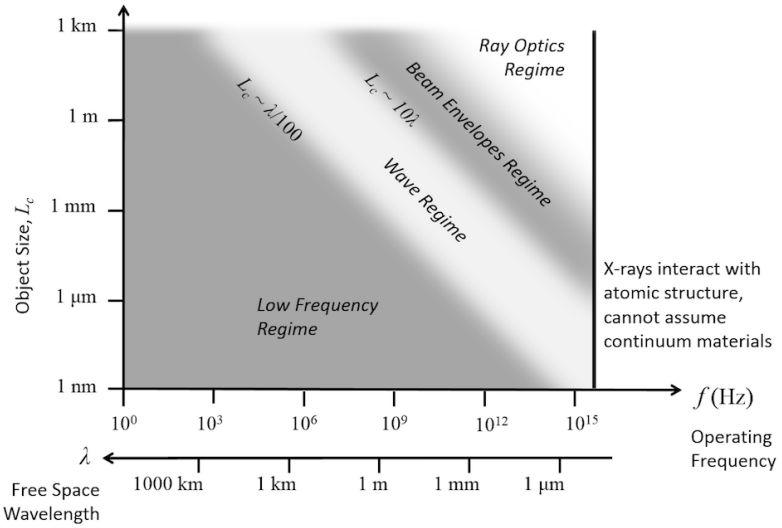

Figure 2.1: Operating frequency–object size domain map indicating the applicable physics modules in COMSOL MULTIPHYSICS. The NIR regime (highlighted in this work) lies in the transition between the RF and Wave Optics modules, where full-wave electromagnetic solutions are required (Wave Regime). In this study, the RF, Electrostatics, Solid Mechanics, and Heat Transfer in Solids modules were combined to evaluate the opto-electromechanical (OEM) and opto-thermo-mechanical (OTM) effects in the NEMSTENNA device [73].

The selection of an appropriate numerical technique depends primarily on two fundamental factors: the *nature* of the physical problem and the *geometry* of the structure. The nature of the problem refers to the governing physical laws and the types of differential equations involved—whether ordinary differential equations (ODEs), partial differential equations (PDEs), or equations that exhibit nonlinearity. These characteristics determine the stability, convergence, and numerical complexity of the simulation.

Geometric features also strongly influence the choice of method. Some numerical techniques are optimized for simple, periodic, or symmetric structures, such as Finite-Difference Time-Domain (FDTD) for uniform grids. However, more ge-

ometrically complex, layered, or irregular structures benefit from methods like the Finite Element Method (FEM), which provides high adaptability and spatial resolution.

In this work, modelling and simulations are categorized into four domains and their corresponding COMSOL modules:

1. **Electromagnetic simulations performed in the RF module:** Used to model the propagation and confinement of electromagnetic waves in the NIR regime. Since the characteristic feature sizes of the antenna are comparable to the operating wavelength, a full-wave solution of Maxwell's equations is necessary. This enabled the calculation of the optical electromagnetic (OEM) effect and the evaluation of field enhancement within the structure.

2. **Electrical simulations performed in the electrostatics module:** Implemented to account for the static electric fields produced by DC bias voltages applied to the structure. These fields play a role in tuning the antenna's optical response and establishing the conditions for optomechanical coupling.

3. **Thermal simulations performed in the heat transfer in solids module:** Incorporated to simulate the thermal response of the system due to optical absorption in the NIR. The resulting temperature distribution couples with solid mechanics to describe the opto-thermo-mechanical (OTM) effect, which is significant for understanding thermal tuning and stability in the device.

4. **Mechanical simulations performed in the solid mechanics module:** Applied to evaluate the structural deformation induced by both electrostatic forces and thermal expansion. Mechanical displacement and stress fields were essential to quantify the optomechanical interaction and to predict resonance shifts caused by nanoscale deformations.

5. **Coupling between modules:** The combination of these modules provided a multiphysics framework that captures the interplay between electromagnetic,

electrostatic, mechanical, and thermal phenomena in the NEMSTENNA device. In particular, the OEM effect was evaluated through the coupling of the RF and Solid Mechanics modules, while the OTM effect was obtained through the coupling of the Heat Transfer and Solid Mechanics modules. This approach ensures that both optical and thermomechanical contributions to the device performance are consistently represented.

While the geometries under investigation in this thesis are largely rectilinear and uniform, specific regions within the structures require high-resolution meshing due to abrupt changes in the physical fields. For instance:

- In metallic regions, electromagnetic fields decay exponentially due to the skin effect, necessitating fine meshing.
- At thermal interfaces with high thermal resistance, steep temperature gradients occur, requiring localized mesh refinement.
- In mechanical simulations, regions of constrained motion or structural discontinuities often experience high stress concentrations, demanding denser mesh coverage.

The **Finite Element Method** is particularly well-suited for these scenarios due to its capability for non-uniform, adaptive meshing, as well as its flexibility in applying complex boundary conditions and material definitions. In contrast to grid-based techniques like FDTD or Finite Volume Method (FVM), FEM allows for more efficient and accurate resolution of localized physical phenomena.

The subsequent sections detail the modeling assumptions, meshing strategies, solver configurations, material properties, and boundary conditions applied in each domain. Where applicable, simulation results are validated through comparison with analytical models or published literature to ensure fidelity and reliability.

2.1.1 Electromagnetic modeling

In this work, we are interested in the design and analysis of optomechanical antennas, which involve engineered electromagnetic structures capable of coupling optical fields with mechanical motion. Understanding the electromagnetic response of these structures is essential for tailoring their resonance behavior and optimizing their interaction with mechanical modes.

To compute the relevant electromagnetic quantities, a time-harmonic solution to the wave equation for the electric field is employed. Specifically, Maxwell's wave equation for the electric field is solved:

$$\nabla \times (\nabla \times \mathbf{E}) - k_0^2 \left(\varepsilon_r - j \frac{\sigma}{\omega \varepsilon_0} \right) \mathbf{E} = 0 \tag{2.1}$$

where:

- $\mathbf{E}$ is the electric field vector,
- k_0 is the free-space wave number,
- ε_r is the relative permittivity of the medium,
- σ is the electrical conductivity of the medium,
- ω is the angular frequency of harmonic excitation,
- ε_0 is the vacuum permittivity.

The boundary conditions for solving Eq. (2.1) depend on the geometry and intended functionality of the optomechanical antenna. Commonly used boundary conditions include:

- **Perfectly Matched Layers (PMLs):** To absorb outgoing waves and simulate open boundaries.

- **Scattering or Port Conditions:** For launching and collecting waves, enabling the calculation of quantities such as reflection, absorption, and transmission.
- **Electric or Magnetic Walls:** Applied where symmetry can be exploited or to constrain specific field components.

All simulations are performed using the RF module in COMSOL Multiphysics®, which utilizes the Finite Element Method (FEM) to solve the frequency-domain Maxwell's equations. This approach provides high spatial resolution near material interfaces and supports the modeling of complex, dispersive, and lossy materials [73].

This electromagnetic simulation framework provides the foundation for analyzing the optical behavior of the proposed optomechanical antenna structures, including field localization, radiation patterns, and resonance characteristics critical to their coupled optomechanical functionality.

2.1.1.1 Boundary Conditions

The **Lumped Port** boundary condition is employed in simulations where the excitation is applied across a small localized region, such as a feed gap in nanoantennas, shown in Figure 2.2. This boundary condition is particularly advantageous when the physical dimensions of the excitation region are much smaller than the operating wavelength, and a full modal description is either unnecessary or computationally inefficient.

In the context of optomechanical antennas, the lumped port is typically defined between two metallic electrodes or across a nanogap within the antenna structure. It acts as a localized source that injects power based on a specified voltage or current, effectively mimicking the feeding mechanism of the antenna.

Using the lumped port allows for:

- Efficient simulation of input impedance and resonance characteristics,

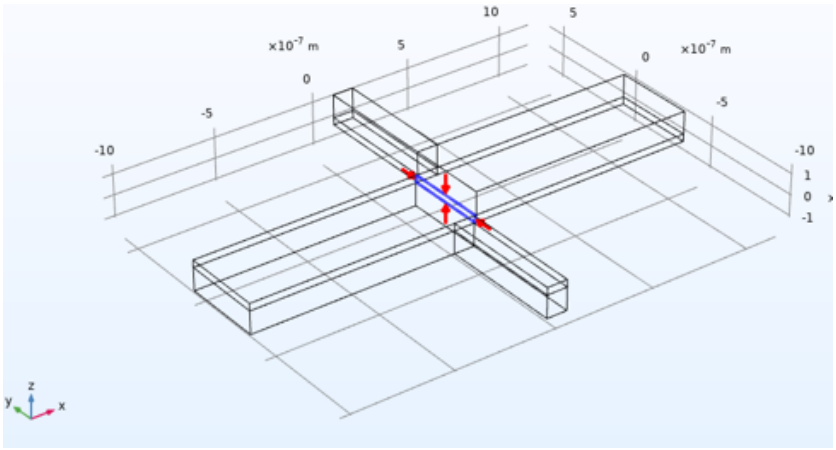

Figure 2.2: Geometry of the NEMSTENNA device Paper 1 (A.1) showing the excitation applied through a lumped port. The lumped port (indicated by the red and blue arrows) was used to excite the antenna structure and evaluate its optical and electromagnetic response in the near-infrared (NIR) regime.

- Accurate computation of reflection (S_{11}) coefficient.
- Enhanced control over the electromagnetic energy coupling into subwavelength regions.

Perfectly Matched Layer (PML) is used to simulate open-space conditions by preventing reflected waves from propagating back into the computational domain. This boundary condition is especially useful when the simulation involves wave propagation or radiation problems, such as electromagnetic waves emitted by an antenna.

In the context of a **PML**, a hypothetical layer is introduced around the computational domain to absorb the outgoing waves, ensuring that they do not reflect back into the simulated environment, which would otherwise distort the results. The PML is not a real material or boundary but rather a mathematical construct designed to simulate a perfect radiation boundary.

In optomechanical antenna simulations, using PML allows the model to replicate realistic far-field behavior, where waves radiate outward without interference from boundary reflections.

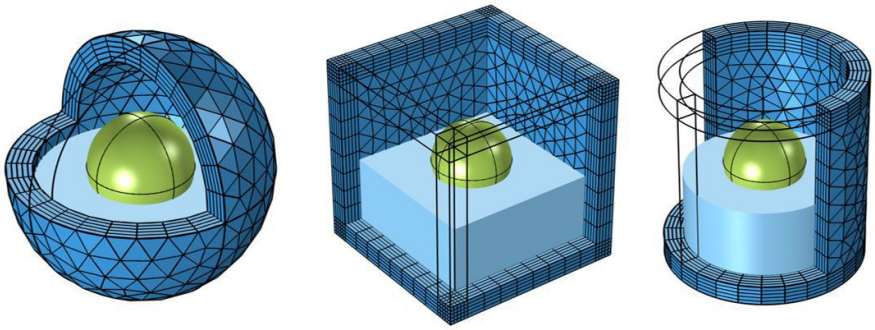

Figure 2.3: Comparison of different PML (Perfectly Matched Layer) geometries used for electromagnetic simulations: (left) spherical PML enclosing a hemispherical scatterer, (center) cuboidal PML surrounding a block-shaped domain, and (right) cylindrical PML adapted to a rotationally symmetric model. PMLs are employed to absorb outgoing waves and prevent artificial reflections at the boundaries of finite simulation domains [73].

PMLs are artificial absorbing materials surrounding the simulation domain that are designed to match the impedance of the interior domain perfectly, thereby eliminating reflections at the interface. Electromagnetic waves entering the PML are absorbed exponentially without reflection, regardless of the angle of incidence or frequency (within a certain bandwidth).

Figure 2.3 presents three common geometries for PML implementations:

Spherical PML (left): Often used in problems involving radially symmetric radiation, such as scattering from nanoparticles or dipoles in spherical domains. The curvature of the PML conforms to the natural propagation of outgoing waves.

Cuboidal PML (center): A more general-purpose geometry, commonly used in Cartesian-based solvers. While easy to implement, care must be taken to ensure sufficient thickness and grading for oblique incident waves.

Cylindrical PML (right): Best suited for axisymmetric problems such as waveguides or structures with rotational symmetry. This geometry provides an efficient trade-off between accuracy and computational cost in such cases.

In this thesis, PMLs are employed in the finite-element simulation of infrared nanoantennas and optomechanical resonators to ensure realistic evaluation of radiation patterns, resonance conditions, and energy absorption characteristics. By

surrounding the computational domain with PMLs, back-reflections from domain boundaries are minimized, improving the fidelity of the computed field distributions and resonance behaviors. In our optomechanical antennas simulations, we have used spherical simulation setup.

2.1.1.2 Structure Excitation

In our laboratory, an infrared (IR) laser has been utilized for the excitation of our optomechanical antennas. In order to model this excitation, we have been using a focused Gaussian laser beam. For a focused laser beam, the paraxial approximation of a Gaussian beam is often employed, governed by the paraxial Helmholtz equation. This approximation assumes that the beam divergence is small and is valid when the beam waist is significantly larger than the wavelength, i.e., $w_0 \gg \lambda$.

The electric field distribution of a Gaussian beam under the paraxial approximation is expressed as:

$$E(x, y, z) = E_0 \sqrt{\frac{w_0}{w(y)}} \exp\left[-\frac{x^2}{w^2(y)} - jky - jk\frac{x^2}{2R(y)} + j\frac{\eta(y)}{2}\right], \tag{2.2}$$

where $w(y)$ is the beam radius at position y, $R(y)$ is the radius of curvature of the wavefront, and $\eta(y)$ is the Gouy phase. These parameters are defined as follows:

$$w(y) = w_0 \sqrt{1 + \left(\frac{y - p_0}{y_0}\right)^2}, \tag{2.3}$$

$$R(y) = (y - p_0)\left[1 + \left(\frac{y_0}{y - p_0}\right)^2\right], \tag{2.4}$$

$$\eta(y) = \tan^{-1}\left(\frac{y - p_0}{y_0}\right), \tag{2.5}$$

$$y_0 = \frac{k w_0^2}{2}, \tag{2.6}$$

where w_0 is the beam waist at the focus, p_0 is the focal position along the prop-

agation direction y, and y_0 is the Rayleigh range, representing the distance over which the beam remains approximately collimated.

In this work, the condition $w_0 > \lambda$ holds, making the paraxial approximation a valid and accurate solution. However, in cases where $w_0 < \lambda$, i.e., for tightly focused beams, the paraxial model becomes insufficient. In such scenarios, a more accurate description involves plane-wave expansion methods that go beyond the paraxial approximation and offer better precision for sub-wavelength beam waists. Figure 2.4 displays the spatial distribution of the x-component of the background electric field (E_x) in units of V/m, of a Gaussian laser beam. The field distribution reveals a strong confinement and periodic oscillation along the beam propagation axis, characteristic of a well-collimated Gaussian profile.

The color map indicates a peak field intensity exceeding 8×10^5 V/m at the center of the structure, where the nanoantenna feedgap is located. The alternating red and blue lobes represent regions of positive and negative electric field, respectively, illustrating the wave nature of the field along the optical axis.

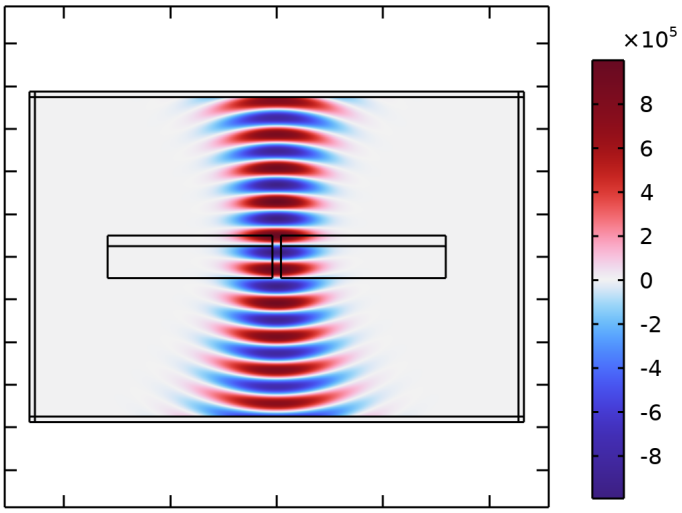

Figure 2.4: Background electric field, x component (V/m), of a laser Gaussian beam focused on the gap of a nanoantenna structure.

2.1.2 Thermal Modeling

The temperature dynamic distribution in the proposed optomechanical antennas is critical for estimating parameters such as energy consumption and the proper functioning of the device, especially in terms of heat dissipation and thermomechanical effects. Dynamics of the temperature field is governed by the heat transfer equation:

$$DC_p \frac{\partial T}{\partial t} - \nabla \cdot (k \nabla T) = Q + q'' \tag{2.7}$$

where D is the mass density, C_p is the specific heat capacity at constant pressure, T is the temperature and k is the thermal conductivity of the material. First term signifies the time derivative of thermal energy per unit volume, and the second term represents the heat flux exiting the unit volume due to a temperature gradient.

Finally, Q and q'' represent the volumetric heat injection and dissipated heat flux (W/m^2), which will arise from optical excitation and thermal convection, respectively. Although this equation is a well-known heat transfer equation for macroscopic media, its applicability to modeling nanoscale material systems is justified. Geometrically, when the thickness of a thin material film approaches the mean free path of heat carriers, a strong boundary scattering effect significantly reduces thermal conductivity. This phenomenon has been extensively described and validated, particularly in the case of gold and Si_3N_4 layers. Modified thermal properties are essential for accurate modeling at the nanoscale, accounting for the distinct geometrical features of thin films. For instance, based on conclusions by Chen and Hui, the thermal conductivity of a 35 nm gold film is only 47% that of bulk gold, and similarly, a 140 nm Si_3N_4 layer exhibits a thermal conductivity of 72% that of bulk Si_3N_4. The significant deviation of thermal properties in submicrometer devices is well-documented in the literature [74–76]. At the nanoscale, Sultan et al. reported a thermal conductivity of 3–4 $W/(m.K)$ for 500 nm thin films in a temperature range of 77–325 K, Stojanovich et al. measured a thermal

conductivity of about 2.1 $W/(m.K)$ for 180 nm thick freestanding specimens, and Bai et al. determined a thermal conductivity of 1.2–2.0 $W/(m.K)$ for stoichiometric silicon nitride films with thicknesses ranging from 37 to 200 nm [77, 78].

2.1.2.1 Thermal Boundary Conditions

In the numerical analysis of heat transfer differential equations, two categories of boundary conditions (BCs) are considered: exterior BCs and interior BCs. Exterior BCs are applied to the outermost boundaries of the geometric model and typically encompass Dirichlet BC, Neumann BC, and BC for the material/air interface. In the case of Dirichlet BC, the temperature at the boundary is fixed, denoted as T=Tfix. A specific instance of the Neumann BC is the thermal-isolation BC, expressed as $\vec{n}.(-k\nabla T) = 0$, signifying that the normal derivative of temperature is zero. Boundary conditions for the material/air interface are elaborated as follows:

$$\vec{n}.(-k\nabla T) = h(T - T_0) + \varepsilon\sigma(T^4 - T_0^4) \tag{2.8}$$

The term on the left side represents the outward conductive heat flux, while on the right side, the first term accounts for convective heat flux to the air environment, and the second term represents radiation heat flux. In these expressions, $\vec{n}$ denotes the outward vector normal to the boundary surface, h is the convective heat transfer coefficient of air with a value of 5 $W/(m^2.K)$, and ϵ signifies the surface emissivity. The Stefan-Boltzmann constant is denoted as $\sigma = 5.67\times10^{-8}$ (W/m^2K^4).

For natural convection in air at large scales, typical values for h are in the range of 5-10 $W/(m^2.K)$. However, in nanoscale devices, the convective heat transfer coefficient (h) should be substantially higher. According to the scaling law proposed in reference [79], the convective coefficient for air has been reported as 100 $W/(m^2.K)$ when the scale is less than 100 μm, representing a tenfold increase compared to macro-scales [80]. This enhanced heat transfer coefficient at the nanoscale is attributed to improved convection heat transfer due to compressed boundary layers at very small scales [80]. The assigned h values in the heat transfer module for the Au/SiN boundary layers are elicited through extrapolation

from reference [79], considering nano dimensions. The ambient temperature is set at T=293 K. Interior boundary conditions are inherently continuous, with the metal/dielectric interface treated as a continuous condition, described by:

$$\vec{n}.(-k_{metal}\nabla T_{metal}) = \vec{n}.(-k_{dielectric}\nabla T_{dielectric}) \tag{2.9}$$

Moreover, at the interface, the temperatures T_{metal} and $T_{\text{dielectric}}$ are considered equal, where k_{metal} and $k_{\text{dielectric}}$ represent the thermal conductivity, and T_{metal} and $T_{\text{dielectric}}$ denote the temperatures of the metal and dielectric, respectively. In the analysis of a multilayer thin film structure such as NEMSTENNA, the impact of finite thermal boundary resistance (TBR) should be taken into account. TBR is defined as:

$$q = \left(\frac{1}{R_{\text{eq}}} + h_r\right)(T_A - T_B) \tag{2.10}$$

The heat flux q across the interface between materials A and B is governed by the combined effect of thermal boundary resistance (TBR), represented by R_{eq}, and radiative conductance h_r. The term $(T_A - T_B)$ denotes the temperature difference at the interface. A finite TBR introduces a temperature discontinuity at the interface, emphasizing its crucial role in thermal transport—especially in nanoscale systems.

Interfaces between different materials, such as metal and dielectric thin films, can significantly influence heat transport, often dominating over the bulk thermal properties of the individual layers [75]. The presence of TBR leads to a localized temperature drop at the interface, a phenomenon first observed by Kapitza at the boundary between solid and liquid helium in 1941 [81, 82]. Importantly, TBR is generally considered independent of film thickness, underlining its persistent impact in layered nanoscale architectures.

TBR originates from mismatches in vibrational (phonon) spectra between dissimilar materials and is influenced by the product of their phonon densities of states [75, 83]. At the Au/SiN_x interface, where heat carriers must transition between electron-dominated (metal) and phonon-dominated (dielectric) transport mecha-

nisms, a pronounced thermal boundary resistance is expected. For instance, Jeong et al. [75] reported a TBR value of 0.81×10^{-8} m^2K/W at the Au/SiN_x interface, as measured using the transient thermoreflectance (TTR) technique [84]. The consideration of thermal boundary resistance (TBR) at the metal–dielectric interface is essential in micro- and nanoelectronic devices, as it significantly affects the apparent thermal conductivity of dielectric layers, especially when their thickness is reduced to the nanoscale regime.

2.1.3 Optothermal coupling equations

This subsection investigates how the temperature distribution in the NEMSTENNA structure is calculated from heat generated by optical absorption. The analysis is based on a fully coupled simulation involving steady-state heat transfer and frequency-domain Maxwell's equations, aiming to capture thermal patterns under optical excitation.

The heating mechanism in the structure arises from optical absorption governed by Maxwell's equations, which in turn generate localized heat through resistive (Joule) losses. The electric field distribution, obtained from the solution of Maxwell's equation, equation (2.1), serves as the input to the thermal model for calculating the volumetric heat source.

The electric field $\mathbf{E}$ obtained from equation (2.1) is used to compute the electromagnetic heat source Q_e, which represents resistive (ohmic) heating in lossy materials:

$$Q_e = \frac{1}{2}\omega\varepsilon_0 \,\mathrm{Im}(\varepsilon_r)|\mathbf{E}|^2 \tag{2.11}$$

This expression quantifies the absorbed optical power density as a function of the electric field intensity and the imaginary part of the material's relative permittivity at the laser frequency (193.41 THz in our case).

Under the assumption of continuous illumination, the thermal problem is modeled in the steady-state regime using the heat conduction equation, derived from equation (2.7):

$$\nabla \cdot (-\kappa \nabla T) = Q_e + q'' \tag{2.12}$$

where κ is the thermal conductivity, T is the temperature distribution, q" corresponds to thermal convection and Q_e acts as the internal heat source.

Solving this equation enables the prediction of the temperature field in response to localized optically induced heating.

2.1.4 Mechanical modeling

2.1.4.1 Thermomechanical

Thermal actuation, based on the fundamental property of materials to change volume with temperature variations, is described here. Each material possesses a coefficient of thermal expansion (CTE), signifying a change in size with temperature variations. The relationship between thermal expansion or strain, thermal expansion coefficient α, and temperature is provided below [85, 86]:

$$\varepsilon_{th} = \alpha(T - T_{ref}) \tag{2.13}$$

In a cantilever structure composed of multiple materials, each having distinct coefficients of thermal expansion (CTE) and layer thicknesses, the portion of the beam with greater thickness—such as a 70 nm gold layer compared to a 35 nm gold layer with the same CTE—undergoes bending and deflection. This effect arises from the expansion strain caused by the increased thickness of the gold layer, leading to thermal-induced deformation.

2.1.4.2 Electromechanical

The electromechanical performance of the proposed optomechanical antennas was analyzed using a fully coupled finite element framework in **COMSOL Multiphysics®** [44, 73]. The model integrates the *Solid Mechanics*, *Electrostatics*, and *Electromagnetic Waves, Frequency Domain* interfaces within a single multiphysics environment, enabling simultaneous simulation of optical excitation, electrostatic

actuation, and mechanical deformation. The *Moving Mesh* method was employed to dynamically track geometry variations in the nanoscale feed gap as the structure deforms [73].

The antenna consists of a gold–silicon nitride bilayer cantilever system, whose free ends form a dipole nanoantenna separated by a narrow gap, as shown in Figure 2.5.

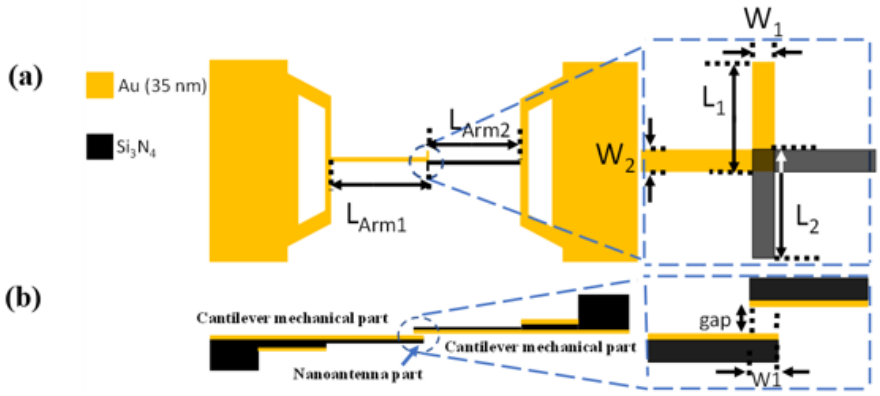

Figure 2.5: Schematic top (a) and side (b) views of the proposed gold–silicon nitride bilayer cantilever system. The free ends of the cantilever form a dipole nanoantenna separated by a narrow gap. The structure parameters are labeled as L_{Arm1}, L_{Arm2}, L_1, L_2, W_1, and W_2. The gold and Si_3N_4 layers have thicknesses of 35 nm and 140 nm, respectively.

The electromagnetic excitation and mechanical response were solved sequentially but coupled through a common field variable representing the induced feed-gap voltage.

The optical excitation was modeled through the *Electromagnetic Waves, Frequency Domain* interface. Maxwell's curl equations were solved in the frequency domain for a Gaussian beam centered at $\lambda = 1.55\ \mu$m (f = 193.41 THz), corresponding to the near-infrared resonance wavelength of interest.

The feed-gap voltage was obtained through line integration of the electric field in the gap region [87, 88]:

$$V_0 = \left| \int_{\mathrm{gap}} \mathbf{E} \cdot d\mathbf{l} \right|, \tag{2.14}$$

and the resulting time-dependent voltage was expressed as

$$V_{\text{gap}}(t) = V_0 \sin(\omega t). \tag{2.15}$$

This voltage acts as the driving signal for the electrostatic coupling.

The *Electrostatics* module was used to determine the attractive electrostatic forces induced between the two cantilever tips. The coupled equation set follows Gauss's law and the constitutive relation [73]:

$$\nabla \cdot \mathbf{D} = \rho_v, \qquad \mathbf{E} = -\nabla V, \tag{2.16}$$

where $\mathbf{D}$ is the electric displacement, ρ_v is the volume charge density, and V is the electrostatic potential.

The feed-gap voltage V_0 obtained from the RF module was applied across terminals defined on the facing surfaces of the antenna arms, while the opposite terminals were grounded. The resulting electrostatic force was expressed as [44]:

$$F_{\text{ee}}(t) = \frac{\varepsilon_0 A}{2[g_0 - z_1 - z_2]^2} (V_0 \sin \omega t)^2, \tag{2.17}$$

where A is the overlap area, g_0 is the initial gap, and z_1 and z_2 are the displacements of the cantilever tips. The oscillatory term at 2ω averages to zero for optical frequencies, leaving the quasi-static DC component [44]:

$$F_{\text{DC}} = \frac{\varepsilon_0 A V_0^2}{4[g_0 - z_1 - z_2]^2}. \tag{2.18}$$

This force was applied as a distributed surface load within the *Electromechanical Forces* multiphysics interface, which automatically couples the *Electrostatics* and *Solid Mechanics* modules through the Maxwell stress tensor formulation.

The mechanical deformation was computed using the *Solid Mechanics* interface with *Linear Elastic Material* properties and geometric nonlinearity enabled. The

governing equation in the time-dependent study was [73]:

$$\rho \frac{\partial^2 \mathbf{u}}{\partial t^2} = \nabla \cdot (\mathbf{FS})^{\mathsf{T}} + \mathbf{F}_v, \qquad \mathbf{F} = \mathbf{I} + \nabla \mathbf{u}, \tag{2.19}$$

where ρ is the density, $\mathbf{u}$ is the displacement field, and $\mathbf{S}$ is the second Piola–Kirchhoff stress tensor. Fixed constraints were applied at the anchored ends of the cantilevers, and free boundaries were maintained elsewhere to allow natural bending.

The *Moving Mesh* interface ensured that the computational mesh followed the deformation, maintaining numerical accuracy when the gap size approached nanoscale values and preventing element distortion [73].

The simulation framework can operate in two distinct regimes [89]:

1. **Static (non-iterative) mode:** the feed-gap voltage is computed once at the initial geometry, and the resulting electrostatic force is applied to calculate the equilibrium deflection. This mode is computationally efficient and valid for small deformations or low optical powers.

2. **Dynamic (iterative) mode:** a two-way coupling updates the geometry after each mechanical solution step, re-evaluating the electromagnetic field and the resulting voltage at the deformed configuration. This iterative loop is essential when large deflections or strong nonlinear electromechanical coupling occur.

2.2 Fabrication methods

The fabrication and structural characterization of the optomechanical antenna structures were carried out using a dual-beam Focused Ion Beam–Scanning Electron Microscope (FIB-SEM) system (Fig. 2.6). High-resolution SEM imaging with precise ion beam milling enables accurate patterning and inspection of sub-micron features.

Figure 2.6: Focused Ion Beam–Scanning Electron Microscope (FIB-SEM) system used for nanoantenna fabrication and structural characterization. The dual-beam setup enables high-resolution SEM imaging and site-specific milling with ion beams, which is essential for preparing and analyzing nanoscale structures. This system was instrumental in prototyping and inspecting the critical dimensions of the fabricated NEMSTENNA devices.

2.2.1 FIB-SEM nanofabrication system and imaging

Prototypes for all optomechanical antenna designs were realized using a dual-beam Focused Ion Beam/Scanning Electron Microscope (FIB-SEM) system. This instrument combines a focused Ga^+ ion beam for nanoscale milling with an electron beam for high-resolution imaging and alignment. The Ga^+ ion column was operated at an accelerating voltage of 30 kV, with beam currents selectable from just a few pA (for highest-resolution milling) up to several nA (for rapid bulk material removal). Such a wide current range allowed each fabrication step to be optimized for either precision or speed. The integrated SEM was essential for non-destructive monitoring: it enabled precise alignment of milling patterns and in-situ inspection of the structures after each milling step. For instance, during mi-

crocantilever thinning (described below), the process was periodically paused to collect SEM images, which helped monitor stress-induced bending and ensure the milling was stopped before structural collapse. Final SEM inspections confirmed the achievement of nanoscale feature sizes and structural integrity in all devices. In summary, the FIB-SEM's dual-beam capabilities – high-energy Ga^+ milling and real-time SEM imaging – were key to fabricating these nano-optomechanical antennas with sub-100 nm features and to overcoming alignment and metrology challenges in the process.

2.2.2 Library of FIB milling procedures

1. **Thinning and top metal removal:** Flip the cantilever and use low-current FIB milling to strip the 70 nm Cr/Au top coating and thin the Si_3N_4 membrane at the free end. This first step (FIB at 700 pA, fast scan) removes the bulk metal and reduces Si_3N_4 to 50 nm (achieving 5–10 nm vertical resolution) (Papers 1 and 3)(A.1)(B.2)(see Appendix (C.1)).

2. **Outline milling (large structures)(micro):** Perform a high-current FIB pass to sketch the antenna outline. In this coarse step the beam mills the perimeter of the antenna shape, removing the surrounding film and isolating the structure (Papers 1 and 3)(A.1)(B.2)(see Appendix (C.1)).

3. **Outline milling (small structures)(nano):** Reduce the FIB beam current and aperture for fine-detail etching. By progressively lowering current (e.g. from 3 nA) and slowing the scan, the antenna's small features are defined with 10 nm lateral precision (Papers 1 and 3)(A.1)(B.2)(see Appendix (C.1)).

4. **Edge polishing:** Optionally, perform a final low-current polish to clean redeposition and smooth sidewalls of the milled features. A gentle FIB or broad-beam polish removes residual debris and sharpens edges (as practiced in related FIB nanofabrication) (Paper 4)(B.3)(see Appendix (C.2)).

5. **Feed-gap trench definition (low resolution):** Coarsely mill the feed-gap region to separate the two antenna arms. A first FIB cut (moderate current, fast scan) creates a rough trench across the feedpoint, roughly defining the gap area (Paper 4)(B.3)(see Appendix (C.2)).

6. **Feed-gap trench definition (high resolution):** Finally, refine the trench with a high-resolution FIB pass. Using a fine (low-current) beam and multiple passes, the feed gap is narrowed to its final width (few nm) for device operation (Paper 4)(B.3)(see Appendix (C.2)).

Chapter 3

Results

This chapter presents the design, fabrication, and characterization of nanoelectromechanical plasmonic antennas (NEMSTENNA) operating at $\lambda = 1.55$ μm. The working principle is detailed by distinguishing the desired optoelectromechanical (OEM) signal—driven by the feedgap voltage—from the parasitic optothermomechanical (OTM) bending. COMSOL simulations quantify the electromagnetic response (S_{11}, V_{gap}) and the resulting static deflections. Finally, we benchmark responsivity against state-of-the-art, outlining a path toward OEM dominated operation.

3.1 Designed structures

Three optomechanical antenna structures were designed and studied. All three designs share the same basic concept: a plasmonic gold nanodipole antenna is integrated at the free end of an N/MEMS structure, forming a NEMSTENNA (micro/nano-electromechanical antenna) device. They differ primarily in the dipole length and width, and the structure geometry configuration and dimensions of the N/MEMS structure [44, 89–91]. Three distinct dipole antenna geometries were implemented and integrated with nano/microelectromechanical system (N/MEMS) structures. Each of the dipole antennas has lengths of approximately 0.8 μm, 1.36 μm, and 2.5 μm, respectively, with each antenna patterned at the free end of an N/MEMS structure to form an optomechanical device. For consistency, all three devices employ a design, providing a uniform mechanical and electrical platform across configurations. Specifically, each N/MEMS structure is made of

a silicon nitride beam of length 200 μm and width 28 μm (thickness 0.6 μm), coated on two sides with thin gold layers (0.07 μm/0.035 μm thicknesses), and incorporating a small capacitive transduction gap of 10 nm/100 nm. The optical dipole antennas themselves share the same cross-sectional dimensions in every design (each antenna is a gold nanostructure 80 nm/100 nm in width and 35 nm/70 nm in thickness), so that the only geometric parameter varied among the three configurations is the dipole length. N/MEMS structures range from a simple triangular microcantilever to a nanocantilever and a nano tuning fork, see Table 3.1. By maintaining a constant cantilever platform and altering only the dipole antenna length, the influence of the antenna's resonant characteristics on light–matter interaction and the resulting mechanical response can be systematically investigated at the operating wavelength.

Table 3.1: Comparison of three different optomechanical antenna structures.

Schematic (Top view)	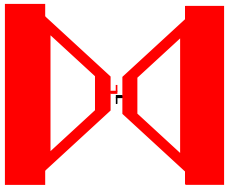 Structure 1	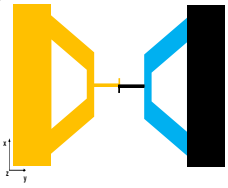 Structure 2	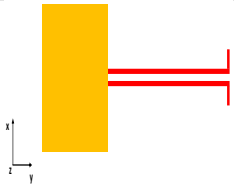 Structure 3
Schematic (Lateral view)	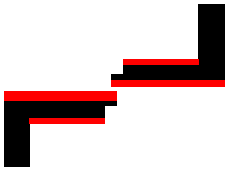 35 nm/70 nm gold thicknesses	 35 nm/70 nm gold thicknesses	 70 nm gold thickness
Dipole's length, L_{dipole}	0.8 μm optimized for S_{11} dB	1.36 μm optimized for V_{gap}	2.5 μm optimized for V_{gap}
Si_3N_4 thickness	140 nm	140 nm	600 nm
Paper and related section	Papers 1 and 2 (A.1)(A.2)	Paper 3 (B.2)	Paper 4 (B.3)

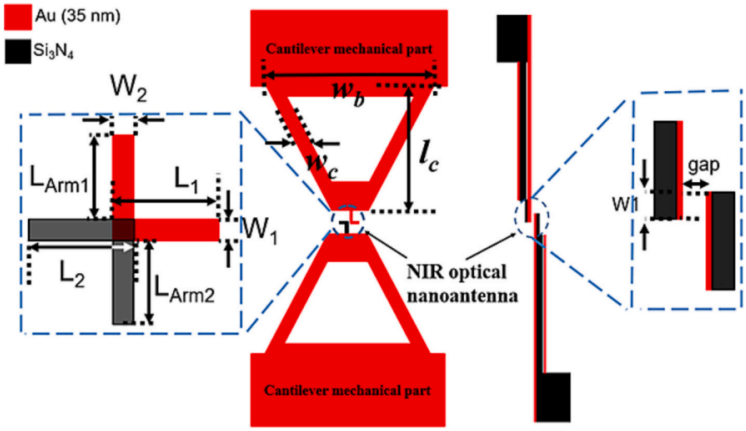

Figure 3.1: Schematic top and side views of the proposed first structure, including nanoantenna and microcantilever (Paper 1)(A.1).

Due to plasmonic effects in the metal, these physical lengths are somewhat shorter than the ideal free-space multiples of $\lambda/2$ (e.g., the $\lambda/2$ antenna's 0.8 μm length is about 0.77× the free-space half-wavelength at 1.55 μm) [89]. This shortening occurs because the effective wavelength of surface plasmons in the gold nanostructure is reduced compared to the free-space wavelength. In all cases the feed gap g_0 – the separation between the two opposing antenna arms – was designed to be on the order of 10 nm/100 nm. This tiny gap is a key feature enabling strong capacitive coupling between the arms. Each structure thus consists of two facing gold "half-antennas" (each on its own cantilever) forming a nanodipole with gap $g_0 \approx 10$ nm. Figure 3.1, Figure 3.2 and Figure 3.3 illustrate the three geometries, highlighting differences in arm length and shape (A.1), (A.2), and (B.2).

Despite their geometric differences, all three designs follow the same operating principle and share similar materials (a gold layer on a Si_3N_4 cantilever). An analysis of the current and electric field distribution shows that the $\lambda/2$ antenna is the most compact, designed for the fundamental dipole resonance, whereas the longer $3\lambda/2$ and $5\lambda/2$ structures support higher-order resonant modes. These higher modes involve additional standing-wave nodes along the antenna length (as evidenced by current and field distribution plots in simulation, e.g., Figure 3.4)(Pa-

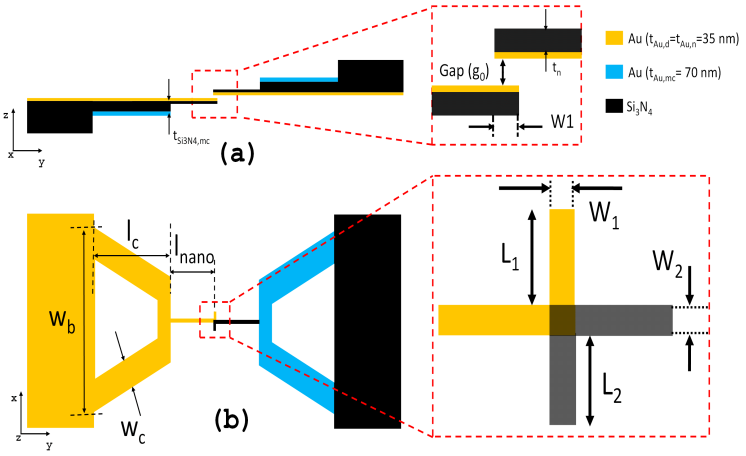

Figure 3.2: Lateral (a) and top (b) views of the second plasmomechanical antenna (Paper 3)(B.2).

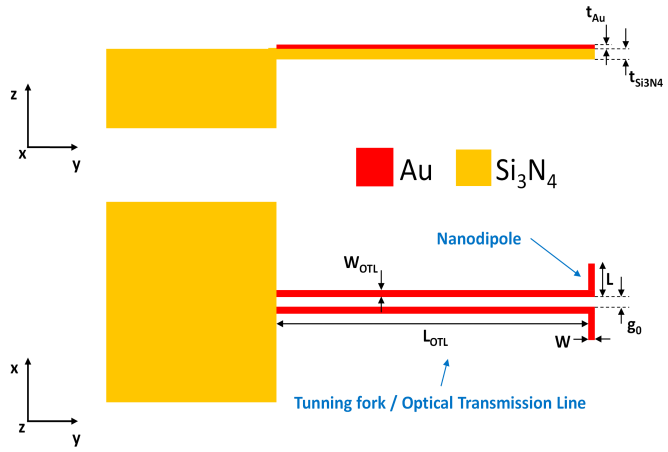

Figure 3.3: Top and lateral view of the third optomechanical antenna (Paper 4)(B.3).

per 2)(A.2) [89].

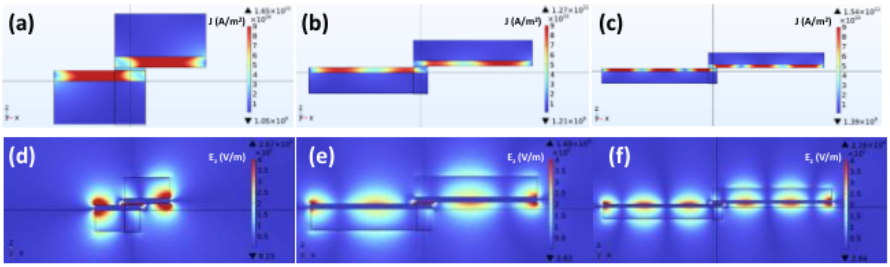

Figure 3.4: Maps of the current density (a-c) and z-component of the electric field (d-f), for the first three detectable resonance modes observed when dipole length is 300 nm (a,d), 810 nm (b,e) and 1361 nm (c,f) (Paper 2)(A.2).

By comparing the designs, one can note a trade-off: the smallest (fundamental) antenna tends to provide the strongest electromagnetic coupling for a given wavelength, but the larger antennas (higher-order modes) were chosen to ease fabrication constraints (since a longer antenna is less sensitive to nano-scale length errors and can be milled with slightly larger features [89]). The structural variations – in dipole length, width, and cantilever arm configuration – therefore allow exploration of different resonant behaviors while using the same basic materials and concept. A summary of key geometric parameters for the optimized designs is given in Table 3.2, Table 3.3 and Table 3.4 (dipole lengths L_1, L_2, arm lengths L_{Arm}, widths W_1, W_2, etc.) [44, 89]. Each of these optomechanical antenna prototypes was fabricated and tested as described below.

3.2 Working principle

The NEMSTENNA device converts incident optical radiation into mechanical deflection through two coexisting transduction mechanisms: an opto-electromechanical (OEM) effect and an undesired opto-thermomechanical (OTM) effect. Figure 3.5 provides a schematic overview of the working principle.

When a laser beam at the design wavelength (1.55 μm in our case) is focused

Table 3.2: Geometry dimensions of the NEMSTENNA device corresponding to Figure 3.1 used in COMSOL simulations (Paper 1)(A.1).

Parameter	Value
Dipole arm length (L_{Am1}/L_{Am2})*, μm	0.72/0.75
Dipole arm width (w_2)*, μm	0.1
Dipole length (L_1/L_2)*, μm	0.82/0.85
Dipole width (w_1)*, μm	0.1
Dipole gold thickness (t_{g0})**, μm	0.035
Dipole silicon nitride thickness (t_{dd})***, μm	0.14
Cantilever length (l_c)**, μm	200
Cantilever width (w_c)**, μm	28
Cantilever base width (w_b)**, μm	184
Cantilever spring constant (k_c)**, N/m	0.08
Cantilever silicon nitride thickness (t_{dc})**, μm	0.6
Cantilever gold thickness (t_{pc})**, μm	0.07
Capacitive gap (g_0)*, nm	10
Overlapping Area (A)*, μm^2	0.01
Dipole resonant wavelength/frequency (f_d), μm/THz	1.55/193.41
* From optimization at 1.55 μm.	
** From [92].	
*** From SEM images.	

Table 3.3: Dimensions of the optimal NEMSTENNA design corresponding to Figure 3.2 (Paper 3)(B.2).

Parameter	Value	Units
Dipole length, $L_1 = L_2$	1360	nm
Dipole width, W_1	80	nm
Dipole–Nanocantilever connection width, W_2	100	nm
Dipole gold thickness, $t_{\mathrm{Au,d}}$	35	nm
Dipole silicon nitride thickness, $t_{\mathrm{Si_3N_4,d}}$	140	nm
Microcantilever length, l_c	200	μm
Microcantilever width, w_c	28	μm
Microcantilever base width, w_b	184	μm
Microcantilever silicon nitride thickness, $t_{\mathrm{Si_3N_4,mc}}$	600	nm
Microcantilever gold thickness, $t_{\mathrm{Au,mc}}$	70	nm
Capacitive gap, g_0	10	nm
Nanocantilever length, l_n	83	μm
Nanocantilever width, w_n	1	μm
Nanocantilever silicon nitride thickness, t_n	140	nm
Nanocantilever gold thickness, $t_{\mathrm{Au,n}}$	35	nm
Overlapping area, $A_{\mathrm{overlap}} = W_1 \cdot W_2$	800	nm^2

Table 3.4: Geometry characteristics of tuning fork optomechanical device corresponding to Figure 3.3 (Paper 4)(B.3).

Parameter	Value	Units
Dipole arm length, $(L_{\text{Arm1}}/L_{\text{Arm2}})$	10 / 10	μm
Dipole width, w_1	0.09	μm
Dipole arm width, w_2	0.18	μm
Dipole length, (L_1/L_2)	2.5 / 2.5	μm
Dipole gold thickness, $t_{g,d}$	0.07	μm
Dipole silicon nitride thickness, $t_{d,d}$	0.6	μm
Capacitive gap, g_0	0.01–0.1	μm

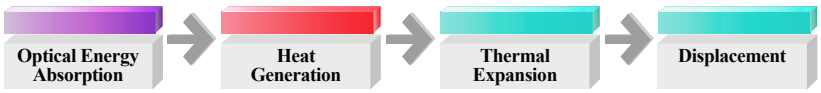

(a)

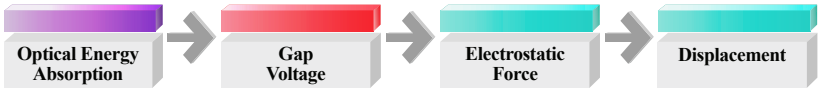

(b)

Figure 3.5: Comparison of opto-thermo-mechanical (OTM) (a) and opto-electro-mechanical (OEM) (b) transduction mechanisms. Both pathways convert incident light into mechanical displacement, but rely on different intermediate physical effects.

onto the nanoscale dipole antenna, the oscillating electromagnetic field drives localized surface plasmons and currents in the metal arms. This induces an alternating voltage V_{gap} across the feed gap of the antenna [44, 89, 93]. The two facing antenna arms essentially form a nanocapacitor, so an ac V_{gap} (at the optical frequency, on the order of 2×10^{14} Hz) appears between them. Typical induced voltage amplitudes are on the order of tens of millivolts for moderate incident powers, as estimated by full-wave simulations [44, 89]. Although V_{gap} oscillates at the optical frequency, it can effectively produce a static force due to the nonlinear nature of electrostatic attraction. The electrostatic force F_{ee} between the charged antenna arms is proportional to the square of the voltage (in a parallel-plate approximation, $F_{\text{ee}} \approx \frac{1}{2}, \frac{dC}{dx}V^2$). As a result, the rapidly oscillating V_{gap} gives rise to a DC component of force in addition to an ac component at twice the optical frequency. The ac force oscillates far too fast for the mechanical structure to respond (frequencies in the hundreds of THz), so its effect is negligible on the cantilever motion. The DC part of F_{ee}, however, continuously pulls the two antenna arms toward each other. In essence, the optical excitation creates a steady electrostatic attraction in the nano-gap – this is the desired OEM transduction pathway. The magnitude of the DC force increases with the intensity of illumination (since $F_{\text{ee}} \propto V_{\text{gap}}^2$, and V_{gap} scales with the incident field). The term $\dfrac{\partial V_{\text{gap}}}{\partial x}$, absent in conventional electrostatic MEMS transducers where V_{gap} is displacement-independent ($\dfrac{\partial V_{\text{gap}}}{\partial x} = 0$), arises here due to the position-dependent voltage distribution. In the following, the formulations of the above sentences have been provided in equations (Paper 4)(B.3) (3.1)-(3.5) [44, 89–91]:

$$V_{\text{gap}}(t) = \left|V_{\text{gap}}\right| \cdot \cos\left(2\pi f_{\text{NIR}} t\right) \tag{3.1}$$

$$F_{\text{ee}}(t) = \frac{1}{2}\frac{\partial C_{\text{gap}}}{\partial x}\left(V_{\text{gap}}(t)\right)^2 + \frac{1}{2}C_{\text{gap}}\frac{\partial\left(V_{\text{gap}}(t)^2\right)}{\partial x} = F_{\text{ee,DC}} + F_{\text{ee,ac}}(t), \tag{3.2}$$

$$C_{\text{gap}} = \frac{\varepsilon_0 A}{g_0 - 2\delta x}, \tag{3.3}$$

$$F_{\text{ee,DC}} = \frac{1}{4}\frac{\partial C_{\text{gap}}}{\partial x}\left|V_{\text{gap}}\right|^2 + \frac{1}{4}C_{\text{gap}}\frac{\partial\left(\left|V_{\text{gap}}\right|^2\right)}{\partial x}$$
$$= \frac{1}{4}\frac{\varepsilon_0 A}{(g_0 - 2\delta x)^2}\left|V_{\text{gap}}\right|^2 + \frac{1}{4}\frac{\varepsilon_0 A}{(g_0 - 2\delta x)}\frac{\partial\left(\left|V_{\text{gap}}\right|^2\right)}{\partial x}, \tag{3.4}$$

$$F_{\text{ee,ac}}(t) = \frac{1}{4}\frac{\partial C_{\text{gap}}}{\partial x}\left|V_{\text{gap}}\right|^2 \cos\left(4\pi f_{\text{NIR}} t\right) + \frac{1}{4}C_{\text{gap}}\frac{\partial\left(\left|V_{\text{gap}}\right|^2\right)}{\partial x}\cos\left(4\pi f_{\text{NIR}} t\right). \tag{3.5}$$

where the definition of symbols has been provided in Table 3.5:

Table 3.5: Definition of parameters used in the electrostatic force and capacitance equations.

Symbol	Description
$V_{\text{gap}}(t)$	Time-dependent voltage applied across the nanoscale capacitor gap
$\lvert V_{\text{gap}}\rvert$	Amplitude (magnitude) of the applied voltage
f_{NIR}	Optical driving frequency in the near-infrared (NIR) range
C_{gap}	Capacitance of the nanoscale gap between electrodes, $C_{\text{gap}} = \frac{\varepsilon_0 A}{g_0 - 2\delta x}$
ε_0	Permittivity of free space (8.854×10^{-12} F/m)
A	Effective overlap area of the capacitor electrodes
g_0	Initial gap distance between the fixed and movable electrodes (at equilibrium)
δx	Mechanical displacement of the movable electrode from its equilibrium position
$F_{\text{ee}}(t)$	Total electrostatic force acting on the movable electrode
$F_{\text{ee,DC}}$	Static (time-independent) component of the electrostatic force
$F_{\text{ee,ac}}(t)$	Time-varying (oscillatory) component of the electrostatic force at frequency $2f_{\text{NIR}}$
$\frac{\partial C_{\text{gap}}}{\partial x}$	Rate of change of capacitance with respect to displacement (electromechanical coupling coefficient)
$\frac{\partial\left(\lvert V_{\text{gap}}\rvert^2\right)}{\partial x}$	Spatial variation of the squared voltage amplitude across the gap

Under illumination, each cantilever experiences an inward pull at its tip (toward the opposite arm), causing a slight deflection from its equilibrium position. The direction of this OEM deflection is primarily in-plane (closing the gap) for the two-cantilever design, as illustrated in Figure 3.6.

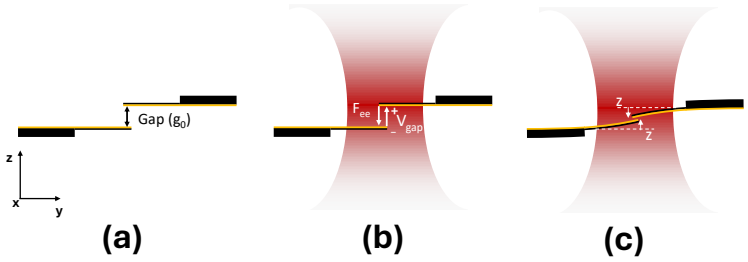

Figure 3.6: Actuation principle of the optomechanical antenna (Paper 3)(B.2).

In parallel with the OEM mechanism, the device is subject to a parasitic opto-thermomechanical (OTM) effect (Paper 2)(A.2) and (B.1). A portion of the incident optical power is absorbed by the metal nanostructure and the cantilever, which converts to heat. This leads to a temperature rise in the illuminated region, which in turn causes thermal expansion of the materials. The NEMSTENNA cantilevers are a composite of metal (Au) and dielectric (Si_3N_4) layers with different coefficients of thermal expansion. When heated, the unequal expansion of these layers induces bending via the bimetallic (thermomechanical) effect [89, 93]. In our devices the metallic coating is only on one side (or significantly thicker on one side) of the cantilever, so heating causes the free end to bend out-of-plane (typically curling toward the side with the thinner or less expansive layer). This bending constitutes the OTM response. Notably, the OTM deflection does not require the presence of a feed gap voltage – it is purely a result of generalized heating in the structure from optical absorption. Therefore, it is present whether or not the antenna is resonant, and it adds to (or biases) the total deflection observed. In the original vertical cantilever configuration, the OTM effect causes an out-of-plane deflection (vertical bending of each cantilever) in the gap closing direction, which is superimposed on the OEM effect, that also causes an out-of-plane gap closing.

In summary, the NEMSTENNA's operation relies on direct light-to-voltage conversion at the nanoantenna (a plasmonic/electromagnetic effect) followed by voltage-to-force conversion (electromechanical). This primary OEM pathway pro-

vides direct transduction of optical power into mechanical displacement, without any intermediate electronics. However, simultaneously, the OTM pathway acts as an indirect, thermal transduction that can mask or interfere with the OEM motion. The overall static deflection of the device under CW (continuous-wave) illumination will thus be a combination of OEM and OTM contributions. In the ideal case, with perfect thermal isolation or symmetric structure or tuning fork structure (Paper 4)(B.3), the OTM effect would be negligible, and the device would purely respond via the fast OEM mechanism. In practice, as we discussed earlier, the OTM "parasitic" response is significant and must be understood and mitigated [89–91, 93]. The next sections will quantify these two contributions (Sections 3.5 and 3.6) after first describing how the devices were fabricated and characterized (Section 3.3) and how the nanoantenna's electromagnetic response behaves (Section 3.4).

3.3 Fabricated prototypes

The NEMSTENNA structures were fabricated through a custom process utilizing focused ion beam (FIB) milling on commercial microcantilevers [44, 92].

Figure 3.7, Figure 3.9 and Figure 3.11 outlines the key fabrication steps. Figure 3.8, Figure 3.10 and Figure 3.12 show SEM images of the proposed devices at various stages. The starting material (Figure 3.7a) was an Atomic Force Microscope (AFM) cantilever: a Si_3N_4 microcantilever of length $l_c \approx 200$ μm and width $w_c \approx 28$ μm, coated in both sides with a thin Cr/Au film, with thickness $t_{Au} \approx 35$ nm (top) and 70 nm (bottom) [44]. The cantilever has a triangular tip region, which we utilize as the site for the nanoantenna. In its original orientation, the gold-coated side was on the bottom; therefore, as a first step the cantilever chip was flipped upside-down on the FIB stage (Figure 3.7b) to allow milling of the 70 nm thick metal-coated face. Next, a localized FIB milling step (using a relatively low ion current to preserve fine control) was performed to thin the cantilever's free end (Figure 3.7c). This involved rastering the Ga^+ ion beam over a small area (a

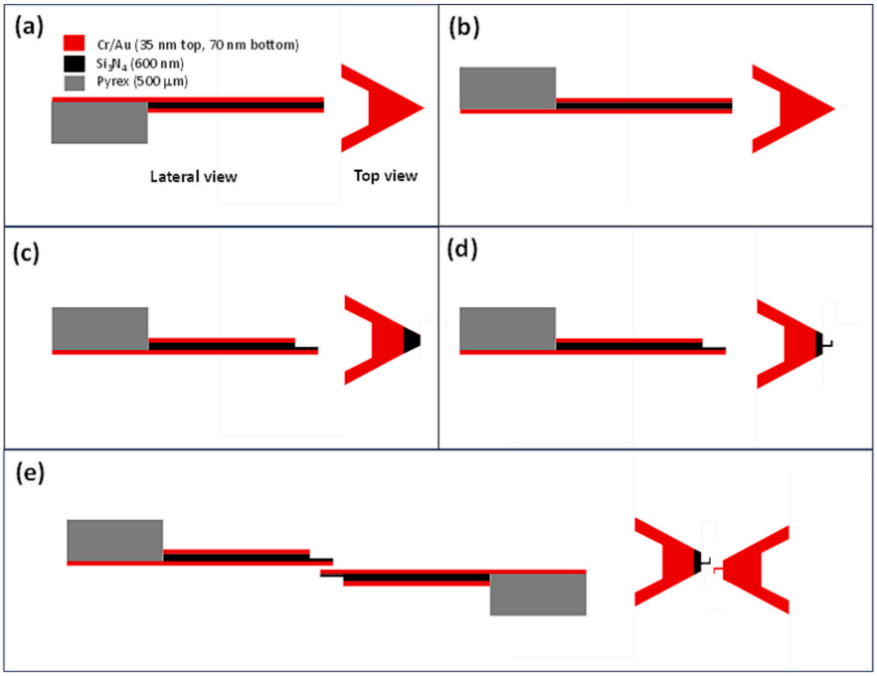

Figure 3.7: FIB based fabrication process steps of the proposed structure: (a) Initial AFM microcantilever structure, (b) microcantilever flipping, (c) local FIB milling thickness reduction, (d) local FIB milling half nanoantenna definition and (e) NEMSTENNA final build-up (Paper 1)(A.1).

few μm) at the tip to sputter away part of the Si_3N_4 and metal, effectively reducing the thickness by about half [44]. The thinning creates a flat, thin membrane area which will host the nanoantenna, and it also reduces the bending stiffness locally – a thinner cantilever end is more compliant for out-of-plane bending and ensures that subsequent milling can penetrate through the full thickness. In our prototypes, the nitride thickness in the antenna region was reduced from the original 600 nm down to roughly 300 nm. We empirically found that thinning beyond a certain point (below ~50% of original thickness) caused the cantilever to become unstable and buckle, likely due to stress release in the bimaterial structure [44]. Thus, a controlled partial thinning was optimal to prepare the substrate for nanoantenna definition. Figure 3.8a shows an SEM view of the cantilever tip after this

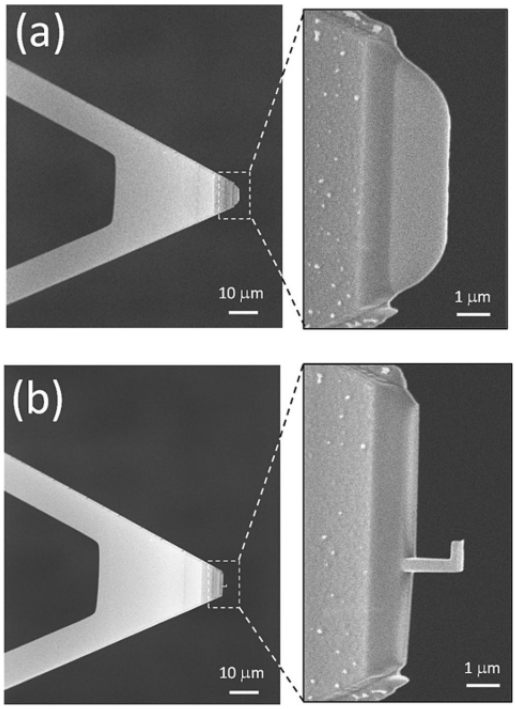

Figure 3.8: SEM images of a fabricated NEMSTENNA prototype after (a) step c (see figure 3.7c) and (b) step d (see figure 3.7d) of the fabrication process.

thickness-reduction step, where the milled region can be discerned.

In the subsequent step, the half-antenna pattern was milled into the cantilever tip (Figure 3.7d). Using a finer ion beam (with a smaller aperture and reduced current for higher resolution), we cut out the shape of one dipole arm. Essentially, the FIB was used to etch away all the material around the intended antenna arm, leaving behind a nanoscale gold-coated peninsula attached to the cantilever. This peninsula is the "half-dipole": a tiny rectangular patch of the Au/nitride bilayer (on the order of 0.8 μm long and 0.1 μm wide) connected by a narrow stem (the supporting arm) to the bulk of the cantilever. The milling defined both the outer edges of this half-antenna and cleared the gap region at its end. Notably, milling the gap entirely through the material effectively removes a slice of length from the cantilever – in our case, approximately a 2 μm segment was removed to isolate the

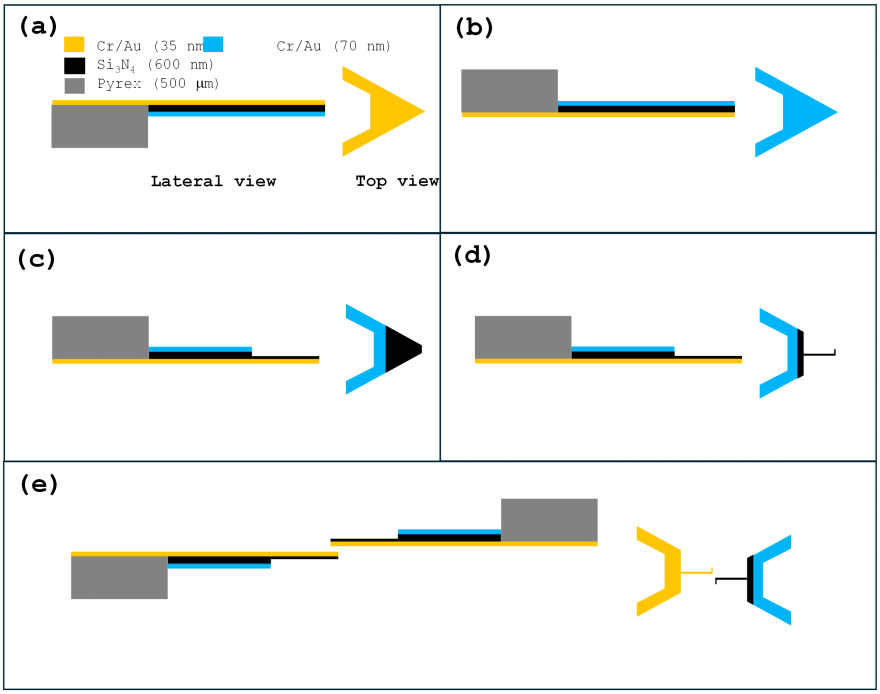

Figure 3.9: NEMSTENNA fabrication process: (a) Unprocessed microcantilever structure, (b) microcantilever flipping, (c) thickness reduction in the nanocantilever and nanodipole area, (d) nanocantilever and one arm nanodipole definition and (e) NEMSTENNA final build-up (Paper 3)(B.2).

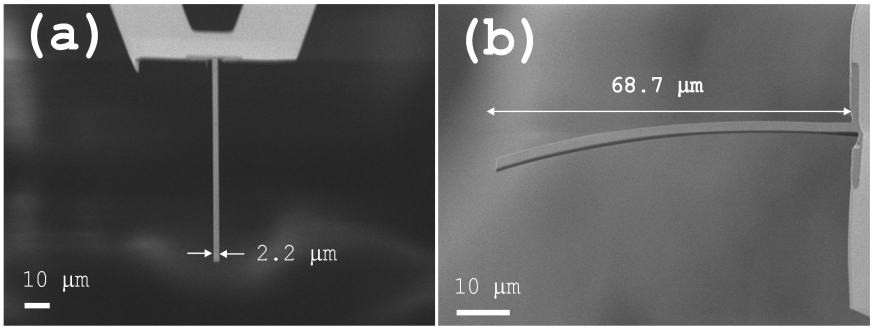

Figure 3.10: SEM images from top (a) and lateral (b) perspectives of a NEMSTENNA nanocantilever in the residual stress limit of slenderness (Paper 3)(B.2).

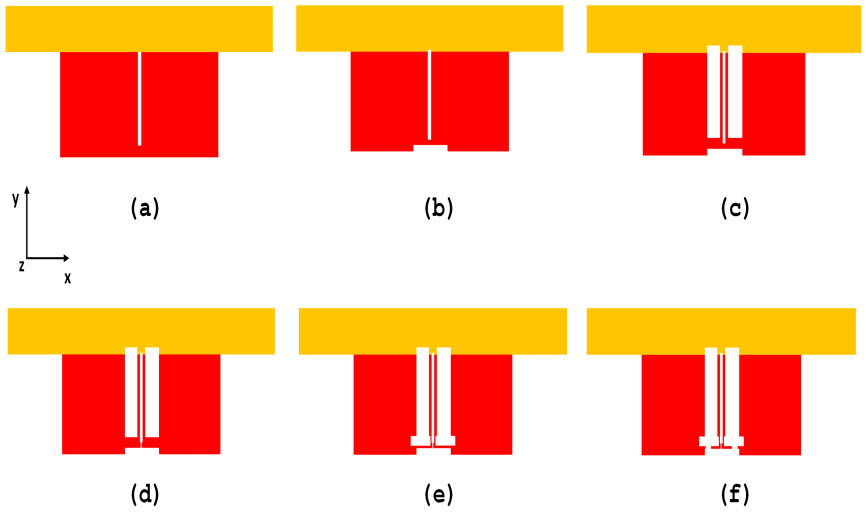

Figure 3.11: Fabrication steps for tuning fork optomechanical antenna (Paper 4)(B.3).

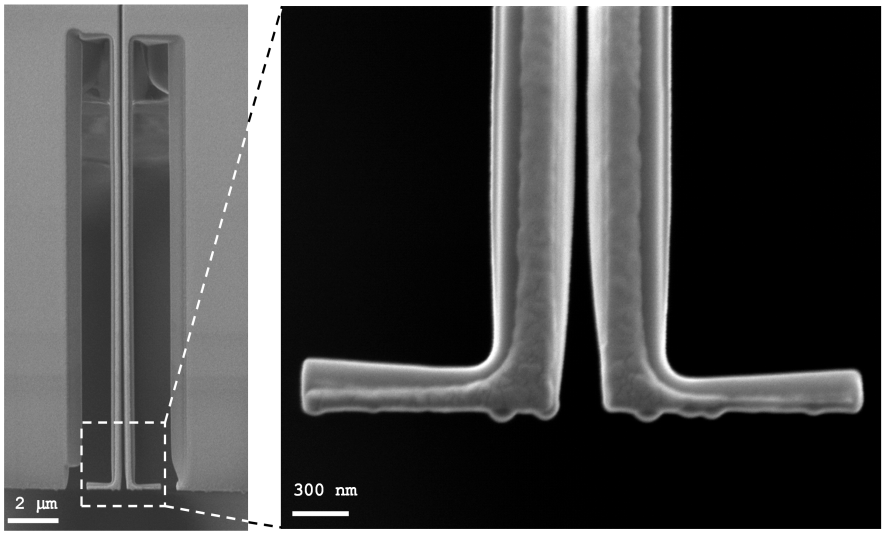

Figure 3.12: SEM images of a tuning fork optomechanical antenna (Paper 4)(B.3).

half-antenna [44]. This leads to a slight shortening of the overall cantilever length (about 1% in a 200 μm beam), which in turn slightly raises its spring constant and resonance frequency (calculated increase on the order of 2–3% [44]). The same procedure was applied to a second identical cantilever to create the complementary half of the dipole antenna. Care was taken to make the two halves as similar as possible in dimensions, though minor differences in milling (or initial cantilever thickness) led to arm length mismatches on the order of a few tens of nanometers (e.g., one half might be 0.72 μm and the other 0.75 μm, as in our optimized design [44]). Figure 3.8b shows an SEM image after defining one half-antenna: the outline of the nanodipole arm is clearly visible, and the narrow feed gap trench has been cut (at this stage the gap is effectively open on three sides, awaiting the second half to face it).

For the final assembly (Figure 3.7e), an ex-situ step has to be done under an optical microscope. One processed cantilever is carefully picked up and flipped (so that its antenna faces upward), and then its tip is aligned opposite the tip of the other cantilever (which faces downward). This is achieved using 3D nanopositioner: the two chips are positioned such that the two half-antennas approach each other with their flat faces confronting, separated by a tiny air gap. The chips are affixed on a common substrate in this configuration. The result is a free-standing nanodipole formed by two gold-coated nanostructures, one on each cantilever, with a gap between them. In a later iteration, a similar approach was used to fabricate the nanoantenna coupled to more compliant nanocantilevers, as shown in the Figure. 3.9 and Figure 3.10 (Paper 3)(B.2) [90]. To eliminate this manual assembly step (see Section 3.6), a monolithic approach was pursued by fabricating both arms on one chip in a tuning-fork geometry, as shown in Figure 3.11 and Figure 3.12, (Paper 4)(B.3) [91].

Throughout the FIB fabrication, maintaining precision was critical. The effective milling resolution in defining lateral features was on the order of 10–20 nm under optimal conditions. However, due to stage drift and charging of the insulating nitride during milling, we observed pattern deviations up to about 50 nm [44]. This

fabrication tolerance ~50 nm is significant relative to the 100 nm feature sizes of the antenna, meaning the realized dimensions (arm length, width, gap) could differ slightly from the intended design. Such variations translate into shifts in resonance frequency or reduced coupling (discussed in Section 3.4). Using a more stable fabrication method like electron-beam lithography (EBL) on a wafer could reduce this uncertainty to ~10 nm or less [44], but that would require integrating the nanoantenna patterning into the original cantilever fabrication process. Our approach with post-fabrication FIB was chosen for rapid prototyping, accepting a looser tolerance. Apart from lateral precision, the vertical milling had to completely penetrate the 0.6 μm thick cantilever to isolate the antenna arm. FIB milling at 30 kV with stepwise reduced current achieved this, though redeposition of sputtered material and sidewall tapering were observed. After fabrication, the prototype devices were examined by SEM and optical microscopy. The SEM images in Figure 3.8, Figure 3.10 and Figure 3.12 confirm that well-defined nanoscale antenna structures were obtained: the feed gaps and arm shapes are clearly resolved. The final device shows two opposing gold pads at the cantilever tips, forming the dipole. The measured arm lengths and widths from SEM match the design targets within the aforementioned ~50 nm uncertainty. The successful fabrication of these prototypes allowed us to proceed with simulation of their performance, as described next.

3.4 Nanoantenna response

3.4.1 S_{11} versus V_{gap} as optimization variables

To characterize the electromagnetic behavior of the devices, we performed full-wave simulations of the antenna's reflection coefficient and feed-gap voltage response. S_{11} vs. frequency and V_{gap} vs. frequency curves were obtained for each design using a COMSOL Multiphysics RF model [44, 89]. Figure 3.13a illustrates a representative S_{11} spectrum for the nanoantenna, and Figure 3.13b shows the corresponding induced voltage spectrum.

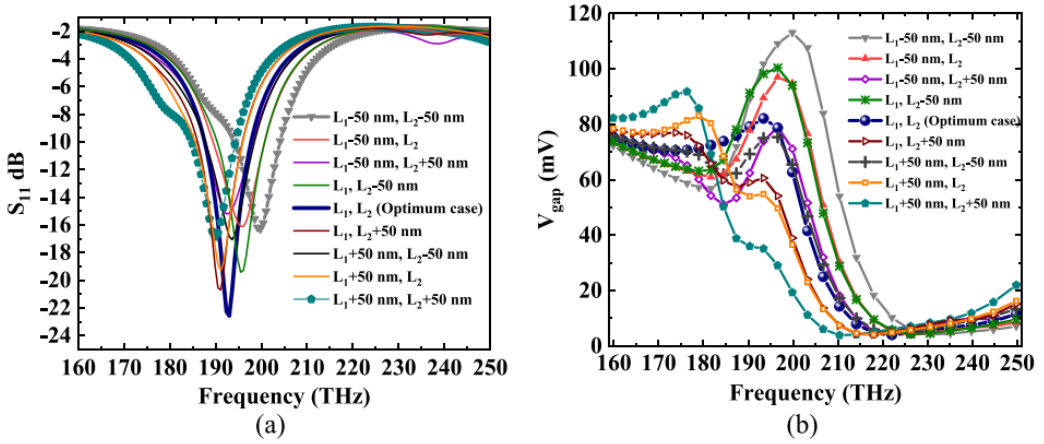

Figure 3.13: The frequency response of S_{11} (a) and V_{gap} (b) obtained from COMSOL simulation is shown for 8 different values of L_1 and L_2 around the optimum case. The laser power is set to 500 mW, and the gap distance is $g_0 = 10$ nm (Paper 1)(A.1).

The reflection coefficient S_{11} (in dB) indicates how much of the incident power is reflected back from the antenna, and a deep notch in S_{11} signifies a strong resonance where the antenna absorbs/accepts energy efficiently. As expected, each antenna design exhibits a pronounced resonance at or near the design frequency. For the Paper 1 dipole design (smallest antenna), the primary resonance occurs around $\nu \approx 193$ THz (which is $\lambda \approx 1.55$ μm) [44]. At this frequency, S_{11} reaches a minimum. In simulations, we achieved a return loss of about -22 dB in the optimized case [44]. This deep S_{11} notch confirms a good impedance match at the design wavelength when the geometry is tuned correctly. On either side of this resonance, S_{11} increases, meaning the antenna becomes reflective (off-resonance, only a small fraction of the light is captured). The bandwidth of the resonance (defined by the S_{11} notch width) was on the order of a few THz in our design, a relatively narrowband response, as is typical for a high-Q plasmonic dipole [94–96].

When the antenna dimensions are altered, the S_{11} resonance shifts in frequency. A sensitivity analysis (Figure 3.13a, multiple curves) was conducted by varying the dipole arm lengths L_1, L_2 by a small tolerance (±50 nm) to mimic fabrication

imperfections [44]. The results showed that if both arms are slightly shorter than optimum (by 50 nm each), the resonance frequency moves higher (to ~200 THz), and the S_{11} notch at 193 THz becomes much shallower (around −9 dB) [44]. Conversely, if both arms are longer by 50 nm, the resonance shifts lower (to ~190 THz) and again the match at 193 THz degrades ($S_{11} \approx -14$ dB) [44]. Only when the antenna is at the correct length (820 nm/850 nm arms in that example) does the deep −22 dB notch occur precisely at 193 THz. This demonstrates that a ~6–7 THz frequency shift (a few nanometers change in wavelength) can result from a 50 nm fabrication error in length. In practical terms, it means the device needs tight dimensional control to hit the desired resonant wavelength. Fortunately, even in off-optimal cases the antenna still resonates – just at a slightly different frequency and with reduced coupling efficiency. In later analyses, we generally tuned our simulations to the actual fabricated dimensions (as measured by SEM) to predict performance more accurately.

The larger antenna designs also show resonant behavior, but their fundamental resonance occurs at a lower frequency since the dipole is physically longer. For instance, the $5\lambda/2$ designs (total length ~2.72 μm) (L=1.36 μm) Paper 2 (A.2) and Paper 3 (B.2) have their first (half-wave) resonance roughly around ~65 THz (wavelength ~4.6 μm, in the mid-infrared), which is outside our band of interest. However, it also supports higher-order resonances: notably, a strong third-order resonance appears near 1.55 μm (this is by design, as 1.55 μm corresponds to the fifth half-wave mode for that length) (Paper 2)(A.2) [89]. In the COMSOL simulations, we excited the structure with a broadband source and observed multiple peaks in $|S_{11}|$: the $n = 1$ mode (fundamental) at longest wavelength, the $n = 3$ mode at shorter wavelength, and the $n = 5$ mode at the shortest (near 1.55 μm). We can thus identify the resonant peaks of these antennas with the standard half-wave dipole modes: for example, current distribution plots (Figure 3.4) confirm one current anti-node for the $n = 1$ mode, two for $n = 3$, and three for $n = 5$, with intervening nodes, exactly as expected for a dipole of length equal to $1/2, 3/2, 5/2$ of the effective wavelength [89]. Because of plasmonic shortening, the effective

wavelength along the gold dipole is shorter, so the condition for resonance (in terms of physical length) is slightly different than in a lossless RF dipole. In our simulations, we quantified this by the ratio $L_{\text{total}}/(\lambda/2)$: which was about 0.77 for the first mode, 0.69 for the third mode, and 0.70 for the fifth mode [89]. All these resonant modes lie within reach of the 1.55 μm laser when we adjust geometry accordingly.

The feed gap voltage response closely mirrors the S_{11} behavior. Figure 3.13b (Paper 1) (A.1) and Figure 3.14 (Paper 3) (B.2) shows V_{gap} as a function of excitation frequency, calculated by simulating a focused Gaussian beam illumination and recording the potential difference across the gap [44].

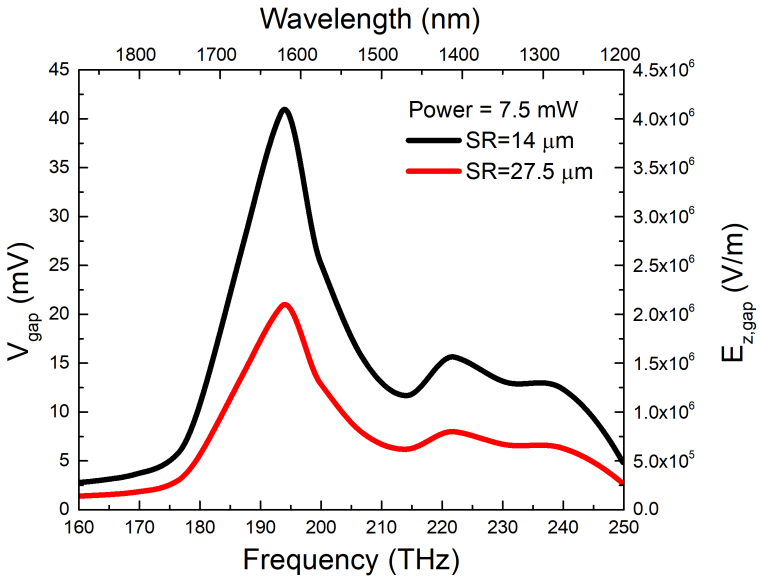

Figure 3.14: V_{gap} and E_z vs. frequency and wavelength for different spot radius (SR) for second proposed optomechanical antenna (Paper 3)(B.2).

At the antenna's resonance, the local field in the gap is maximized, which translates to a peak in V_{gap}. In the first design (Paper 1)(A.1), V_{gap} reaches its maximum at 193 THz, concurrently with the S_{11} dip [44]. For a given incident power (say 10 mW), the peak V_{gap} was around tens of millivolts (e.g., ~80 mV

in one simulation) at resonance, and it dropped off significantly off-resonance [44]. This reinforces that the device is most effective when the antenna is tuned to the laser wavelength. The tolerance analysis showed that if the antenna is slightly detuned, the peak V_{gap} shifts in frequency along with the resonance. One interesting finding was that in one detuned scenario (with arms slightly shorter, pushing resonance above 1.55 μm), the value of V_{gap} at the fixed 193 THz frequency could actually increase a bit even though S_{11} got worse [44]. This was attributed to impedance mismatches: the free-space to antenna coupling vs. antenna to 50 Ω port coupling can differ, meaning a slightly off-resonant antenna might generate a higher open-circuit voltage even if it reflects more power. Nonetheless, the general trend is that a well-matched resonance yields the highest V_{gap} available to drive the mechanical motion.

3.4.2 Nanoantenna resonant mode selection

When comparing the three modes in the first design, for instance, (Paper 2) (A.2) $\lambda/2$ antenna produces the largest V_{gap} for a given illumination, because it has the strongest near-field confinement when perfectly resonant (Paper 2)(A.2). The higher modes ($n = 3$ and $n = 5$ at 1.55 μm) produce a somewhat lower peak V_{gap} under the same power [89]. In our simulations, the $\lambda/2$ design had the highest gap electric field and voltage, the $5\lambda/2$ design was second, and the $3\lambda/2$ design was lowest (Paper 2)(A.2) [89]. For example, at 7.5 mW input power, one can obtain a qualitative ranking: the $n = 1$ mode gave the strongest gap field, the $n = 5$ mode about 10–20% lower, and the $n = 3$ mode slightly below that [89]. This is consistent with the fact that higher-order modes distribute the excitation along a longer antenna, and thus the intensity at the gap is not as concentrated as in the fundamental. Still, the $5\lambda/2$ antenna's performance was relatively close to the $\lambda/2$ case – a "small" sacrifice in V_{gap} (and return loss) in exchange for the easier fabrication of a larger device (Paper 2)(A.2) [89]. Indeed, we deliberately chose the $5\lambda/2$ design for final optimization because its arms (1.36 μm each) were much larger than the tiny 0.3 μm arms of the $\lambda/2$ device, making it more robust to mill

with FIB (Paper 2)(A.2) [89]. The trade-off was only a slight reduction in peak V_{gap} and a shift in resonance, which was acceptable (Paper 1)(A.1), (Paper 2)(A.2), (Paper 3)(B.2) and (Paper 4)(B.3).

In conclusion, the nanoantenna electromagnetic response measurements (simulated) show that all three structures function as intended: each has a well-defined resonant frequency where the reflection drops and a voltage is induced in the gap. The resonant frequency and the effectiveness (depth of S_{11} dip, magnitude of V_{gap}) are strongly dependent on the dipole length and precise geometry. These simulation results set the stage for understanding the mechanical outcomes. In the next section, we examine the opto-thermomechanical response – essentially how heat from absorption causes deflection – followed by the opto-electromechanical response, which is the direct mechanical actuation from the induced V_{gap}.

3.5 OTM response: parasitic optothermomechanical effect

When the NEMSTENNA is illuminated, a significant parasitic deflection arises from opto-thermomechanical (OTM) transduction. This section describes the OTM response based on our simulation studies and experimental observations [44, 89, 90]. The OTM effect is essentially a photothermal actuation: absorption of light causes heating, which induces thermal stress and bending in the bimaterial cantilevers. In our device, the free end of each cantilever bends out-of-plane upon heating, much like a bimetallic thermostat strip. This parasitic bending adds to the overall deflection but does not directly result from the antenna's electrostatic force – rather, it comes from material expansion mismatch. We modeled the OTM response by coupling electromagnetic, heat transfer, and structural mechanics simulations in COMSOL [44, 89]. The RF simulation provided the distribution of power dissipation (ohmic losses) in the device, which served as a heat source in a thermal conduction simulation. The resulting temperature rise across the cantilever was then fed into a mechanical model that calculates deformation due to thermal

expansion. All relevant modes of heat transport were included: conduction within the solid, convective and radiative cooling at surfaces, and even a thermal boundary resistance at the Au–Si_3N_4 interface (though the cantilever is so thin that conduction dominates) (Paper 2)(A.2) and (B.1) [89, 93]. The temperature distribution under laser illumination was found to be fairly uniform across the illuminated spot on the cantilever, with a slight gradient along its length. Importantly, the presence of the nanoantenna gap and tiny metal features did not significantly localize the heat: simulations showed that whether we include the detailed antenna geometry or approximate the tip as a continuous metal coating, the overall temperature rise and profile remained almost the same [89]. This indicates that most of the optical absorption occurs in the gold film over the broader area of the cantilever tip, not only in the nano-gap region. In other words, the entire free end of the cantilever warms up, so the photothermal bending behaves much like that of a uniformly heated bimorph cantilever.

The mechanical deformation from this heating is driven by the material stack asymmetry. Our cantilevers consist of Si_3N_4 (thermal expansion coefficient $\alpha_{SiN} \approx 3 \times 10^{-6}\ K^{-1}$) coated with Au ($\alpha_{Au} \approx 14 \times 10^{-6}\ K^{-1}$). Moreover, in the fabricated devices the top vs. bottom gold thickness can differ (one side might have, say, 70 nm Au vs. 35 nm on the other side) [89]. This asymmetry means one side of the cantilever expands more than the other when heated, causing it to curl. In our case, the thicker Au side experiences a larger expansion, so the cantilever bends toward the thinner side [89]. The steady-state OTM deflection z_{OTM} (out-of-plane displacement at the tip) was computed as a function of laser power. It scales approximately linearly with power at low levels, since temperature rise is proportional to absorbed power and deflection is roughly proportional to temperature for small strains. For example, simulations predicted on the order of a few nanometers of deflection for a 5 mW CW laser on a single cantilever [89]. To validate this, we performed an experiment using a laser to directly illuminate one cantilever (one half of the device, with the other half removed so that only OTM effect is present). Using our laboratory setup, we measured the static displacement of the cantilever

tip as the laser was turned on and off.

Figure 3.15a shows the deflection response over time when the laser is switched on, and the magnitude of the steady-state displacement for various power levels. The dynamic behavior of the NEMSTENNA microcantilever was characterized by measuring its out-of-plane vibration amplitude (Z_{dynamic}) as a function of frequency under an intensity modulated IR laser source. As shown in Figure 3.15b, a clear resonance peak is observed around 14.5 kHz, corresponding to the fundamental mechanical eigenmode of the cantilever, yielding a quality factor of about $Q \approx 46$ (see Figure 3.15b).

In Figure 3.16, the experimental data (points) align very well with the COMSOL simulation (solid line), verifying that our thermomechanical model is accurate [89]. For instance, at $P_{\text{in}} = 7.5$ mW (the maximum used in tests), the cantilever deflected on the order of several nanometers due to heating. The response time was observed to be on the order of milliseconds: the cantilever reaches about 90% of its final deflection within a few ms of the laser being turned on, consistent with a small thermal time constant (the cantilever's thermal mass and cooling path yield a fast response, which is beneficial for speed but still many orders slower than the OEM effect which is quasi-instantaneous). In Figure 3.17a, the simulated steady-state response of temperature and static displacement at cantilever free end are illustrated, and volumetric maps are provided as inset for 5.8 mW IR laser power. Figure 3.17b presents the time-dependent temperature response of the cantilever's free-end under pulsed IR laser illumination at different power levels. As shown, the temperature rises rapidly upon laser exposure and gradually saturates toward a steady-state value within a few milliseconds. The rate and magnitude of this temperature increase are strongly dependent on the input laser power. For instance, at 5.8 mW, the tip temperature reaches over 530 K in less than 5 ms, whereas for lower powers such as 1.33 mW, the maximum temperature remains below 400 K. This behavior reflects the balance between laser-induced photothermal heating and thermal dissipation through the cantilever and substrate. The exponential-like rise suggests a first-order thermal time constant characteristic, governed by

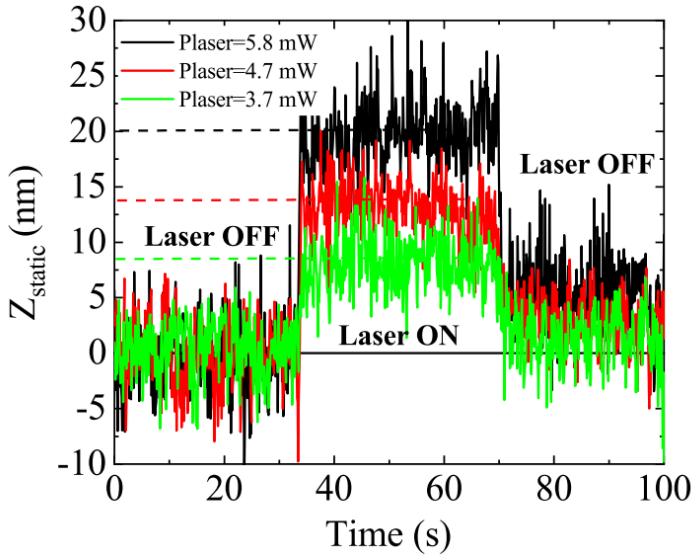

(a)

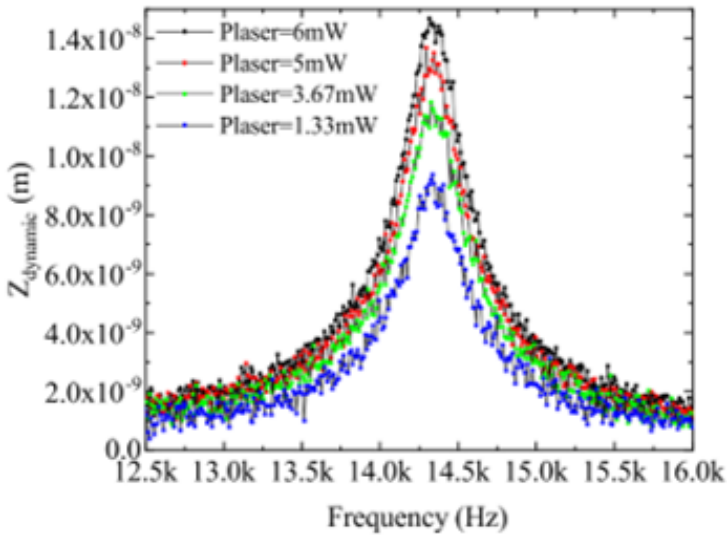

(b)

Figure 3.15: Laser-induced mechanical responses of the NEMSTENNA cantilever. (a) Measured static deflection vs. time in the OFF–ON–OFF transients for 5.8 mW, 4.7 mW, and 3.7 mW IR laser powers [93]. (b) Measured dynamic oscillation amplitude (Z_{dynamic}) vs. laser modulated frequency for different IR laser powers (1.33 mW to 6 mW).

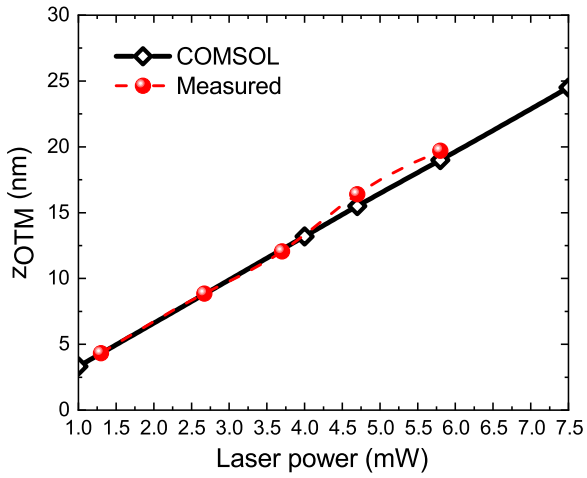

Figure 3.16: Experimental and COMSOL simulated steady-state displacement of the cantilever free-end in the out-of-plane direction, z, after laser power OFF-ON switching transient for different laser powers ranging from 1 to 7.5 mW. Spot radius is SR = 27.5 μm and gap distance is g_0 = 10 nm (Paper 2)(A.2) [89].

the cantilever's heat capacity and thermal conductivity. The calculated thermal time constant τ is equal to 0.533 ms, which corresponds to a cutoff frequency of 1.66 kHz, which is in agreement with Figure 3.17b. The characteristic time constant is defined as:

$$\tau = \beta^{-1} = \frac{c_p\,\rho\,d}{h} \tag{3.6}$$

Given the following parameters (Papers 2 and 3)(A.2)(B.2)[89, 90]:

$$\begin{aligned} c_{p,\mathrm{Au}} &= 129\ \mathrm{J/kg{\cdot}K}, \\ \rho_{\mathrm{Au}} &= 19280\ \mathrm{kg/m^3}, \\ h &= 10^5\ \mathrm{W/m^2{\cdot}K}. \end{aligned}$$

For Au and Si_3N_4 materials, the effective specific heat and density are:

$$c_p^* = \frac{129 \times 35 + 700 \times 600}{35 + 600} = 668.5\ \mathrm{J/kg{\cdot}K}$$

$$\rho^* = \frac{19280 \times 35 + 3100 \times 600}{35 + 600} = 3991.8\,\mathrm{kg/m^3}$$

Then, substituting into the time constant formula:

$$\tau^* = \frac{c_p^* \rho^* d}{h}$$

For $d = 20\,\mu$m:

$$\tau^* = 0.533\,m\mathrm{s}$$

These results highlight the dynamic thermal response of the device, which is critical for understanding both the transient mechanical deformation and thermal limits of the NEMSTENNA during operation.

When the laser is turned off, the cantilever relaxes back to its original position as it cools. No permanent deformation was seen for the power levels used; the process is repeatable and purely elastic/thermal.

The magnitude of the OTM deflection is much larger than the OEM deflection in static conditions. For example, at 7.5 mW, we measured several nm of OTM bending versus, at most, tens of picometers of OEM gap-closing (as inferred from simulation) [89]. This means that if one looks at the total out-of-plane displacement of the cantilever under a continuous laser, it is almost entirely due to photothermal effect.

In summary, the opto-thermomechanical response of the NEMSTENNA manifests as a heat-induced bending of the microcantilevers, which is a slow (thermal time-limited) and significant deflection under CW illumination. It has been thoroughly analyzed via multiphysics simulation and confirmed by experimental data [89, 93]. The OTM effect, while useful for bolometric sensors, is undesirable here because it overwhelms the fast OEM signal. Nevertheless, understanding this parasitic effect is crucial for interpreting the device behavior and for guiding modifications to improve the overall performance. The next sections focus on the opto-electromechanical response (OEM) – the very small but instantaneous deflection due to the induced electrostatic force – and how it compares to the OTM

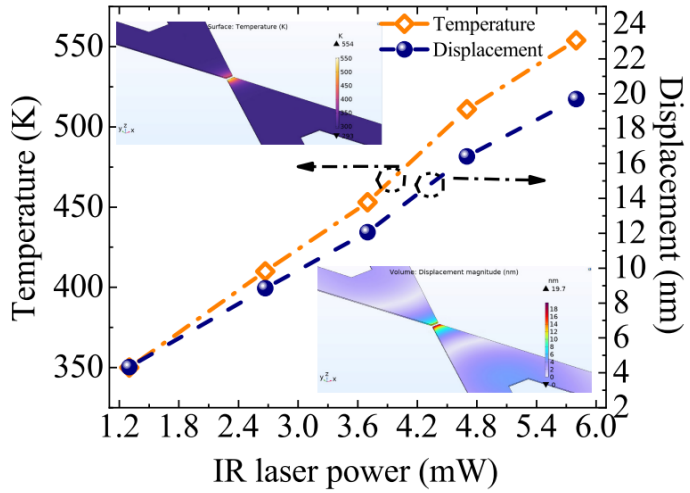

(a)

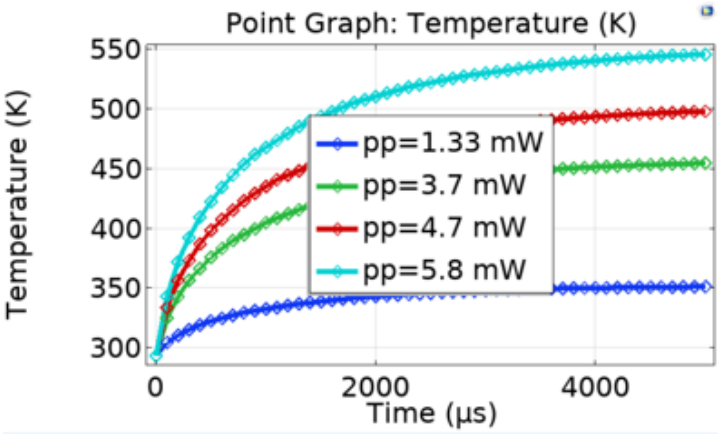

(b)

Figure 3.17: Thermal response of the microcantilever under IR illumination. (a) Simulated temperature and static displacement at the cantilever free end as a function of IR laser power, with spatial maps of temperature and displacement shown for the 5.8 mW case. (b) Time-resolved temperature evolution at the cantilever tip for various laser powers, showing faster saturation and higher steady-state temperatures at increased IR power.

effect and other state-of-the-art devices.

3.6 OEM response: opto-electromechanical effect

The opto-electromechanical (OEM) response is the core transduction mechanism of the NEMSTENNA: it is the deflection driven by the electrostatic force F_{ee} in the antenna feed gap, arising from the induced V_{gap}. In contrast to the OTM bending, the OEM deflection is much smaller in magnitude but can, in principle, operate at high speed (limited only by mechanical dynamics, not by thermal inertia). Here we analyze the OEM response based on simulation results from papers [44, 89–91] (A.1), (A.2), (B.2) and (B.3) plus discuss the achieved deflection amplitudes and the inferred responsivity.

In the original two-cantilever designs (A.1) and (A.2), the OEM effect causes each cantilever tip to bend inward, reducing the gap. The displacement can be thought of as the two free ends moving toward each other symmetrically (each covering half the gap closure). The mechanical stiffness of the cantilevers is very low (spring constant $k_c \approx 0.08$ N/m for the 200 μm long beam [44]), which means even a tiny electrostatic force can produce a measurable deflection. However, because the induced V_{gap} is on the order of 10^{-2} V, the force is extremely small. From a parallel-plate capacitor model, one can estimate $F_{ee} \sim \frac{\varepsilon_0 A}{2g^2} V_{gap}^2$ for gap $g \sim 10$ nm and overlapping area $A \sim 1\times10^{-13}$ m^2 (100 nm $\times$ 1 μm scale). Plugging $V_{gap} \sim 0.05$ V, we get F_{ee} on the order of 10 pN. Indeed, our detailed simulations yielded electrostatic force magnitudes in the low pN range per cantilever at a few mW laser power. Such a force, acting on a spring of $k \approx 0.08$ N/m, produces a deflection $\Delta x = F/k$ on the order of 10^{-10} m, which is 0.1 nm. The COMSOL coupled simulations (RF + electrostatic + solid mechanics) are more precise: they predicted a static OEM displacement (cantilever tip deflection due to F_{ee}) on the order of 0.01–0.1 nm for laser powers in the 1–10 mW range [44, 89], in accordance to the back-of-envelope calculation. In one reported scenario, a 10 mW illumination produced about 0.05 nm of gap closure [44]. For the maximum 7.5 mW used

in experiments, the simulation gave roughly $z_{\mathrm{OEM}} \approx$ 50–80 pm (per cantilever tip) [89]. These numbers mean the gap (initially 10 nm) would shrink by only ~0.1%, which is indeed a very small motion. Nonetheless, displacements in the tens-of-picometer range are within reach of sensitive detection techniques (e.g., interferometry or capacitive sensing). They also indicate a responsivity on the order of 10^{-2} nm/mW in this static configuration – i.e., each milliwatt of optical power yields 0.01 nm of deflection.

Interestingly, later design study anticipates a higher responsivity (B.2) and (B.3). In [90], we projected a responsivity of about 0.67 nm/mW for an optimized NEMSTENNA at 1.55 μm (Paper 3)(B.2). This figure was of the same order as some existing optomechanical detectors [42, 97] and was considered a promising value. If we were to modulate the light at the cantilever's resonant frequency (17 kHz) and read out the vibration amplitude, we could amplify the motion by the Q-factor of the resonance (which for a cantilever in air might be on the order of a few tens). That could potentially raise the effective responsivity by that factor, bringing it closer to the nm/mW range in a narrowband detection scheme. In this chapter, however, we focus on steady-state (or quasi-static) deflection under CW illumination for simplicity.

We implemented an iterative simulation scheme in (Paper 2)(A.2)[89] where the RF and mechanical solvers were run in a loop: after a small deflection, the new gap distance was used to recompute V_{gap}, which in turn gave an updated force. This iteration converges to a self-consistent deflected state; see the end of subsection 2.1.4. At low powers, the difference between this iterative solution and a simpler one-way calculation (assuming constant V_{gap}) was negligible. At the highest power (7.5 mW), the iterative method yielded about 78 pm deflection vs. 64 pm in the non-iterative method – roughly a 20% increase due to the positive feedback of narrowing the gap [89]. This shows that the electromechanical coupling is in the weakly nonlinear regime: the device does soften the gap (making V_{gap} rise slightly) as it deflects, but not dramatically at these power levels. At even higher power, one could imagine more pronounced self-enhancement, or even a static pull-in if

the force overcame the spring restoring force (though our device is far from that regime with only pN forces). The safe operation range has a large stability margin; the gap would need to be reduced from 10 nm to on the order of 1 nm to approach instability, which is far beyond the ~0.01 nm deflections we have.

A major advancement in enhancing the OEM response came from design evolution. In a recent work (Paper 4)(B.3) [91], we introduced a monolithic tuning-fork optomechanical antenna that achieves significantly larger OEM motion. Instead of two separate cantilevers facing each other vertically, this design uses two much shorter nano-cantilever beams connected at a base (forming a tuning fork), which deflect laterally toward each other under electrostatic force. This lateral configuration is inherently stiffer out-of-plane (to resist OTM bending) but very compliant in-plane. Simulations of the tuning-fork NEMSTENNA showed that with a similar optical drive (1.55 μm laser), the lateral deflection could reach tens of nanometers (Paper 4)(B.3) [91]. In fact, for a device with a 100 nm gap and 7.5 mW input, a lateral displacement over 13.5 nm was predicted (Paper 4)(B.3) [91], as shown in Figure 3.18.

Even accounting that this is the sum of both arms moving (say each arm moves 6.5 nm inward), this is orders of magnitude higher than the 0.06 nm we had with the original design. The key reasons for this improvement are: (1) a much lower effective spring constant in the lateral direction for the nano-scale tuning fork beams, (2) a larger initial gap (100 nm) that, while reducing V_{gap} somewhat, allows more travel range without pull-in and also reduces capacitance loading, and (3) incorporation of an optical transmission line so that the induced voltage is applied effectively along a length of the beam, augmenting the force (the design in [91] has the antenna integrated with a coplanar strip line that runs along the beams, so the electrostatic attraction acts over an extended area, not just at the tip). The result is a dramatic boost in OEM actuation: responsivity in that system can be estimated around ~ 1.8 nm/mW (since 13.5 nm at 7.5 mW scales to 1.8 nm/mW), which far exceeds our initial prototype (Paper 1)(A.1) and (Paper 3)(B.2).

In summary, the OEM response in our initial NEMSTENNA prototypes is a

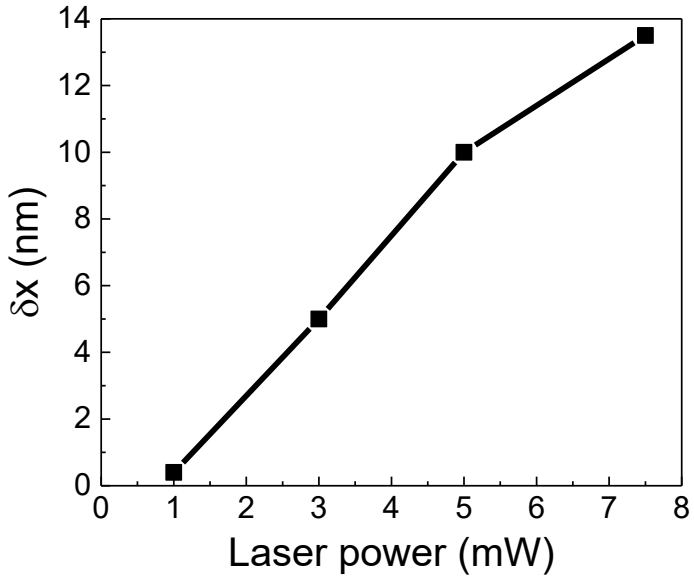

Figure 3.18: Lateral displacement in the x-direction, δ_x, vs. laser power. All simulations have been performed for a laser beam excitation with $\lambda = 1.55$ μm and spot radius, $SR = 8$ μm (Paper 4)(B.3) [91].

small but quantifiable displacement that directly follows the optical excitation. It is the fastest part of the response (in principle, the cantilever can respond up to its resonant frequency, thousands of times faster than thermal effects). The deflection amplitudes are on the order of 10–100 pm per mW in the static regime for the first designs and 13.5 nm for 7.5 mW, translating to a maximum 1.8 nm/mW-scale responsivity. While this is modest, it is within the realm of other experimental optomechanical detectors, and importantly, it can be potentially amplified (through resonance or design improvements). Our findings from papers [44, 89–91] collectively show that the concept works (light generates an electrostatic force and mechanical motion), and that there is room to optimize this effect. Table 3.6 (Paper 3)(B.2) [90] in the next section will place these numbers in context with existing technologies. The challenge ahead lies in boosting the OEM signal while suppressing the OTM background.

3.7 OEM versus OTM comparison optomechanical transducers

To compare the opto-electromechanical (OEM) and opto-thermomechanical (OTM) effects, we define a figure of merit (FoM) as the ratio of the OEM deflection to the OTM deflection under the same conditions, i.e. FoM = $z_{\mathrm{OEM}}/z_{\mathrm{OTM}}$, which quantifies how "clean" the electromechanical signal is [89]. For a broad illumination (laser spot radius $\sim 27.5\ \mu$m covering the whole cantilever), this FoM was found to be much less than 1 – typically on the order of a few 10^{-3}–10^{-2} depending on power – indicating that the parasitic thermal bending is roughly two orders of magnitude larger than the useful motion [89, 93]. Using COMSOL Multiphysics simulations and experimental validation (Paper 2) (A.2), the OTM deflection at $P_{\mathrm{in}} = 7.5$ mW was approximately $z_{\mathrm{OTM}} \approx 25$ nm, while the corresponding OEM displacement was $z_{\mathrm{OEM}} \approx 50$ pm, giving a ratio of about 2×10^{-3} for the largest laser spot radius. As the laser beam is focused more tightly onto the nanoantenna (reducing the spot radius from 27.5 μm to 14 μm and 8 μm), the OTM component drops drastically to a few nanometers ($z_{\mathrm{OTM}} \approx 3$ nm at 14 μm and ≈ 0.7 nm at 8 μm), while the OEM deflection increases due to the enhanced optical power density at the feed gap ($z_{\mathrm{OEM}} \approx 0.06$–$0.15$ nm). Consequently, the FoM improves nearly two orders of magnitude, reaching $\sim 2\times10^{-2}$–2×10^{-1}, as shown in Fig. 3.19 [89].

However, further analysis (Paper 3) (B.2) revealed that for very small spot radii ($< 4\ \mu$m), the OTM contribution starts increasing again due to enhanced localized heating, eventually reducing the FoM. In that work, the refined dual-cantilever NEMSTENNA structure exhibited an optimum at $SR = 4\ \mu$m with a maximum FoM ≈ 0.04 (Fig. 3.20), which is roughly one order of magnitude below the FoM ≈ 0.2 obtained in the previous design (Paper 2) (A.2). This difference arises because, although the NEMSTENNA's nanocantilever geometry significantly enhances the OEM displacement per optical power (responsivity ~ 0.67 nm/mW versus ~ 0.007 nm/mW in the previous version), the associated mechanical compliance also makes it more sensitive to thermally induced bending,

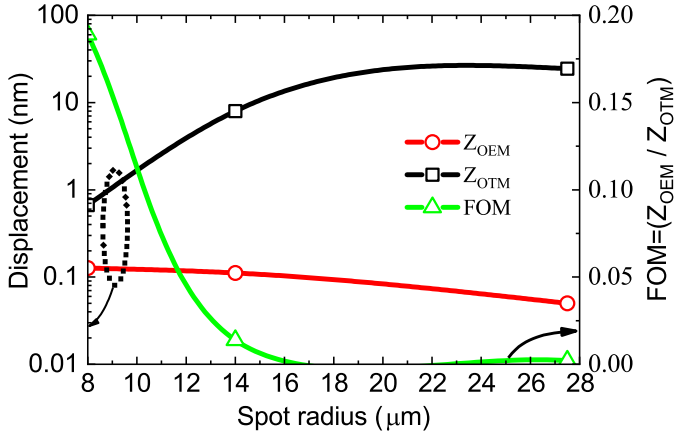

Figure 3.19: OEM and OTM displacements and their corresponding OEM/OTM ratio as defined by the FoM as a function of the laser spot radii, ranging from 8 to 27.5 μm. Laser power is $P_{\text{in}} = 7.5\,\text{mW}$ and gap distance is $g_0 = 10\,\text{nm}$ (Paper 2)(A.2) [89].

thus maintaining a similar or even lower OEM/OTM ratio overall.

Overall, focusing the beam can increase the FoM by roughly a factor of 2–3 in the current configuration, but the OTM response remains dominant in all cases. This highlights a key design imperative: to truly capitalize on the faster OEM mechanism, the parasitic OTM effect must be reduced as much as possible—either through structural design or optimized measurement conditions. Possible mitigation strategies include (i) localizing the laser illumination to the nanoantenna feed region rather than the entire cantilever, (ii) introducing structural symmetry (e.g., equal gold thicknesses on both sides or symmetric bimetallic layers) to cancel uniform thermal bending, and (iii) employing differential operating modes, for instance tuning-fork configurations as discussed in (Section 3.6) to cancel common-mode thermal expansions. Implementing these optimizations would suppress the slow, large-amplitude OTM response while preserving or even enhancing the fast OEM actuation, thereby improving the FoM and overall detector performance for NIR optomechanical applications.

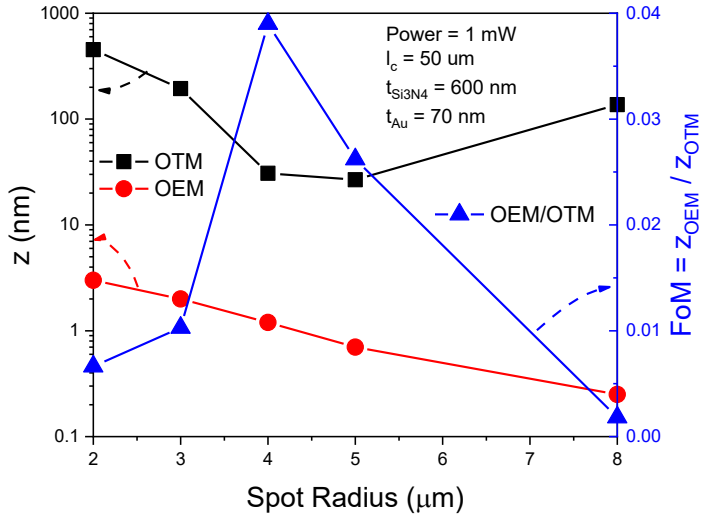

Figure 3.20: OTM and OEM responses (left axis) together with the figure of merit FoM = $z_{\mathrm{OEM}}/z_{\mathrm{OTM}}$ (right axis), as a function of spot radius SR. Nanocantilever dimensions are $l_n = 50$ μm, $t_n = 600$ nm, $t_{\mathrm{Au},n} = 70$ nm; and the laser power is 1 mW in all cases (Paper 3)(B.2) [90].

3.8 Comparison with state of the art

We now compare the performance of our NEMSTENNA optomechanical antenna to other state-of-the-art optomechanical transducers. Key metric of interest is responsivity (displacement or signal per optical power). It should be noted that the NEMSTENNA is a novel type of detector, so direct one-to-one comparisons are not easily available; however, we can benchmark against devices with a similar purpose, direct detection of NIR radiation via mechanical means. A benchmarking analysis based on the responsivity, defined as $\mathcal{R} \equiv \delta x/P_{\mathrm{laser}}$, was carried out to evaluate and compare the transduction performance of our optomechanical antennas including tuning-fork optomechanical NIR antenna, with that of state-of-the-art optomechanical transducers [26, 44, 64, 89–91, 98–100]. The results of this analysis are summarized in Table 3.6, where the responsivity $\mathcal{R}$ is provided. At the optical communication wavelength of $\lambda = 1.55$ μm ($f = 193.55$ THz), our

recent design (Paper 4)(B.3) exhibits a responsivity of $\mathcal{R} = 1.8$ nm/mW, showing a clear improvement over our previous designs [44, 89, 90].

Table 3.6: Responsivity values of some of the state-of-the-art optomechanical transducers [90, 91].

R_1 ($= z_{\mathrm{OEM}}/P_{\mathrm{laser}}$)	Units	Frequency	Wavelength	Reference
1.8	nm/mW	193.55 THz	1.55 μm	(Paper 4)(B.3) [91]
0.67	nm/mW	193.55 THz	1.55 μm	(Paper 3)(B.2) [90]
$6.7 \cdot 10^{-3}$	nm/mW	193.55 THz	1.55 μm	(Paper 2)(A.2) [89]
10^{-3}	nm/mW	193.55 THz	1.55 μm	(Paper 1)(A.1) [44]
0.49	nm/mW	2.6 THz	115 μm	[26]
$24.8 \cdot 10^{6}$	nm/mW	3.24–3.98 THz	92.6–75.4 μm	[98]
$3 \cdot 10^{4}$	nm/mW	2.5 THz	120 μm	[101]
$1.5 \cdot 10^{2}$	nm/mW	2.5 THz	120 μm	[100]

In addition to higher responsivity, the present tuning-fork architecture offers a remarkable improvement in immunity to parasitic thermal effects compared to earlier optomechanical antenna designs [44, 89, 90]. In previous cantilever-based structures, both the signal and the parasitic optothermal responses occurred along the same vertical direction (z-axis), leading to partial masking of the desired mechanical signal. In contrast, the current tuning-fork configuration introduces a geometric and mechanical decoupling of these two effects: the optomechanical signal manifests as a lateral displacement along the x-axis, while the thermally induced bending due to the Au/Si_3N_4 bilayer occurs along the z-axis. As a result, the thermal contribution does not interfere with the measured displacement δx, substantially improving signal fidelity and measurement accuracy.

Other optomechanical devices employing a similar transduction principle demonstrate comparable responsivity values but typically operate at much lower EM frequencies (around 2.6 THz) [26]. On the other hand, when comparing our device to optothermal transducers, i.e., devices based on an optically induced heating effect combined with a bimetallic mechanical bending, more than one order of magnitude responsivity enhancements are found with respect to the present work [98, 100, 101]. However, it is important to note that optothermal mechanisms inherently produce slower temporal responses and narrower bandwidths due to thermal

diffusion limits. In contrast, the direct optical-to-mechanical (OEM) transduction mechanism exploited in our design enables significantly faster response times and wider operational bandwidths, making it a superior approach for high-speed NIR detection applications (Paper 4)(B.3).

In summary, NEMSTENNA offers high-speed, passive, frequency-selective detection with a mechanical output. Its performance in terms of responsivity is competitive with other experimental optomechanical detectors and THz MEMS sensors, but it currently suffers from a large parasitic thermal background and a non-scalable fabrication. The footprint is moderate, and with new designs (like the tuning fork) the complexity can be reduced. The approach is advantageous when one desires to avoid electronics at the sensor or when operating in regimes where traditional sensors are too slow or not feasible. On the other hand, for mainstream optical sensing (e.g. telecommunications or imaging), substantial improvements in sensitivity and manufacturing would be required to make this technology a viable alternative. Our ongoing work addresses some of these issues, aiming to combine the fast, wide-band response of direct electromechanical transduction with improved responsivity (through mechanical amplification and better antenna design) and reduced thermal interference (through design/material changes). We believe that by leveraging the strengths of plasmonic field enhancement and MEMS tailoring, future optomechanical antennas could complement or even surpass certain state-of-the-art sensors in niche applications, especially where conventional electronics reach their limits.

Finally, we emphasize that while the NEMSTENNA's performance is not yet superior to all existing detectors in every metric, it introduces a new platform combining plasmonics and NEMS. The results in this chapter demonstrate the viability of this platform and provide a detailed understanding of both its capabilities and challenges, setting the stage for future improvements that could leverage the best of both electromagnetic and mechanical domains.

Chapter 4

Conclusions and Future Work

4.1 Conclusions

In this thesis, we introduced a novel near-infrared optomechanical nanoantenna (NEMSTENNA) capable of converting 1.55 μm light directly into mechanical motion. We establish the underlying optoelectromechanical (OEM) transduction mechanism and perform comprehensive design, simulation, fabrication, and experimental analysis to characterize the device's operation. The main achievements and findings of this work include:

- **Concept and principle of operation:** We developed and demonstrated a novel near-infrared optomechanical nanoantenna (NEMSTENNA) device capable of converting near-infrared (NIR) light directly into mechanical motion. The underlying physical mechanism was established: incident NIR light excites plasmonic modes in a gold dipole antenna, generating a localized gap voltage (V_{gap}) that induces electrostatic attraction and mechanical deflection. This phenomenon constitutes the **optoelectromechanical (OEM)** effect. In addition, a competing **optothermomechanical (OTM)** effect, arising from photothermal absorption and bending, was identified and analyzed in detail.

- **Design and simulation:** Plasmonic gold dipole antennas were designed and integrated on compliant silicon nitride (Si_3N_4) microcantilevers, optimized for resonance at the 1.55 μm telecom wavelength. Comprehensive *COMSOL Multiphysics* simulations were conducted, coupling electromagnetic, thermal, and mechanical domains. The simulations revealed a pronounced

antenna resonance at the design wavelength, a deep S_{11} notch corresponding to a lower mode, and strong field confinement in the ∼10 nm-100 nm feed gap, which induced a significant V_{gap}, voltage of the order of 10-100 mV, and electrostatic stress. Three different NEMSTENNA geometries were investigated to evaluate resonance tunability, fabrication tolerances, and mechanical response.

- **Fabrication:** The nanoscale optomechanical antenna structures were realized using focused ion beam (FIB) milling on gold-coated silicon nitride (Si_3N_4) cantilevers. The fabricated nanocantilevers exhibited a low spring constant ($\sim 10^{-1}$ N/m), ensuring high mechanical compliance suitable for optical actuation.

- **Parasitic optothermomechanical (OTM) effects:** Strong static deflection was observed under illumination experimentally and in simulations, which was attributed to photothermal heating of the gold/Si_3N_4 bilayer. The mechanical response exhibited a slow thermal time constant of the order of 0.533 ms, consistent with heat diffusion and bending mechanisms. Thermal simulations and experimental calibration confirmed that the OTM effect is dominant in the current device configuration.

- **Performance analysis and figure of merit:** A figure of merit (FoM = $z_{\text{OEM}}/z_{\text{OTM}}$) was defined to quantify the balance between direct OEM and parasitic OTM effects. The current prototypes achieved a FoM $\approx$ 0.04, indicating that the OTM effect remains approximately 20–50 times stronger than the OEM effect. Despite the dominance of thermal effects, the best device, a tuning fork optomechanical antenna, demonstrated a maximum static responsivity of 1.8 nm/mW, comparable to other NIR optomechanical transducers reported in the literature.

- **Benchmarking and comparative evaluation:** The NEMSTENNA´s displacement responsivity was benchmarked against state-of-the-art NIR optomechanical detectors, showing competitive values. Both simulation and

fabrication data confirmed that improved gap control and reduced absorption can substantially enhance the dominance of the OEM effect.

In conclusion, this thesis successfully established a proof-of-concept for direct NIR optomechanical transduction and clarified its fundamental limitations. By mitigating OTM effects, enhancing OEM forces, integrating on-chip optical delivery, and adopting scalable fabrication approaches, NEMSTENNA devices can evolve into fast and fully integrated NIR actuators. The results presented here provide both a solid foundation and a roadmap for the continued development of plasmomechanical transducers [44, 89–91].

4.2 Future Work

Future research should focus on overcoming the identified limitations and enhancing overall device performance. The following directions are proposed:

- **Minimizing photothermal bending:** Future design modifications should aim to minimize photothermal bending. Possible strategies include employing symmetric or athermal cantilever stacks, using thinner or lower-absorption metals, incorporating thermal isolation slots, or designing narrower and thinner cantilevers to improve heat dissipation. Additionally, applying surface coatings could further reduce optical absorption. The overarching goal is to decouple heating effects from mechanical deflection.

- **Enhancing the direct OEM signal:** To strengthen the direct OEM response, smaller feed gaps ($g_0 \rightarrow$ few nm) could be implemented to increase electrostatic forces quadratically, though such fabrication presents technical challenges. Driving the cantilever dynamically at its mechanical resonance (in the kHz range) could amplify the OEM motion through the Q-factor resonance while filtering out slower thermal responses. Furthermore, alternative antenna geometries, such as bowtie or multi-gap configurations,

may enhance field concentration and transduction efficiency. The ultimate objective is to increase the figure of merit (FoM = $z_{\mathrm{OEM}}/z_{\mathrm{OTM}}$) beyond unity.

- **On-chip optical delivery:** Integrating on-chip delivery of NIR light via waveguides or fibers would eliminate free-space alignment losses and improve optical efficiency. Such integration would also enable scalable excitation of NEMSTENNA arrays, advancing practical device packaging, reliability, and robustness.

- **Transition to CMOS-compatible fabrication:** Transitioning from FIB-milled prototypes to lithographic, CMOS-compatible fabrication processes—such as electron-beam or nanoimprint lithography with MEMS materials—would enable wafer-scale production and array-level fabrication. This approach would allow integration with on-chip electronic readout and control systems, ultimately leading to fully integrated optoelectromechanical NIR detection chips.

4.3 Scientific contributions of the author

The work presented in this thesis has resulted in several peer-reviewed journal publications and international conference contributions.

4.3.1 Publications

4.3.1.1 Journal publications

1. D. Khosh Maram, X. Borrisé, J. J. Garcia-Garcia, R. Ruiz, X. Cartoixà, G. Abadal, "Design and fabrication of an opto-mechanical antenna in the NIR range," *Micro and Nano Engineering*, vol. 23, p. 100241, Elsevier, June 2024.
   DOI: 10.1016/j.mne.2024.100241

2. D. Khosh Maram, J. J. Garcia-Garcia, X. Cartoixà, G. Abadal, "Impact of the parasitic photothermal effect on the performance of an optomechanical nanoantenna for NIR radiation detection," *Sensors and Actuators A: Physical*, p. 116966, Elsevier, August 2025.
DOI: 10.1016/j.sna.2025.116966

3. D. Khosh Maram, X. Borrisé, J. J. Garcia-Garcia, X. Cartoixà, G. Abadal, "Plasmomechanical actuation at the nanoscale activated by NIR radiation," *Results in Physics*, Elsevier, 2025, under review.
DOI: http://dx.doi.org/10.2139/ssrn.5544681

4. D. Khosh Maram, X. Borrisé, J. J. Garcia-Garcia, Guy A.E. Vandenbosch, X. Cartoixà, G. Abadal, "Tuning fork optomechanical NIR antenna with integrated optical transmission line," *Sensors and Actuators A: Physical*, Elsevier, 2025, under review.

4.3.1.2 Conference proceedings publications

1. D. Khosh Maram, X. Cartoixà, G. Abadal, "Analysis of the Photothermal Parasitic Effect on an Optomechanical Antenna," *2024 IEEE SENSORS*, Kobe, Japan, October 2024, 4 pp, IEEE, ISBN:979-8-3503-6351-7, ISSN: 2168-9229.
DOI: 10.1109/SENSORS60989.2024.10785153

4.3.2 Conference contributions

1. D. Khosh Maram, X. Borrisé, J. J. Garcia-Garcia, R. Ruiz, X. Cartoixà, G. Abadal, "Design and fabrication of an opto-mechanical antenna in the NIR range," *49th International Conference on Micro and Nano Engineering (MNE 2023)*, Berlin, Germany, September 2023.
URL: https://mne-2023.org/

2. D. Khosh Maram, X. Borrisé, J. J. Garcia-Garcia, R. Ruiz, X. Cartoixà, G. Abadal, "Improved opto-mechanical nanoantenna in the NIR range," *50th International Conference on Micro and Nano Engineering (MNE 2024)*, Montpellier, France, September 2024.
URL: https://mne2024.imnes.org/

3. D. Khosh Maram, X. Cartoixà, G. Abadal, "Analysis of the Photothermal Parasitic Effect on an Optomechanical Antenna," *2024 IEEE SENSORS*, Kobe, Japan, October 2024, IEEE.
DOI: 10.1109/SENSORS60989.2024.10785153

4. D. Khosh Maram, X. Borrisé, J. J. Garcia-Garcia, R. Ruiz, X. Cartoixà, G. Abadal, "Tuning fork optomechanical NIR antenna with integrated optical transmission line," *51st International Conference on Micro and Nano Engineering (MNE 2025)*, Southampton, United Kingdom, September 2025.
URL: https://mne2025.imnes.org/

5. R. Ruiz, D. Khosh Maram, X. Cartoixà, G. Abadal "A MEMSTENNA relay: coupling a slot dipole antenna with a MEMS relay for wireless and batteryless switching control," *50th International Conference on Micro and Nano Engineering (MNE 2024)*, Montpellier, France, September 2024.
URL: https://mne2024.imnes.org/

6. R. Ruiz, D. Khosh Maram, X. Cartoixà, G. Abadal, "Integrating a MEMS Speaker with a Slot Dipole Antenna: A Wireless and Batteryless Acoustic Transducer," *23rd International Conference on Solid-State Sensors, Actuators and Microsystems (Transducers 2025)*, Orlando, Florida, USA, June 2025, IEEE.
DOI: 10.1109/Transducers61432.2025.11111607

7. D. Khosh Maram, J. J. Garcia-Garcia, R. Ruiz, X. Cartoixà, G. Abadal, "From radiofrequency to infrared antennas: downscaling a rectangular loop geometry," *International Workshop on Computational Nanotechnology*, Barcelona,

Spain, June 2023.
URL: https://iwcn2023.uab.es/

4.3.3 Publications not directly related to the thesis

1. R. Ruiz, D. Khosh Maram, X. Cartoixà, G. Abadal, "Integrating a MEMS Speaker with a Slot Dipole Antenna: A Wireless and Batteryless Acoustic Transducer," *23rd International Conference on Solid-State Sensors, Actuators and Microsystems (Transducers 2025)*, Orlando, Florida, USA, June 2025, pp. 1807–1810, IEEE, ISBN:979-8-3315-1381-8, ISSN: 2167-0021. DOI: 10.1109/Transducers61432.2025.11111607

2. R. Ruiz, D. Khosh Maram, X. Cartoixà, G. Abadal, "A MEMSTENNA relay: coupling a slot dipole antenna with a MEMS relay for wireless and batteryless switching control" *Micro and Nano Engineering (2025)*, Under review,

Bibliography

[1] J. Huang, B. Luo, Y. Cao, B. Li, M. Qian, N. Jia, and W. Zhao, "Fusion of THz-TDS and NIRS-based detection of moisture content for cattle feed," *Front. Phys.*, vol. 10, p. 833278, 2022. https://doi.org/10.3389/fphy.2022.833278

[2] A. A. Firoozi and A. A. Firoozi, "A comprehensive survey: The role of terahertz (THz) communication systems in urban infrastructure development," *Measurement*, vol. 251, p. 117318, 2025. https://doi.org/10.1016/j.measurement.2025.117318

[3] M. Jamrógiewicz, "Application of near-infrared (NIR) spectroscopy in pharmaceutical technology," *J. Pharm. Biomed. Anal.*, vol. 66, pp. 1–10, 2012. https://doi.org/10.1016/j.jpba.2012.03.009

[4] J. Ajayan, S. Sreejith, M. Manikandan, W.-C. Lai, and S. Saha, "Terahertz (THz) sensors for next-generation biomedical and other industrial electronics applications: A critical review," *Sens. Actuators A Phys.*, vol. 369, p. 115169, 2024. https://doi.org/10.1016/j.sna.2024.115169

[5] M. Selvaraj, S. B. Sreeja, and M. A. S. Aly, "Terahertz (THz)-based biosensors for biomedical applications: A review," *Methods*, vol. 234, pp. 54–66, 2025. https://doi.org/10.1016/j.ymeth.2024.12.001

[6] J. M. Jornet, E. W. Knightly, and D. M. Mittleman, "Wireless communications, sensing, and security above 100 GHz," *Nat. Commun.*, vol. 14, no. 1, p. 841, 2023. https://doi.org/10.1038/s41467-023-36621-x

[7] S. Latreche, H. Bellahsene, and A. Taleb-Ahmed, "Terahertz (THz) for radar applications and wireless communication," *arXiv preprint*, arXiv:2507.23076, 2025. https://doi.org/10.48550/arXiv.2507.23076

[8] L. Nevou, M. Tchernycheva, L. Doyennette, F. H. Julien, E. Warde, R. Colombelli, F. Guillot, S. Leconte, E. Monroy, T. Remmele, and M. Albrecht, "New developments for nitride unipolar devices at 1.3–1.5 m wavelengths," *Superlattices Microstruct.*, vol. 40, no. 4, pp. 412–417, 2006. https://doi.org/10.1016/j.spmi.2006.09.016

[9] H. Ahmad, B. Nizamani, M. Z. Samion, and M. Yasin, "Wideband ultrafast mode-locked praseodymium- and erbium-doped fiber lasers using zinc phosphate at 1.3- and 1.5 μm," *Opt. Fiber Technol.*, vol. 76, p. 103241, 2023. https://doi.org/10.1016/j.yofte.2023.103241

[10] W. Huang, S. Luo, D. Yang, and S. Zhang, "Applications of smartphone-based near-infrared (NIR) imaging, measurement, and spectroscopy technologies to point-of-care (POC) diagnostics," *J. Zhejiang Univ. Sci. B*, vol. 22, no. 3, pp. 171–189, 2021. https://doi.org/10.1631/jzus.B2000388

[11] L. Liu, B. Li, and P. Wang, "Editorial: Near-infrared (NIR) fluorescence probes for biomedical applications," *Front. Bioeng. Biotechnol.*, vol. 11, p. 1267302, 2023. https://doi.org/10.3389/fbioe.2023.1267302

[12] Y. Kravchenko, K. Sikora, A. A. Wireko, and M. Lyndin, "Fluorescence visualization for cancer detection: Experience and perspectives," *Heliyon*, vol. 10, no. 2, p. e24390, 2024. https://doi.org/10.1016/j.heliyon.2024.e24390

[13] N. Gomidze, L. Kalandadze, M. Khajishvili, O. Nakashidze, I. Jabnidze, D. Jakobia, and K. Makharadze, "Fluorescence spectroscopy as a novel tool in hematological diagnostics," *APL Bioeng.*, vol. 9, no. 2, p. 026102, 2025. https://doi.org/10.1063/5.0264155

[14] Specim, "The importance of near-infrared (NIR) sensors and their typical applications," online resource, 2025. https://www.specim.com/technology/nir-hyperspectral-imaging/

[15] J. Deng, H. Jiang, and Q. Chen, "Qualitative and quantitative analysis of mineral oil pollution in peanut oil by Fourier transform near-infrared (FT-NIR) spectroscopy," *Food Chem.*, vol. 469, p. 142590, 2025. https://doi.org/10.1016/j.foodchem.2024.142590

[16] K. B. Beć, J. Grabska, and C. W. Huck, "Principles and applications of miniaturized near-infrared (NIR) spectrometers," *Chem. Eur. J.*, vol. 27, no. 5, pp. 1514–1532, 2021. https://doi.org/10.1002/chem.202002838

[17] M. Liu, Y. Li, Z. Ren, Y. Wang, H. Zhu, Q. Qiu, N. Ali, H. Zhu, J. Zhu, W. Lai, *et al.*, "High-performance room-temperature terahertz photodetection using two-dimensional electron gas channel transport," *Research*, vol. 8, p. 0656, 2025. https://doi.org/10.34133/research.0656

[18] R. Degl'Innocenti, L. Xiao, D. S. Jessop, S. J. Kindness, Y. Ren, H. Lin, J. A. Zeitler, J. A. Alexander-Webber, H. J. Joyce, P. Braeuninger-Weimer, S. Hofmann, H. E. Beere, and D. A. Ritchie, "Fast room-temperature detection of terahertz quantum cascade lasers with graphene-loaded bow-tie plasmonic antenna arrays," *ACS Photonics*, vol. 3, no. 10, pp. 1747–1753, 2016. https://doi.org/10.1021/acsphotonics.6b00405

[19] D. Li, Z. Bai, X. Zuo, Y. Wu, J. Sheng, and H. Wu, "Room-temperature single-photon terahertz detection with thermal Rydberg atoms," *Appl. Phys. Rev.*, vol. 11, no. 4, p. 041420, 2024. https://doi.org/10.1063/5.0219879

[20] A. Kosarev, S. Rumyantsev, M. Moreno, A. Torres, S. Boubanga, and W. Knap, "SiGe:H-based micro-bolometers studied in the terahertz frequency range," *Solid-State Electron.*, vol. 54, no. 4, pp. 417–419, 2010. https://doi.org/10.1016/j.sse.2009.12.032

[21] A. J. Holden, "Pyroelectric sensor arrays for detection and thermal imaging," in *Infrared Technology and Applications XXXIX*, B. F. Andresen, G. F. Fulop, C. M. Hanson, P. R. Norton, and P. Robert, Eds., vol. 8704, SPIE, 2013, p. 87041N. https://doi.org/10.1117/12.2014239

[22] Z. Xiang, M. Shi, N. Zhou, C. Zhang, X. Ding, Y. Ni, D. Chen, and H. Mao, "A highly accurate method for measuring response time of MEMS thermopiles," *Micromachines*, vol. 13, no. 10, p. 1717, 2022. https://doi.org/10.3390/mi13101717

[23] E. Moisello, P. Malcovati, and E. Bonizzoni, "Thermal sensors for contactless temperature measurements, occupancy detection, and automatic operation of appliances during the COVID-19 pandemic: A review," *Micromachines*, vol. 12, no. 2, p. 148, 2021. https://doi.org/10.3390/mi12020148

[24] W. Guo, Z. Dong, Y. Xu, C. Liu, D. Wei, L. Zhang, X. Shi, C. Guo, H. Xu, G. Chen, L. Wang, K. Zhang, X. Chen, and W. Lu, "Sensitive terahertz detection and imaging driven by the photothermoelectric effect in ultrashort-channel black phosphorus devices," *Adv. Sci.*, vol. 7, no. 5, p. 1902699, 2020. https://doi.org/10.1002/advs.201902699

[25] M. S. Hasan, A. A. Khan, S. Shahzadi, M. H. Bagheri, and D. Ban, "Terahertz radiation detectors using CMOS-compatible SOI substrates," *Adv. Funct. Mater.*, vol. 34, no. 41, p. 2400313, 2024. https://doi.org/10.1002/adfm.202400313

[26] C. Belacel, Y. Todorov, S. Barbieri, D. Gacemi, I. Favero, and C. Sirtori, "Optomechanical terahertz detection with single meta-atom resonator," *Nat. Commun.*, vol. 8, no. 1, p. 1578, 2017. https://doi.org/10.1038/s41467-017-01840-6

[27] F. Sizov, "Terahertz radiation detectors: The state of the art," *Semicond. Sci. Technol.*, vol. 33, no. 12, p. 123001, 2018. https://doi.org/10.1088/1361-6641/aae473

[28] M. J. E. Golay, "A pneumatic infra-red detector," *Rev. Sci. Instrum.*, vol. 18, no. 5, pp. 357–362, 1947. https://doi.org/10.1063/1.1740949

[29] “Golay cell,” *Wikipedia*, 2007. https://en.wikipedia.org/wiki/Golay$_cell$ (accessed May 16, 2025)

[30] “THz Detectors Overview: Application Note,” GentecEO, 2024. https://www.gentec-eo.com/Content/downloads/application-note/AN$_2$01924$_T$Hz$_R$1.pdf

[31] S. K. Kamilla and M. Ojha, “Review on nano-electro-mechanical-system devices,” *Mater. Today: Proc.*, vol. 81, pp. 133–136, 2023. https://doi.org/10.1016/j.matpr.2021.02.801

[32] R. Ruiz, J. Bonache, and G. Abadal, “A flexible dipole antenna for direct transduction of microwave radiated power into DC mechanical deflection,” *Sens. Actuators A Phys.*, vol. 340, p. 113536, 2022. https://doi.org/10.1016/j.sna.2022.113536

[33] X. Fan, C. He, J. Ding, Q. Gao, H. Ma, M. C. Lemme, and W. Zhang, “Graphene MEMS and NEMS,” *Microsyst. Nanoeng.*, vol. 10, no. 1, p. 154, 2024. https://doi.org/10.1038/s41378-024-00791-5

[34] L. Welburn, A. M. M. Javadi, L. Nguyen, and S. Desai, “Prospects and trends in biomedical microelectromechanical systems (MEMS) devices: A review,” *Biomolecules*, vol. 15, no. 6, p. 898, 2025. https://doi.org/10.3390/biom15060898

[35] H. Qu, “CMOS MEMS fabrication technologies and devices,” *Micromachines*, vol. 7, no. 1, p. 14, 2016. https://doi.org/10.3390/mi7010014

[36] J. L. Muñoz Gamarra, “NEMS/MEMS integration in submicron CMOS technologies,” Ph.D. dissertation, Universitat Autònoma de Barcelona, 2014. https://www.tesisenred.net/handle/10803/285060

[37] B. Sharma, M. Kumar, and A. Sharma, “Recent advances in micro- and bio-electromechanical system architectures for energy efficient chemire-

sistors," *Microelectronic Engineering*, vol. 288, p. 112168, 2024. https://doi.org/10.1016/j.mee.2024.112168

[38] M. Jedari Ghourichaei, U. Kerimzade, L. Demirkazik, B. Pruchnik, K. Kwoka, D. Badura, T. Piasecki, A. T. Toymus, O. Aydin, B. Aksoy, C. Aydogan, G. Nadar, I. W. Rangelow, L. Beker, A. D. Yalcinkaya, H. Bayraktar, T. Gotszalk, and B. E. Alaca, "Multiscale fabrication and characterization of a NEMS force sensor," *Advanced Materials Technologies*, vol. 10, no. 4, p. 2400022, 2025. https://doi.org/10.1002/admt.202400022

[39] X. Li, B. Bhushan, K. Takashima, C.-W. Baek, and Y.-K. Kim, "Mechanical characterization of micro/nanoscale structures for MEMS/NEMS applications using nanoindentation techniques," *Ultramicroscopy*, vol. 97, no. 1, pp. 481–494, 2003. https://doi.org/10.1016/S0304-3991(03)00077-9

[40] R. Ruiz and G. Abadal, "Remote dynamic actuation of an electrostatically driven microcantilever by a wireless power transfer system," *Sensors and Actuators A: Physical*, vol. 345, p. 113798, 2022. https://doi.org/10.1016/j.sna.2022.113798

[41] R. Ruiz and G. Abadal, "Direct transduction from radiofrequency radiated power to static and dynamic flexural mechanical modes," in *Proc. 21st Int. Conf. on Solid-State Sensors, Actuators and Microsystems (TRANSDUCERS)*, 2021, pp. 144–147. https://doi.org/10.1109/Transducers50396.2021.9495668

[42] H. Zhu, K. Wang, G. Liu, G. Wang, J. Mou, W. Zhang, and G. Wei, "A terahertz optomechanical detector based on metasurface and bimaterial micro-cantilevers," *Micromachines*, vol. 13, p. 805, May 2022. https://doi.org/10.3390/mi13050805

[43] C. Li, Y. Zhang, and K. Hirakawa, "Terahertz detectors using microelectromechanical system resonators," *Sensors*, vol. 23, p. 5938, Jul. 2023. https://doi.org/10.3390/s23135938

[44] D. K. Maram, X. Borrisé, J. Garcia-Garcia, R. Ruiz, X. Cartoixà, and G. Abadal, "Design and fabrication of an opto-mechanical antenna in the NIR range," *Micro and Nano Engineering*, vol. 23, p. 100241, 2024. https://doi.org/10.1016/j.mne.2024.100241

[45] A. Kainz, H. Steiner, J. Schalko, A. Jachimowicz, F. Kohl, M. Stifter, R. Beigelbeck, F. Keplinger, and W. Hortschitz, "Distortion-free measurement of electric field strength with a MEMS sensor," *Nature Electronics*, vol. 1, no. 1, pp. 68–73, 2018. https://doi.org/10.1038/s41928-017-0009-5

[46] A. S. Algamili, M. H. M. Khir, J. O. Dennis, A. Y. Ahmed, S. S. Alabsi, S. S. Ba Hashwan, and M. M. Junaid, "A review of actuation and sensing mechanisms in MEMS-based sensor devices," *Nanoscale Research Letters*, vol. 16, 2021. https://api.semanticscholar.org/CorpusID:231706481

[47] L. Zheng, J. Zhang, H. Wang, and J. Liu, "RF NEMS switches based on graphene for low pull-in voltage and excellent RF performance," *Scientific Reports*, vol. 14, Oct. 2024. https://doi.org/10.1038/s41598-024-74334-3

[48] A. Ashkin, "Trapping of atoms by resonance radiation pressure," *Physical Review Letters*, vol. 40, no. 12, pp. 729–732, Mar. 1978. doi: 10.1103/PhysRevLett.40.729.

[49] M. Aspelmeyer, T. J. Kippenberg, and F. Marquardt, "Cavity optomechanics," *Rev. Mod. Phys.*, vol. 86, no. 4, pp. 1391–1452, Dec. 2014. https://doi.org/10.1103/RevModPhys.86.1391

[50] J. D. Thompson, B. M. Zwickl, A. M. Jayich, F. Marquardt, S. M. Girvin, and J. G. E. Harris, "Strong dispersive coupling of a high-finesse cavity to a micromechanical membrane," *Nature*, vol. 452, no. 7183, pp. 72–75, Mar. 2008. https://doi.org/10.1038/nature06715

[51] Z. Zhu, S. Joshi, B. Pelz, and G. Moddel, "Overview of optical rectennas for solar energy harvesting," in *Next Generation (Nano) Photonic*

and Cell Technologies for Solar Energy Conversion IV, O. V. Sulima and G. Conibeer, Eds., *Proc. SPIE*, vol. 8824, p. 88240O, Sept. 2013. https://doi.org/10.1117/12.2024700

[52] A. E. Krasnok, I. S. Maksymov, A. I. Denisyuk, P. A. Belov, A. E. Miroshnichenko, C. R. Simovski, and Yu. S. Kivshar, "Optical nanoantennas," *Physics-Uspekhi*, vol. 56, no. 6, pp. 539–564, Jun. 2013. https://doi.org/10.3367/UFNe.0183.201306a.0561

[53] C. Huang, X. Guan, H. Lin, L. Liang, Y. Miao, Y. Wu, H. Bao, X. Wu, A. Shen, M. Wei, and J. Huang, "Efficient photoacoustic imaging with biomimetic mesoporous silica-based nanoparticles," *Frontiers in Bioengineering and Biotechnology*, vol. 9, 2021. https://doi.org/10.3389/fbioe.2021.762956

[54] T. Larsen, S. Schmid, L. G. Villanueva, and A. Boisen, "Photothermal analysis of individual nanoparticulate samples using micromechanical resonators," *ACS Nano*, vol. 7, no. 7, pp. 6188–6193, Jul. 2013. https://doi.org/10.1021/nn402057f

[55] N. Luhmann, R. G. West, J. P. Lafleur, and S. Schmid, "Nanoelectromechanical infrared spectroscopy with *in situ* separation by thermal desorption: NEMS-IR-TD," *ACS Sensors*, vol. 8, no. 4, pp. 1462–1470, Apr. 2023. https://doi.org/10.1021/acssensors.2c02435

[56] E. Sesto, *Application of NEMS-FTIR for micro- and nanoplastic detection in water: a study on artificially weathered polymer samples*, Dissertation, Technische Universität Wien, 2025. https://doi.org/10.34726/hss.2025.119392

[57] D. Ramos, J. Tamayo, J. Mertens, and M. Calleja, "Photothermal excitation of microcantilevers in liquids," *Journal of Applied Physics*, vol. 99, no. 12, p. 124904, Jun. 2006. doi: 10.1063/1.2205409.

[58] C. A. Reynaud, D. Duché, J.-J. Simon, E. Sanchez-Adaime, O. Margeat, J. Ackermann, V. Jangid, C. Lebouin, D. Brunel, F. Du-

mur, D. Gigmes, G. Berginc, C. A. Nijhuis, and L. Escoubas, "Rectifying antennas for energy harvesting from the microwaves to visible light: A review," *Prog. Quantum Electron.*, vol. 72, p. 100265, 2020. https://doi.org/10.1016/j.pquantelec.2020.100265

[59] S. Joshi and G. Moddel, "Efficiency limits of rectenna solar cells: theory of broadband photon-assisted tunneling," *Appl. Phys. Lett.*, vol. 102, no. 8, p. 083901, Feb. 2013. https://doi.org/10.1063/1.4793425

[60] A. Y. Tang, "Modelling of terahertz planar Schottky diodes," in *Proc. Conf.*, 2011. https://api.semanticscholar.org/CorpusID:54764002

[61] R. Citroni, F. Di Paolo, and P. Livreri, "Progress in THz rectifier technology: research and perspectives," *Nanomaterials*, vol. 12, no. 14, p. 2479, 2022. https://doi.org/10.3390/nano12142479

[62] A. Sharma, V. Singh, T. L. Bougher, and B. A. Cola, "A carbon nanotube optical rectenna," *Nat. Nanotechnol.*, vol. 10, no. 12, pp. 1027–1032, 2015. https://doi.org/10.1038/nnano.2015.220

[63] D. Matsuura, M. Shimizu, and H. Yugami, "High-current density and high-asymmetry MIIM diode based on oxygen-non-stoichiometry controlled homointerface structure for optical rectenna," *Sci. Rep.*, vol. 9, no. 1, p. 19639, 2019. https://doi.org/10.1038/s41598-019-55898-x

[64] Z. Liu, S. Abe, M. Shimizu, and H. Yugami, "Enhanced current density and asymmetry of metal–insulator–metal diodes based on self-assembly of Pt nanoparticles," *Appl. Phys. Lett.*, vol. 122, no. 9, p. 093502, 2023. https://doi.org/10.1063/5.0123591

[65] R. Citroni, A. Leggieri, D. Passi, F. Di Paolo, and A. Di Carlo, "Nano energy harvesting with plasmonic nano-antennas: A review of MID-IR rectenna and application," *Adv. Electromagn.*, vol. 6, no. 2, pp. 1–13, 2017. https://doi.org/10.7716/aem.v6i2.462

[66] R. Grimming, "Uncooled microbolometer imaging systems for machine vision," M.S. thesis, Electronic Theses and Dissertations, 2020–2023, Univ. of Central Florida, 2022. https://stars.library.ucf.edu/etd2020/1379

[67] Optris Inc., "Advantages of uncooled infrared cameras," 2025. https://optris.com/lexicon/uncooled-thermal-infrared-camera/

[68] C.-D. Lee, S.-F. Tang, and T.-C. Chen, "Novel performance evaluation of thermal camera based on VOx bolometer focal plane array via analysis of sigma NETD, mean NETD, and roughness index," *Sensors and Materials*, vol. 30, pp. 1283–1296, Jan. 2018. https://doi.org/10.18494/SAM.2018.1913

[69] C. Fried, B. J. Russell, E. G. Arnault, B. Huang, G.-H. Lee, D. Englund, E. A. Henriksen, and K. C. Fong, "Performance limits due to thermal transport in graphene single-photon bolometers," *Physical Review Applied*, vol. 21, no. 1, p. 014006, Jan. 2024. https://doi.org/10.1103/PhysRevApplied.21.014006

[70] A. Blaikie, D. Miller, and B. J. Alemán, "A fast and sensitive room-temperature graphene nanomechanical bolometer," *Nature Communications*, vol. 10, no. 1, p. 4726, Oct. 2019. https://doi.org/10.1038/s41467-019-12562-2

[71] A. V. Sergeev, "Superconducting thermal detector (bolometer) of terahertz radiation," U.S. Patent US20160018267A1, filed 2014.

[72] X. Huang, A. Shen, R. Peng, S. Chen, S. Lin, S. Ding, H. Li, and D. Zhou, "A novel biomimetic nanoprobe as a photoacoustic contrast agent," *Frontiers in Chemistry*, vol. 9, p. 721799, 2021. doi: 10.3389/fchem.2021.721799.

[73] *COMSOL Multiphysics*, version 6.1, COMSOL AB, Stockholm, Sweden, 2022. Available: https://www.comsol.com/ [Accessed: May 16, 2025].

[74] X. Chen, Y. Chen, M. Yan, and M. Qiu, "Nanosecond photothermal effects in plasmonic nanostructures," *ACS Nano*, vol. 6, no. 3, pp. 2550–2557, Mar. 2012. https://doi.org/10.1021/nn2050032

[75] T. Jeong, J.-G. Zhu, S. Chung, and M. R. Gibbons, "Thermal boundary resistance for gold and CoFe alloy on silicon nitride films," *Journal of Applied Physics*, vol. 111, no. 8, p. 083510, Apr. 2012. https://doi.org/10.1063/1.3703571

[76] M. I. Flik, B. I. Choi, and K. E. Goodson, "Heat transfer regimes in microstructures," *Journal of Heat Transfer*, vol. 114, no. 3, pp. 666–674, Aug. 1992. https://doi.org/10.1115/1.2911332

[77] S. Bai, Z. Tang, Z. Huang, and J. Yu, "Thermal characterization of Si_3N_4 thin films using transient thermoreflectance technique," *IEEE Transactions on Industrial Electronics*, vol. 56, no. 8, pp. 3238–3243, 2009. https://doi.org/10.1109/TIE.2009.2022078

[78] R. Sultan, A. D. Avery, G. Stiehl, and B. L. Zink, "Thermal conductivity of micromachined low-stress silicon-nitride beams from 77 to 325 K," *Journal of Applied Physics*, vol. 105, no. 4, p. 043501, Feb. 2009. https://doi.org/10.1063/1.3078025

[79] J. Peirs, D. Reynaerts, and H. Van Brussel, "Scale effects and thermal considerations for micro-actuators," in *Proceedings of the 1998 IEEE International Conference on Robotics and Automation*, vol. 2, pp. 1516–1521, 1998. https://doi.org/10.1109/ROBOT.1998.677333

[80] X. J. Hu, A. Jain, and K. E. Goodson, "Investigation of the natural convection boundary condition in microfabricated structures," *International Journal of Thermal Sciences*, vol. 47, no. 7, pp. 820–824, 2008. https://doi.org/10.1016/j.ijthermalsci.2007.07.011

[81] R. J. Stevens, A. N. Smith, and P. M. Norris, "Measurement of thermal boundary conductance of a series of metal–dielectric interfaces by the transient thermoreflectance technique," *Journal of Heat Transfer*, vol. 127, no. 3, pp. 315–322, 2005. https://doi.org/10.1115/1.1857944

[82] E. T. Swartz and R. O. Pohl, "Thermal boundary resistance," *Reviews of Modern Physics*, vol. 61, no. 3, pp. 605–668, 1989. https://doi.org/10.1103/RevModPhys.61.605

[83] R. Stoneback, "The dipole impedance of an aperture," *Progress In Electromagnetics Research B*, vol. 26, pp. 401–423, 2010. https://doi.org/10.2528/PIERB10062406

[84] O. W. Käding, H. Skurk, and K. E. Goodson, "Thermal conduction in metallized silicon-dioxide layers on silicon," *Applied Physics Letters*, vol. 65, no. 13, pp. 1629–1631, 1994. https://doi.org/10.1063/1.112933

[85] J. W. Hutchinson, "Stresses and failure modes in thin films and multilayers," in *Proceedings of the Conference on Thin Films and Multilayers*, 1996. https://api.semanticscholar.org/CorpusID:11726712

[86] Z. D. Wang and S. Q. Jiang, "Coefficient of thermal expansion of stressed thin films," *Transactions of Nonferrous Metals Society of China*, vol. 16, pp. s220–s225, 2006. https://doi.org/10.1016/S1003-6326(06)60179-9

[87] Z. Ma and G. A. E. Vandenbosch, "Optimal solar energy harvesting efficiency of nanorectenna systems," *Solar Energy*, vol. 88, pp. 163–174, 2013. https://doi.org/10.1016/j.solener.2012.11.023

[88] Z. Ma and G. A. E. Vandenbosch, "Input impedance of optical metallic nano dipole over 300 nm–1200 nm wavelength," in *Proc. 7th European Conf. Antennas Propag. (EuCAP)*, 2013, pp. 3810–3813.

[89] D. K. Maram, J. Garcia-Garcia, X. Cartoixà, and G. Abadal, "Impact of the parasitic photothermal effect on the performance of an optomechanical nanoantenna for NIR radiation detection," *Sensors and Actuators A: Physical*, vol. 394, p. 116966, Aug. 2025. https://doi.org/10.1016/j.sna.2025.116966

[90] D. K. Maram, X. Borrisé, J. Garcia-Garcia, X. Cartoixà, and G. Abadal, "Plasmomechanical actuation at the nanoscale activated by NIR radiation,"

unpublished manuscript, submitted to *Results in Physics*, manuscript RINP-D-25-01855, Sep. 2025.

[91] D. K. Maram, X. Borrisé, J. Garcia-Garcia, G. A. E. Vandenbosch, X. Cartoixà, and G. Abadal, "Tuning fork optomechanical NIR antenna with integrated optical transmission line," *unpublished manuscript*, submitted for publication.

[92] "AFM Probe PNP-TR-TL-Au," NanoAndMore, 2024. [Online]. Available: https://www.nanoandmore.com/AFM-Probe-PNP-TR-TL-Au. [Accessed: May 16, 2025].

[93] D. K. Maram, X. Cartoixà, and G. Abadal, "Analysis of the photothermal parasitic effect on an optomechanical antenna," in *Proc. 2024 IEEE SENSORS*, 2024, pp. 1–4. doi: 10.1109/SENSORS60989.2024.10785153.

[94] L. Novotny and N. van Hulst, "Antennas for light," *Nature Photonics*, vol. 5, no. 2, pp. 83–90, Feb. 2011. doi: 10.1038/nphoton.2010.237.

[95] H. Ditlbacher, A. Hohenau, D. Wagner, U. Kreibig, M. Rogers, F. Hofer, F. R. Aussenegg, and J. R. Krenn, "Silver nanowires as surface plasmon resonators," *Physical Review Letters*, vol. 95, no. 25, p. 257403, Dec. 2005. doi: 10.1103/PhysRevLett.95.257403.

[96] M. W. Knight, H. Sobhani, P. Nordlander, and N. J. Halas, "Photodetection with active optical antennas," *Science*, vol. 332, no. 6030, pp. 702–704, May 2011. doi: 10.1126/science.1203056.

[97] X. Liu, W. Liu, Z. Ren, Y. Ma, B. Dong, G. Zhou, and C. Lee, "Progress of optomechanical micro/nano sensors: a review," *International Journal of Optomechatronics*, vol. 15, no. 1, pp. 120–159, 2021. doi: 10.1080/15599612.2021.1986612.

[98] H. Zhu, F. Yi, and E. Cubukcu, "Plasmonic metamaterial absorber for broadband manipulation of mechanical resonances," *Nature Photonics*, vol. 10, no. 11, pp. 709–714, Nov. 2016. doi: 10.1038/nphoton.2016.183

[99] Z. Buch and S. Schmid, "Design considerations of gold nanoantenna dimers for plasmomechanical transduction," *Optics Express*, vol. 30, no. 4, pp. 5294–5303, Feb. 2022. doi: 10.1364/OE.450837.

[100] K. Froberger, B. Walter, M. Lavancier, R. Peretti, G. Ducournau, J.-F. Lampin, M. Faucher, and S. Barbieri, "SOI-based micro-mechanical terahertz detector operating at room temperature and atmospheric pressure," *Applied Physics Letters*, vol. 120, no. 26, p. 261103, June 2022. doi: 10.1063/5.0095126.

[101] J. Liu, B. Chomet, P. Beoletto, D. Gacemi, K. Pantzas, G. Beaudoin, I. Sagnes, A. Vasanelli, C. Sirtori, and Y. Todorov, "Ultrafast detection of terahertz radiation with miniaturized optomechanical resonator driven by dielectric driving force," *ACS Photonics*, vol. 9, no. 5, pp. 1541–1546, May 2022. doi: 10.1021/acsphotonics.2c00227.

.

Appendix A

Compendium Papers

A.1 Design and fabrication of an opto-mechanical antenna in the NIR range

Journal paper (Paper 1), Published in Micro and Nano Engineering.

MNE 23 (2024) 100241

Contents lists available at ScienceDirect

Micro and Nano Engineering

journal homepage: www.sciencedirect.com/journal/micro-and-nano-engineering

Design and fabrication of an opto-mechanical antenna in the NIR range

Daniyal Khosh Maram [a,*], Xavier Borrisé [b], Joan Garcia-Garcia [a], Raul Ruiz [a], Xavier Cartoixà [a], Gabriel Abadal [a]

[a] Departament d'Enginyeria Electrònica, Universitat Autònoma de Barcelona, 08193 Bellaterra, Barcelona, Spain
[b] Catalan Institute of Nanoscience and Nanotechnology (ICN2) and Barcelona Institute of Science and Technology (BIST), Barcelona, Spain

ARTICLE INFO

Keywords:
Opto-mechanical antenna
NIR optical detector
Plasmonic optical nanoantenna
MEMS/NEMS resonators

ABSTRACT

In this study we present a novel device for the direct transduction of optical radiation in the near-infrared region into mechanical actuation, which is based on a plasmonic optical nanoantenna integrated in a microcantilever. We propose and demonstrate the feasibility of a simple fabrication process consisting in the nano-tailoring of a commercially available Atomic Force Microscope (AFM) cantilever by means of the Focused Ion Beam (FIB) milling technique. Furthermore, the comprehensive analysis of the device performance characteristics included in this work reveals the different sensitivity values of these characteristics to the fabrication process tolerances of the most relevant geometric design parameters.

1. Introduction

The concept of MEMSTENNA, a term derived from MEMS (Micro-Electro-Mechanical Systems) and antenna introduced in previous works by R. Ruiz et al. [1–3], has demonstrated to enable direct transduction from the electromagnetic domain in the radiofrequency range to the mechanical domain, within the feed-gap of radiofrequency antenna structures. In such MEMSTENNA devices, both static and dynamic actuation is remotely achieved, so that capacitive MEMS structures are mechanically excited without any reliance on a local power supply. An extension of the MEMSTENNA concept to the 1–10 THz frequency range was proposed previously by C. Belacel et al. [4] as a novel THz detector, whose operating principle is also based on the direct transduction from the electromagnetic domain to the mechanical domain. Unlike other THz bolometric detectors based on MEMS structures, such as clamped-clamped beam resonators [5], clamped-free beams with an absorbing metasurface [6] or clamped-clamped beams driven by dielectric forces [7], direct transduction allows to enhance the THz detector frequency response at room temperature, since thermal domain is not present in the transduction mechanism. Other examples of electromagnetic to mechanical direct transduction are found in the optical range. In cavity optomechanical systems, for instance, direct light matter interaction, which is in the basis of atom cooling foundational works [8], is used to amplify to the self-sustained level or to cool-down to the ground state the vibrations of a mechanical oscillator [9]. In most of the cases, cavity optomechanical devices consist of Fabry-Perot interferometers built using highly reflective MEMS membranes [10], but more complex structures such as wine glass mode NEMS resonators [11] or suspended photonic crystals [12] have demonstrated to show quantum effects related to photon-phonon interaction.

On the other hand, optical nanoantenna technology [13,14] emerged as a promising alternative to semiconductor detectors [15] and photovoltaic energy harvesting transducers [16–18]. However, here again, slow time constants of the thermal mechanisms involved in bolometric detection schemes [19] limits the frequency response of these optical nanoantenna detectors, and optical rectenna configurations based on the combination of an optical nanoantenna and a fast integrated rectifier are limited by the impedance mismatch of the antenna and the diode rectifier [20].

In the present study, we propose to extend the MEMSTENNA concept to the near-infrared (NIR) optical frequency range, in order to keep the advantage of direct transduction in terms of frequency response [1–3], namely to get a faster response of the device and a wider frequency bandwidth than traditional bolometric based detector of radiation, which are based in a slow opto-thermally induced mechanical actuation effect. We name the novel device with the new term NEMSTENNA, denoting the fusion in this case of a plasmonic optical nanoantenna [21] with a MEMS structure. A NIR NEMSTENNA has applications beyond the optical sensors field as the fast transducer of a wide bandwidth NIR detector, in, for instance, the actuators area. Here, for example, the NIR

* Corresponding author.
E-mail address: daniyal.khoshmaram@uab.cat (D.K. Maram).

https://doi.org/10.1016/j.mne.2024.100241
Received 17 November 2023; Received in revised form 23 February 2024; Accepted 2 March 2024
Available online 4 March 2024
2590-0072/© 2024 The Authors. Published by Elsevier B.V. This is an open access article under the CC BY-NC license (http://creativecommons.org/licenses/by-nc/4.0/).

NEMSTENNA can be used as the basic element of a nano-switch or a nano-relay actuated remotely by a NIR control signal. Since the IR radiation can be used as the control switch-on and switch-off signal but at the same time as the power means, NEMSTENNA would enable a wireless and batteryless switch/relay nanodevice. A switch/relay with these characteristics can benefit by its reduced dimensions and power autonomy to be integrated, for instance, in implanted microsystems where the use of batteries becomes an issue. In following, this study has been outlined. In section 2, we present the NEMSTENNA device layout and the transduction mechanisms involved in the operation principle. Section 3 covers the fabrication process and presents results concerning the geometry characterization of the fabricated structures. In Section 4, we delve into a sensitivity analysis of both S_{11} resonance and gap induced voltage vs. frequency conducted using COMSOL, along with discussions on NEMSTENNA deflection and gap voltage induction within varying gap distances.

2. Device structure and working principle

2.1. Opto-mechanical antenna structure

Our proposed device structure consists of a NIR optical dipole nanoantenna ($\lambda = 1.55$ μm) integrated in one of the metal sides of the free-end of two Au-coated silicon nitride triangular microcantilevers, as shown in Fig. 1. The dipole nanoantenna geometry is defined by its two components' length and width (L_1, L_2, W_1) as well as the dimensions of the supporting arms (L_{Arm1}, L_{Arm2}, W_2) which connect the dipole components to the microcantilevers. Notice that the cross shape is a geometry that allows to define the dipole in one direction (the polarization direction of the IR linearly polarized beam) and the supporting arms connected to the dipole in the feed-gap area in the perpendicular direction, in order not to interfere the dipole behaviour. The Si_3N_4 thickness in the nanoantenna area is also considered as a design parameter. Both components of the nanoantenna are parallelly placed at a gap distance in an overlap area in the feed region of the antenna, defining a transduction capacitance that will electrically load the nanoantenna (Fig. 1).

2.2. Opto-mechanical antenna working principle

The working principle of the opto-mechanical antenna hinges upon a well-defined transduction chain. Specifically, when the nanoantenna is exposed to a resonant radiation source (a NIR laser with $\lambda_{NIR} = 1.55$ μm –$f_{NIR} = 193.41$ THz–, for instance), a voltage denoted as V_{gap} is induced within the feed gap region of the antenna. This induced voltage stems from the interaction between the incident radiation and the plasmonic optical nanoantenna, and is an ac voltage with the same frequency of the exciting radiation ($f_{NIR} = 193.41$ THz), as described by the following equation:

$$V_{gap} = V_0 \cdot sin(\omega_{NIR} t) \tag{1}$$

Using Eq. (2) [22,23], we can calculate V_{gap} from the electric field in the feed gap region by the integration of this electric field E along the gap distance.

$$V_{gap} = -\int_{gap} \vec{E} \cdot d\vec{l} \tag{2}$$

Subsequently, this voltage V_{gap} will induce an electrostatic force. This force will be applied at both components of the nanoantenna dipole in the gap region and, eventually, it will produce their mutual attraction (see Fig. 2). Remarkably, this electrostatic force exhibits a nonlinear relationship with the voltage V_{gap} as shown in Eq. (3) [2]:

$$F_{ee} = \frac{\varepsilon_0 A V_{gap}^2}{2\,(g_0 - z_1 - z_2)^2}, \tag{3}$$

where A is overlapping area, ε_0 is the air dielectric constant, V_{gap} is the

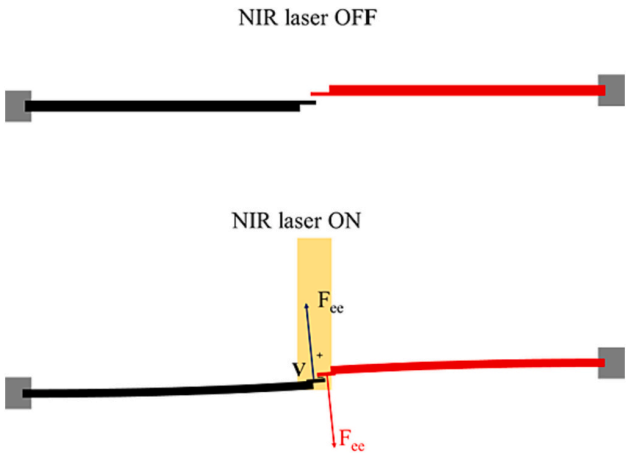

Fig. 2. Actuation principle of the opto-mechanical antenna.

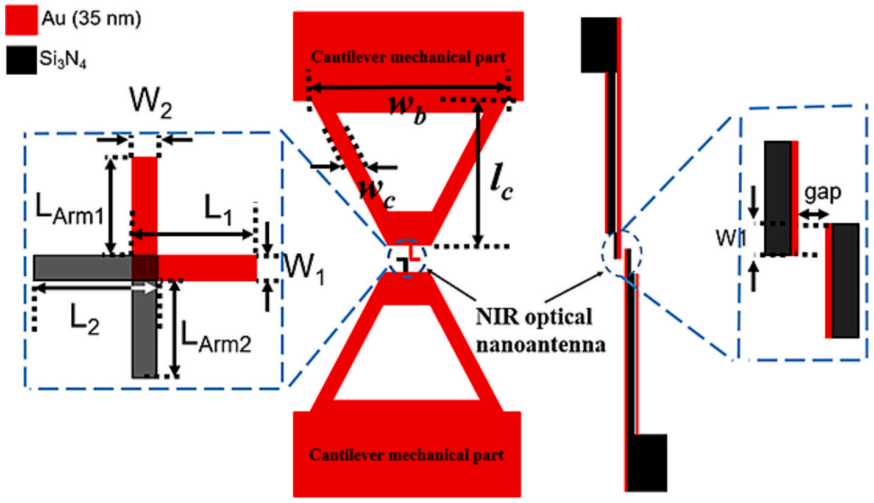

Fig. 1. Schematic top and side views of the proposed structure including nano-antenna and microcantilever.

induced voltage within the gap area, g_0 is the gap distance, z_1 and z_2 are the deflections of each one of the beams and F_{ee} is the electrostatic force. This nonlinearity leads to the emergence of a DC component of the force, which can be obtained by combining Eqs. (1) and (3):

$$F_{ee} = \frac{\epsilon_0 A}{2(g_0 - z_1 - z_2)^2}\cdot(V_0 sin(\omega_{NIR}t))^2 = \frac{\epsilon_0 A V_0^2}{2(g_0 - z_1 - z_2)^2}\cdot\left[\frac{1}{2} - \frac{1}{2}cos(2\omega_{NIR}t)\right] \quad (4)$$

Thus, the first term in the right side of Eq. (4) corresponds to the DC component of the force:

$$F_{ee,DC} = \frac{\epsilon_0 A V_0^2}{4(g_0 - z_1 - z_2)^2} \quad (5)$$

This resultant DC component of the electrostatic force is applied within the overlap region of the antenna structure and consequently it also induces a mutual attraction between both microcantilevers at their free ends, since they are mechanically attached to the nanoantenna through the connection arms.

The second term in the right side of Eq. (4) corresponds to an ac component of the force at a frequency twice the radiation frequency ($2\cdot\omega_{NIR}$), that will not induce any significant mechanical vibration on the microcantilevers, since both the excitation force (hundreds of THz) and the natural vibration frequency (tenths of kHz) of the microcantilevers are orders of magnitude different.

3. Fabrication process

The fabrication process of the optical nanoantenna is carried out on the free end of tipless Atomic Force Microscope (AFM) microcantilevers, which are commercially available [24]. These cantilevers, characterized by their triangular geometry, as shown in (Fig. 1 and 3a), serve as the fundamental starting point for the subsequent nanoantenna integration. The structural material is 600 nm thick silicon nitride (Si_3N_4) with a 70/35 (top/bottom) nm thick Cr/Au coating layer. The V-shape structure is geometrically defined (Fig. 1) by the base width, w_b, arm length, l_c and arm width, w_c, and is supported by a Pyrex anchor. Nominal resonance frequency and spring constant are 17 kHz and 0.08 N/m respectively. After turning upside down the microcantilever (Fig. 3.b), the first step involves the local removal of the 70 nm Cr/Au layer and the subsequent thickness reduction of the silicon nitride (Si_3N_4) layer in a limited area at the free end of the cantilevers (Fig. 3c), by means of the FIB (Focused Ion Beam) milling nanolithography. In this first FIB step, the ion beam is scanned using a low Ga^+ beam current (700 pA) and a fast scan speed (1 s/scan) to avoid the redeposition of material and get a sort of brushing effect on the cantilever surface. A systematic calibration of the etch rate in previous conditions gives a value of around 33 nm/min which is translated to a resolution of the Si_3N_4 vertical etching process of 5–10 nm. However, as Si_3N_4 thickness is reduced below 50 nm, the structure starts to be unstable and bending collapse is finally produced, probably due to residual stress of the Au layer. So, 50 nm is a reliable lower limit of the Si_3N_4 thickness. After that, FIB milling is also employed to precisely define the structure of one of the nanoantenna's components. This is achieved through the complete removal of both the Si_3N_4 layer and the underlying bottom 35 nm thick Cr/Au layer (Fig. 3d). In this second

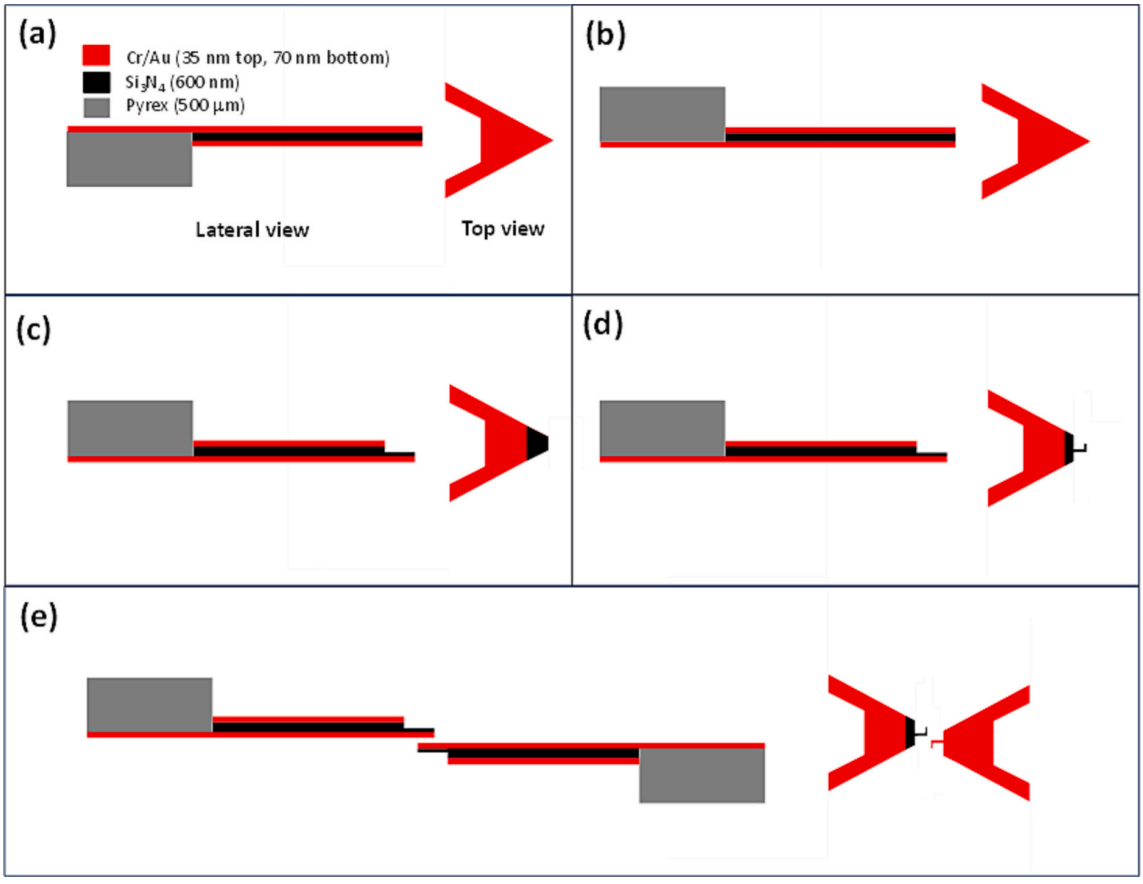

Fig. 3. FIB based fabrication process steps of the proposed structure: (a) Initial AFM microcantilever structure, (b) microcantilever flipping, (c) local FIB milling thickness reduction, (d) local FIB milling half nanoantenna definition and (e) NEMSTENNA final build-up.

FIB step, higher beam currents (3 nA) and slower scan speeds (10 s/scan) are used to enhance the etching throughput. However, in this case, these values, together with the beam aperture, are progressively reduced in order to increase the lateral etching resolution as we approach the final lateral dimensions of the antenna structure. In standard conditions, the fabrication tolerance associated to the lateral milling resolution would be around 10–20 nm. However, this value is increased to a maximum level of 50 nm due to lateral drifts and fluctuations of the suspended cantilever structure which is subjected to the charging effects of the Si_3N_4 layer. Alternative nanofabrication techniques as e-beam lithography (EBL), that would tighten the fabrication tolerance to 10 nm or below, would only be applicable if the antenna fabrication steps were included in the whole cantilever fabrication process.

FIB process implies an approximately 2 μm reduction in the cantilever length, translating into a 1% length reduction in this case, which consequently produces an increase of 2.8% in the spring constant and 1.8% in the resonance frequency. This process is repeated to define the second nanoantenna component in the very end of a second AFM microcantilever. Once the two components of the NEMSTENNA have been fabricated, one of them is flipped upside down and both are carefully placed, each bearing its nanostructured tip, in close proximity to each other (Fig. 3e) to complete the nanodipole antenna of the NEMSTENNA device. SEM images of Fig. 4 show the structural details and dimensions of a fabricated prototype of NEMSTENNA along its fabrication process described above. In particular, the transformation of the AFM microcantilever free end after silicon nitride thickness reduction (Fig. 4.a, corresponding to step c in Fig. 3), as well as the half nanoantenna definition (Fig. 4.b, corresponding to step d in Fig. 3) are shown.

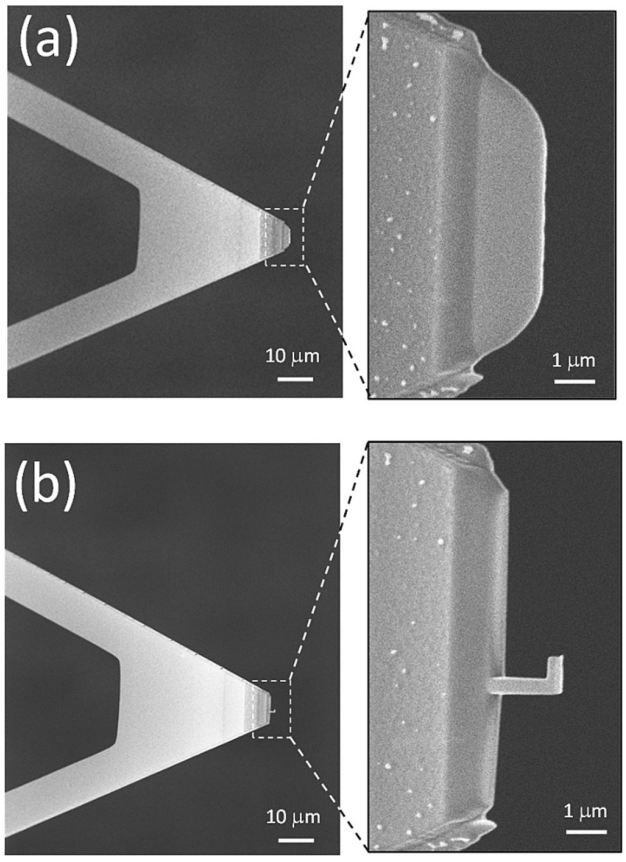

Fig. 4. SEM images of a fabricated NEMSTENNA prototype after (a) step c (see Fig. 3.c) and (b) step d (see Fig. 3.d) of the fabrication process.

4. Results and discussion

4.1. Simulation conditions

After demonstrating the fabrication of a NEMSTENNA structure, we have carried out an optimization process to tune the nanoantenna to the $\lambda = 1.55$ μm wavelength. Besides, we have performed a detailed sensitivity analysis of the most important NEMSTENNA characteristics to the dispersion of the fabrication parameters, to elucidate which are the most critical parameters that could mainly affect the performance of future fabricated devices.

To obtain a good prediction of the transduction response of the NEMSTENNA needed to optimize its performance and analyse its sensitivity to the fabrication tolerances, we have modelled and simulated the NEMSTENNA using COMSOL multiphysics simulation setup. Specifically, to follow the phenomenological sequence described in section 2.2, we have first modelled and simulated the optical nanoantenna part of the NEMSTENNA by means of the COMSOL multiphysics RF module to obtain, among other parameters, the nanoantenna voltage in the feedgap, V_{gap}. Next, we have coupled the RF module to the electrostatics and solid mechanics through this nanoantenna feed gap voltage, to obtain the mechanical deflection of the two microcantilevers, as the main simulation output. On the one hand, RF simulation conditions are characterized by the definition of a lumped port or a Gaussian laser beam as excitation sources, depending on the analysed output magnitude. Thus, to obtain the S_{11} frequency response of the nanoantenna, lumped port excitation is needed, whilst a gaussian beam excitation is more convenient to calculate the feed gap voltage. Geometry characteristics and material properties used in the simulations are provided in Table 1 and Table 2, respectively. Values reported in Table 1 are mainly obtained from the microcantilevers datasheet [24], from SEM images shown in Fig. 4 and from the nanoantenna optimization to 1.55 μm wavelength process described below. Among the properties reported in Table 2, the most important, and not specified there, are the permittivity vs. wavelength ($\varepsilon_r(\lambda)$), which are inferred from [25], and correspond to Johnson and Christy (for Au) and Luke et al. (for Si_3N_4) experimental data. The simulation procedure involves constructing a 3D model of the NEMSTENNA design and considering a perfect match layer (PML) boundary condition [26] as an outer layer of the simulation box. In addition, the NEMSTENNA is surrounded by air including the gap area. Furthermore, a high mesh refinement has been taken into account in the gap area [22]. For the focused laser beam the paraxial approximation of a Gaussian beam has been used, and the laser power and beam radius are between 10 mW and 500 mW and 27.5 μm, respectively.

Table 1
Geometry dimensions of the NEMSTENNA device used in COMSOL simulations.

Parameter	Value
Dipole arm length ($L_{Arm1}/L_{Arm\ 2}$)*, μm	0.72/0.75
Dipole arm width (w_2)*, μm	0.1
Dipole length (L_1/L_2)*, μm	0.82/0.85
Dipole width (w_1)*, μm	0.1
Dipole gold thickness (t_{gd})**, μm	0.035
Dipole silicon nitride thickness (t_{dd})***, μm	0.14
Cantilever length (l_c)**, μm	200
Cantilever width (w_c)**, μm	28
Cantilever base width (w_b)**, μm	184
Cantilever spring constant (k_c)**, N/m	0.08
Cantilever silicon nitride thickness (t_{dc})**, μm	0.6
Cantilever gold thickness (t_{gc})**, μm	0.07
Capacitive gap (g_0)*, nm	10
Overlapping Area (A)*, μm^2	0.01
Dipole resonant wavelength/frequency (f_d), $\mu m/THz$	1.55/193.41

* From optimization at 1.55 μm.
** From [24].
*** From SEM images of Fig. 4.

Table 2
Material properties used in our NEMSTENNA COMSOL design and modelling.

Parameter	Air	Gold	Silicon Nitride
Young Modulus *E*, *(Pa)*	–	79×10^9	250×10^9
Poisson's ratio ν	–	0.44	0.23
Density ρ, kg/m^3	–	19,300	3100
Relative permittivity ε_r	1	$\varepsilon_r(\lambda)$	$\varepsilon_r(\lambda)$
Electrical conductivity σ, *(S/m)*	0	45.6×10^6	0

To examine the NEMSTENNA deflection in a steady-state response, the study started with the RF design module and it ended using electromechanical forces multiphysics (including coupling between solid mechanics and electrostatics physics). First, nano-antennas, located on the tip of the cantilevers, were excited using a Gaussian laser beam to generate the V_{gap} induced voltage. Then, this calculated voltage was employed as an input for the electromechanical forces multiphysics approach, integrating solid mechanics and electrostatics physics. To simulate the system, a dynamic approach was taken, utilizing a moving mesh within the simulation box that housed the NEMSTENNA in an air environment, which prevented non-convergence issues. Convergence was achieved using COMSOL segregated solver for observing stationary steady-state responses, while accounting for geometric nonlinearity in the simulation.

4.2. Optimization and tolerance analysis

4.2.1. Design of the optimum nanoantenna

Prior to the tolerance analysis, we have designed the nanoantenna to optimize S_{11} at 1.55 μm (193.41 THz). In this process, L_1, L_2, L_{Arm1}, L_{Arm2} and W_1=W_2 are taken as free parameters for optimization, while Si_3N_4 thickness is supposed to be 140 nm, as observed in SEM images of Fig. 4. The gap distance is initially fixed to $g_0 = 10$ nm. Thus, deepest S_{11} notch is achieved for $L_1 = 820$ nm, $L_2 = 850$ nm, $L_{Arm1} = 720$ nm, $L_{Arm2} = 750$ nm and $W_1 = W_2 = 100$ nm as shown in Fig. 5a (bold blue curve). It is worth to note that the nanoantenna design is not optimized in terms of receiving efficiency, since the large mismatch between the illumination spot area ($2.4 \cdot 10^{-9}$ m^2) and the nanoantenna aperture ($1.6 \cdot 10^{-13}$ m^2) implies that only the $1.6 \cdot 10^{-3}$% of the radiated power is harnessed by the nanoantenna. In future applications, such an efficiency can be improved by arraying several nanodipoles in parallel, to extend in the transversal direction the effective area of the device.

4.2.2. Tolerance analysis of the nanoantenna

Once the optimum dimensions have been found, an analysis of the fabrication tolerance effects on the S_{11} vs. frequency curves has been also carried out. In this analysis, we have considered 50 nm as an upper limit of the geometry tolerance, which is given by the resolution of the particular FIB milling process we have used. The results of this analysis are summarized in Fig. 5a. As it can be observed, if L_1 and L_2 optimum values are deviated simultaneously along the same direction by 50 nm, which corresponds to the two worst cases, the S_{11} notch is produced at 190 THz (L_1 + 50 nm and L_2 + 50 nm) or 200 THz (L_1–50 nm and L_2–50 nm), as shown in the dark cyan and gray curves in Fig. 5.a, respectively. Alternatively, if we suppose that the excitation radiation cannot be tuned to the nanoantenna resonance and its frequency is fixed to 193.41 THz, then a change in S_{11} from −22 dB (optimum L_1 and L_2) to −9 dB (L_1–50 nm and L_2–50 nm) or − 14 dB (L_1 + 50 nm and L_2 + 50 nm) will be produced at the excitation frequency.

Given the relevance of the feed gap voltage, V_{gap}, in the transduction mechanism of the NEMSTENNA, we have also analysed the fabrication tolerance effect on this magnitude. The results of this analysis are portrayed in Fig. 5b, which are obtained by taking a radiation power of 500 mW, as considered a moderately high limit of experimentally achievable laser source. As expected, we first notice that the optimum V_{gap} vs. frequency curve has its peak at the same frequency that maximizes S_{11}, i.e. the design frequency 193.41 THz. In other words, both S_{11} and V_{gap} get their maximum simultaneously. Also as expected, we find that the effect on V_{gap} of L_1 and L_2 worst case deviations is like the effect observed in S_{11}. In this case, however, voltage V_{gap} is increased to 100 mV (20 mV up from the optimum 80 mV value), which suppose an improvement, when deviation on L_1 and L_2 is in the reduction direction (L_1–50 nm and L_2–50 nm). Such an increase of V_{gap}, which does not correspond to an increase of the S_{11} notch depth, is probably produced because the matching between the dipole impedance and the free space impedance is better than the matching between the dipole impedance and the 50 Ω of the port used to calculate S_{11}. In the other worst case (L_1 + 50 nm and L_2 + 50 nm) voltage is reduced to 40 mV. From this analysis we can derive a maximum sensitivity value of $\partial V_{gap}/\partial L_{1,2} = -0.4$ mV/nm at f = 193.41 THz.

On the other hand, we have been also interested in analysing the sensitivity of V_{gap} to the Si_3N_4 layer thickness in the nanoantenna. The resulting data of this analysis are shown in Fig. 6, which are obtained for 500 mW of laser power. As it can be observed, V_{gap} is almost insensitive to Si_3N_4 thickness variations between 350 nm and 600 nm, but presents

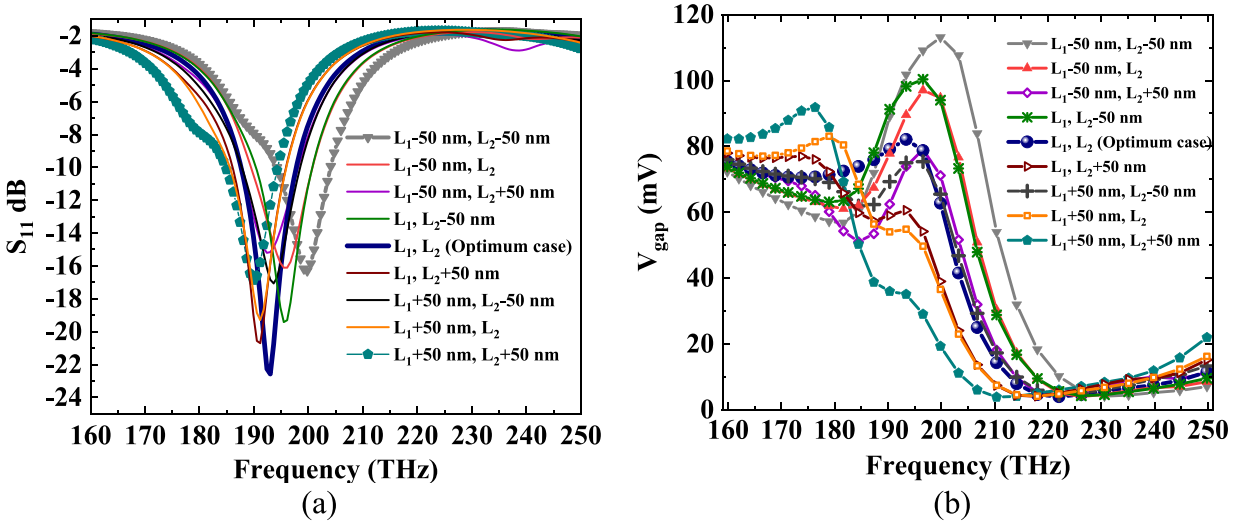

Fig. 5. Frequency response of S_{11} (a) and V_{gap} (b) obtained from COMSOL simulation, for 8 different values of L_1 and L_2 around the optimum case. Laser power is 500 mW and gap distance is $g_0 = 10$ nm.

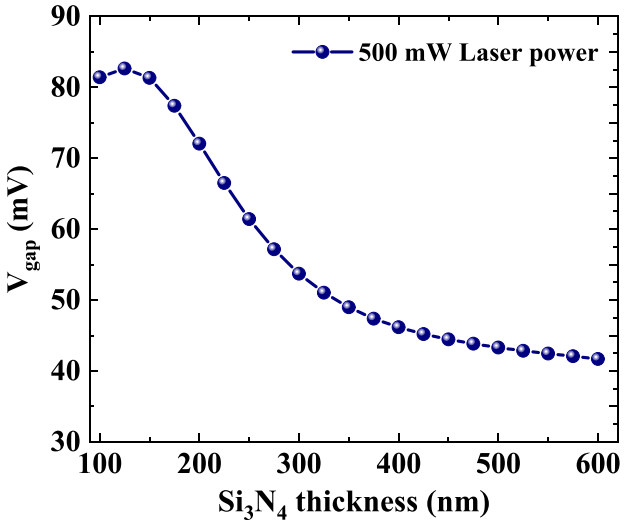

Fig. 6. V_{gap} vs Si_3N_4 thickness at 193.41 THz ($\lambda = 1.55$ μm) for a laser power of 500 mW and a gap distance of $g_0 = 10$ nm.

a maximum sensitivity of $V_{gap}/\partial t_{Si3N4} = -0.16$ mV/nm around 200 nm. On the other hand, according to the curve of Fig. 6, the optimum Si_3N_4 thickness that maximize V_{gap} is around 125 nm, which is above the lower fabrication limit of 50 nm.

4.2.3. Tolerance analysis of the NEMSTENNA opto-mechanical response

Finally, after coupling RF, electrostatics and solid mechanics modules in a multi-physics setup, we have calculated the feed gap voltage, V_{gap}, and the microcantilever deflection induced by the electrostatic force in terms of the cantilever free end displacement, for different initial gap distances and for three different laser powers: 10 mW as the maximum power achievable in our experimental setup in the DUT (Device Under Test) position, 100 mW as an intermediate value and 500 mW as the upper limit of experimentally achievable power. This calculation has been carried out for the optimum case (L_1,L_2), for the upper deviation case (L_1 + 50 nm and L_2 + 50 nm) and for the lower deviation case (L_1–50 nm and L_2–50 nm). The corresponding family of curves are shown in Fig. 7.a, Fig. 7.b and Fig. 7.c, respectively.

In accordance with the findings outlined in section 4.2.2, the application of a laser beam with a power of 0.5 W and a wavelength $\lambda = 1.55$ μm, yields a V_{gap} of 84 mV within the nanoantenna feed gap, as depicted in Fig. 7.a, for an initial gap $g_0 = 10$ nm. In these conditions, the induced free end displacement of the cantilevers is around 0.02 nm, which is unpractical since it is too close to the detectability limit. Notably, while it is apparent that in the lower deviation case (L_1–50 nm, L_2–50 nm) a higher gap voltage can be generated, 110 mV at f = 200 THz and 100 mV

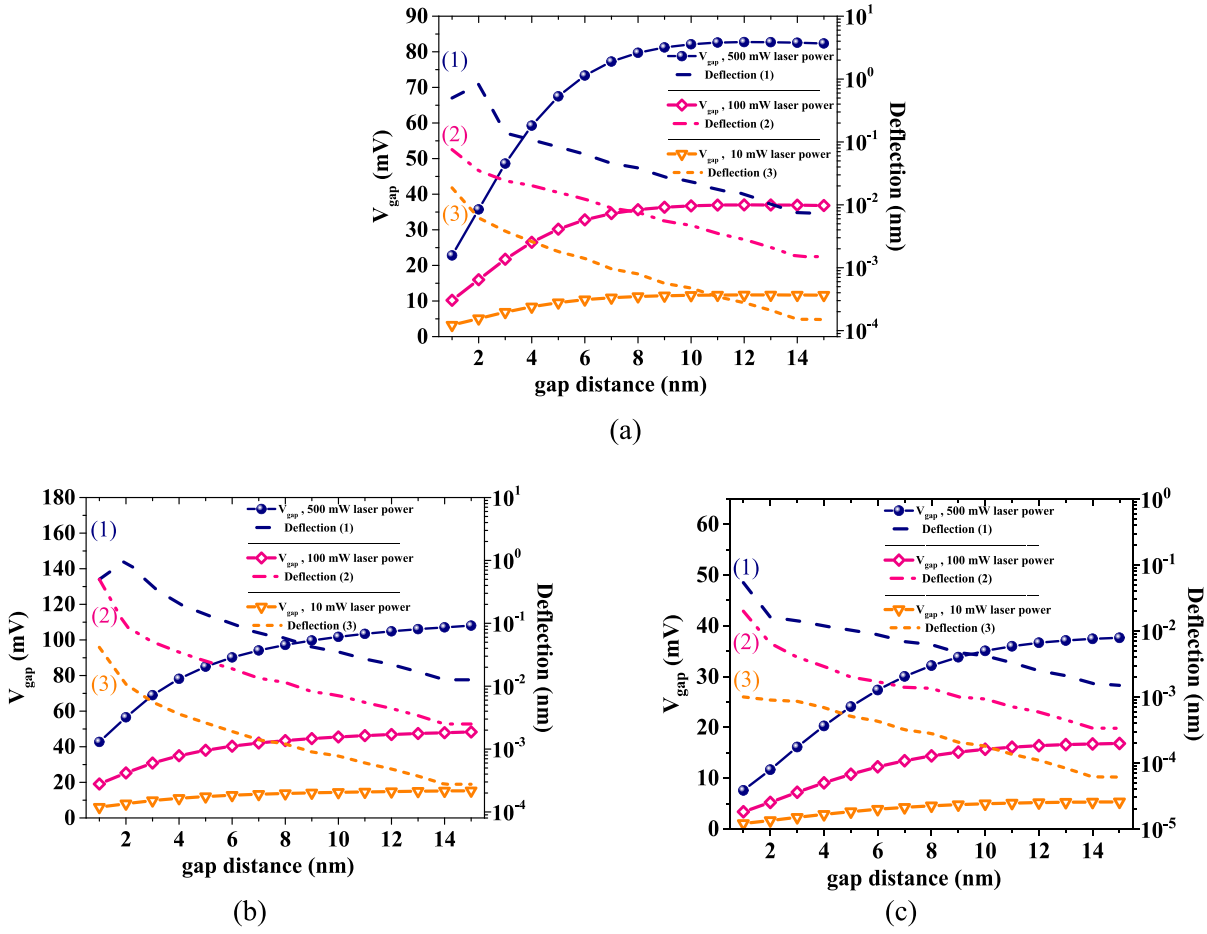

Fig. 7. Free end displacement (dashed lines referred to right y-axis) of one of the microcantilever components and gap voltage (symbol-continuous lines referred to left y-axis) as a function of the different feed gap distances of the nanoantenna for the optimum case (L_1, L_2) (a), the lower deviation case (L_1–50 nm, L_2–50 nm) (b), and the upper deviation case (L_1 + 50 nm, L_2 + 50 nm) (c) at 193.41 THz ($\lambda = 1.55$ μm), for 3 different laser power values 10, 100 and 500 mW.

at f = 193.41 THz, it cannot be considered an optimal configuration because, in comparison to the optimum case (L_1, L_2), it corresponds to a resonance frequency, in the vicinity of 200 THz, which means that it exhibits a deep notch and resonance at this higher frequency rather than the targeted 193.41 THz. Therefore, if the (L_1–50 nm, L_2–50 nm) dimensions were chosen, it would come at the cost of having a lower S_{11} value at 193.41 THz, given that the deepest notch occurs not at 193.41 THz but at a higher frequency near 200 THz. Moreover, the increase of V_{gap} obtained in the lower deviation case does not imply a significant increase on the cantilevers free end displacement, which is only grown from 0.02 nm to 0.03 nm, as it is observed in Fig. 7.b. In Fig. 7.c the results of the upper deviation case (L_1 + 50 nm, L_2 + 50 nm) are presented. In this least favourable scenario, characterized by the lowest induced voltage and a shift in resonance frequency to a lower value, approximately at 190 THz, the cantilever free end displacement is dramatically reduced to 3 pm, as illustrated in Fig. 7.c.

On the other hand, according to Eq. (3), the electrostatic force and, consequently, the induced free end cantilever displacement can be increased by reducing the initial gap distance, g_0. This trend, which can be observed in all free end cantilever displacement curves in Fig. 7, is even enhanced when pull-in conditions are achieved, as indicated by the abrupt displacement change observed for a gap distance around $g_0 = 2$ nm. In summary, if the NEMSTENNA is illuminated by a high laser power (500 mW), a detectable 0.02–0.03 nm cantilever free end displacement can be induced for an initial gap distance of $g_0 = 10$ nm, in both the optimum and lower deviation cases. This displacement is reduced to a fully unpractical 3 pm in the upper deviation case. However, even in this least scenario, a reduction of the initial gap to $g_0 = 2$ nm or below produces an increase of the cantilever free end displacement up to 0.1 nm, that reaches up to 1 nm in the most favourable cases. Note that in such cases, the displacement for an initial gap $g_0 = 2$ nm is limited to 1 nm by the collapse of the cantilevers produced by the pull-in effect. Similarly, for an initial gap $g_0 = 1$ nm the displacement is limited to 0.5 nm.

On the contrary, if the laser power is at the level of our current experimental setup (10 mW), then only the optimum and lower deviation cases would reach a displacement over 0.01 nm when the initial gap has the most favourable value of $g_0 = 2$ nm. It is worth to notice that, in practice, the gap distance in the feed gap area of the nanoantenna can be adjusted and controlled with a resolution below 1 nm using a state-of-the-art 3D nanopositioner, that can even allow the tuning of the overlapping distance too.

5. Conclusions

In conclusion, our study explores a novel device that directly converts near-infrared optical radiation into mechanical motion. Utilizing a plasmonic optical nanoantenna integrated within a microcantilever, we demonstrate a feasible fabrication process using Focused Ion Beam (FIB) milling. Our analysis reveals the sensitivity of device characteristics to fabrication tolerances, expanding the MEMSTENNA concept into the near-infrared range. The effect of the excitation power, the Si_3N_4 thickness and the feed gap distance on the NEMSTENNA mechanical response in terms of cantilevers deflection has been analysed. A mechanical response of 0.01–0.1 nm, which is clearly inside the detectability range, makes the designed NEMSTENNA for 1.55 μm appropriate as a proof of concept demonstrator, but unsuitable for practical purposes. Thus, a refinement of the NEMSTENNA design is still needed. This innovative device offers remote actuation through the conversion of electromagnetic signals into mechanical movement, presenting a promising avenue for energy-efficient applications in opto-mechanical systems which could be investigated in upcoming research.

Declaration of competing interest

The authors declare that they have no known competing financial interest or personal relationships that could have appeared to influence the work reported in this paper.

Data availability

Data will be made available on request.

Acknowledgements

This work was funded by Spain's Ministerio de Ciencia e Innovación under Grant No. PID2021-127840NB-I00 (MICINN/AEI/FEDER, UE).

References

[1] R. Ruiz, G. Abadal, Direct transduction from radiofrequency radiated power to static and dynamic flexural mechanical modes, in: 2021 21st Int. Conf. Solid-State Sensors, Actuators Microsystems, 2021, pp. 144–147, https://doi.org/10.1109/Transducers50396.2021.9495668.
[2] R. Ruiz, J. Bonache, G. Abadal, A flexible dipole antenna for direct transduction of microwave radiated power into DC mechanical deflection, Sensors Actuators A Phys. 340 (2022) 113536, https://doi.org/10.1016/j.sna.2022.113536.
[3] R. Ruiz, G. Abadal, Remote dynamic actuation of an electrostatically driven microcantilever by a wireless power transfer system, Sensors Actuators A Phys. 345 (2022) 113798, https://doi.org/10.1016/j.sna.2022.113798.
[4] C. Belacel, Y. Todorov, S. Barbieri, D. Gacemi, I. Favero, C. Sirtori, Optomechanical terahertz detection with single meta-atom resonator, Nat. Commun. 8 (2017) 1578, https://doi.org/10.1038/s41467-017-01840-6.
[5] C. Li, Y. Zhang, K. Hirakawa, Terahertz detectors using microelectromechanical system resonators, Sensors (Basel) 23 (2023), https://doi.org/10.3390/s23135938.
[6] H. Zhu, K. Wang, G. Liu, G. Wang, J. Mou, W. Zhang, G. Wei, A terahertz optomechanical detector based on metasurface and bi-material micro-cantilevers, Micromachines 13 (2022), https://doi.org/10.3390/mi13050805.
[7] J. Liu, B. Chomet, P. Beoletto, D. Gacemi, K. Pantzas, G. Beaudoin, I. Sagnes, A. Vasanelli, C. Sirtori, Y. Todorov, Ultrafast detection of TeraHertz radiation with miniaturized optomechanical resonator driven by dielectric driving force, ACS Photonics 9 (2022) 1541–1546, https://doi.org/10.1021/acsphotonics.2c00227.
[8] A. Ashkin, Trapping of atoms by resonance radiation pressure, Phys. Rev. Lett. 40 (1978) 729–732, https://doi.org/10.1103/PhysRevLett.40.729.
[9] M. Dykman, Heating and cooling of local and quasilocal vibrations by a nonresonance field, Sov. Phys. Solid State 20 (1978) 1306–1311.
[10] S. Gröblacher, J.B. Hertzberg, M.R. Vanner, G.D. Cole, S. Gigan, K.C. Schwab, M. Aspelmeyer, Demonstration of an ultracold micro-optomechanical oscillator in a cryogenic cavity, Nat. Phys. 5 (2009) 485–488, https://doi.org/10.1038/nphys1301.
[11] E. Verhagen, S. Deléglise, S. Weis, A. Schliesser, T.J. Kippenberg, Quantum-coherent coupling of a mechanical oscillator to an optical cavity mode, Nature 482 (2012) 63–67, https://doi.org/10.1038/nature10787.
[12] J. Chan, T.P.M. Alegre, A.H. Safavi-Naeini, J.T. Hill, A. Krause, S. Gröblacher, M. Aspelmeyer, O. Painter, Laser cooling of a nanomechanical oscillator into its quantum ground state, Nature 478 (2011) 89–92, https://doi.org/10.1038/nature10461.
[13] C. Fumeaux, J. Alda, G.D. Boreman, Lithographic antennas at visible frequencies, Opt. Lett. 24 (1999) 1629–1631, https://doi.org/10.1364/ol.24.001629.
[14] A.E. Krasnok, I.S. Maksymov, A.I. Denisyuk, P.A. Belov, A.E. Miroshnichenko, C. R. Simovski, Y.S. Kivshar, Optical nanoantennas, Physics-Uspekhi. 56 (2013) 539, https://doi.org/10.3367/UFNe.0183.201306a.0561.
[15] F.J. Gonzalez, B. Ilic, J. Alda, G.D. Boreman, Antenna-coupled infrared detectors for imaging applications, IEEE J. Sel. Top. Quantum Electron. 11 (2005) 117–120, https://doi.org/10.1109/JSTQE.2004.841474.
[16] E. Briones, J. Alda, F.J. González, Conversion efficiency of broad-band rectennas for solar energy harvesting applications, Opt. Express 21 (2013) A412–A418, https://doi.org/10.1364/OE.21.00A412.
[17] Z. Zhu, S. Joshi, B. Pelz, G. Moddel, Overview of optical rectennas for solar energy harvesting, in: O.V. Sulima, G. Conibeer (Eds.), Next Gener. Photonic Cell Technol. Sol. Energy Convers. IV, 2013, p. 88240O, https://doi.org/10.1117/12.2024700.
[18] Z. Ma, G.A.E. Vandenbosch, Optimal solar energy harvesting efficiency of nano-rectenna systems, Sol. Energy 88 (2013) 163–174, https://doi.org/10.1016/j.solener.2012.11.023.
[19] J. Alda, C. Fumeaux, M.A. Gritz, D. Spencer, G.D. Boreman, Responsivity of infrared antenna-coupled microbolometers for air-side and substrate-side illumination, Infrared Phys. Technol. 41 (2000) 1–9, https://doi.org/10.1016/S1350-4495(99)00036-5.
[20] C. Di Garbo, P. Livreri, G. Vitale, Optimal matching between optical rectennas and harvester circuits, in: 2017 IEEE Int. Conf. Environ. Electr. Eng. 2017 IEEE Ind. Commer. Power Syst. Eur. (EEEIC / I&CPS Eur), 2017, pp. 1–6, https://doi.org/10.1109/EEEIC.2017.7977686.
[21] J. Dorfmüller, R. Vogelgesang, W. Khunsin, C. Rockstuhl, C. Etrich, K. Kern, Plasmonic nanowire antennas: experiment, simulation, and theory, Nano Lett. 10 (2010) 3596–3603, https://doi.org/10.1021/nl101921y.
[22] J.-S. Huang, T. Feichtner, P. Biagioni, B. Hecht, Impedance matching and emission properties of Nanoantennas in an optical Nanocircuit, Nano Lett. 9 (2009) 1897–1902, https://doi.org/10.1021/nl803902t.

[23] R. Stoneback, The dipole impedance of an aperture, Prog. Electromagn. Res. B 26 (2010) 401–423, https://doi.org/10.2528/PIERB10062406.
[24] https://www.nanoandmore.com/AFM-Probe-PNP-TR-TL-Au, 2024.
[25] M.N. Polyanskiy, Refractive Index Database, 2024.
[26] Z. Ma, G.A.E. Vandenbosch, Input impedance of optical metallic nano dipole over 300 nm – 1200 nm wavelength, in: 2013 7th Eur. Conf. Antennas Propag, 2013, pp. 3810–3813.

A.2 Impact of the parasitic photothermal effect on the performance of an optomechanical nanoantenna for NIR radiation detection

Journal paper (Paper 2), Published in Sensors and Actuators: A. Physical

Sensors & Actuators: A. Physical 394 (2025) 116966

Contents lists available at ScienceDirect

Sensors and Actuators: A. Physical

journal homepage: www.journals.elsevier.com/sensors-and-actuators-a-physical

Impact of the parasitic photothermal effect on the performance of an optomechanical nanoantenna for NIR radiation detection

Daniyal Khosh Maram *, Joan Garcia-Garcia, Xavier Cartoixà, Gabriel Abadal

Departament d'Enginyeria Electrònica, Universitat Autònoma de Barcelona, 08193 Bellaterra, Barcelona, Spain

ARTICLE INFO

Keywords:
Optomechanical nanoantennas
Near-infrared (NIR) radiation detection
Opto-thermomechanical transduction
Opto-electromechanical transduction
COMSOL Multiphysics simulations
Design optimization

ABSTRACT

This paper investigates the impact of the opto-thermomechanical (OTM) parasitic response of an optomechanical nanoantenna on the main opto-electromechanical (OEM) transduction mechanism involved in the near-infrared (NIR) radiation detection. Through comprehensive experimental and computational analyses, we have modelled how this parasitic effect overlaps with the desired opto-electromechanical response. Utilizing COMSOL Multiphysics, we have simulated thermal, optical, and mechanical interactions within the optomechanical structure. Our findings indicate that the parasitic OTM effect significantly influences the device's mechanical deflection, driven primarily by localized heating at the microcantilever's free end. Experimental data validates simulation results, demonstrating the parasitic response's dominance over the intended functionality. A figure of merit (FoM), defined as the ratio between the transducing OEM signal over the parasitic OTM response has been defined to quantify the performance of the optomechanical nanoantenna detector, as well as to propose geometry design improvements to optimize this performance.

1. Introduction

Micro Electro Mechanical Systems (MEMS) is a well stablished discipline that emerged as a cornerstone technology for a wide range of applications, leveraging their ability to integrate electrical and mechanical components at the microscale [1]. These systems rely on electromechanical transduction mechanisms, which convert signals and energy from the mechanical into the electrical domain and vice versa, to enable functionalities such as sensing [2], actuation [3], and energy harvesting [4]. Among the wide range of transduction mechanisms that make such conversion processes possible, thermal [5], piezoresistive [6], piezoelectric [7], electrostatic [8], and magnetomotive [9] are the most commonly used. Although MEMS technology has reached a level of maturity for long time now that allows us to find it in daily consumer electronics devices [10] or healthcare [11] and industrial [12] applications, new challenges such as MEMS computing [13], MEMS-based neurotechnology [14] or 3D-MEMS technology [15] are still being faced in the frontiers of this field.

In particular, RF-MEMS sub-technology initially devoted to the interaction of MEMS with electromagnetic radiofrequency (RF) radiation [16] is being extended in the recent years to the terahertz and optical domains to bring forward new applications in tuneable THz metamaterials [17], imaging [18] and uncooled IR detection [19].

In terms of signal reception, MEMS technology has also seen contributions from cutting edge examples such as the nanotube radio [20], where a single carbon nanotube was used as a mechanical antenna that integrated also the demodulator and the speaker of a complete AM reception system. Later, RF signal detection was also demonstrated with a much simpler mechanical antenna based on an unpolarized microcantilever [3] and the new mechanical antenna topic was born, inspired by Jensen's work, showing promising capabilities in the Low Frequency (LF) [21] and Very Low Frequency (VLF) [22] telecommunications.

In earlier research, R. Ruiz et al. [23–25] investigated a novel mechanical antenna concept called MEMSTENNA, that combined an antenna component with a resonant MEMS. Through the use of MEMSTENNA technology, radiofrequency electromagnetic energy can be directly converted to mechanical motion. C. Belacel et al. [26] applied the MEMSTENNA concept to the 1–10 THz frequency range and proposed a new type of THz detector that directly transforms electromagnetic signals into mechanical responses. The authors demonstrate the improvement in frequency response at room temperature of this THz detector by avoiding the thermal mechanisms commonly found in other types of THz bolometric detectors [27–29].

Very recently, a preliminary study of an extension of the

* Corresponding author.
E-mail address: daniyal.khoshmaram@uab.cat (D.K. Maram).

https://doi.org/10.1016/j.sna.2025.116966
Received 10 February 2025; Received in revised form 18 June 2025; Accepted 12 August 2025
Available online 13 August 2025
0924-4247/© 2025 The Author(s). Published by Elsevier B.V. This is an open access article under the CC BY-NC license (http://creativecommons.org/licenses/by-nc/4.0/).

MEMSTENNA concept to the optical domain has been published by the authors [30]. In that work, the design and fabrication process of a NIR NEMSTENNA, a combination of a dipole optical nanoantenna with commercial microcantilevers, was first presented. In that same work, a detailed analysis of the opto-electromechanical transduction mechanism was also reported, showing that such NEMSTENNAS exhibit mechanical responses in the 0.01–0.1 nm range, but the parasitic impact on the device performance of the thermally induced deflection of cantilevers by bimetallic effect was neglected and not included in the analysis. In this article, on the one hand, the opto-thermally induced deflection of the cantilevers has been calculated and validated experimentally in order to predict its effect on the opto-electromechanical signal. On the other hand, an improved version of the NEMSTENNA based on an optimized nanodipole geometry which maximizes the electrostatic transducing voltage in the feed gap of the nanoantenna has been designed. The article is organized in the following way: In Section 2, the opto-mechanical nanoantenna device (NEMSTENNA), which is a combination of a dipole nanoantenna integrated in the free end of two mechanical microcantilevers, is defined. It is also discussed how the device operates and the mechanisms that initiate transduction. Next, the nanoantenna's design is described in Section 3, along with results of the optimal geometry. In Section 4, we examine the COMSOL prediction of the mechanical response, which includes opto-electromechanical (OEM) and parasitic opto-thermomechanical (OTM) features. Finally, we also define the optomechanical nanoantenna design's Figure of Merit as the ratio between the transducing OEM signal over the parasitic OTM response, which highlights the importance of optimizing opto-mechanical responses over optothermal effects.

2. Device definition and working principle

The proposed optomechanical nanoantenna (NEMSTENNA) structure features a near-infrared (NIR) optical dipole nanoantenna, designed to resonate at a wavelength of 1.55 μm, integrated into one of the Au layers of two triangular Si_3N_4 microcantilevers at their free end, as shown in Fig. 1. The geometry of the dipole nanoantenna shown in Fig. 2, is defined by the length and width of its two components (L_1, L_2, W_1), as well as the dimensions of the supporting arms (L_{Arm1}, L_{Arm2}, W_2) that link the dipole components to the microcantilevers. Additionally, the thickness of the silicon nitride layer in the nanoantenna region is another critical design parameter that will have an important effect on the nanoantenna response, because this layer is the dielectric substrate that determine wave propagation velocity and dielectric losses. The two components of the dipole nanoantenna are positioned parallel to each other and separated by a gap distance, g_0, in the overlapping area located in the feed region of the antenna. In this feed gap area, an electrostatic transduction capacitance is created, which at the same time is electrically loading the nanoantenna. When the dipole nanoantenna is illuminated by a focused NIR laser beam with a wavelength of 1.55 μm (corresponding to a frequency of 193.41 THz), an alternating AC voltage, referred to as V_{gap}, is generated within the feed gap of the nanoantenna, as shown in Fig. 1(b). This voltage arises due to the interaction between the incoming radiation and the plasmonic properties of the optical nanoantenna. The generated AC voltage V_{gap}, which oscillates at the same frequency as the incident radiation, 193.41 THz in this case, induces an electrostatic force between the two components of the dipole nanoantenna which acts attracting the microcantilevers at their free end. Since this force depends quadratically on the inducing voltage, a DC component of the force and the consequent static deflection of the cantilevers are both produced. On the other hand, the AC component of the force, which oscillates at twice the frequency of the incident NIR radiation (hundreds of THz), will not induce any significant mechanical vibration of the microcantilevers because their natural vibration frequencies are 12 orders of magnitude lower (tens of kHz). This frequency mismatch ensures that the microcantilevers primarily respond to the DC component, maintaining stable mechanical operation without interference from high-frequency noise.

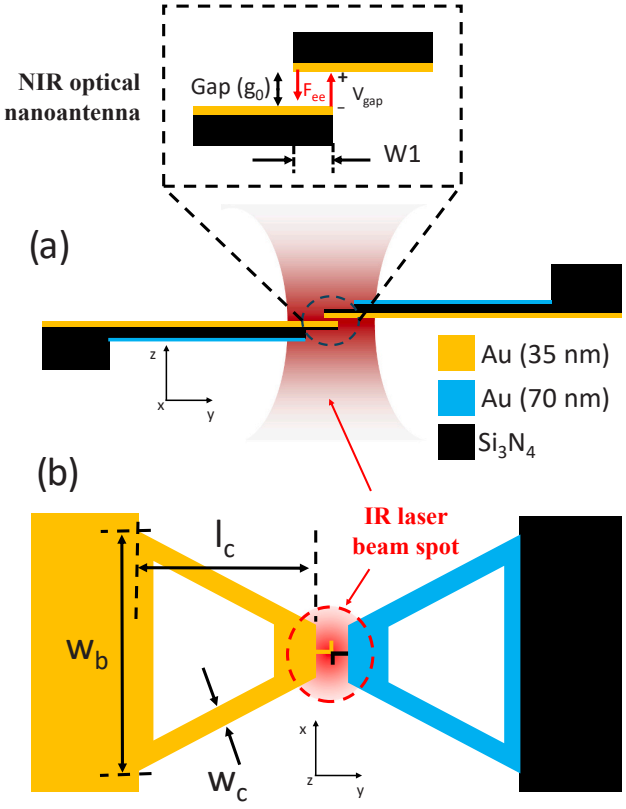

Fig. 1. Schematics of the lateral view (a) and top view (b) of the proposed optomechanical nanoantenna (NEMSTENNA) structure including the dipole NIR nano-antenna integrated at the free end of two microcantilevers, which is placed at the beam waist of a focused gaussian laser beam. In the zoom detail of the lateral view, voltage in the gap region, V_{gap}, induces an attractive electrostatic force, F_{ee}, on each optomechanical nanoantenna component.

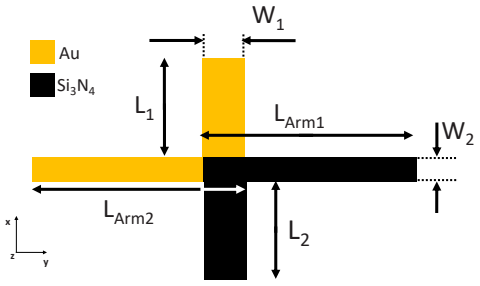

Fig. 2. Dipole nano-antenna layout with all dimensions that define its geometry.

3. Design of the nanoantenna

The electromagnetic resonance modes of a dipole nanoantenna are determined by its physical dimensions, and specially by its length. This section aims to investigate the relationship between dipole length and resonance occurrence, in terms of gap voltage and z-direction electric field in the nanoantenna feed gap, for a constant incident radiation wavelength (1.55 μm in this case), power (7.5 mW) and spot radius (27.5 μm, see Fig. 1) for the first three detectable resonance modes. As it is inferred from the results shown in the curves of Fig. 3 and cross-

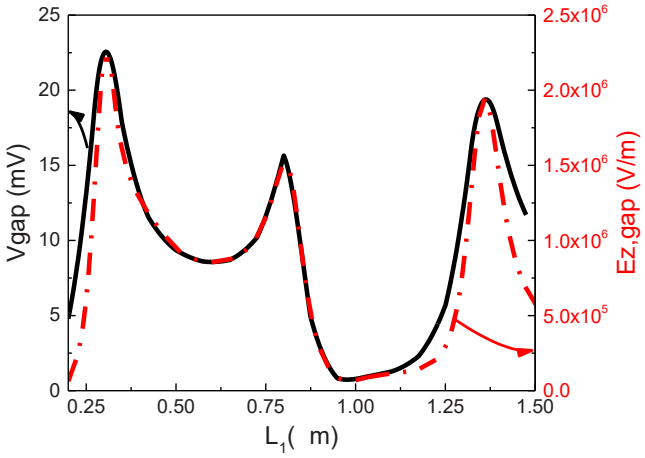

Fig. 3. Voltage and z-component of the electric field in the gap region as a function of dipole length L_1. The three peaks at 300 nm, 810 nm and 1361 nm correspond to the first three detectable resonance modes, which can be identified with the λ/2, 3λ/2 and 5λ/2 modes of a λ/2 dipole structure. Constant parameters of the laser source considered in the calculations are: radiation wavelength λ= 1.55 μm, power P_{in}= 7.5 mW and spot radius SR= 27.5 μm.

section maps of Fig. 4 corresponding to a preliminary analysis, for our proposed dipole nanoantenna, which dimensions are reported in Table 1, the first, second and third resonance detectable modes are found when dipole is approximately 300 nm, 810 nm and 1361 nm long, respectively. In particular, each one of the three peaks observed in the graphs of the gap voltage (V_{gap}) and the electric field in z-direction in the centre point of the dipole nanoantenna gap vs. dipole length (L_1) (Fig. 3) can be identified with the expected patterns of the current density distribution flowing through the nanoantenna metallic part, as shown in Fig. 4.a-c and the z-component of the electric field in the dielectric regions around the metal layer of the nanoantenna, as shown in Fig. 4.d-f Indeed, an examination of the computed current density and electric field distributions indicate that the first three detectable modes correspond to the standard λ/2 (Fig. 4.a,d), 3λ/2 (Fig. 4.b,e) and 5λ/2 (Fig. 4.c,e) dipole antenna modes. Notice, however, that our nanoantenna is not a standard RF dipole antenna, where the total length L (L=2·L1 or L=L1+L2 when consider the non-symmetric case) equals λ/2 in the first resonant mode. In our case, we have a plasmonic nanoantenna in which the wavelength of electromagnetic waves propagating in the metal of the nanoantenna is reduced with respect to the free space propagation. Consequently, the ratio L/(λ/2) which is 1 for a RF antenna, is slightly reduced for a plasmonic one [31,32], as it is verified by our results:

Table 1
Geometry characteristics of cantilevers and nanoantenna.

Parameter	Value	Units
Dipole arm length, (L_{Arm1}/$L_{Arm\ 2}$)	2/2	μm
Dipole width, w_1	0.08	μm
Dipole arm width, w_2	0.1	μm
Dipole length, (L_1/L_2)	1.36/1.36	μm
Dipole gold thickness, (t_{gd})	0.035	μm
Dipole silicon nitride thickness, (t_{dd})	0.14	μm
Cantilever length, (l_c)	200	μm
Cantilever width, (w_c)	28	μm
Cantilever base width, (w_b)	184	μm
Cantilever silicon nitride thickness, (t_{dc})	0.6	μm
Cantilever gold thickness, (t_{gc})	0.07	μm
Capacitive gap, (g_0)	0.01	μm
Overlapping Area, (A)	0.01	μm^2

2·L1/(λ/2)= 600 nm/(1550/2 nm)= 0.77 for the first detectable mode (n = 1), 2·L1/(3λ/2)= 1620 nm/(3·1550 nm/2)= 0.69 for the second detectable mode (n = 3), and 2·L1/(5λ/2)= 2722 nm/(5·1550 nm/2)= 0.70 for the third detectable mode (n = 5). In summary, the results demonstrate that the resonant behaviour of the nanoantenna is highly dependent on the dipole length, with distinct mode profiles observed for each configuration. Additionally, it is observed that the maximum voltage and z-component electric field in the gap region is obtained for the first detectable mode (n = 1), followed by the third (n = 5) and second (n = 3) detectable modes.

3.1. COMSOL optimization

After the previously described preliminary analysis of the V_{gap} and electric field dependence on the dipole nanoantenna length, a refinement of the final design dimensions has been performed through a COMSOL optimization process defining V_{gap} as the variable to be maximized for a radiation wavelength of 1.55 μm. The lengths $L_1 = L_2$ and $L_{Arm1} = L_{Arm2}$ were considered as free parameters for optimization, while the Si_3N_4 thickness was assumed to be fixed at 140 nm, since it is the optimal value from a fabrication point of view as it was demonstrated in a previous work [30]. All simulations of the optimization process were carried out using a laser power of 7.5 mW and a 27.5 μm beam radius. For an initial gap distance fixed at g_0= 10 nm, the set of parameters resulting from an optimization process limited to a range of dipole nanoantenna lengths around the length of the fifth mode is the following: $L_1 = L_2 = 1360$ nm, $L_{Arm1} = L_{Arm2} = 2$ μm, and $W_1 = 80$ nm, $W_2 = 100$ nm. The reason for choosing the 5th mode is that its longer length of 1360 nm allows for an easier fabrication process, at an acceptable tradeoff of a small reduction in V_{gap} and return loss compared to the first mode with a 300 nm dipole length. The optimized dimensions

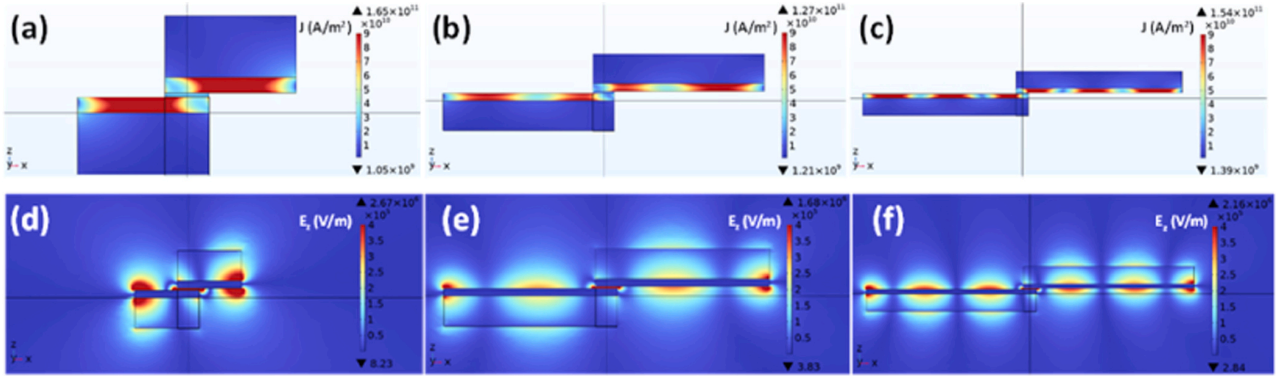

Fig. 4. Maps of the current density (a-c) and z-component of the electric field (d-f), for the first three detectable resonance modes observed when dipole length is 300 nm (a,d), 810 nm (b,e) and 1361 nm (c,f).

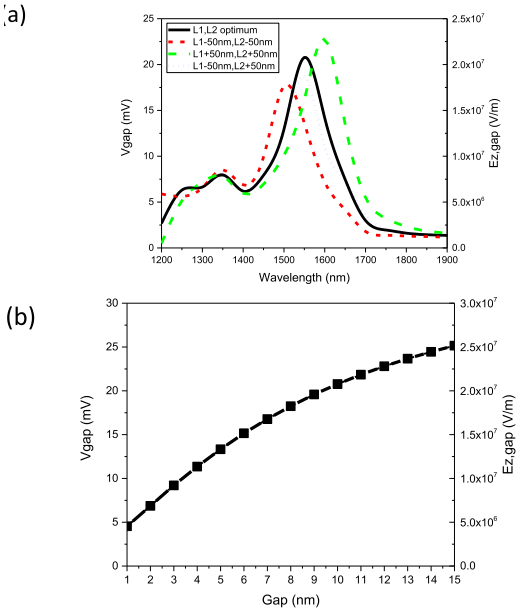

Fig. 5. (a) Spectral response of V_{gap} obtained from COMSOL simulations for L_1 and L_2 at and around the optimum case (L_1=L_2=1360 nm). Gap distance is g_0 = 10 nm. (b) Voltage induced within the feed gap area vs. gap distance. Laser power is P_{in}= 7.5 mW and spot radius is SR= 27.5 μm.

are included in Table I.

In order to quantify the effect of the fabrication tolerance on the response of V_{gap} versus wavelength, simulations for four different values of L_1 and L_2 around the optimal case, with a gap distance g_0= 10 nm were conducted. This analysis considered a 50 nm tolerance limit, reflecting the resolution of the focused ion beam (FIB) milling process used [30]. The results of this analysis summarised in Fig. 5.a demonstrate that simultaneous deviations of L_1 and L_2 by 50 nm in the same direction result in the V_{gap} (and z-direction electric field in the middle of the gap) peak to the right shifting at 1600 nm (for L_1 + 50 nm and L_2+50 nm) or to the left at 1500 nm (for L_1−50 nm and L_2−50 nm), as illustrated by the orange and purple curves in Fig. 5.a, respectively. If the excitation radiation is fixed at 1550 nm and cannot be tuned to match the nanoantenna resonance, the V_{gap}, and correspondingly the z-direction voltage in the middle of the gap, decreases from 21 mV at optimal L_1 and L_2) to approximately 15 mV for both the shortened (L_1−50 nm and L_2−50 nm) and elongated (L_1+50 nm and L_2+50 nm) cases at the excitation wavelength. Additionally, the voltage induced within the feed gap area V_{gap} together with the electrical field in the z direction at the middle point of the gap were analysed as a function of gap distance as presented in Fig. 5.b. It is worth noting that since the z-component of the electric field, $E_{z,gap}$, is not constant along the gap region in the z direction, V_{gap} and gap distance, g, values in the plot of Fig. 5.b are not linearly related by $E_{z,gap}$=V_{gap} /g, as it is evidenced, for instance, by the non-linear V_{gap} vs. gap distance curve. Most importantly, this figure shows that gap voltage decreases as the gap is decreased and that the smaller the gap the faster the gap voltage decreasing rate is.

4. Mechanical response

After settling nanoantenna dimensions and feed gap voltage, the deflection of the microcantilevers, caused by the electrostatic force induced in the transduction gap, has been self-consistently calculated by coupling RF, electrostatics, and solid mechanics COMSOL modules. This deflection was quantified by calculating the displacement at the cantilever's free end. Additionally, to this displacement produced by the optically induced electrostatic force, also called opto-electromechanical (OEM) displacement, we have also considered the parasitic displacement caused by the optically induced heating of the cantilevers and transduced by a bimetallic effect, denoted as opto-thermomechanical (OTM) displacement, combining in this case RF, thermal and solid mechanics COMSOL modules. Both calculations were performed for laser powers ranging from 1 mW to 7.5 mW (the lower and upper limits of our experimental setup) and considering the optimal case (optimal L_1 and L_2) in terms of V_{gap}, an initial gap of g_0= 10 nm and a spot radius of 27.5 μm, corresponding to the beam waist as we have considered the paraxial approximation and a Gaussian beam to describe the focused laser beam. In COMSOL simulations, the NEMSTENNA is placed inside a spherical air-domain simulation box of 345 μm radius, which is large enough to minimize boundary reflections. The outer faces of this domain are assigned scattering boundary conditions in the Electromagnetic Waves module to emulate free-space propagation. Module couplings are setup as follows: the Joule Heating feature of the RF module is used to compute the volumetric power density generated mainly in the gold layer of the NEMSTENNA, which is passed directly to the Heat Transfer in Solids module as a heat source. The resulting temperature rise induces mechanical stress, which is handled by coupling the Heat Transfer module to the Solid Mechanics module via the Thermal Expansion multiphysics node. Then, at each time step of a time-dependent study, the Heat Transfer and Solid Mechanics solvers are coupled, allowing the structure to heat up and deform gradually. To capture the deformation of the NEMSTENNA geometry under thermal expansion, we enable COMSOL's Moving Mesh (Arbitrary Lagrangian–Eulerian) interface. This deformed geometry feature updates the finite-element mesh at each time step based on the computed displacement field, so that the shape of the NEMSTENNA evolves dynamically with temperature.

4.1. Opto-electromechanical (OEM)

Two computational approaches have been evaluated for simulating the OEM displacement induced by near-infrared (IR) laser excitation in the feed gap area of our device: an iterative or feedback method, and a non-iterative one. In the iterative approach, the voltage induced within the feed gap area is recalculated in an RF simulation step, each time the gap distance is reduced by the OEM displacement of the cantilevers (evaluated at their free-end) as calculated in the previous electrostatic and mechanical simulation step. In contrast, the non-iterative method assumes V_{gap} to be constant and independent of changes in gap distance, maintaining its initial value corresponding to the initial gap distance throughout the whole simulation. The findings indicate that at high power levels, the iterative method introduces slight variations in displacement compared to the non-iterative method. Nevertheless, at lower power levels, both methods agree closely in terms of displacement calculations, suggesting that using the non-iterative method to determine displacement values is acceptable within permissible margins of error. Additionally, the iterative method requires more batches of simulations, which implies more computational resources than the non-iterative simple constant sweep approach. In Fig. 6, the displacement values obtained by both calculation methods and the corresponding errors (difference between iterative and non-iterative displacement values) as a function of IR laser power levels are presented. Overall, both iterative and non-iterative methods yield comparable results for laser powers below 3 mW, with negligible differences below 1 pm, and non-negligible discrepancies with a linearly increasing error for laser power levels over 3 mW. For instance, at 7.5 mW IR laser power, the iterative method shows a static deflection of approximately 50 pm, while the non-iterative method shows a displacement of 64 pm, resulting in a deviation error of 14 pm and a relative error of 28 %. In order to relax the computational load, we have used the non-iterative method,

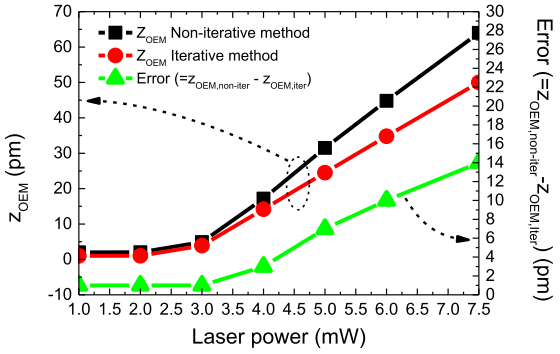

Fig. 6. Static opto-electromchanical OEM deflection calculated with and without the iterative method and the difference between both vs. laser power. Spot radius is SR= 27.5 μm and gap distance is g_0 = 10 nm.

keeping in mind that the error grows with the incident power level.

4.2. Opto-thermomechanical (OTM)

In order to analyse the opto-thermomechanical (OTM) transduction mechanism as the parasitic effect that will screen the desired opto-electromechanical (OEM) signal, we have also combined multiple physical domains to couple the interactions between IR light, heat, and mechanical deformation. The COMSOL Multiphysics setup has integrated in this case RF, thermal and solid mechanics domains. The material properties used in the simulations are summarized in Table 2 and also detailed in reference [33]. The properties are inferred from experimental data on the materials' thermal, optical, electrical, and mechanical characteristics. Here, in the EM simulation analysis performed by the RF module the absorption of the optical energy in the material is calculated using Maxwell's equations. Using the refractive index values for Au measured by Johnson and Christy [34], as tabulated in [35], we have calculated with a coherent summation of multiple passes model that the Au surface of our optomechanical nanoantenna device reflects 96.8 % and absorbs about 2.5 % of the total incident power. Only a 0.7 % is transmitted to the Si_3N_4 layer underneath. Subsequently, the thermal module uses as a simulation input the heat generated by the currents as obtained from the RF analysis to calculate the resulting temperature distribution. For this, the heat transfer equations of the thermal COMSOL module consider the effects of conduction, convection and radiation with the corresponding appropriate parameters [33]. It is worth to notice that as the opto-thermomechanical transduction is mainly produced in the body of the triangular microcantilever, the current distribution at the nanoantenna is not contributing to this calculation. Indeed, when we have calculated the thermal distribution and the corresponding opto-thermomechanical OTM response, no significant differences have been found on whether the nanoantenna is present or absent in the simulations.

Next, the temperature distribution from the thermal analysis is imported into the structural mechanics module. The resulting mechanical deformation is then computed, considering the thermal strain effects. Our optomechanical antenna device is composed of a sandwich of three materials, Au(35 nm)/Si_3N_4(600 nm)/Au(70 nm) (Fig. 1), each one with different coefficients of thermal expansion (CTE) [33]. The asymmetry introduced by the difference in the Au thickness will be the responsible of the cantilever bending by the bimetallic effect. Indeed, the thicker Au layer will suffer a large expansion strain than the thinner one, and the cantilever will bend in the gap closing direction. In order to validate experimentally the COMSOL predictions of OTM parasitic signal, we have measured the opto-thermally induced displacement on a single cantilever component. In the measurement setup, as described in previous works [23,33], focusing of the IR laser beam (Thorlabs SFL1550P current/temperature controlled by ITC4001) is achieved through three different microscope objectives: 100X, 50X and 20X (Mitutoyo M Plan APO SL), that produce 8 μm, 14 μm and 27.5 μm spot radius, respectively. The deflection at the free-end of the cantilever is detected by a red diode laser (Thorlabs CPS670F 670 nm 4.5 mW) coupled to a 4-quadrants position photodetector (New Focus Quadcell Photoreceiver 2901) readout system. The transient signal obtained at the output of the photodetector when IR laser power is switched (OFF-ON-OFF transients) is then analysed by means of an oscilloscope (Tektronix MDO3024). The stationary deflection signal difference between the ON and OFF states (in terms of cantilever free-end displacement) for different laser power levels is obtained as presented in Fig. 7.

As illustrated in this figure, there is an excellent agreement between COMSOL model predictions and experimental values.

Finally, in the last analysis which consisted of comparing the OEM signal with the OTM parasitic, we have used a figure of merit (FoM) simply defined as the ratio between the OEM and the OTM induced vertical displacements of the cantilevers fre-end (z): FoM=z_{OEM}/z_{OTM}. The as defined FoM has been then evaluated for the three different achievable laser spot radii, i.e. 8, 14 and 27.5 μm and represented together with both displacements (OEM and OTM) in Fig. 8. Here, we observe that as laser beam radius decreases from 27.5 μm to 8 μm, OTM parasitic decreases from 25 nm to 0.7 nm because the area illuminated of the cantilever decreases too, OEM increases from 50 pm to 150 pm

Table 2
Optical, thermal and mechanical properties of the materials involved in COMSOL simulations.

Property	Au	Si_3N_4	Units
Heat capacity, C_p	129	700	J/(kg·K)
Thermal conductivity, κ	150[a], 230[b]	2.1[c], 4[d]	W/(m·K)
Convective heat transfer coeficient, h	$3.8{\cdot}10^5$	$4{\cdot}10^5$	W/(m^2·K)
Thermal Boundary Resistance, TBR	$0.81{\cdot}10^{-8}$	$0.8{\cdot}10^{-8}$	m^2·K/W
Surface emissivity, ϵ	0.05	0.5	
Density, ρ	19280	3100	kg/m^3
Refractive index, n	0.52406	1.9963	
Extinction coeficient, k	10.742	0	
Electrical conductivity, σ	$45{\cdot}10^6$	0	S/m
CTE, α	$14.1{\cdot}10^{-6}$	$2.3{\cdot}10^{-6}$	K^{-1}
Young's modulus, E	80	250	GPa
Poisson's ratio, ν	0.44	0.23	

[a] Au thickness= 35 nm
[b] Au thickness= 70 nm
[c] Si_3N_4 thickness= 140 nm
[d] Si_3N_4 thickness= 600 nm

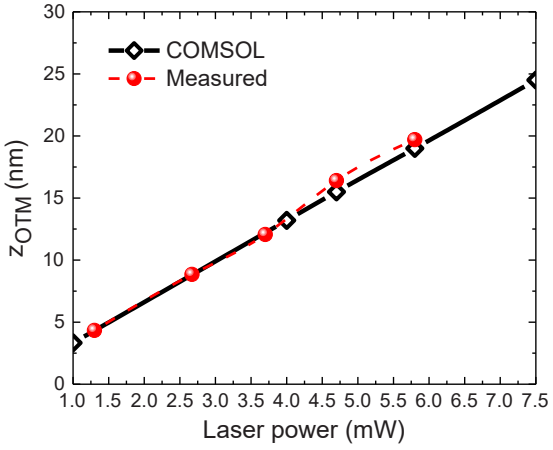

Fig. 7. Experimental and COMSOL simulated steady state displacement of the cantilever free-end in out-of-plane direction, z, after laser power OFF-ON switching transient for different laser powers ranging from 1 to 7.5 mW. Spot radius is SR= 27.5 μm and gap distance is g_0 = 10 nm.

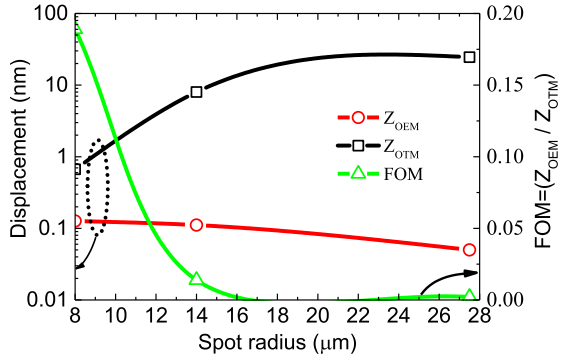

Fig. 8. OEM and OTM displacements and their corresponding OEM/OTM ratio as defined by the FoM as a function of the laser spot radii, ranging from 8 to 27.5 μm. Laser power is P_{in}= 7.5 mW and gap distance is g_0 = 10 nm.

because the power density in the nanoantenna region is increased, thereby maximizing the opto-electromechanical effect and minimizing the opto-thermomechanical parasitic. Consequently, the FoM is increased from $2{\cdot}10^{-3}$ to 0.2, which means an enhancement of two orders of magnitude. Since both OTM and OEM dependences on the spot radius are non-linear, and OTM decreases much faster than OEM grows when spot radius is decreased, the FoM and its rate of change grows very significantly when spot radius is approaching 8 μm. The marginal change in the FoM underscores the need for improved design geometry to achieve higher performance. Future research should focus on reducing the opto-thermomechanical parasitic effect but specially on enhancing the opto-electromechanical transduction signal.

5. Conclusion

In this study we have demonstrated that the parasitic opto-thermomechanical response (OTM) substantially impacts the performance of the optomechanical naoantenna device, overshadowing the intended opto-electromechanical (OEM) response. Experimental validation of the OTM displacement component closely matches our COMSOL Multiphysics simulations, confirming the influence of localized heating on the microcantilever's deflection. To improve the overall performance and FoM of the device, future work will focus on optimizing the design geometry. This optimization aims to reduce the undesired slow but large amplitude response of the OTM effect, while enhancing the fast OEM response, thereby advancing towards a practical application of optomechanical antenna devices in NIR radiation detection.

CRediT authorship contribution statement

Khoshmaram Daniyal: Writing – original draft, Visualization, Validation, Software, Resources, Methodology, Investigation, Formal analysis, Data curation, Conceptualization. **Gabriel Abadal:** Writing – review & editing, Validation, Supervision, Project administration, Investigation, Formal analysis, Conceptualization. **Garcia Joan Garcia:** Writing – review & editing, Validation, Methodology. **Xavier Cartoixà:** Writing – review & editing, Supervision, Software, Funding acquisition.

Declaration of Competing Interest

The authors declare the following financial interests/personal relationships which may be considered as potential competing interests: Xavier Cartoixa reports financial support was provided by Spain's ministry of science and innovation. If there are other authors, they declare that they have no known competing financial interests or personal relationships that could have appeared to influence the work reported in this paper.

Acknowledgements

This work was funded by Spain's Ministerio de Ciencia e Innovación under Grant No. PID2021-127840NB-I00 (MICINN/AEI/FEDER, UE).

Data availability

Data will be made available on request.

References

[1] K.E. Petersen, Silicon as a mechanical material, Proc. IEEE 70 (5) (1982) 420–457, https://doi.org/10.1109/PROC.1982.12331.
[2] R. Hajare, V. Reddy, R. Srikanth, MEMS based sensors – a comprehensive review of commonly used fabrication techniques, Mater. Today Proc. 49 (2021), https://doi.org/10.1016/j.matpr.2021.05.223.
[3] F. Ghazali, M. Hasan, T. Rehman, M. Nafea, M.S. Mohamed Ali, K. Takahata, MEMS actuators for biomedical applications: a review, J. Micromech. Microeng. 30 (2020) 73001–73020, https://doi.org/10.1088/1361-6439/ab8832.
[4] H. Sun, M. Yin, W. Wei, J. Li, H. Wang, X. Jin, MEMS based energy harvesting for the Internet of things: a survey, Microsyst. Technol. 24 (2018), https://doi.org/10.1007/s00542-018-3763-z.
[5] L. Ni, R.M. Pocratsky, M.P. de Boer, Demonstration of tantalum as a structural material for MEMS thermal actuators, Microsyst. Nanoeng. 7 (1) (2021) 6, https://doi.org/10.1038/s41378-020-00232-z.
[6] D. Thuau, C. Ayela, P. Poulin, I. Dufour, Highly piezoresistive hybrid MEMS sensors, Sens. Actuators A Phys. 209 (2014) 161–168, https://doi.org/10.1016/j.sna.2014.01.037.
[7] G. Pillai, S.-S. Li, Piezoelectric MEMS resonators: a review, IEEE Sens. J. 21 (11) (2021) 12589–12605, https://doi.org/10.1109/JSEN.2020.3039052.
[8] S. Nabavi, M. Ménard, F. Nabki, A SOI out-of-plane electrostatic MEMS actuator based on in-plane motion, J. Micro Syst. 31 (5) (2022) 820–829, https://doi.org/10.1109/JMEMS.2022.3190829.
[9] M. Moczała, et al., Technology of thermally driven and magnetomotively detected MEMS microbridges, Sens. Actuators A Phys. 240 (2016) 17–22, https://doi.org/10.1016/j.sna.2016.01.041.
[10] J.-C. Chiou, C.-C. Hung, C.-Y. Lin, Design, fabrication and actuation of a MEMS-based image stabilizer for photographic cell phone applications, J. Micromech. Microeng. 20 (7) (2010) 75025, https://doi.org/10.1088/0960-1317/20/7/075025.
[11] B. Padha, I. Yadav, S. Dutta, S. Arya, Recent developments in wearable NEMS/MEMS-based smart infrared sensors for healthcare applications, ACS Appl. Electron. Mater. 5 (10) (2023) 5386–5411, https://doi.org/10.1021/acsaelm.3c00860.
[12] R.N. Dean, A. Luque, Applications of microelectromechanical systems in industrial processes and services, IEEE Trans. Ind. Electron 56 (4) (2009) 913–925, https://doi.org/10.1109/TIE.2009.2013691.
[13] X. Guo, W. Yang, X. Xiong, Z. Wang, X. Zou, MEMS reservoir computing system with stiffness modulation for multi-scene data processing at the edge, Microsyst. Nanoeng. 10 (1) (2024) 84, https://doi.org/10.1038/s41378-024-00701-9.
[14] Y. Yoon, I.-J. Cho, A review of human augmentation and individual combat capability: focusing on MEMS-based neurotechnology, Micro Nano Syst. Lett. 12 (1) (2024) 17, https://doi.org/10.1186/s40486-024-00205-1.
[15] T. Xu, J. Sun, H. Wu, H. Li, H. Li, Z. Tao, 3D MEMS in-chip solenoid inductor with high inductance density for power MEMS device, IEEE Electron Device Lett. 40 (11) (2019) 1816–1819, https://doi.org/10.1109/LED.2019.2941003.
[16] K. Entesari, G.M. Rebeiz, A 12-18-GHz three-pole RF MEMS tunable filter, IEEE Trans. Microw. Theory Tech. 53 (8) (2005) 2566–2571, https://doi.org/10.1109/TMTT.2005.852761.
[17] K. Shih, et al., Active MEMS metamaterials for THz bandwidth control, Appl. Phys. Lett. 110 (16) (2017) 161108, https://doi.org/10.1063/1.4980115.
[18] G. Zhou, Z.H. Lim, Y. Qi, G. Zhou, Single-pixel MEMS imaging systems, Micromachines 11 (2) (2020), https://doi.org/10.3390/mi11020219.
[19] G. Demirhan Aydin, O.S. Akar, T. Akin, Wafer level vacuum packaging of MEMS-based uncooled infrared sensors, Micromachines 15 (8) (2024), https://doi.org/10.3390/mi15080935.
[20] K. Jensen, J. Weldon, H. Garcia, A. Zettl, Nanotube radio, Nano Lett. 7 (2007) 3508–3511, https://doi.org/10.1021/nl0721113.
[21] Y. Cui, et al., A survey of mechanical antennas applied for low-frequency transmitting, iScience 26 (1) (2023) 105832, https://doi.org/10.1016/j.isci.2022.105832.
[22] N. Barani, K. Sarabandi, Mechanical antennas: emerging solution for Very-Low frequency (VLF) communication. 2018 IEEE International Symposium on Antennas and Propagation & USNC/URSI National Radio Science Meeting, 2018, pp. 95–96, https://doi.org/10.1109/APUSNCURSINRSM.2018.8608412.
[23] R. Ruiz, G. Abadal, Remote dynamic actuation of an electrostatically driven microcantilever by a wireless power transfer system, Sens. Actuators A Phys. 345 (2022) 113798, https://doi.org/10.1016/j.sna.2022.113798.
[24] R. Ruiz, G. Abadal, Direct transduction from radiofrequency radiated power to static and dynamic flexural mechanical modes, 2021 21st International Conference

on Solid-State Sensors, Actuators and Microsystems (Transducers) (2021) 144–147, https://doi.org/10.1109/Transducers50396.2021.9495668.
[25] R. Ruiz, J. Bonache, G. Abadal, A flexible dipole antenna for direct transduction of microwave radiated power into DC mechanical deflection, Sens. Actuators A Phys. 340 (2022) 113536, https://doi.org/10.1016/j.sna.2022.113536.
[26] C. Belacel, Y. Todorov, S. Barbieri, D. Gacemi, I. Favero, C. Sirtori, Optomechanical terahertz detection with single meta-atom resonator, Nat. Commun. 8 (1) (2017) 1578, https://doi.org/10.1038/s41467-017-01840-6.
[27] Y. Zhang, S. Hosono, N. Nagai, K. Hirakawa, Novel bolometric THz detection by MEMS resonators, 2018 43rd International Conference on Infrared, Millimeter, and Terahertz Waves (IRMMW-THz) (2018) 1–2, https://doi.org/10.1109/IRMMW-THz.2018.8510488.
[28] Y. Zhang, S. Hosono, N. Nagai, S.-H. Song, K. Hirakawa, Fast and sensitive bolometric terahertz detection at room temperature through thermomechanical transduction, J. Appl. Phys. 125 (15) (2019) 151602, https://doi.org/10.1063/1.5045256.
[29] Y. Zhang, B. Qiu, N. Nagai, M. Nomura, S. Volz, K. Hirakawa, Enhanced thermal sensitivity of MEMS bolometers integrated with nanometer-scale hole array structures, AIP Adv. 9 (8) (2019) 85102, https://doi.org/10.1063/1.5113521.
[30] D.K. Maram, X. Borrisé, J. Garcia-Garcia, R. Ruiz, X. Cartoixà, G. Abadal, Design and fabrication of an opto-mechanical antenna in the NIR range, Micro Nano Eng. 23 (2024) 100241, https://doi.org/10.1016/j.mne.2024.100241.
[31] R. Esteban, et al., Direct Near-Field optical imaging of higher order plasmonic resonances, Nano Lett. 8 (10) (2008) 3155–3159, https://doi.org/10.1021/nl801396r.
[32] A.F. McKinley, T.P. White, K.R. Catchpole, Theory of the circular closed loop antenna in the terahertz, infrared, and optical regions, J. Appl. Phys. 114 (4) (2013) 44317, https://doi.org/10.1063/1.4816619.
[33] D.K. Maram, X. Cartoixá, G. Abadal, Analysis of the photothermal parasitic effect on an optomechanical antenna, 2024 IEEE Sensors (2024) 1–4, https://doi.org/10.1109/SENSORS60989.2024.10785153.
[34] P.B. Johnson, R.W. Christy, Optical constants of the noble metals, Phys. Rev. B 6 (12) (1972) 4370–4379.
[35] Polyanskiy, M.N., Refractive index database, (n.d.), ⟨https://refractiveindex.info⟩.

Daniyal Khosh Maram received the M.Sc. (with Hons.) degree in electrical engineering (nano and microelectronics) from the Amirkabir University of Technology (Tehran Polytechnic), Tehran, Iran, in 2020. He is currently working toward the Ph.D. degree in electrical engineering with the Department of Electronics and Telecommunication Engineering, Universidad Autónoma de Barcelona (UAB), Bellaterra, Spain. His research interests include nanoantennas, plasmonic structures, optoelectronic devices, device physics, and nanoelectromechanical systems.

Appendix B

Non-Compendium Papers

B.1 Analysis of the Photothermal Parasitic Effect on an Optomechanical Antenna

Conference paper, published in IEEE Sensors conference proceedings.

Analysis of the Photothermal Parasitic Effect on an Optomechanical Antenna

Daniyal Khosh Maram
Departament d'Enginyeria Electrònica, Universitat Autònoma de Barcelona,
08193 Bellaterra, Barcelona, Spain
daniyal.khoshmaram@uab.cat

Xavier Cartoixà
Departament d'Enginyeria Electrònica, Universitat Autònoma de Barcelona,
08193 Bellaterra, Barcelona, Spain
xavier.cartoixa@uab.cat

Gabriel Abadal
Departament d'Enginyeria Electrònica, Universitat Autònoma de Barcelona,
08193 Bellaterra, Barcelona, Spain
gabriel.abadal@uab.cat

***Abstract*—In this paper, we investigate the parasitic opto-thermo-mechanical transduction in nano-optomechanical antenna, focusing on its impact on the performance of a previously designed structure. This study encompasses both experimental and computational analyses to model the parasitic effects that overlap with the intended opto-electromechanical responses. Utilizing COMSOL Multiphysics, we simulate the thermal, optical, and mechanical interactions within the optomechanical structure. Our findings indicate that the parasitic opto-thermo-mechanical effect significantly influences the device's mechanical deflection, driven primarily by localized heating at the microcantilever's free end. Experimental validation aligns well with simulation results, showcasing the parasitic response's dominance over the intended functionality. This research contributes to the broader understanding and optimization of our nano optomechanical devices for advanced applications in radiation detection and sets the future efforts to mitigate these parasitic effects.**

***Index Terms*—Multi-physics, NIR opto-thermomechanical antennas, finite element analysis, experimental validation.**

I. Introduction

In recent years, significant advancements have been made in developing nano-optoelectromechanical systems (NOEMS). Photonic crystal cavities, for example, enable the confinement and control of light in sub-wavelength dimensions, making them highly effective for optical filtering and switching [1]–[3]. For instance, nano-optoelectromechanical resonators can detect minute environmental changes by monitoring shifts in resonance frequencies [4]. Moreover, the NOEMS capability to manipulate optical signals at the nanoscale makes them ideal for advanced signal-processing applications in telecommunications and information processing [5]. Midolo et al. discussed hybrid NOEMS devices that couple optical, electrical, and mechanical degrees of freedom, highlighting their potential for high-speed, low-power light manipulation in nanophotonic structures [6]. In the domain of infrared detectors, Rogalski provides a comprehensive review of infrared detector technologies, focusing on NOEMS for enhanced sensitivity and resolution [7]. In a previous work [8], we presented a design of an optomechanical antenna for the detection of NIR radiation, which was based on the MEMSTENNA concept [9]–[11]. As it was demonstrated, in a MEMSTENNA which combines a MEMS structure in an antenna, direct transduction from the electromagnetic to the mechanical domain is achieved. In this paper, we investigate the parasitic optothermomechanical transduction that can overlap with optoelectromechanical transduction, screening the response of the previously designed optomechanical antenna.

II. Device Description and Operation Principle

Our proposed optomechanical antenna structure, called NEMSTENNA from now on, features a near-infrared (NIR) optical dipole nanoantenna, designed for a wavelength of 1550 nm, integrated into one of the metal sides at the free end of two gold-coated silicon nitride triangular microcantilevers, as illustrated in Fig. 1. The geometry of the dipole nanoantenna is characterized by the lengths and widths of its two main components (L_1, L_2, W_1) and the dimensions of the supporting arms (L_{Arm1}, L_{Arm2}, W_2) that connect the dipole elements to the microcantilevers, as described in [8] and Table I.

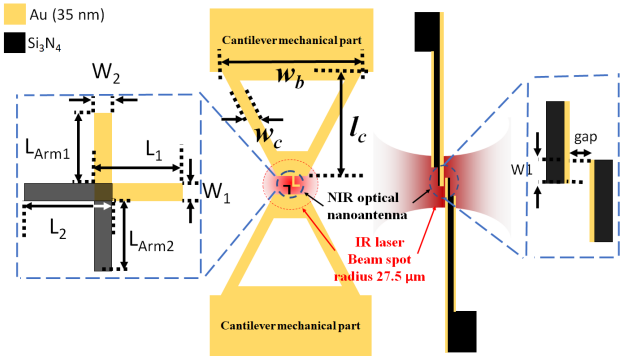

Fig. 1: Schematic top and side views of the proposed structure including nano-antenna and microcantilever illuminated by IR laser Gaussian beam with 27.5 μm spot radius.

The working principle of the opto-mechanical antenna relies on a well-defined transduction chain. When the nanoantenna is exposed to the radiation of a NIR laser with a wavelength of $\lambda_{\text{NIR}} = 1.55$ μm (frequency $f_{\text{NIR}} = 193.41$ THz), a voltage V_{gap} is induced in the feed gap region. This induced voltage is an ac voltage at the same frequency as the incident radiation ($f_{\text{NIR}} = 193.41$ THz). The induced voltage $V_{\text{gap}}(t) = V_0 \sin(2\pi f_{\text{NIR}} t)$ creates an electrostatic force between the two components of the dipole nanoantenna within this gap, leading

2024 IEEE SENSORS | 979-8-3503-6351-7/24/$31.00 ©2024 IEEE | DOI: 10.1109/SENSORS60989.2024.10785153

Authorized licensed use limited to: Universitat Autonoma De Barcelona. Downloaded on September 27,2025 at 12:43:17 UTC from IEEE Xplore. Restrictions apply.

to mutual attraction and driving the mechanical deflection of the microcantilever. This electrostatic force is given by $F = 0.5\frac{A\epsilon_0(V_{\text{gap}})^2}{d^2}$, where A is the overlapping area, ϵ_0 is the air dielectric constant, and d is the gap distance. Substituting V_{gap} into the force equation gives a DC term of the force $\frac{A\epsilon_0 V_0^2}{4d^2}$, inducing the static deflection of the microcantilever.

III. Multiphysics Model and Simulation Results

To investigate the parasitic effects alongside the optoelectromechanical response of our proposed device [8], we simulate opto-thermo-mechanical transduction. The simulation uses COMSOL Multiphysics, enabling comprehensive modeling by coupling optical, thermal, and mechanical phenomena. The geometry characteristics and material properties used in the simulations are detailed in Tables I to IV.

TABLE I

Geometry values: cantilevers, nanoantenna, laser used in our modeling.

Parameter	Value	Units
Dipole arm length, ($L_{Arm1}/L_{Arm\ 2}$)	0.75/0.72	μm
Dipole and Dipole arm width, (w_1=w_2)	0.1	μm
Dipole length, (L_1/L_2)	0.85/0.82	μm
Dipole gold thickness, (t_{gd})	0.035	μm
Dipole silicon nitride thickness, (t_{dd})	0.14	μm
Cantilever length, (l_c)	200	μm
Cantilever width, (w_c)	28	μm
Cantilever base width, (w_b)	184	μm
Cantilever silicon nitride thickness, (t_{dc})	0.6	μm
Cantilever gold thickness, (t_{gc})	0.07	μm
Capacitive gap, (g_0)	0.01	μm
Overlapping Area, (A)	0.01	μm^2

TABLE II

Material thermal properties used in our modeling.

Material properties	Gold	Si_3N_4
Heat capacity C_p, $J/(kg.K)$	129	700
Thermal conductivity κ, $W/(m.K)$	150^a, 230^b	2.1^c, 4^d
Density ρ, kg/m^3	19280	3100
Surface emissivity ϵ,	0.05	0.5

Gold layer with these thicknesses=35^a nm, 70^b nm
Si_3N_4 layer with these thicknesses=140^c nm, 600^d nm

TABLE III

Material optical and electrical properties used in our modeling.

Material properties	Gold	Si_3N_4
Refractive index n,	0.52406	1.9963
Extinction coefficient k,	10.742	0
Electrical conductivity σ, (S/m)	45×10^6	0

TABLE IV

Material mechanical properties used in our modeling.

Material properties	Gold	Si_3N_4
Density ρ, kg/m^3	19280	3100
Coefficient of thermal expansion α, (V/K)	14.1×10^{-6}	2.3×10^{-6}
Young's modulus E, (Pa)	80×10^9	250×10^9
Poisson's ratio ν	0.44	0.23

The values in Table I were primarily derived from the microcantilevers datasheet [12]. The properties in Tables II to IV are inferred from [13]–[20], corresponds to thermal, optical, electrical, and mechanical properties of materials. The simulation procedure involved constructing a 3D model of the NEMSTENNA design and implementing a perfect match layer (PML) boundary condition [21] as the outer layer of the simulation box. The NEMSTENNA was surrounded by air, including the gap area and a high mesh refinement was applied in the gap region [22]. The paraxial approximation of a Gaussian beam was utilized for the focused laser beam, with laser power and beam radius parameters ranging between 1 mW and 5.8 mW, and 27.5 μm, respectively. The simulation framework involves a coupled multiphysics approach encompassing electromagnetic (EM), thermal, and mechanical simulations. An EM simulation analyzes the material's distribution and absorption of optical energy using Maxwell equations. This step is crucial for determining the localized heating effects due to electromagnetic wave interactions. we have calculated that the power absorbed by the NEMSTENNA device is about 11% of the total incident power [23]. Subsequently, the thermal simulation utilizes the heat generation data from the EM analysis to calculate the resulting temperature distribution. The heat transfer module in COMSOL accurately models the thermal response, capturing the effects of conduction, convection, and radiation as necessary. Within our modeling simulation configuration, the heat transport equation (1) is effectively solved, considering that the illumination time has reached a steady-state regime. According to equation (2), Q_e denotes the resistive loss, establishing a connection with the electric field and the imaginary part of the permittivity of the lossy material at the frequency of 193.41 THz for the laser radiation.

$$\rho C_p \frac{\partial T}{\partial t} - \nabla.(k\nabla T) = +Q_e \tag{1}$$

$$Q_e = \frac{1}{2}\omega\varepsilon_0 \operatorname{Im}(\varepsilon_r)|E|^2 \tag{2}$$

Modified thermal properties are essential for accurate modeling at the nanoscale, accounting for the distinct geometrical features of thin films. For instance, based on conclusions by Chen and Hui, the thermal conductivity of a 35 nm gold film is only 47% that of bulk gold, and similarly, a 140 nm Si_3N_4 layer exhibits a thermal conductivity of 72% that of bulk Si_3N_4, as shown in Table II [24]. The significant deviation of thermal properties in submicrometer devices is well-documented in the literature [24]–[27]. At the nanoscale, Sultan et al. reported thermal conductivity of 3–4 $W/(m.K)$ for 500 nm thin films in a temperature range of 77–325 K [20], Stojanovich et al. measured thermal conductivity of about 2.1 $W/(m.K)$ for 180 nm thick freestanding specimens, and Bai et al. determined a thermal conductivity of 1.2–2.0 $W/(m.K)$ for stoichiometric silicon nitride films with thicknesses ranging from 37 to 200 nm [17], [19], [20]. In the numerical analysis of heat transfer differential equations, two categories of boundary conditions (BCs) are considered: exterior BCs and interior BCs. Exterior BCs are applied to the outermost boundaries of the geometric model. In our model, we considered outward conductive heat flux, convective heat flux to the air environment, and radiation heat flux [28]. For natural convection in the air at large scales, typical values for h are in the range of 5-10 $W/(m^2.K)$. However, in nanoscale devices, the convective heat transfer coefficient (h) should be substantially higher. According to the scaling law proposed in reference [29], the convective coefficient for air has been reported as 100 $W/(m^2.K)$ when the scale is less than 100 μm, representing a tenfold increase compared to macro-scales [30]. This enhanced heat transfer coefficient at the nanoscale is attributed to improved convection heat transfer due to compressed boundary layers at very small scales [30]. The assigned h values in the heat transfer module for the Au/SiN boundary layers are elicited through extrapolation from reference [29], considering nano dimensions. The ambient temperature is set at T=293 K. In the analysis of a multilayer thin film structure such

Authorized licensed use limited to: Universitat Autonoma De Barcelona. Downloaded on September 27,2025 at 12:43:17 UTC from IEEE Xplore. Restrictions apply.

as NEMSTENNA, the impact of finite thermal boundary resistance (TBR) should be taken into account. Moreover, the heat transport and thermal properties of thin film structures can be strongly influenced by the interface between a metal and dielectric thin film [25]. TBR at the interface may dominate overall heat transport rather than the thermal properties of each thin film. TBR induces an abrupt change in temperature across interfaces between two different materials, a phenomenon first observed by Kapitza for a solid and liquid helium interface in 1941 [31], [32]. Notably, in ref. [25], a thermal boundary resistance of 0.81×10^{-8} (m^2K/W) for the Au/SiN interface was reported using the transient thermoreflectance (TTR) technique [33] and this value considered as an input for our COMSOL simulation. Finally, the mechanical simulation is conducted to assess the structural deformations induced by thermal expansion. The temperature distribution obtained from the thermal analysis serves as an input for the mechanical simulation, enabling the evaluation of stresses, strains, and resultant displacements within the material. The coefficient of thermal expansion (CTE), shown in Table IV, is the parameter that governs this thermomechanical transduction. To simulate the system, a dynamic approach was employed, utilizing a moving mesh within the simulation enclosure housing the NEMSTENNA in an air environment, thus mitigating convergence issues. Convergence was attained using the COMSOL fully coupled solver to observe stationary steady-state responses [34]. In a preliminary batch of simulations, we have analyzed the influence of nanoantenna on the thermomechanical response of the NEMSTENNA, by calculating the temperature and deflection of structures with and without nanoantenna part. The simulation results of this analysis show that the nanoantenna is not generating a significant heating effect and the bending of the microcantilever is mainly produced by the heating of its free end illuminated region. In, Fig. 2a, simulated steady-state response of temperature and static displacement at cantilever free end are illustrated, and volumetric maps are provided as inset for 5.8 mW IR laser power.

IV. Experimental validation

A single microcantilever has been tested to validate the COMSOL simulated predictions. The used experimental setup is described in previous work [11]. The NIR laser beam is focused by 20X optical microscope objective on top of the free end of the microcantilever. The deflection of the microcantilever at its free end produced by the optothermomechanical effect is detected using a red diode laser coupled with a four-quadrant photodetector readout system. The readout signal was captured using an oscilloscope in order to analyze the transient response produced by the switch OFF-ON-OFF of the laser beam. These measured transients are observed in Fig. 2b, which show that the microcantilever free end is deflected 8 nm, 14 nm, and 20 nm, when 3.7 mW, 4.7 mW, and 5.8 mW laser powers are used, respectively. A good agreement between measured and simulated displacements is obtained. However, our results reveal that in the present version of our NEMSTENNA design the parasitic optothermomechanical response is still orders of magnitude larger compared to the optoelectromechanical response predicted in [8], which avoids a practical application of our NEMSTENNA device.

V. Conclusion

In this research, we have successfully demonstrated the agreement of experimental and modeling approaches to enhance the understanding and design of near-infrared (NIR) opto-mechanical antennas. Our findings reveal that the parasitic opto-thermo-mechanical response significantly affects the performance of the NEMSTENNA device, overshadowing the desired opto-electromechanical response. The experimental validation aligns closely with our COMSOL Multiphysics simulations, confirming the substantial impact of localized heating on the microcantilever's deflection. These results highlight the necessity to address and minimize parasitic effects to improve the practical applicability of our nano optomechanical devices in radiation detection applications. Future work will focus on strategies to mitigate these parasitic effects in order to enhance our overall device performance.

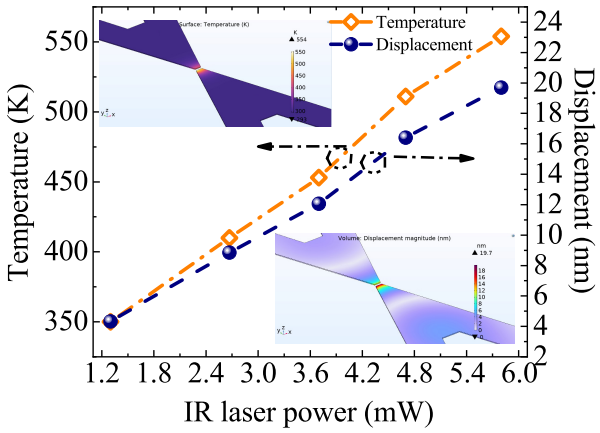

(a)

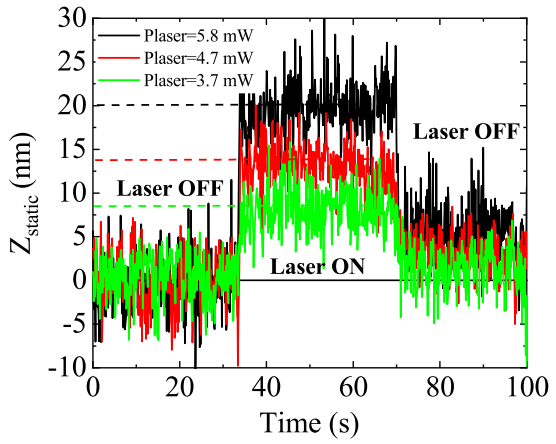

(b)

Fig. 2: (a) Simulated temperature and static displacement at free-end vs. different laser power. Inset: volumetric temperature and displacement maps around free end cantilever region for 5.8 mW IR laser power. (b) Measured static deflection vs. time in the OFF-ON-OFF transients for 5.8 mW, 4.7 mW, 3.7 mW IR laser power.

Acknowledgment

The authors thank Spain's Ministerio de Ciencia e Innovación y Universidades under Grant No. PID2021-127840NB-I00 (MICINN/AEI/FEDER, UE) for their support and funding of this research project.

References

[1] H. Du, L. Yang, Y. Xu, W. Wang, W. Zhang, N. Fang, and D. Fan, "Mechanically-tunable photonic devices with on-chip integrated mems/nems actuators," *Micromachines*, vol. 7, no. 4, p. 69, 2016. [Online]. Available: https://doi.org/10.3390/mi7040069

Authorized licensed use limited to: Universitat Autonoma De Barcelona. Downloaded on September 27,2025 at 12:43:17 UTC from IEEE Xplore. Restrictions apply.

[2] Y. Kim, G. S. Yoon, J. Lee, H. J. Kim, B.-S. Lee, H. B. Jang, K.-Y. Lee, and J. Rho, "Light engineering in nanometer space," *Advanced Materials*, vol. 32, no. 51, p. e2003051, 2020. [Online]. Available: https://doi.org/10.1002/adma.202003051

[3] J. H. Cho, M.-K. Lim, K.-W. Seo, J. H. Park, D. H. Kim, and S. K. Choi, "Towards repeatable, scalable graphene integrated micro-nano electromechanical systems (mems/nems)," *Micromachines*, vol. 13, no. 1, p. 27, 2021. [Online]. Available: https://doi.org/10.3390/mi13010027

[4] S. Liu, H. Xiao, Y. Chen, P. Chen, W. Yan, Q. Lin, B. Liu, X. Xu, Y. Wang, X. Weng, L. Liu, and J. Qu, "Nano-optomechanical resonators based on suspended graphene for thermal stress sensing," *Sensors (Basel)*, vol. 22, no. 23, p. 9068, Nov 2022.

[5] A. Fratalocchi, C. M. Dodson, R. Zia, P. Genevet, E. Verhagen, H. Altug, and V. J. Sorger, "Nano-optics gets practical," *Nature Nanotechnology*, vol. 10, no. 1, pp. 11–15, 2015.

[6] L. Midolo, A. Schliesser, and A. Fiore, "Nano-opto-electro-mechanical systems," *Nature Nanotechnology*, vol. 13, no. 1, pp. 11–18, 2018. [Online]. Available: https://doi.org/10.1038/s41565-017-0039-1

[7] A. Rogalski, "Infrared detectors: an overview," *Infrared Physics & Technology*, vol. 43, pp. 187–210, 2002. [Online]. Available: https://api.semanticscholar.org/CorpusID:18234614

[8] D. K. Maram, X. Borrisé, J. Garcia-Garcia, R. Ruiz, X. Cartoixà, and G. Abadal, "Design and fabrication of an opto-mechanical antenna in the nir range," *Micro and Nano Engineering*, vol. 23, p. 100241, 2024. [Online]. Available: https://www.sciencedirect.com/science/article/pii/S2590007224000042

[9] C. Belacel, Y. Todorov, S. Barbieri, D. Gacemi, I. Favero, and C. Sirtori, "Optomechanical terahertz detection with single meta-atom resonator," *Nature Communications*, vol. 8, p. 1578, 2017. [Online]. Available: https://doi.org/10.1038/s41467-017-01840-6

[10] R. Ruiz, J. Bonache, and G. Abadal, "A flexible dipole antenna for direct transduction of microwave radiated power into dc mechanical deflection," *Sensors and Actuators A: Physical*, vol. 340, p. 113536, 2022. [Online]. Available: https://www.sciencedirect.com/science/article/pii/S0924424722001741

[11] R. Ruiz and G. Abadal, "Remote dynamic actuation of an electrostatically driven microcantilever by a wireless power transfer system," *Sensors and Actuators A: Physical*, vol. 345, p. 113798, 2022. [Online]. Available: https://www.sciencedirect.com/science/article/pii/S0924424722004332

[12] "Afm probe pnp-tr-tl-au," https://www.nanoandmore.com/AFM-Probe-PNP-TR-TL-Au, 2024.

[13] M. N. Polyanskiy, "Refractive index database," 2024.

[14] A. J. Schmidt, R. Cheaito, and M. Chiesa, "Characterization of thin metal films via frequency-domain thermoreflectance," *Journal of Applied Physics*, vol. 107, no. 2, p. 024908, 01 2010. [Online]. Available: https://doi.org/10.1063/1.3289907

[15] J. M. Lugo and A. I. Oliva, "Thermal properties of metallic films at room conditions by the heating slope," *Journal of Thermophysics and Heat Transfer*, vol. 30, no. 2, pp. 452–460, 2016. [Online]. Available: https://doi.org/10.2514/1.T4605

[16] M. T. Alam, M. P. Manoharan, M. A. Haque, C. Muratore, and A. Voevodin, "Influence of strain on thermal conductivity of silicon nitride thin films," *Journal of Micromechanics and Microengineering*, vol. 22, no. 4, p. 045001, mar 2012. [Online]. Available: https://dx.doi.org/10.1088/0960-1317/22/4/045001

[17] S. Bai, Z. Tang, Z. Huang, and J. Yu, "Thermal characterization of Si_3N_4 thin films using transient thermoreflectance technique," *IEEE Transactions on Industrial Electronics*, vol. 56, no. 8, pp. 3238–3243, 2009.

[18] H. Ftouni, C. Blanc, D. Tainoff, A. D. Fefferman, M. Defoort, K. J. Lulla, J. Richard, E. Collin, and O. Bourgeois, "Thermal conductivity of silicon nitride membranes is not sensitive to stress," *Phys. Rev. B*, vol. 92, p. 125439, Sep 2015. [Online]. Available: https://link.aps.org/doi/10.1103/PhysRevB.92.125439

[19] N. Stojanovic, J. Yun, E. B. K. Washington, J. M. Berg, M. W. Holtz, and H. Temkin, "Thin-film thermal conductivity measurement using microelectrothermal test structures and finite-element-model-based data analysis," *Journal of Microelectromechanical Systems*, vol. 16, no. 5, pp. 1269–1275, 2007.

[20] R. Sultan, A. Avery, G. Stiehl, and B. Zink, "Thermal conductivity of micromachined low-stress silicon-nitride beams from 77 to 325 k," *Journal of Applied Physics*, vol. 105, pp. 043 501 – 043 501, 03 2009.

[21] Z. Ma and G. A. E. Vandenbosch, "Input impedance of optical metallic nano dipole over 300 nm – 1200 nm wavelength," 2013, pp. 3810–3813.

[22] J.-S. Huang, T. Feichtner, P. Biagioni, and B. Hecht, "Impedance matching and emission properties of nanoantennas in an optical nanocircuit," *Nano Lett.*, vol. 9, pp. 1897–1902, 2009.

[23] D. Ramos, J. Tamayo, J. Mertens, and M. Calleja, "Photothermal excitation of microcantilevers in liquids," *Journal of Applied Physics*, vol. 99, no. 12, p. 124904, 06 2006. [Online]. Available: https://doi.org/10.1063/1.2205409

[24] X. Chen, Y. Chen, M. Yan, and M. Qiu, "Nanosecond photothermal effects in plasmonic nanostructures," *ACS Nano*, vol. 6, no. 3, pp. 2550–2557, 2012, pMID: 22356648. [Online]. Available: https://doi.org/10.1021/nn2050032

[25] T. Jeong, J.-G. Zhu, S. Chung, and M. R. Gibbons, "Thermal boundary resistance for gold and CoFe alloy on silicon nitride films," *Journal of Applied Physics*, vol. 111, no. 8, p. 083510, 04 2012. [Online]. Available: https://doi.org/10.1063/1.3703571

[26] H. Neumann, "C. r. tellier, a. j. tosser. size effects in thin films. aus der reihe thin films science and technology", vol. 2 (editor: G. siddall). elsevier scientific publishing company, amsterdam-oxford-new york 1982, 310 seiten mit 102 abbildungen, 19 tabellen und 428 literaturzitaten, preis: Us $ 74.50 bzw. dfl. 160.00," *Crystal Research and Technology*, vol. 18, no. 11, pp. 1358–1358, 1983. [Online]. Available: https://onlinelibrary.wiley.com/doi/abs/10.1002/crat.2170181108

[27] M. I. Flik, B. I. Choi, and K. E. Goodson, "Heat Transfer Regimes in Microstructures," *Journal of Heat Transfer*, vol. 114, no. 3, pp. 666–674, 08 1992. [Online]. Available: https://doi.org/10.1115/1.2911332

[28] X. Chen, S. C. Bae, L.-L. Chau, D. L. Farkas, T. Rajh, Y. Liu, A. Pearson, J. Šefčík, M. Bleuel, I. E. Dimitrov, M. T. Brehmer, Y.-J. Hu, B. Lee, Y. Wang, H. W. Yoon, M. Tiemann, M. Pruski, and S. Jin, "Nanosecond photothermal effects in plasmonic nanostructures," *ACS Nano*, vol. 6, no. 3, pp. 2550–2557, 2012. [Online]. Available: https://doi.org/10.1021/nn2050032

[29] J. Peirs, D. Reynaerts, and H. Van Brussel, "Scale effects and thermal considerations for micro-actuators," in *Proceedings. 1998 IEEE International Conference on Robotics and Automation (Cat. No.98CH36146)*, vol. 2, 1998, pp. 1516–1521 vol.2.

[30] X. J. Hu, A. Jain, and K. E. Goodson, "Investigation of the natural convection boundary condition in microfabricated structures," *International Journal of Thermal Sciences*, vol. 47, no. 7, pp. 820–824, 2008. [Online]. Available: https://www.sciencedirect.com/science/article/pii/S1290072907001731

[31] R. J. Stevens, A. N. Smith, and P. M. Norris, "Measurement of Thermal Boundary Conductance of a Series of Metal-Dielectric Interfaces by the Transient Thermoreflectance Technique," *Journal of Heat Transfer*, vol. 127, no. 3, pp. 315–322, 03 2005. [Online]. Available: https://doi.org/10.1115/1.1857944

[32] E. T. Swartz and R. O. Pohl, "Thermal boundary resistance," *Rev. Mod. Phys.*, vol. 61, pp. 605–668, Jul 1989. [Online]. Available: https://link.aps.org/doi/10.1103/RevModPhys.61.605

[33] O. W. Käding, H. Skurk, and K. E. Goodson, "Thermal conduction in metallized silicon-dioxide layers on silicon," *Applied Physics Letters*, vol. 65, no. 13, pp. 1629–1631, 09 1994. [Online]. Available: https://doi.org/10.1063/1.112933

[34] C. Multiphysics, *COMSOL Multiphysics*, 6th ed., 2022.

Authorized licensed use limited to: Universitat Autonoma De Barcelona. Downloaded on September 27,2025 at 12:43:17 UTC from IEEE Xplore. Restrictions apply.

B.2 Plasmomechanical actuation at the nanoscale activated by NIR radiation

Journal paper (Paper 3), submitted to Results in Physics.

Plasmomechanical actuation at the nanoscale activated by NIR radiation

Daniyal Khosh Maram[a,*], Xavier Borrisé[b], Joan Garcia-Garcia[a], Xavier Cartoixà[a], Gabriel Abadal [a]

[a] *Dept. Enginyeria Electrònica, Campus UAB, 08193-Bellaterra, Spain,*
[b] *Catalan Institute of Nanoscience and Nanotechnology (ICN2) and Barcelona Institute of Science and Technology (BIST), Barcelona, Spain*

* *Corresponding author.*
E-mail address: daniyal.khoshmaram@uab.cat

Abstract

The design of a plasmomechanical actuator based on an optical nanodipole antenna integrated in the overlapped free moving end of two micro-nanocantilevers is presented here. The static steady state deflection of the cantilevers, which defines the actuator response, is produced by means of two transduction phenomena activated by a continuous power NIR illumination: a desired opto-electromechanical (OEM) mechanism, in which the cantilevers are mutually attracted directly by the electrostatic force induced in the nanodipole feed gap, and a non-desired parasitic opto-thermomechanical (OTM) mechanism associated to the bimetallic effect induced by the optical heating of the structure. COMSOL Multiphysics has been chosen to carry out a design of the actuator based on an optimized optical response of the nanodipole antenna to the 1.55 μm wavelength radiation. COMSOL simulations have been also performed to evaluate the parasitic OTM response and the responsivity, defined as the OEM signal per unit radiation power. Predicted responsivity values of 0.67 nm/mW are of the same order of magnitude of similar state-of-the-art transducers.

Keywords: Mechanical antenna; NIR nanoantenna; plasmomechanical transduction; MEMS/NEMS resonators

1. Introduction

The interaction between electromagnetic (EM) fields and matter is the foundation of Information and Communications Technologies (ICTs). Phenomenologically, this interaction is diverse since it depends on the frequency of photons associated to the EM fields and the nature of the matter considered. Thus, in electronics, for instance, EM fields with frequencies below 10 THz interact with electrons. In photonics, however, light interact with the atoms of matter whenever it is generated, controlled, manipulated or detected and the term light-matter interaction is used to refer the case of EM fields and matter coupling.

A particular sort of light-matter interaction that was already theoretically predicted by Maxwell is the responsible of the radiation pressure which, for example, gave an explanation to ancient observations at astronomic scale such as comet tale dynamics [1]. At a smaller scale, particle trapping and manipulation achieved by means of this phenomenon, was demonstrated in the seminal works of Nobel laureate A. Ashkin [2], leading to notable applications as optical tweezers [3]. The forces involved in light-matter manipulation can be described classically when objects have dimensions larger than light wavelength [4] but need a quantum mechanical description if particle dimensions are in the sub-wavelength range [5]. This is the case of laser trapping and cooling of neutral atoms [6], where temperatures as low as few microkelvin are achieved by means of the so-called magneto-optic trap (MOT) technique [7], enabling the groundbreaking research in Bose–Einstein condensate [8]. Optical forces induced in light-matter interactions are also involved in the field of nano-optomechanics, where the extremely small inertial masses of nanomechanical structures can be moved by momentum exchange of optical photons. In this case, light-matter interaction is described through a photon-phonon coupling which is usually produced in an optical cavity integrated in the nanomechanical structure to resonantly enhance this coupling. Since the interaction of light with the mechanical structure introduces an extra dissipative term named opto-mechanical (OM) damping in the mechanical dynamics of the system [9], which can be tuned modifying the resonance conditions of the cavity, amplification to a self-sustained regime [10] leading to mechanical lasing [11] can be achieved when OM damping cancels the intrinsic mechanical damping. On the contrary, cooling to the ground-state of a mechanical oscillator [12], [13] can be achieved when total dissipation is dominated by the OM damping term. An equivalent enhancement effect to that produced by optical cavities in the above-described light-matter interaction, is reproduced when plasmonic and nanomechanical structures are co-integrated in a unique plasmomechanical system [14]. In a plasmonic component of a plasmomechanical system like, for example, an optical nanoantenna [15] light is confined in sub-wavelength regions giving rise to huge electric field gradients and near-field forces [16], resulting in giant optical actuation on the nanomechanical component [17], [18], [19].

From a practical engineering point of view, opto-mechanical phenomena driving plasmomechanical systems are seen as an opportunity to propose novel transduction mechanisms between EM and mechanical domains as well as new promising applications such as plasmonic nanomotors [20] or reconfigurable metasurfaces [21], [22]. Thus, for instance, photothermally induced heat generated by the enhanced optical absorption in a plasmonic structure can be converted in mechanical self-oscillations by a bimetallic effect on a Fabry-Perot cavity with a suspended Frequency Selective Surface (FSS) metamaterial [23], [24] or in a MIM cavity [25]. Such an opto-thermomechanical transduction mechanism has been exploited in MEMS-based bolometric sensors to detect and analyse THz [26], [27] and NIR radiation [28], [29]. However, EM to mechanical conversion through a fast intermediate electrostatic transduction step compared to the thermal one, is advantageous in terms detection bandwidth, as demonstrated by Belacel et al. [30]. This much faster transduction scheme is the basis of authors' previous works on the N/MEMSTENNA concept, which combine an antenna and a N/MEMS structure to convert the energy of microwave [31] or near-infrared [32] EM radiation into a local static [33] or dynamic [34] deflection of the mechanical compliant structure.

In this paper we propose an optimized version of the NEMSTENNA based plasmomechanical transducer presented previously [32], that includes a nanocantilever to reduce significantly the spring constant of the mechanical structure and, consequently, improve the responsivity of the transducer. In section 2, the NEMSTENNA structure and its working principle are described. Section 3 contains the details of the COMSOL setup used to model the NEMSTENNA, the coupling procedures between the different physics domains and the design of the nanodipole antenna and the nanocantilever which integrate the NEMSTENNA. In section 4, the fabrication process based on Focused Ion Beam (FIB) nanolithography is described and the maximum nanocantilever slenderness before the stress collapse is empirically determined. In section 5, the NEMSTENA performance in terms of the opto-electromechanical (OEM) response and the corresponding responsivity predicted by COMSOL simulations are presented and discussed.

2. Structure definition and transduction mechanism

2.1. Plasmomechanical antenna structure

The plasmomechanical device is composed of two components with three different structural parts (Fig.1). The first and central part is a nanodipole optical antenna which is suspended through a couple of nanocantilevers (the second part) symmetrically connected at its feed port. The third structural part is based on double clamped-free beam trapezoidal microcantilevers which are connected at their free end to the nanocantilevers and anchored at the clamped end to the chip substrate. Both left and right micro-nanocantilever-antenna components are initially separated by a distance, g_0, defining an air gap in the vertical z direction at the nanoantenna feed port, as described in Fig.1.a. The overlap area, $A_{overlap}=W_1 \cdot W_2$, of both components defines a capacitive coupling, C_{gap}, between them at the feed gap region, as described in Fig.1.b. The nanodipole antenna and nanocantilevers are defined in a 35 nm thick Au layer on top of a 100 nm Si_3N_4 substrate. The same applies for the trapezoidal microcantievers except that the Si_3N_4 here is 600 nm thick. All relevant geometry dimensions are defined in the top and lateral views of the device structure in figure 1 and summarized in Table II with their corresponding values.

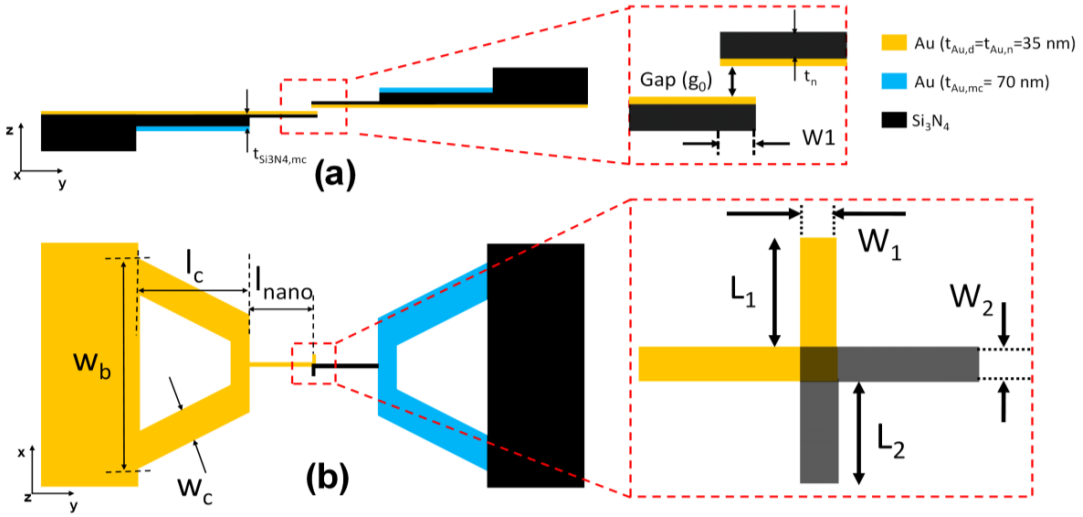

Figure 1: Lateral (a) and top (b) views of the plasmomechanical antenna

2.2. Transduction principle

When the nanoantenna (Fig.2.a) is illuminated by a focused IR laser beam with a wavelength λ_{NIR}=1.55 μm, an AC voltage, V_{gap}, oscillating at f_{NIR}=193.41 THz (=c/λ) is induced at its feed gap region (Fig.2.b) as described by:

$$\mathbf{V_{gap}(t) = |V_{gap}| \cdot cos(2\pi f_{NIR}\, t)} \tag{1}$$

This V_{gap} voltage generates an attractive electrostatic force in the z-direction, F_{ee}, between the two nanoantenna arms that contains a DC component, as a consequence of the quadratic dependence of the force with the voltage:

$$\mathbf{F_{ee}(t) = \frac{1}{2} \cdot \frac{\partial C_{gap}}{\partial z} \cdot \left(V_{gap}(t)\right)^2 = F_{ee,DC} + F_{ee,AC}(t)} \tag{2}$$

where the electrostatic transduction capacitance, C_{gap}, and both DC and AC components of the electrostatic force, $F_{ee,DC}$ and $F_{ee,AC}$, are consequently expressed by:

$$\mathbf{C_{gap} = \frac{\epsilon_0 \cdot w_1 \cdot w_2}{(g_0 - 2 \cdot z)}} \tag{3}$$

$$\mathbf{F_{ee,DC} = \frac{1}{4} \cdot \frac{\partial C_{gap}}{\partial z} \cdot |V_{gap}|^2} \tag{4}$$

$$\mathbf{F_{ee,AC}(t) = \frac{1}{4} \cdot \frac{\partial C_{gap}}{\partial z} \cdot |V_{gap}|^2 \cdot cos(4\pi f_{NIR}\, t)} \tag{5}$$

The DC component of the electrostatic force (equation 4), which acts in the vertical direction (z-axis) is finally the responsible of the out-of-plane static displacement of each component of the nanodipole optical antenna, z, associated with the bending of the micro-nanocantilever elements of the plasmomechanical antenna (Fig.2.c). The AC component (equation 5) does not produce any significant mechanical response since its frequency, $2 \cdot f_{NIR}$=386.82 THz, is many orders of magnitude above the natural oscillation frequency of the mechanical structure (in the kHz range).

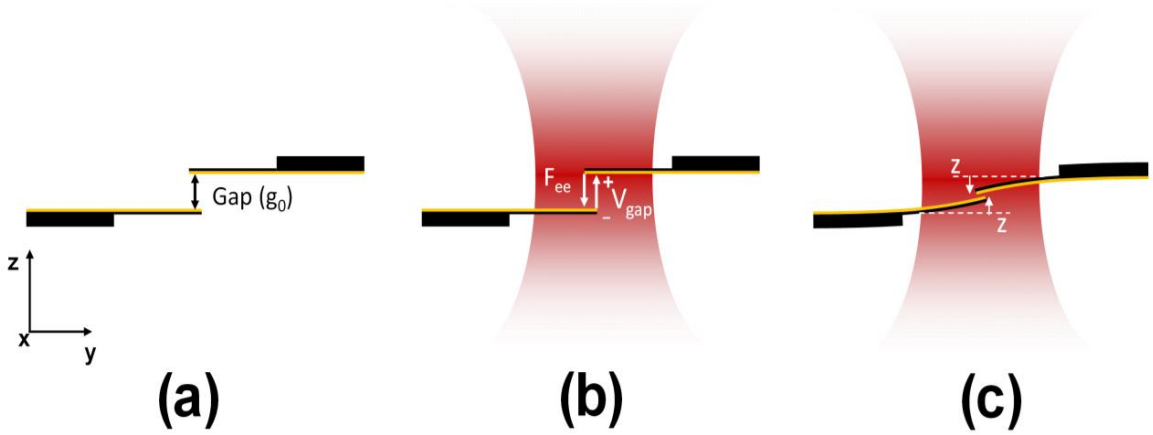

Figure 2: Lateral schematic view for the operation principle description. When both components of the plamomechanical antenna initially separated by a gap distance, g_0, in the capacitive overlapping region (a) are illuminated by a focused IR laser beam (b), the voltage, V_{gap}, and the corresponding DC component of the electrostatic force, F_{ee}, induces a static bending, z, in the out-of-plane direction (c)

3. Modelization and prototype design

3.1. Multiphysics model

The modelling of the NEMSTENNA's nanodipole optical antenna has been performed by means of the COMSOL RF module. RF simulation conditions are characterized by the definition of a spherical simulation box that envelopes only the nanodipole and a Gaussian laser beam as excitation source. Beam waist in terms of spot radius (SR) and power are defined as the main Gaussian beam characteristics and paraxial approximation is chosen to describe EM wave propagation. A Perfectly Matched Layer (PML) is used as boundary condition covering the spherical simulation box to avoid reflections and $\lambda/5$ mesh size has been chosen to optimize finite element calculations. The main simulation outputs of this first module are the electric field and the nanoantenna voltage in the feed gap, V_{gap}, which is obtained by integrating the z-component of the electric field along the gap length.

This voltage is then used to couple the RF module to the electrostatics and solid mechanics modules, to obtain as a main simulation output the static displacement, z, of the nanodipole arms (Fig2.c). This static mechanical displacement resulting from the electrostatic interaction induced by the optical excitation of the NEMSTENNA will be called the opto-electromechanical (OEM) response, z_{OEM}, from now on.

At the same time and using an independently defined simulation setup, the RF module is fully coupled to thermal and mechanical modules in a larger rectangular simulation box, which now includes the whole NEMSTENNA structure. The resistive losses obtained as an output of the RF simulations are used as a heat source input in thermal transport simulations, so that RF and thermal modules are coupled in this way. Thus, heat generated by the absorbed optical radiation in the Au layer and its transport through the NEMSTENNA structure, as well as its dissipation to the surrounding air and anchoring substrate can be accurately calculated. To do that, COMSOL thermal module solves heat transport equation by considering convection, Au/Si_3N_4 interface heat transfer and radiation as the three main dissipation mechanisms [35]. The most relevant parameters involved in this transduction step are heat capacitance, C_p, thermal conductivity, κ, convective heat transfer coefficient, h, Thermal Boundary Resistance, TBR and surface emissivity, ϵ. The main resulting simulation output of this thermal module is the temperature distribution map. Finally, the temperature field is used as the input magnitude of the mechanical module to calculate the thermally induced mechanical bending. Here, the coefficient of thermal expansion (CTE) is the main parameter to model the bimetallic effect in the Au/Si_3N_4 interface, which is the cause of such a thermomechanical deformation. The resulting static mechanical displacement of the micro-nanocantilever free end produced by the optical induced heating of the NEMSTENNA will be called the opto-thermomechanical (OTM) response, z_{OTM}, from now on.

Parameters summarized in Table I correspond to the optical, thermal and mechanical properties of the constituent materials of the NEMSTENNA structure that has been used to setup all above described COMSOL simulations. Notice that one of the most important set of parameters corresponds to the permittivity vs. wavelength ($\varepsilon_r(\lambda)$) couples of values, which correspond to Johnson and Christy for Au and Luke et al. for Si_3N_4 experimental data [36], [37], [38].

3.2. Nanoantenna design

The dimensions of the nanodipole antenna design have been obtained through a COMSOL optimization process where V_{gap} is used as the maximization variable at a radiation wavelength of 1.55 μm. Arm lengths of the nanodipole L_1 and L_2 were considered as free parameters for optimization and forced to be equal ($L_1 = L_2$). Nanodipole arms' width W_1 and nanodipole connection to nanocantilevers' width W_2 were also free parameters but were kept nonsymmetrical to allow the optimization process to adapt to the asymmetry of the structure. Si_3N_4 thickness was fixed at the value of 140 nm, which was demonstrated to be optimal in a previous paper [32]. The optimization process was carried out with a laser power of 7.5 mW, a 27.5 μm beam spot radius and an initial gap distance fixed at g_0=10 nm. The resulting set of parameters from the optimization process are: $L_1 = L_2 = 1360$nm, and $W_1 = 80$ nm, $W_2 = 100$ nm. It must be noticed that the seed conditions of the optimization process were set around nanodipole dimensions corresponding to the 5th mode, so that the optimization solution lead to a structure easier to fabricate and with a higher effective area to maximize radiation absorption [39]. The optimized dimensions together with the rest of geometry parameters are included in Table II. The radiation frequency dependence of the gap voltage, V_{gap}, and of the electric field in the z-direction in the gap, $E_{z,gap}$, presented by the optimal structure as shown in figure 3, demonstrate that the optimization process would deliver the same design dimensions independently of the spot radius considered.

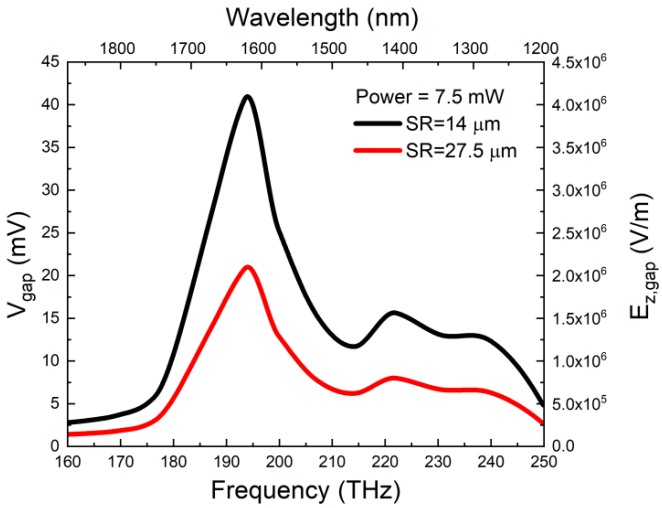

Figure 3: Vgap and Ez vs. frequency and wavelength for different SR

3.3. Nanocantilever design

A simple analysis of the effect of the nanocantilever length (l_n) on the total vertical spring constant of the structure has been performed, by considering the triangular microcantilever coupled in series with the nanocantilever. For the sake of simplicity, we have neglected the 35 and 70 nm thick Au layers in front of the 600 nm thick Si_3N_4 layer for the calculation of the micro and nanocantilever components' spring constants. As sketched in the top part of figure 4, the analysis starts from a structure purely micro, where no nanocantilever is present at the free end (l_n=0), to a structure with a nanocantilever l_n=80 μm long, close to the maximum fabricable length (l_n=83 μm). Notice that as l_n grows, the length of the triangular microcantilever decreases correspondingly, so that the total length of the structure is kept constant. Figure 4 shows the results of this analysis, where it is clearly seen that above a certain threshold nanocantilever length the low spring constant of the nanocomponent dominates over the large and growing spring constant of the micro component, leading to a lowering effect on the total structure rigidity. Consequently, structures with a nanocantilever longer than this threshold value will improve the mechanical transduction performance of the single microcantilever based NEMSTENNAS proposed previously [32]. In the two plots of figure 4 (panels (c) and (d)), corresponding to nanocantilevers with three different transversal cross section areas ($w_n \cdot t_n$) from wider and thick ($2 \cdot 0.6$ μm^2) to narrower and thinner ($0.5 \cdot 0.1$ μm^2) values, it is shown that the threshold length is around 53 μm for the wider/thicker case, but decreases to 7.5 μm for the narrower/thinner case. If we define a slenderness factor as SF=$l_n/(w_n \cdot t_n)$, it is trivially concluded that the larger the SF is, the better in terms of structure compliance and mechanical transduction response. In the next section we will discuss the limits on the nanocantilever dimensions imposed by the residual stresses that show up during the fabrication process of the structures.

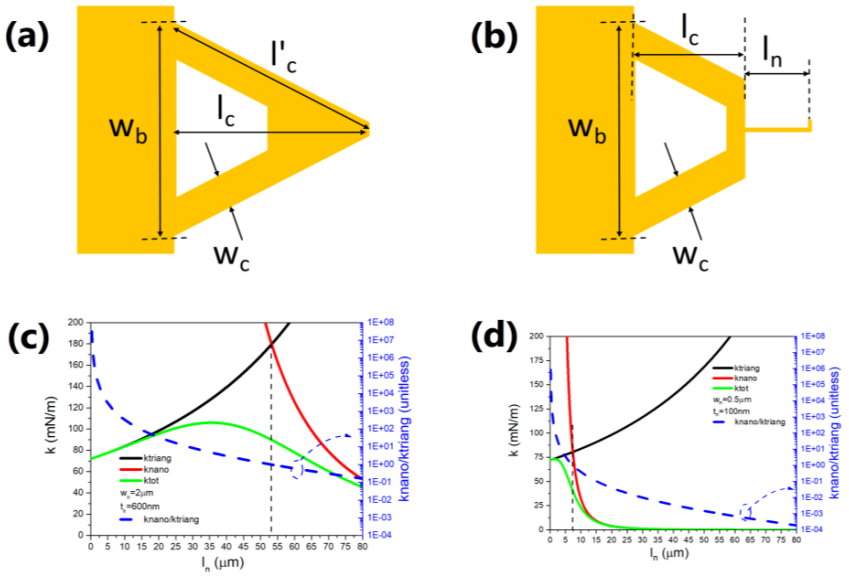

Figure 4: Sketches of a triangular microcantilever without (a) and with (b) a nanocantilever component integrated at the free end. Plots of the spring constant of the triangular mirocantilever (ktriang), of the nanocantilever (knano) and of the assembled components (ktot) as a function of the nanocantilever length, l_n, for a wide (c) and a narrow (d) nanocantilever.

4. Fabrication process

The fabrication of the NEMSTENNA structure is performed on a commercially available tipless Atomic Force Microscope (AFM) microcantilever [40], made of 600 nm thick silicon nitride (Si_3N_4) with a 70/35 (top/bottom) nm thick Cr/Au coating layer and clamped on a Pyrex substrate. The fabrication process is based on a FIB (Focused Ion Beam) nanolithography technique whose conditions are detailed in a previous paper [32]. The triangular microcantilever (Fig. 5.a) is turned upside down (Fig. 5.b) and the 70 nm Cr/Au layer is removed, while the thickness of the silicon nitride (Si_3N_4) layer is reduced (Fig. 5.c), by means of FIB milling nanolithography. This step is restricted to the region where nanocantilever and nanodipole will be structured. Then, FIB milling is used to remove completely both the Si_3N_4 layer and the underlying bottom 35 nm thick Cr/Au film, as to define one of the arms of the nanodipole, as well as the corresponding nanocantilever (Fig. 5.d). The whole process is repeated to define the second NEMSTENNA component in an identical AFM microcantilever. Finally, the two components of the NEMSTENNA are carefully faced in close proximity to achieve the overlap described in Fig. 1.b. This last step is carried out with the assistance of a xyz nanopositioner.

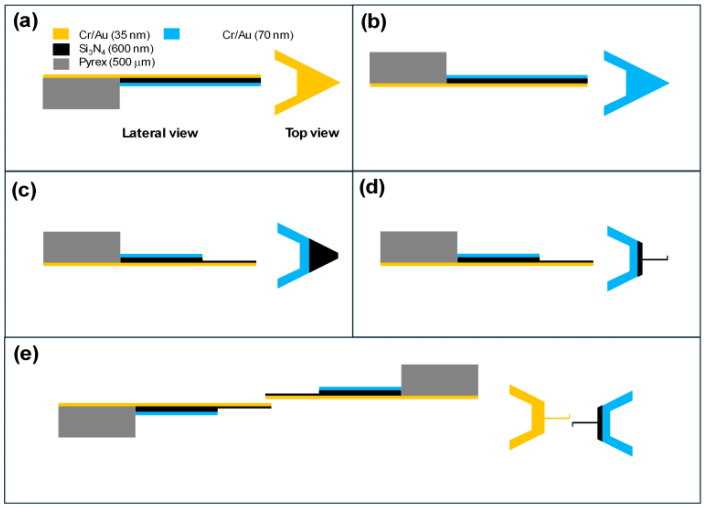

Figure 5: NEMSTENNA fabrication process: (a) Unprocessed microcantilever structure, (b) microcantilever flipping, (c) thickness reduction in the nanocantilever and nanodipole area, (d) nanocantilever and one arm nanodipole definition and (e) NEMSTENNA final build-up.

Once the FIB milling conditions have been tuned for each step of the fabrication process, the overall sequence has been set up and a first NEMSTENNA version has been successfully fabricated [32], it is foreseen that the next challenge to overcome will be found on the fabrication of the most slender nanocantilever that does not show a residual stress induced flexural collapse.

To determine the maximum feasible slenderness factor, before the structure collapse produced by the residual stress in the Si_3N_4/Au interface, a nanocantilever 68.7 μm long (close to the maximum 80 μm) and 2.2 μm wide has been fabricated by means of a fabrication sequence as the one described above (Fig. 5), but skipping the second thickness reduction step (Fig. 5.c), so that the original 600 nm thickness is not modified in the first instance. Next, the skipped vertical milling step is progressively applied, and the Si_3N_4 layer is slowly removed at a rate of approximately 50 nm/min. This etching rate allows to alternate etching and imaging to monitor and control the growing stress induced bending and stop the process before collapse. SEM images of figure 6 show that when the thickness is reduced to 100 nm, the residual stress bending is still small enough to leave the functionality of the structure unchanged. We have considered that these dimensions are of the same order and compatible with the final design dimensions (see Table II) used in the simulations described in the next sections.

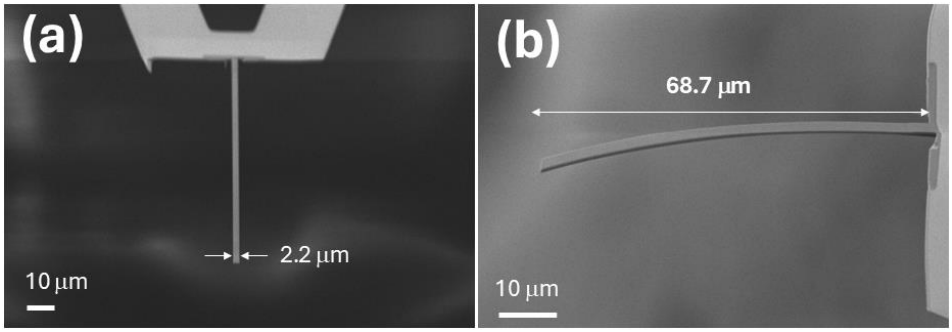

Figure 6: SEM images from top (a) and lateral (b) perspectives of a NEMSTENNA nanocantilever in the residual stress limit of slendernes s.

Table I: Optical, thermal and mechanical properties of the materials involved in COMSOL simulations.

Property	**Au**	**Si_3N_4**	**Units**
Heat capacity, C_p	129	700	J/(kg·K)
Thermal conductivity, κ	150[a], 230[b]	2.1[c], 4[d]	W/(m·K)
Convective heat transfer coeficient, h	10^6	$4 \cdot 10^6$	W/(m^2·K)
Thermal Boundary Resistance, TBR	$0.81 \cdot 10^{-8}$	$0.81 \cdot 10^{-8}$	m^2·K/W
Surface emissivity, ϵ	0.05	0.5	
Density, ρ	19280	3100	kg/m^3
Refractive index, n	0.52406	1.9963	
Extinction coeficient, k	10.742	0	
Electrical conductivity, σ	$45 \cdot 10^6$	0	S/m
CTE, α	$14.1 \cdot 10^{-6}$	$2.3 \cdot 10^{-6}$	K^{-1}
Young's modulus, E	80	250	GPa
Poisson's ratio, ν	0.44	0.23	

[a] Au thickness=35 nm

[b] Au thickness=70 nm

[c] Si_3N_4 thickness=140 nm

[d] Si_3N_4 thickness=600 nm

Table II: Dimensions of the optimal NEMSTENNA design.

Parameter	Value	Units
Dipole length, L_1=L_2	1360	nm
Dipole width, W_1	80	nm
Dipole-Nanocantilever connection width, W_2	100	nm
Dipole gold thickness, $t_{Au,d}$	35	nm
Dipole silicon nitride thickness, $t_{Si3N4,d}$	140	nm
Microcantilever length, l_c	200	µm
Microcantilever width, w_c	28	µm
Microcantilever base width, w_b	184	µm
Microcantilever silicon nitride thickness, $t_{Si3N4,mc}$	600	nm
Microcantilever gold thickness, $t_{Au,mc}$	70	nm
Capacitive gap, g_0	10	nm
Nanocantilever length, l_n	83	µm
Nanocantilever width, w_n	1	µm
Nanocantilever silicon nitride thickness, t_n	140	nm
Nanocantilever gold thickness, $t_{Au,n}$	35	nm
Overlapping Area, $A_{overlap}$= $W_1 \cdot W_2$	800	nm^2

5. Results and discussion

5.1. Coupling EM, electrostatics and mechanics

In a first set of COMSOL simulations, results of the opto-electromechanical response, z_{OEM}, have been obtained by coupling EM, solid mechanics and electrostatics physics on the NEMSTENNA structure designed in section 3.2 (Table II). The calculation procedure described in section 3.1 has been applied, but following two slightly different approaches. In a simple and faster computational approach, the actuation voltage, V_{gap}, is kept constant during the gap closing transient produced by the mutual attraction of the nanodipole arms (Fig. 2.c). As is shown in figure 7, this approximates what is really happening since V_{gap} is decreasing as the gap, g, is reduced. Thus, in a more complex iterative procedure V_{gap} is recalculated in an EM simulation, each time the free end of the micro-nanocantilevers, z_{OEM}, and the corresponding gap distance, g, reach a new stationary position as calculated in the previous electrostatic and mechanical simulation step. A comparative analysis performed previously between both procedures [39] concluded that the error grows with the laser power, involving an overestimation of the non-iterative with respect to the iterative method below 30%, when illumination power is maximum (7.5 mW). To relax the computational load, we have used the non-iterative method.

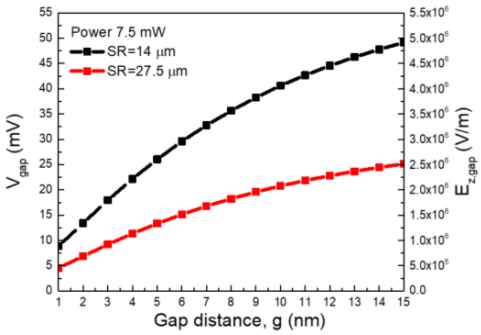

Figure 7: Voltage, V_{gap}, and z-direction electric field, $E_{z,gap}$, in the feed gap as a function of the gap distance, g.

To understand the complex opto-electromechanical stationary state, z_{OEM}, dependence on the initial gap distance, g_0, we have performed non-iterative calculations of z_{OEM}, for different g_0 and SR values. Indeed, as figure 7 shows, when the initial separation of the NEMSTENNA's components, i.e. the initial gap distance (g_0), is decreased, the voltage in the gap, V_{gap}, is also decreased and this would be translated to a decrease in the electrostatic force, if it weren't for the fact that the force also depends inversely

on g_0^2 (equations 3 to 5). The result of this analysis is shown in figure 8.a. The effect of the initial gap, g_0, decrease on the electrostatic force is more important than the decrease of V_{gap} and, consequently, the force is increased as the initial gap is decreased. When the initial gap is reduced to 2 μm, the electrostatic force is intense enough to collapse the structure. This analysis has been repeated for the medium (14 μm) and the smallest (8 μm) SR values. In those cases (Fig. 8.b), collapse is produced when each micro-nanocantilever is displaced half the gap distance: $g_0/2$=2.5 μm and $g_0/2$=5 μm respectively.

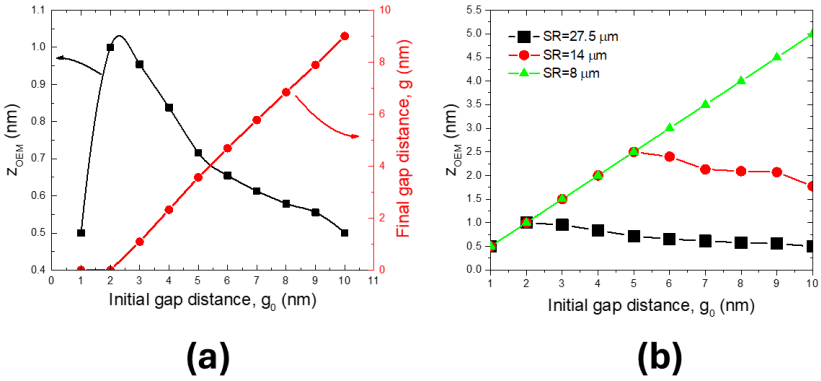

Figure 8: (a) OEM response, z_{OEM}, (left axis) and the corresponding final gap distance ($g=g_0-2\cdot z_{OEM}$) (rigth axis) as a function of the initial gap separation, g_0. (b) OEM response, z_{OEM}, as a function of the initial gap separation, g_0, for different laser spot radius (SR). All calculations have been performed non-iteratively at 7.5 mW of laser power.

Finally, in figure 9 the maximum OEM displacements and the corresponding initial gap distances, g_0, obtained from figure 8.b are represented as a function of the spot radius, showing that when SR is reduced, then power density is increased, voltage in the gap and electrostatic force are both consequently increased and OEM displacement is increased.

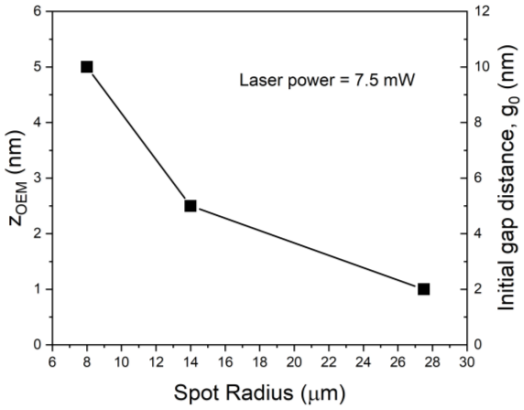

Figure 9: Maximum OEM response, z_{OEM} (left axis), and the corresponding initial gap distance, g_0 (right axis), as a function of spot radius, SR. Laser power is 7.5 mW in all cases.

5.2. Coupling EM, thermal and mechanics

In a second set of COMSOL simulations, the opto-thermomechanical response, z_{OTM}, considered here as a screening parasitic effect for the desired OEM response, has been obtained by coupling EM, thermal and solid mechanics physics on the NEMSTENNA design (Table II) in the way described in section 3.1. It is worth saying that all thermal parameters values summarized in Table I except h_{Au}, correspond to the same values used in a previous paper [35], since we use the same commercial cantilever in both works. The exception is because in the previous paper, air convective dissipation is mainly produced in the Au surface of the triangular microcantilever (10 μm scale range) whereas that in the present work convection area corresponds mainly to that of the nanocantilever component (100 nm scale range). So, we have extrapolated the $h_{Au}=10^6$ W/m^2·K value from $h_{Au}=3.8\cdot10^5$ W/m^2·K used in [35], considering an increase of one order of magnitude in h per each two orders of magnitude of reduction in the scale range, as reported in [41]. Besides, nanocantilever dimensions and simulation conditions have been modified (see figure 10 caption) with respect to the previous section to avoid OTM overresponses. The results of the OTM simulations are

shown in figure 10. As it was found previously [39], the opto-thermomechanical response decreases as the SR is reduced, because the nanocantilever area exposed to the IR heating radiation is decreased and, additionally, this area is more and more localized close to the free end of the structure, where stress based transduction of the bimetallic effect becomes less efficient. However, this trend is reversed when SR is reduced to below 5 μm and OTM response starts to grow because in this regime the increase of temperature produced by the increase of power density would prevail over the previously described area reduction effect.

5.3. Comparison between OEM and OTM responses

To compare the opto-electromechanical signal, z_{OEM}, and the opto-thermomechanical parasitic response, z_{OTM}, new values of the OEM response adapted to the new conditions used in OTM simulations (see figure 10 caption) have been calculated. Then, a figure of merit defined as FoM= z_{OEM}/z_{OTM}, is used to analyze how OEM compares to OTM and how this figure of merit is improved when SR is changed. Figure 10 shows the dependence of the as defined FoM on the SR. As expected, for large SR values (above 4 μm) the ratio z_{OEM}/z_{OTM} grows as the SR decreases because the opto-electromechanical signal grows and the opto-thermomechanical parasitic response decreases simultaneously. Below SR=4 μm the FoM decreases as SR decreases because OTM starts to increase faster than OEM grows. Thus, the maximum FoM=0.04 is reached for SR=4 μm, which is one order of magnitude worse than the FoM=0.2 found in our previous NEMSTENNA design [39].

To compare the performance of our NEMSTENNA transducer with the state-of-the-art of similar optomechanical transducers we have calculated the responsivity in terms of the ratio between mechanical response and input optical power, i.e. $R_1= z_{OEM}/P_{laser}$, and alternatively relative to the irradiance (optical power density), i.e. $R_2= z_{OEM}/(P_{laser}/SA)$, being $SA= \pi \cdot SR^2$ the spot laser area. The results of this analysis summarized in Table III show that the NEMSTENNA design presented here improves in terms of responsivity the two previous designs [39], [32]. Besides, when comparing our device to detectors with the same transduction principle it equals their performance [30] or it overpasses in almost two orders of magnitude [17]. On the other hand, when comparing to optothermal THz detectors based on large area microcantilevers, irradiance-based responsivity, R_2, has to be used and values, R_2=815 nm/(mW/μm^2) [27], almost one order of magnitude above this work's values, R_2=815 nm/(mW/μm^2), are found [27]. Responsivity enhancements of several orders of magnitude with respect to the present work have been recently demonstrated in optothermal THz detectors based on resonant optomechanical structures [42], [43], due to the amplifying effect on the responsivity of their high quality factor.

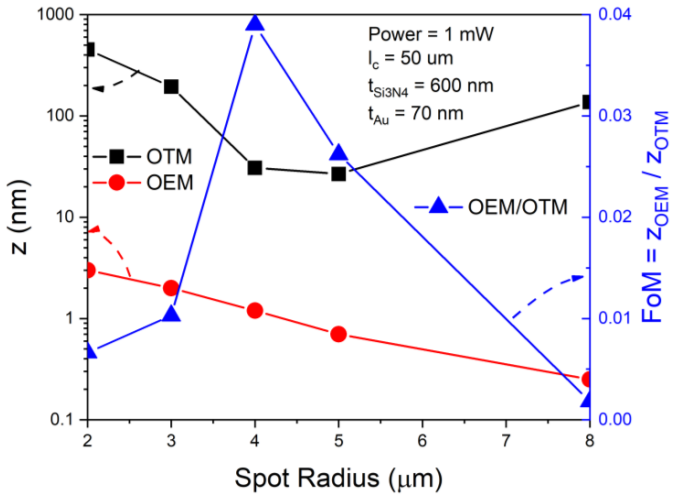

Figure 10: OTM and OEM responses (left axis) together with FoM=z_{OEM}/z_{OTM} (right axis), as a function of spot radius, SR. Nanocantilever dimensions are: l_n=50 μm, t_n=600 nm, $t_{Au,n}$=70 nm; and laser power is 1 mW in all cases.

Table III: Responsivity values of some of the state-of-the-art optomechanical transducers.

R_1 ($=z_{OEM}/P_{laser}$)	Units	R_2 ($=z_{OEM}/(P_{laser}/SA)$)	Units	Frequency	Wavelength	Reference
0.67	nm/mW	134	nm/(mW/μm^2)	193.55 THz	1.55 μm	This work
$6.7\cdot10^{-3}$	nm/mW			193.55 THz	1.55 μm	[39]
10^{-3}	nm/mW			193.55 THz	1.55 μm	[32]
0.49	nm/mW			2.6 THz	115 μm	[30]
$24.8\cdot10^{6}$	nm/mW	815	nm/(mW/μm^2)	3.24-3.98 THz	92.6-75.4 μm	[24]
		1.34	nm/(mW/μm^2)	273-600 THz	1.1-0.5 μm	[17]
$3\cdot10^{4}$	nm/mW			2.5 THz	120 μm	[42]
$1.5\cdot10^{2}$	nm/mW			2.5 THz	120 μm	[43]

6. Conclusions

A new optomechanical actuator design, which combines a plasmonic optical nanodipole antenna with two capacitively coupled micro-nanocantilevers, has been presented. The device converts efficiently the optical power of an infrared radiation at 1.55 μm absorbed in the nanoantenna into the static mechanical deflection of the micro-nanocantilevers. The maximum nanocantilever slenderness achievable before the residual stress induced collapse has been empirically determined through the fabrication of test structures by means of Focused Ion Beam nanolithography. In the design and analysis process, COMSOL Multiphysics has been used to optimize the antenna dimensions at the 1.55 μm target wavelength, to predict the opto-electromechanical transduction (OEM) and to evaluate the parasitic opto-thermomechanical response (OTM) as well. Although the performance of the actuator evaluated in terms of the OEM/OTM ratio does not improve compared to our previous designs, the achieved responsivity values of 0.67 nm/mW are in the same order of magnitude of the state-of-the-art detectors of EM radiation based on the same opto-electromechanical transduction principle.

Declaration of Competing Interest

The authors declare that they have no known competing financial interest or personal relationships that could have appeared to influence the work reported in this paper.

Data availability

Data will be made available on request.

Acknowledgements

This work was funded by Spain's Ministerio de Ciencia e Innovación under Grant No. PID2021-127840NB-I00 (MICINN/AEI/FEDER, UE).

References

[1] Nichols, E. F., and Hull, G.F. "The application of radiation pressure to cometary theory." *Astrophysical Journal, vol. 17, p. 352* 17 (1903): 352.

[2] Ashkin, A. "History of optical trapping and manipulation of small-neutral particle, atoms, and molecules." *IEEE Journal of Selected Topics in Quantum Electronics* 6.6 (2000): 841-856.

[3] McGloin, D. "Optical tweezers: 20 years on." *Philosophical transactions of the royal society A: mathematical, physical and engineering sciences* 364.1849 (2006): 3521-3537.

[4] Ashkin, A. "Acceleration and trapping of particles by radiation pressure." *Physical review letters* 24.4 (1970): 156.

[5] Ashkin, A. "Trapping of atoms by resonance radiation pressure." *Physical Review Letters* 40.12 (1978): 729.

[6] Chu, S, et al. "Experimental observation of optically trapped atoms." *Physical review letters* 57.3 (1986): 314.

[7] Höschele, J., Buob, S., Rubio-Abadal, A., Makhalov, V., & Tarruell, L. (2023). Atom-number enhancement by shielding atoms from losses in strontium magneto-optical traps. *Physical Review Applied*, *19*(6), 064011.

[8] Ketterle, W. "Nobel lecture: When atoms behave as waves: Bose-Einstein condensation and the atom laser." *Reviews of Modern Physics* 74.4 (2002): 1131.

[9] Torres, J.M., Betzholz, R., and Bienert, M. "Optomechanical damping basis." *Journal of Physics A: Mathematical and Theoretical* 52.8 (2019): 08LT02.

[10] Krause, A.G., et al. "Nonlinear radiation pressure dynamics in an optomechanical crystal." *Physical Review Letters* 115.23 (2015): 233601.

[11] Mahboob, I., et al. "Phonon lasing in an electromechanical resonator." *Physical review letters* 110.12 (2013): 127202.

[12] Qiu, L., et al. "Laser cooling of a nanomechanical oscillator to its zero-point energy." *Physical review letters* 124.17 (2020): 173601.

[13] Metzger, C.H., and Karrai, K. "Cavity cooling of a microlever." *Nature* 432.7020 (2004): 1002-1005.

[14] Koya, A. N., Cunha, J., Guerrero-Becerra, K.A., Garoli, D., Wang, T., Juodkazis, S., & Proietti Zaccaria, R. (2021). Plasmomechanical systems: principles and applications. *Advanced Functional Materials*, *31*(41), 2103706.

[15] Alda, J., et al. "Optical antennas for nano-photonic applications." *Nanotechnology* 16.5 (2005): S230.

[16] Raziman, T.V., Wolke, R.J., and Martin, O.J.F. "Optical forces in nanoplasmonic systems: how do they work, what can they be useful for?." *Faraday discussions* 178 (2015): 421-434.

[17] Buch, Z., & Schmid, S. (2022). "Design considerations of gold nanoantenna dimers for plasmomechanical transduction". *Optics Express*, *30*(4), 5294-5303.

[18] Thijssen, R., et al. "Parallel transduction of nanomechanical motion using plasmonic resonators." *ACS photonics* 1.11 (2014): 1181-1188.

[19] Thijssen, R., et al. "Plasmomechanical resonators based on dimer nanoantennas." *Nano letters* 15.6 (2015): 3971-3976.

[20] Tanaka, Y.Y., Albella, P., Rahmani, M., Giannini, V., Maier, S.A., and Shimura, T. "Plasmonic linear nanomotor using lateral optical forces," Sci. Adv. **6**(45), eabc3726 (2020).

[21] Roy, T., et al. "Dynamic metasurface lens based on MEMS technology." *Apl Photonics* 3.2 (2018).

[22] Arbabi, E., et al. "MEMS-tunable dielectric metasurface lens." *Nature communications* 9.1 (2018): 812.

[23] Agustí, J., Cuadrado, A., Martínez-Antón, J.C., Alda, J., Abadal, G. "An analytical model for the opto-thermo-mechanical conversion mechanisms in a MOEMS-based energy harvester" in Nanoengineering: Fabrication, Properties, Optics, and Devices IX, Proceedings of SPIE Vol. 8463 (SPIE, Bellingham, WA, 2012).

[24] Zhu, H., Yi, F., and Cubukcu, E. "Plasmonic metamaterial absorber for broadband manipulation of mechanical resonances." *Nature Photonics* 10.11 (2016): 709-714.

[25] Rutger, T., et al. "Plasmon nanomechanical coupling for nanoscale transduction." *Nano letters* 13.7 (2013): 3293-3297.

[26] Li, Chao, Ya Zhang, and Kazuhiko Hirakawa. "Terahertz detectors using microelectromechanical system resonators." *Sensors* 23.13 (2023): 5938.

[27] Zhu, H., et al. "A terahertz optomechanical detector based on metasurface and Bi-material micro-cantilevers." *Micromachines* 13.5 (2022): 805.

[28] Yi, F., et al. "Plasmonically enhanced thermomechanical detection of infrared radiation." *Nano letters* 13.4 (2013): 1638-1643.

[29] Jeon, J., et al. "Visible to near-infrared single pixel microspectrometer using electrothermal MEMS grating." *Optics Express* 31.9 (2023): 14583-14592.

[30] Belacel, C., et al. "Optomechanical terahertz detection with single meta-atom resonator." *Nature communications* 8.1 (2017): 1578.

[31] Ruiz, R., Bonache, J., and Abadal, G. "A flexible dipole antenna for direct transduction of microwave radiated power into DC mechanical deflection." *Sensors and Actuators A: Physical* 340 (2022): 113536.

[32] Khosh Maram, D., et al. "Design and fabrication of an opto-mechanical antenna in the NIR range." *Micro and Nano Engineering* 23 (2024): 100241.

[33] Ruiz, R., and Abadal, G.. "Remote dynamic actuation of an electrostatically driven microcantilever by a wireless power transfer system." *Sensors and Actuators A: Physical* 345 (2022): 113798.

[34] Ruiz, R., and Abadal, G. "Direct transduction from radiofrequency radiated power to static and dynamic flexural mechanical modes." *2021 21st International Conference on Solid-State Sensors, Actuators and Microsystems (Transducers)*. IEEE, 2021.

[35] Khosh Maram, D., Cartoixà, X., and Abadal, G. (2024, October). "Analysis of the Photothermal Parasitic Effect on an Optomechanical Antenna". In *2024 IEEE SENSORS* (pp. 1-4). IEEE.

[36] P. B. Johnson & R. W. Christy, (1972) "Optical constants of the noble metals," Physical Review B, vol. 6, no. 12, pp. 4370–4379.

[37] K. Luke, Y. Okawachi, M. R. E. Lamont, A. L. Gaeta & M. Lipson, (2015) "Broadband mid-infrared frequency comb generation in a Si_3N_4 microresonator," Optics Letters, vol. 40, no. 21, pp. 4823–4826.

[38] Polyanskiy, M.N., Refractive index database, (n.d.), https://refractiveindex.info.

[39] Khosh Maram, D., Garcia-Garcia, J., Cartoixà, X., and Abadal, G. (2025). "Impact of the parasitic photothermal effect on the performance of an optomechanical nanoantenna for NIR radiation detection". *Sensors and Actuators A: Physical*, 116966.

[40] https://www.nanoandmore.com/AFM-Probe-PNP-TR-TL-Au, (n.d.).

[41] Peirs, J., Reynaerts, D., and Van Brussel, H. (1998, May). Scale effects and thermal considerations for micro-actuators. In Proceedings. 1998 IEEE International Conference on Robotics and Automation (Cat. No. 98CH36146) (Vol. 2, pp. 1516-1521). IEEE.

[42] Liu, J., Chomet, B., Beoletto, P., Gacemi, D., Pantzas, K., Beaudoin, G., Sagnes, I., Vasanelli, A., Sirtori, C. and Todorov, Y. (2022). "Ultrafast detection of terahertz radiation with miniaturized optomechanical resonator driven by dielectric driving force". ACS photonics, 9(5), 1541-1546.

[43] Froberger, K., Walter, B., Lavancier, M., Peretti, R., Ducournau, G., Lampin, J. F., ... & Barbieri, S. (2022). SOI-based micro-mechanical terahertz detector operating at room-temperature and atmospheric pressure. Applied Physics Letters, 120(26).

B.3 Tuning fork optomechanical NIR antenna with integrated optical transmission line

Journal paper (Paper 4), submitted to Sensors and Actuators: A. Physical.

Tuning fork optomechanical NIR antenna with integrated optical transmission line

Daniyal Khosh Maram[a,*], Xavier Borrisé[b], Joan Garcia-Garcia[a], Guy A.E. Vandenbosch [c], Xavier Cartoixà[a], Gabriel Abadal[a]

[a] *Dept. Enginyeria Electrònica, Campus UAB, 08193-Bellaterra, Spain,*
[b] *Catalan Institute of Nanoscience and Nanotechnology (ICN2) and Barcelona Institute of Science and Technology (BIST), Barcelona, Spain*
[c] *Department of Electrical Engineering, ESAT-WaveCoRE Research Division, KU Leuven, Leuven, Belgium*

* *Corresponding author.*
E-mail address: daniyal.khoshmaram@uab.cat

Abstract

We present a novel optomechanical antenna that directly converts near-infrared (λ=1.55 μm) light into mechanical motion using a tuning fork architecture with an integrated optical transmission line (OTL). The device consists of two parallel nanocantilever arms, made of gold-coated silicon nitride, forming a lateral tuning fork, with a plasmonic nanodipole antenna at the free end. Upon focused NIR laser illumination, the nanodipole's feed gap concentrates the optical field and induces an oscillating voltage across the gap. This produces a strong DC electrostatic attraction between the tuning fork arms, causing an in-plane deflection. The integrated coplanar optical transmission line significantly enhances the antenna's performance by improving impedance matching, leading to nearly an order-of-magnitude higher gap voltage compared to designs without OTL. We fabricated a test structure of the proposed device via focused ion beam nanomilling to validate the fabrication process, achieving a ~65 nm gap, and verified the static mechanical response using COMSOL multiphysics simulations. An optimized design exhibits a lateral displacement up to 13.5 nm at 7.5 mW optical power, which corresponds to a responsivity of 1.8 nm/mW at 1.55 μm, outperforming previous NIR optomechanical transducers.

Keywords: Mechanical antenna; NIR nanoantenna; plasmonic nanoantenna; optomechanical transduction; MEMS/NEMS resonators

1. Introduction

Nanophotonics and nanomechanics are rapidly advancing fields, with a key goal being the conversion of light into mechanical motion at extremely small scales. At optical frequencies, plasmonic nanoantennas have become essential elements because they can capture incoming light and concentrate its electromagnetic energy into nanoscale regions, creating intensely localized fields. This ability to focus light into sub-wavelength hotspots makes plasmonic nanoantennas highly useful for applications such as molecular sensing, surface-enhanced spectroscopy, energy harvesting, and infrared detection [1][2][3][4]. Numerous studies and reviews have highlighted how plasmonic resonances in nanoantennas enable fine control of light at visible and infrared wavelengths [2][3][5].

Beyond passive nanoantennas, researchers have explored active nanoantenna systems by coupling optical antennas with micro/nanomechanical elements. For example, Chen et al. demonstrated an electromechanically tunable suspended optical nanoantenna whose resonance and field enhancement could be adjusted by applying a voltage, effectively changing its geometry in situ [6]. Other groups have shown that plasmonic nanoantennas can even be driven electrically, for instance, by feeding current or bias to stimulate light emission at optical frequencies [7][8][9]. These efforts illustrate the potential of combining plasmonic nanostructures with mechanical or electrical actuation to achieve tunable or reconfigurable optical behavior.

More recently, attention has turned to optomechanical nanoantennas based on the combination of optical antennas and NEMS structures, which use light itself to induce mechanical motion in a nanoscale device. This transduction mechanism offers not only an unprecedent way to implement a nanoactuator controlled by light, but also provides advantages of NEMS such as their high responsivity and sensitivity, when applied to the detection of optical radiation.

Thus, for instance, a near-infrared optomechanical antenna was recently reported at telecom wavelengths (λ=1.55 μm), demonstrating that incident NIR light can be directly converted into mechanical deflection [10][11]. In that pioneering work, a

plasmonic nanoantenna was used to enhance the optical field and generate a force on a tiny cantilever, confirming the feasibility of light-to-motion transduction at optical frequencies. However, those early optomechanical antenna designs had significant limitations: they required very precise alignment of separate cantilever components and relied on out-of-plane (vertical) bending, which produced only small mechanical displacements. Moreover, the photothermal response of metal–dielectric bilayers often interfered with the mechanical signal because both occurred along the same axis [10][11][12].

In this work, we introduce a new approach to optomechanical antennas that overcomes these challenges by using a tuning-fork architecture with an integrated optical transmission line (OTL). The tuning-fork optomechanical antenna with integrated OTL offers several key advantages over earlier designs [10][11][13]. First, the actuation is lateral (in-plane) rather than vertical, allowing larger mechanical displacements and eliminating crosstalk with thermally induced bending. The desired mechanical signal (in-plane deflection) is orthogonal to any photothermal deformation (out-of-plane), making the response inherently thermally decoupled. Second, integrating a coplanar OTL with the nanoantenna improves impedance matching and guides optical-frequency currents along the structure, producing a much higher gap voltage—up to an order of magnitude larger than that of an isolated antenna. Third, the monolithic tuning-fork structure simplifies fabrication, increases reproducibility, and ensures symmetrical operation.

In the following sections, we describe the device design, fabrication process, and Multiphysics simulation of its optomechanical response. We then compare the results to previous optomechanical and optothermal transducers.

2. Optomechanical antenna structure

The proposed device is a tuning fork–based optomechanical antenna with an integrated optical transmission line (OTL). It is designed to convert near-infrared (NIR) light into mechanical motion. As described in Figure 1, the structure is built on a Si_3N_4 flange (600 nm thick) coated by a thin Au layer (70 nm) that stands out from a Pyrex substrate. Two nanocantilevers placed in parallel make up the in-plane (x-y) tuning fork, which is clamped in the Pyrex substrate. At the free end of the tuning fork, the device has a nanodipole antenna made of the Au layer on top of Si_3N_4. Both arms of the nanodipole, with length L and width W, are separated by a feed gap (g_0), which will be the active region where the NIR induced electric field becomes strongly enhanced. The nanodipole is directly connected to a coplanar OTL with a width W_{OTL} and a length L_{OTL}. The OTL runs along the cantilevered arms of the tuning fork and transmits the induced optical electromagnetic fields from the nanodipole toward the Pyrex support of the structure. Both OTL Au lines are mutually disconnected at the mechanical anchor point ($y=L_{OTL}$), so the electrical termination corresponds to an open circuit.

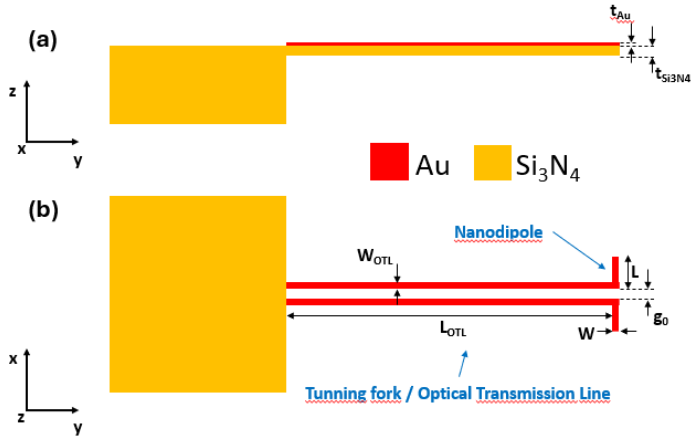

Figure 1: Lateral (a) and top (b) views of the tuning fork optomechanical antenna.

3. Transduction principle

As schematically described in figure 2, when a NIR laser beam (λ=1.55 μm) is focused on the nanodipole antenna, an electric field enhanced with respect to the laser background is strongly confined in its feed gap. In particular, the enhanced electric field in the x-direction creates an optical voltage across the gap, V_{gap}, that oscillates at the NIR frequency.

$$V_{gap}(t) = |V_{gap}| \cdot cos(2\pi f_{NIR} t) \tag{1}$$

The x-direction electric field and the corresponding voltage are both propagated along the OTL and tuning fork structure. This voltage distribution produces a similarly distributed attractive electrostatic force, F_{ee}, between the metallic arms of the tuning fork, which mainly acts at the free end of the structure, since the voltage at this point (y=0) is maximum and decays along the y-direction. The electrostatic force depends on the square of the induced voltage ($F_{ee} \propto V^2$) and the transduction capacitance gradient as follows:

$$F_{ee} = \frac{1}{2}\frac{\partial C_{gap}}{\partial x}\left(V_{gap}(t)\right)^2 + \frac{1}{2}C_{gap}\frac{\partial (V_{gap}(t)^2)}{\partial x} = F_{ee,DC} + F_{ee,ac}(t) \tag{2}$$

where the electrostatic transduction capacitance, C_{gap}, depends on the transduction area, A, and the gap dependent on bending of the tuning fork arms, δx:

$$C_{gap} = \frac{\epsilon_0 A}{g_0 - 2\delta x} \tag{3}$$

As a result of the quadratic dependence of the electrostatic force on the voltage, two components arise when equation (1) is introduced on equation (2) (as indicated in the right term of equation (2)): a DC component, $F_{ee,DC}$, and an oscillating component, $F_{ee,ac}(t)$, at twice the optical frequency. The DC component is associated to a steady attractive force, equation (4), that pulls the arms of the tuning fork toward each other, producing a lateral displacement, δx. If the tuning fork geometry is symmetric, both arms will move in a balanced way. The ac component, equation (5), does not produce any significant mechanical response, since its frequency, $2f_{NIR}$ = 386.82 THz, is many orders of magnitude higher than the natural resonance frequency of the mechanical structure, which lies in the kHz range.

$$F_{ee,DC} = \frac{1}{4}\frac{\partial C_{gap}}{\partial x}|V_{gap}|^2 + \frac{1}{4}C_{gap}\frac{\partial (|V_{gap}|^2)}{\partial x} = \frac{1}{4}\frac{\epsilon_0 A}{(g_0 - 2\delta x)^2}|V_{gap}|^2 + \frac{1}{4}\frac{\epsilon_0 A}{g_0 - 2\delta x}\frac{\partial (|V_{gap}|^2)}{\partial x} \tag{4}$$

$$F_{ee,ac} = \frac{1}{4}\left[\frac{\partial C_{gap}}{\partial x}|V_{gap}|^2 + C_{gap}\frac{\partial (|V_{gap}|^2)}{\partial x}\right] \cdot cos(4\pi f_{NIR} t) \tag{5}$$

Note that the gradient of V_{gap} term, $\partial V_{gap}/\partial x$, (second term in equations (4) and (5), and in left side of equation (3)), which is cancelled in standard electrostatic MEMS transducers where the applied voltage does not change with displacement ($\partial V_{gap}/\partial x = 0$), is present in our transducer as shown in figure 7.

This working principle allows the optomechanical antenna to act as a remote, optically driven actuator, without needing any local power source. The integrated optical transmission line (OTL) not only carries the induced voltage along the cantilever arms but also increases the attractive force. This improves the efficiency of the light-to-motion conversion mechanism.

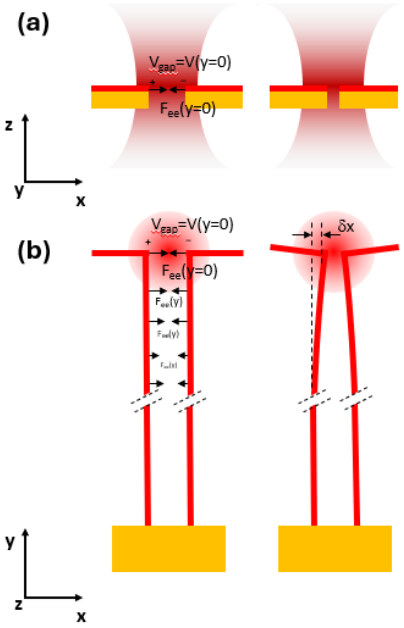

Figure 2: Lateral (a) and top (b) views for the transduction principle description. When both components of the tuning fork optomechanical antenna are illuminated by a focused IR laser beam, the electrostatic force along the OTL, $F_{ee}(y)$, induced by the voltage in the gap of the structure, V(y), produces a static bending, δx, in the on-plane direction.

4. Fabrication process

The nanoscale features of the tuning fork were fabricated on a commercially available suspended Au on Si_3N_4 structure (figure 1), using a six-step nano-milling process based on Focused Ion Beam (FIB) lithography, as illustrated in Fig. 3. In a first step (Fig. 3(a)), the optical transmission line (OTL) gap was first opened by etching a trench 150–200 nm wide at 50 pA and 30 kV. After that, and using the same beam current and voltage, material was removed from the nanoantenna region to prepare the final feed gap cut (Fig. 3(b)). The nanocantilevers of the OTL/tuning fork structure were then defined in two stages (Fig. 3(c)): an initial etching step at 300 pA followed by polishing at 50 pA to improve edge quality. In the next step (Fig. 3(d)) magnification was increased above 1000 X and the beam current was reduced to 2 pA to achieve higher resolution in the definition of the nanodipole feed gap. A final etching step at 50 pA (Fig. 3(e)-Fig. 3(f)) was used to fine-tune the nanodipole antenna length (L) and width (W).

Scanning electron microscopy (SEM) images (Fig. 4) confirm the successful fabrication of well-defined nanoscale gaps and precise antenna dimensions. In the fabrication demonstrator of the figure, the nanodipole feed gap was reduced to ~65 nm, while the antenna arms and cantilever structures maintained uniform geometry with lengths and widths in the 200–400 nm range. These results demonstrate that FIB lithography enables controlled, reproducible fabrication with high structural integrity, validating this method as a reliable strategy for the definition of the nanoscale antenna and of the overall optomechanical structure.

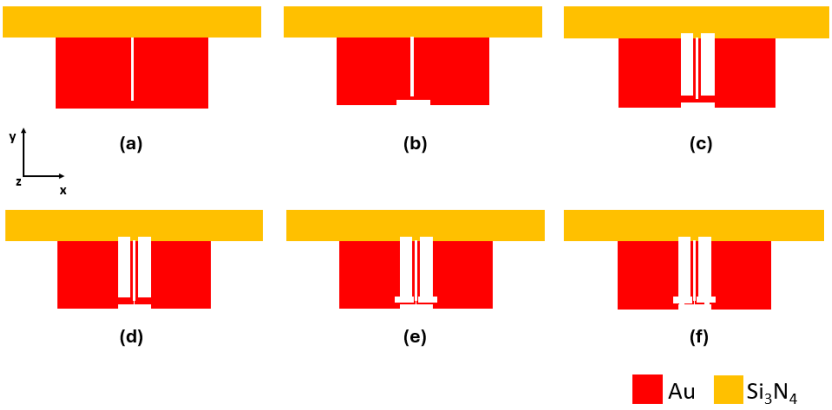

Figure 3: FIB nano-milling fabrication steps of a tuning fork optomechanical antenna.

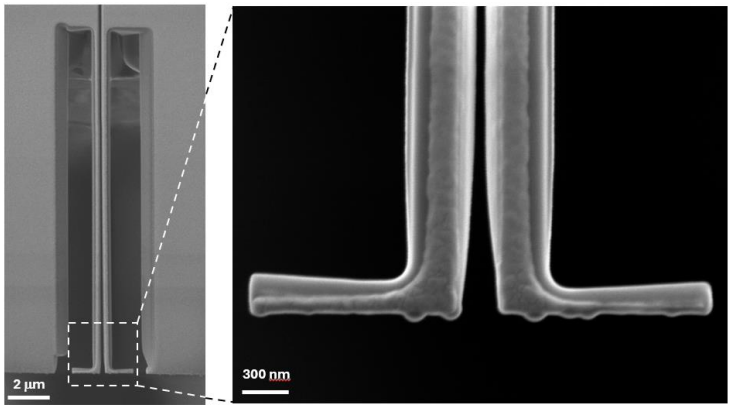

Figure 4: SEM images of a tuning fork optomechanical antenna fabricated by means of the as defined FIB nano-milling process.

5. Modelization

5.1. Multiphysics model

In a first step, the electromagnetic behavior of the tuning fork optomechanical device has been modelled using the RF module of COMSOL Multiphysics. The RF simulation environment is defined by a spherical simulation box that encloses both the nanodipole antenna and its optical transmission line (OTL). A Gaussian laser beam has been used as an excitation source. Its beam waist, in terms of spot radius (SR) of 8 µm, and a 1mW optical power, are defined as the main parameter characteristics of the beam. The paraxial approximation is used to describe the electromagnetic wave propagation. A Perfectly Matched Layer (PML) is defined as the boundary condition in the outer layer of the spherical simulation box to suppress back-reflections. A mesh size of $\lambda/5$ is selected to optimize the finite element calculations. Apart from values of refractive index, n, and extinction coefficient, κ, at λ=1.55 µm reported in Table I, one of the most critical parameter sets to reproduce plasmonic phenomena in our EM simulations are $n(\lambda)$ and $\kappa(\lambda)$ pairs, which were extracted from data by Johnson and Christy for Au, and by Luke et al. for Si_3N_4 [14][15]. The main simulation outputs of this first module are the x-direction electric field distribution along the OTL inside its gap, $E_x(y)$, and the corresponding voltage V(y), which is computed by integrating the x-component of the electric field along the gap length [11]. The voltage V_{gap}, i.e. the voltage V at y=0 (at the nanodipole antenna gap) will be the maximum value of V(y) since, as explained in the transduction principle section, it will decay along the OTL length. For this reason, it will serve as a maximization variable in the device design process.

In a second step, the mechanical arms deflection of the tuning fork optomechanical device in its steady-state response has been also calculated. For this to be done, the output of the previous RF simulation, V(y), is then used as a link variable to couple the RF module with the solid mechanics module, through electrostatics as one of its build-in transduction mechanisms. At this point,

the tuning fork/OTL structure is divided into 5 sections along its length to assign a constant voltage value obtained from V(y) distribution to each section. This 5-value discretization of V(y) and its corresponding electrostatic force values allows us to simplify the V(y) calculation, which is made manually.

In the simplified and computationally faster method that has been adopted in this work, the actuation voltage, V(y), is kept constant during the gap-closing transient caused by the mutual electrostatic attraction of the nanodipole arms. As mentioned in reference [10], this simplification approximates the physical behavior, although V(y) naturally decreases as the gap reduces [11][10]. In contrast, in a more complex iterative method disesteemed here for simplicity, V(y) is recalculated through a new EM simulation at the end of each mechanical simulation step. This is, each time the free end displacement of the tuning fork arms, and thus the corresponding gap, reaches a new stationary value.

The most relevant parameter values used in our solid mechanics simulations are also found in Table I. The obtained static mechanical deflection, resulting from the interaction of the optical beam and the tuning fork optomechanical device, will be referred to as the opto-electromechanical (OEM) response [11][10]. In all simulations, a dynamic approach was taken, utilizing a moving mesh within the simulation box that housed the tuning fork optomechanical device in an air environment, which prevented non-convergence issues.

6. Results and discussion

6.1. Design of the tuning fork optomechanical transducer

A first approach to the design of the full tuning fork optomechanical device consisted in the determination of the nanodipole antenna dimensions. This has been done by calculating V_{gap} resulting from a 1.55 μm laser illumination, as a function of the nanoantenna arm's length, L, assuming that this is the dimension that has the strongest impact on the antenna frequency response, compared to the rest of geometry parameters, which are kept constant. The results of this preliminary study are shown in figure 5, where the effect in the gap voltage of the OTL is highlighted. Indeed, V_{gap} maxima are produced at slightly different dipole lengths, depending on whether the OTL is present or absent, except for the last peak, produced around L=2.5 μm. But, most notably, almost one order of magnitude enhancement on V_{gap} is achieved, compared to the case where the OTL is absent, when an OTL 10 μm long is attached to the dipole antenna. Besides, no enhancement is observed when the attached OTL is only 1 μm long. Such an effect of OTL on V_{gap} can be attributed to the impedance matching between the tuning fork optomechanical antenna and the free space propagation medium of the IR radiation. A maximum value of V_{gap}=222 mV is achieved in the last right peak of the 10 μm long OTL (figure 5) placed at L=2.5 μm, which has been chosen as the nanodipole length of the designed device. It is worth noting that this peak corresponds to the fifth plasmonic resonance mode [10]. This choice led to a final structure that is not only easier to fabricate but also offers a larger effective area, which could enhance radiation absorption.

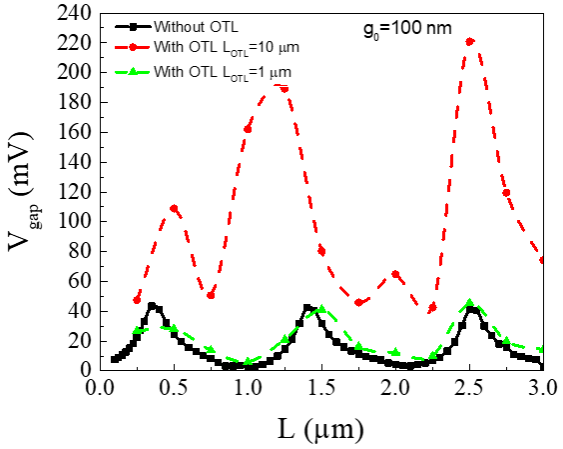

Figure 5: V_{gap} vs. nanodipole length without and with OTL. The rest of dimensions are found in Table II. All simulations have been performed for a 1 mW laser beam excitation with λ=1.55 um and SR=8 μm.

In a second approach, the final dimensions of the complete tuning fork optomechanical transducer have been obtained through an optimization process in which the gap voltage, V_{gap}, has been used again as the maximization variable at the design radiation wavelength of 1.55 μm. The arm's lengths of the nanodipole have been fixed at the previously obtained value L=2.5 μm. Thicknesses of Au and Si_3N_4 layers have been fixed at 70 nm and 600 nm respectively. The dipole arms' width W, the width and

length of the tuning fork/OTL, W_{OTL} and L_{OTL}, and gap distance, g_0, have been treated as free parameters. The optimization was performed with a laser power of 1 mW, a beam spot radius of 8 μm, and an initial feed gap distance fixed at g_0=100 nm. The resulting optimal design parameters are W=90 nm, W_{OTL}=180 nm, L_{OTL}=10 μm and g_0=100 nm (see Table II).

Figures 6 and 7 show two of the most relevant dependences of V_{gap} on geometry parameters found throughout this second optimization process. Figure 6, for instance, shows two effects: V_{gap} grows with L_{OTL}, achieving the maximum value for L_{OTL}=10 μm and decreases as the gap closes, which is especially evident at L_{OTL}=10 μm. The dependence on L_{OTL} can be explained by an improvement of the impedance matching between the tuning fork optomechanical antenna and free space, as argued previously (see figure 5). The gap dependence can be attributed to a combination of a device impedance change and a resonance frequency shift of the nanodipole, like that found in our previous works [11][10]. New details of this second effect are observed in figure 7, where V_{gap} presents a clear oscillatory decrease as gap closes. Such oscillations, which were not observed in our previous optomechanical antenna designs lacking in OTL structure [11][10], are characteristic of the OTL impedance dependence on its gap and reinforce the hypothesis that the OTL is strongly affecting the response of the whole device.

It is worth noting that we restricted our optimization analysis to a maximum OTL length of 10 μm, because this is the limit imposed by the length of the Au/Si3N4 slab where we fabricate the device. Quite likely, an optimal LOTL value would be found beyond 10 μm.

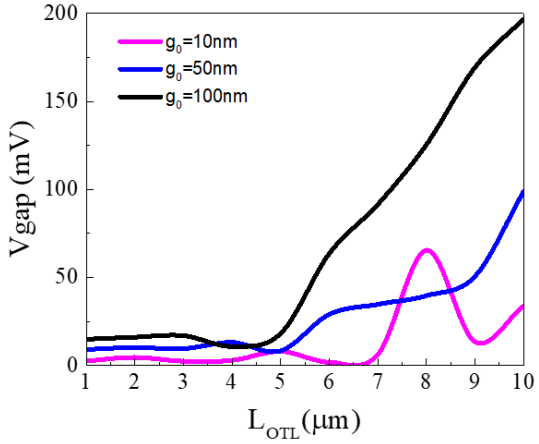

Figure 6: Vgap vs. OTL length for different gap values. The rest of dimensions are found in Table II. All simulations have been performed for a 1 mW laser beam excitation with λ=1.55 um and SR=8 μm.

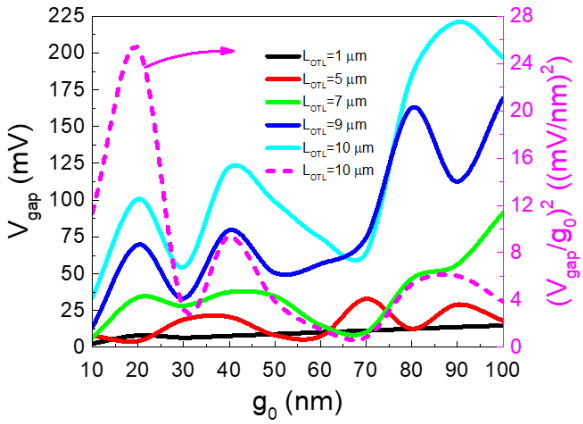

Figure 7: Vgap vs. gap distance, g0, for different OTL lengths (left y-axis) and $(Vgap/g0)^2$ vs. gap distance for LOTL=10 μm (right y-axis). The rest of dimensions are found in Table II. All simulations have been performed for a 1 mW laser beam excitation with λ=1.55 um and SR=8 μm.

A final analysis has been performed to verify whether the optimal parameters for Vgap are also optimal for the electrostatic force, Fee, and, ultimately, for the mechanical displacement, δx, so that we could confirm that Table II parameters are also optimal in a

broader sense. Thus, we realize that the initial electrostatic force in the gap position (δx=0, y=0), as computed with equation (4), depends linearly on (Vgap/g0)2 and, consequently, is not necessarily maximized when Vgap is maximized. Indeed, if we calculate (Vgap/g0)2 for Vgap-g0 pairs corresponding to the LOTL=10 μm curve in figure 7 and we plot them (right axis), we discover that the electrostatic force is optimized at g0=20 nm. However, we decided to choose g0=100 nm instead of g0=20 nm to facilitate manufacturing and to help avoiding possible snap-in collapse induced by FIB charging during fabrication. Besides, as observed in the decay dependence shown in figure 8, the election of g0=100 nm is also advantageous, because Vgap decays more slowly than in the smaller gap case (g0=10 nm) and, consequently, it will revert to a larger electrostatic force in an OTL region (y-range) where it is efficiently transduced into a mechanical displacement.

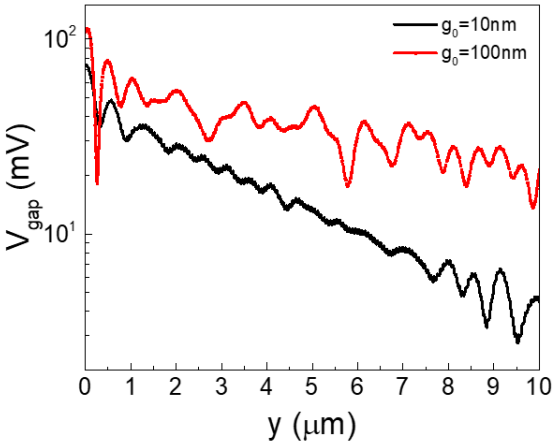

Figure 8: Vgap vs. y position along the OTL. The rest of dimensions are found in Table II. All simulations have been performed for a 1 mW laser beam excitation with λ=1.55 um and SR=8 μm.

Regarding the optimization of the mechanical displacement, δx, the analysis is much simpler. Since δx and Fee are proportional through the spring constant of the tuning fork arms, k, (δx=Fee·k-1) and k depends strongly on LOTL (k-1∝LOTL3), a constant growth of Vgap (and consequently of Fee) with LOTL together with a constant increase of k-1 ensures that δx is maximized at LOTL=10 μm.

6.2. Transducer responsivity and benchmarking analysis

Once the geometry of the device has been optimized to maximize Vgap and, ultimately, the mechanical displacement for a λ=1.55 um optical radiation, we have quantified this last variable as a function of the radiation power. Plot of figure 9 shows the simulations results of the mechanical displacement obtained when laser power is swept from 1 mW to the maximum power achievable in our experimental setup (7.5 mW). As can be observed, a predicted maximum value of δx=13.5 nm is obtained for a 7.5 mW illumination.

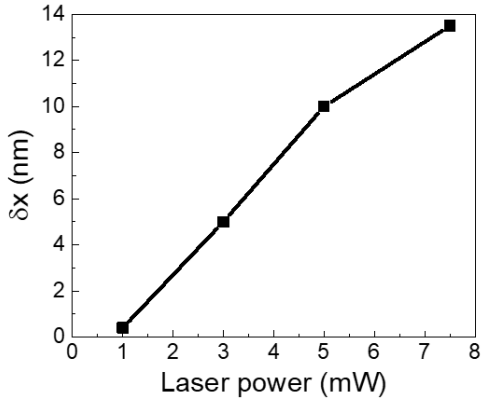

Figure 9: Lateral displacement in x-direction, δx, vs. laser power. All dimensions of the device are found in Table II. All simulations have been performed for a laser beam excitation with λ=1.55 um and SR=8 μm.

A benchmarking analysis in terms of the as defined responsivity, $\Re \equiv \delta x / P_{laser}$, has been performed to compare the transduction performance of our tuning fork optomechanical NIR antenna with the state-of-the-art optomechanical transducers.
The results of this analysis are summarized in figure 10, where responsivity, $\Re$, is represented as a function of the EM radiation frequency. Thus, for instance, when we compare the responsivity of our device, $\Re$=1.8 nm/mW, with that of our previous designs at f=193.55 THz (λ=1.55 um) [10][11][13] an improvement is clearly observed. It is worth noting here that the design presented in this work supposes an additional improvement in terms of insensitivity to parasitic thermal effects, compared to our previous optomechanical antennas. Indeed, we have moved from mechanical structures (cantilevers) where signal and optothermal parasitic response are found together in the same vertical direction (z-direction), so the second masked the first, to a tuning fork structure were signal (x-direction) and thermal parasitic unavoidably induced by the Au/Si3N4 bilayer (z-direction) are orthogonally decoupled. Consequently, thermal effects do not affect mechanical displacement, δx, in this case.
Other devices applied to the detection of EM radiation using the same transduction principle demonstrated comparable performance with our device [16], but they operate at a radiation frequency 2 orders of magnitude lower (2.6 THz). On the other hand, when comparing our device to optothermal transducers, i.e. devices based on an optically induced heating effect combined with a bimetallic mechanical bending, more than one order of magnitude responsivity enhancements are found with respect to the present work [17][18][19]. However, a slow optothermal transduction mechanism will produce long temporal responses and low frequency bandwidths than the faster and more straightforward optical to mechanical transduction mechanism exploited in this work.

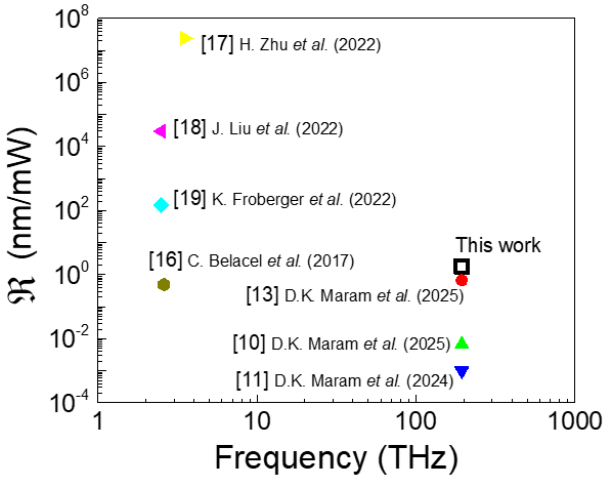

Figure 10: Responsivity vs. operation frequency corresponding to some of the most relevant state-of-the-art optomechanical transducers, including the tuning fork optomechanical antenna of present work.

TABLE I: Optical and mechanical properties of the materials involved in COMSOL simulations.

Property	**Au**	**Si_3N_4**	**Units**
Refractive index, n *	0.52406	1.9963	
Extinction coeficient, k *	10.742	0	
Electrical conductivity, σ *	$45 \cdot 10^6$	0	S/m
Density, ρ	19280	3100	kg/m^3
Young's modulus, E	80	250	GPa
Poisson's ratio, ν	0.44	0.23	

*@λ=1.55μm

TABLE II: Geometry characteristics of tuning fork optomechanical device

Parameter	Value	Units
Dipole width, W	90	*nm*
Dipole length, L	2.5	*μm*
Gold thickness, t_{Au}	70	*nm*
Silicon nitride thickness, t_{Si3N4}	600	*nm*
Tuning fork/OTL arm width, w_{OTL}	180	*nm*
Tuning fork/OTL arm length, L_{OTL}	10	*μm*
Capacitive gap, g_0	100	*nm*

7. Conclusions

The design, fabrication and performance analysis of a novel optomechanical transducer based on a combination of a nanodipole antenna, an optical transmission line (OTL) and a tuning fork have been presented.
The as called tuning fork optomechanical antenna transduces NIR (λ=1.55 um) optical power into static mechanical deflection of the tuning fork arms in the on-plane direction. No opto-thermomechanical effects are involved in the transduction mechanism, since mechanical deflection is exclusively produced by the DC component of the electrostatic force. This force is induced by the voltage oscillating at optical frequencies and propagated from the nanoantenna feed gap along the optical transmission line integrated on top of the tuning fork. An ad-hoc fabrication process based on Focused Ion Beam nano-milling has been defined and validated. COMSOL Multiphysics has been employed for the design and performance analysis of an optimized tuning fork optomechanical antenna. In the design process, the effects of the nanodipole and OTL dimensions produced on the full device performance in terms of voltage in the feed gap nanoantenna, electrostatic force and lateral displacement have been carefully discussed. Finally, a maximum displacement response of δx=13.5 nm has been obtained, giving rise to a responsivity value of ℜ=1.8 nm/mW, which has been compared to some of the more relevant examples found in the literature.

Declaration of Competing Interest

The authors declare that they have no known competing financial interest or personal relationships that could have appeared to influence the work reported in this paper.

Data availability

Data will be made available on request.

Acknowledgements

This work was funded by Spain's Ministerio de Ciencia e Innovación under Grant No. PID2021-127840NB-I00 (MICINN/AEI/FEDER, UE) and Ministerio de Ciencia, Innovación y Universidades under Grant No. PID2024-161603NB-I00 (MICIU/ AEI / 10.13039/501100011033 / FEDER, UE).

References

[1] L. Novotny and N. van Hulst, "Antennas for light," *Nat Photonics*, vol. 5, no. 2, pp. 83–90, 2011, doi: 10.1038/nphoton.2010.237.

[2] P. Biagioni, J.-S. Huang, and B. Hecht, "Nanoantennas for visible and infrared radiation," *Reports on Progress in Physics*, vol. 75, no. 2, p. 24402, Jan. 2012, doi: 10.1088/0034-4885/75/2/024402.

[3] P. Bharadwaj, B. Deutsch, and L. Novotny, "Optical Antennas," *Adv. Opt. Photon.*, vol. 1, no. 3, pp. 438–483, Nov. 2009, doi: 10.1364/AOP.1.000438.

[4] A. Bonakdar and H. Mohseni, “Impact of optical antenna and plasmonics on infrared imagers,” *Infrared Phys Technol*, vol. 59, pp. 142–145, 2013, doi: https://doi.org/10.1016/j.infrared.2012.12.029.
[5] {Stefan Alexander} Maier, *Plasmonics - Fundamentals and Applications*. Springer, 2007.
[6] K. Chen, G. Razinskas, T. Feichtner, S. Grossmann, S. Christiansen, and B. Hecht, “Electromechanically Tunable Suspended Optical Nanoantenna,” *Nano Lett*, vol. 16, no. 4, pp. 2680–2685, 2016, doi: 10.1021/acs.nanolett.6b00323.
[7] E. S. Jeon, Y. Ko, and S. Yoo, “Design principles for electrically driven Luttinger liquid-fed plasmonic nanoantennas,” *Nanophotonics*, vol. 12, no. 13, pp. 2507–2516, 2023, doi: 10.1515/nanoph-2022-0782.
[8] M. S. Eggleston, “Optical antenna enhanced nanoLEDs for on-chip optical interconnects,” in *2015 IEEE Summer Topicals Meeting Series (SUM)*, 2015, pp. 152–153. doi: 10.1109/PHOSST.2015.7248244.
[9] M. Fleischer, D. Zhang, and A. J. Meixner, “Optically and electrically driven nanoantennas,” *Beilstein Journal of Nanotechnology*, vol. 11, pp. 1542–1545, Oct. 2020, doi: 10.3762/bjnano.11.136.
[10] D. K. Maram, J. Garcia-Garcia, X. Cartoixà, and G. Abadal, “Impact of the parasitic photothermal effect on the performance of an optomechanical nanoantenna for NIR radiation detection,” *Sens Actuators A Phys*, vol. 394, p. 116966, 2025, doi: https://doi.org/10.1016/j.sna.2025.116966.
[11] D. Khosh Maram, X. Borrisé, J. García-García, R. Ruiz, X. Cartoixà, and G. Abadal, “Design and fabrication of an opto-mechanical antenna in the NIR range,” *Micro and Nano Engineering*, vol. 23, p. 100241, Sep. 2024, doi: 10.1016/j.mne.2024.100241.
[12] G. Baffou and R. Quidant, “Thermo-plasmonics: using metallic nanostructures as nano-sources of heat,” *Laser Photon Rev*, vol. 7, no. 2, pp. 171–187, 2013, doi: https://doi.org/10.1002/lpor.201200003.
[13] D. Khosh Maram, X. Borrisé, J. Garcia-Garcia, X. Cartoixà, and G. Abadal, “Plasmomechanical actuation at the nanoscale activated by NIR radiation,” Oct. 2025. doi: 10.2139/ssrn.5544681.
[14] K. Luke, Y. Okawachi, M. R. E. Lamont, A. L. Gaeta, and M. Lipson, “Broadband mid-infrared frequency comb generation in a Si3N4 microresonator,” *Opt. Lett.*, vol. 40, no. 21, pp. 4823–4826, Nov. 2015, doi: 10.1364/OL.40.004823.
[15] P. B. Johnson and R. W. Christy, “Optical Constants of the Noble Metals,” *Phys Rev B*, vol. 6, pp. 4370–4379, 1972, doi: 10.1103/PhysRevB.6.4370.
[16] C. Belacel, Y. Todorov, S. Barbieri, D. Gacemi, I. Favero, and C. Sirtori, “Optomechanical terahertz detection with single meta-atom resonator,” *Nat Commun*, vol. 8, no. 1, p. 1578, 2017, doi: 10.1038/s41467-017-01840-6.
[17] H. Zhu *et al.*, “A Terahertz Optomechanical Detector Based on Metasurface and Bi-Material Micro-Cantilevers,” *Micromachines (Basel)*, vol. 13, no. 5, 2022, doi: 10.3390/mi13050805.
[18] J. Liu *et al.*, “Ultrafast Detection of TeraHertz Radiation with Miniaturized Optomechanical Resonator Driven by Dielectric Driving Force,” *ACS Photonics*, vol. 9, no. 5, pp. 1541–1546, May 2022, doi: 10.1021/acsphotonics.2c00227.
[19] K. Froberger *et al.*, “SOI-based micro-mechanical terahertz detector operating at room-temperature and atmospheric pressure,” *Appl Phys Lett*, vol. 120, no. 26, p. 261103, Jun. 2022, doi: 10.1063/5.0095126.

Appendix C

Library of FIB milling procedures

C.1 Nanodipole coupled to a micro or nanocantilever (Papers 1 and 3) (A.1)(B.2)

To fabricate Paper 1 and Paper 2 designs we utilized two separate microcantilevers as the base, in a configuration where the plasmonic nanodipole has to be connected to directly to the micro cantilever (Paper 1) (A.1) or to a nano cantilever (Paper 3)(B.2). Each microcantilever was a commercial tipless AFM cantilever made of Si_3N_4 (triangular in shape, 200–300 μm in length) with a nominal thickness of 600 nm, coated on both sides with a metal layer (typically Cr/Au, 70 nm and 35 nm thick). The cantilevers were originally clamped on a rigid substrate (Pyrex) at their base. In these designs, one-half of the nanoantenna would be fabricated on the tip of each cantilever, and later the two cantilevers would be aligned facing each other to form the complete antenna feed gap. The fabrication process on each microcantilever involved two main FIB milling stages (plus a final assembly), with careful control of beam parameters to create a nanotailored cantilever tip that is thinner and more compliant than the original, as well as to define the nanoantenna structures. The steps on each cantilever were (Figure 3.9):

1. Thinning and Top Metal Removal: First, the microcantilever was inverted (flipped upside-down) so that the FIB could directly access the side coated with 70 nm Au/Cr. Using FIB milling, the entire metal coating was removed from the tip region of the cantilever, and crucially, the underlying Si_3N_4 was thinned down in that same region. This was done to "nanotailor" the cantilever – i.e., to locally reduce its thickness and stiffness – which would enhance its mechanical deflection under optical forces (Paper 3)(B.2). To avoid Ga^+ redeposition and to achieve a uniform thinning (a "brushing" effect on the surface), a relatively low ion beam current of 700 pA was used for this step, combined with a fast raster scan (on the order of 1s per frame). The low current minimizes sputtered material redepositing on the surface, while the fast scanning prevents localized overheating or excessive

milling in one spot. This step was confined to the area at the cantilever's free end where the nanocantilever and/or the antenna would be formed (Figure 3.8, section 3.3), ensuring the rest of the cantilever beam remained at full thickness for structural support.

2. Nanostructure Definition: In the second FIB milling stage, the fine structures – namely the slender auxiliary nanocantilever (Paper 3)(B.2) and the nanodipole antenna arm (Papers1 and 3)(A.1)(B.2)– were cut out from the thinned region of the cantilever. Essentially, this step carved a tiny protruding beam (the nanocantilever) at the cantilever's tip and at the same time defined one half of the dipole antenna on that protrusion. The FIB milled completely through the Si_3N_4 layer (and the remaining metal) to isolate the nanocantilever and antenna arm from the surrounding material. To efficiently remove material for the coarse outlines, a higher beam current of about 3 nA was employed, with a slower scan speed (10s per scan) to increase milling depth per pass. After the major cuts, the beam current and aperture were progressively reduced as the milling approached the final delicate features. In practice, this meant using intermediate currents (e.g. 1 nA, 300 pA, etc.) in a stepwise fashion to refine the antenna arm shape and the nanocantilever width, and finally a very low current (tens of pA) for the most critical edges and the antenna feed gap region. This gradual reduction in beam size improved the lateral resolution and edge smoothness of the nanostructures. By the end of this step, one half of the plasmonic dipole – consisting of a metal pad/arm on a now-freely suspended Si_3N_4 nanocantilever – was fully defined on the tip of the AFM cantilever.

The above two steps were performed on two identical cantilevers, each producing one half of the NEMSTENNA device. After FIB milling, the thickness of the tailored nanocantilever sections was typically in the range of 100–150 nm (down from 600 nm originally), as controlled by the first milling step. It was empirically found that thinning the Si_3N_4 much below 100 nm for a long (tens of micron)

nanocantilever led to bending and collapse of that structure due to residual stress in the metal/nitride film. In fact, the 70 nm Au coating introduces stress such that extremely thin and narrow nanocantilevers will curl or buckle if over-thinned. The fabrication strategy addressed this challenge by limiting the thinning to ∼100 nm thickness to maintain stability. In an ad-hoc experiment, the maximum slenderness of these nanocantilevers without collapse was determined: for a length of about 68.7 µm and width 2.2 µm (nearly the design's full span), the nitride could be thinned to ≈ 100 nm before the onset of irreversible bending. Thus, the process was optimized to stop at that thickness, using intermittent SEM imaging to monitor the deflection during milling.

With both halves of the nanoantenna fabricated, a final assembly has to be carried out by carefully aligning the two microcantilevers so that their nanostructured tips face each other in close proximity. This fabrication approach is more complex than the tuning-fork method, primarily because of the delicate final alignment step and the need to fabricate two separate components. However, FIB milling proved capable of producing the required features on the AFM cantilevers: e.g., the antenna arm widths (W1) of 80 nm and gap on the order of 10–100 nm were targeted, and the process achieved the necessary precision within a tolerance of around ±50 nm. The use of a low-current polishing strategy and stepwise milling ensured the edge quality and reproducibility of the patterned features on each cantilever. Overall, this "nanotailored cantilever" fabrication successfully increased the device's compliance and optical response (by thinning the cantilever and increasing overlap capacitance), at the cost of additional fabrication complexity in the assembly stage.

C.2 Tuning fork NEMSTENNA with integrated optical transmission line (Paper 4)(B.3)

The tuning-fork optomechanical antenna was fabricated from a suspended bilayer consisting of a 600 nm thick silicon nitride (Si_3N_4) film coated with a 70 nm Au

layer on its top surface. This bilayer membrane ("flange") is anchored to a Pyrex substrate at one end, while the other end is free-standing to form the nanocantilever tuning fork structure. All nanoscale patterning was accomplished via a six-step FIB milling sequence (Figure 3.11), carefully designed to define the tuning-fork arms, the integrated optical transmission line (OTL), and the plasmonic nanodipole antenna at the free end. The key fabrication steps were as follows:

1. OTL Gap Trench: First, the gap separating the two coplanar OTL strips along the tuning-fork arms was opened by ion milling a narrow trench through the Au/Si_3N_4 bilayer. This trench was milled to a width of approximately 150–200 nm using a low ion beam current of 50 pA at 30 kV acceleration. The low current ensured minimal lateral milling damage and high fidelity in the gap width.

2. Nanoantenna Region Clearing: Next, using the same 30 kV, 50 pA Ga^+ beam conditions, material was removed at the intended nanoantenna site. This created a clear region where the nanodipole antenna's feed gap would be defined, essentially pre-milling the area around the antenna to prevent redeposition or obstruction during the final gap cut.

3. Cantilever Outline Milling: The outline of the two parallel nanocantilever arms (which form the tuning fork) was then milled in the Au/Si_3N_4 layer. For this relatively larger-scale material removal, a higher ion beam current of 300 pA was used to etch the rough shape of the cantilevers and OTL in a time-efficient manner. This step cuts through the bilayer, releasing the sides of the nanocantilevers from the surrounding membrane.

4. Edge Polishing: After coarse milling, the beam current was reduced back to 50 pA to perform a "polishing" pass along the newly cut cantilever edges. This lower-current cleanup improved the edge smoothness and removed any Ga^+-induced redeposition or milling damage, ensuring high-quality, straight sidewalls on the OTL and cantilever structures.

5. Feed Gap High-Resolution Cut: To define the nanodipole antenna's feed gap – the critical nanoscale separation between the two antenna arms – the process parameters were adjusted for maximum resolution. The FIB magnification was increased above 1000×, and the ion beam current was minimized to 2 pA. Using this focused, gentle beam, a narrow cut was milled to split the Au/Si_3N_4 at the antenna tip, yielding a feed gap on the order of a few tens of nanometers. This step required precise alignment (facilitated by SEM imaging at high magnification) to position the cut exactly where the antenna gap was desired.

6. Antenna Length/Width Trimming: In the final step, the nanodipole antenna's dimensions were fine-tuned by FIB milling at 50 pA. Small milling passes adjusted the antenna arm length L and width W to their design specifications, without significantly altering the gap. This ensured the plasmonic resonance of the dipole would be at the target wavelength (1.55 μm) and that both arms were symmetric.

Throughout the above steps, the SEM was intermittently used to inspect the milled structures and verify that the OTL lines remained intact and that the narrow gaps were being cleanly produced. (Figure 3.12, section 3.3) confirms the outcome: the completed tuning-fork device showed a well-defined nanoscale feed gap (reduced to about 65 nm in the prototype) and uniform cantilever/antenna dimensions in the 200–400 nm range. The FIB-based process thus proved capable of reliably sculpting the delicate tuning-fork geometry with sub-100 nm features. Notably, the entire antenna, OTL, and tuning-fork structure were defined monolithically from the single Au/Si_3N_4 membrane, avoiding the need for assembling separate parts. This monolithic approach simplified fabrication and improved reproducibility: the multi-step FIB milling strategy yielded high structural integrity and consistent nanoscale features across devices.

Appendix D

Measurement setup

D.1 Measurement setup

The measurement setup described here has been used to carry out the optothermomechanical response measurements reported in (section 3.5).

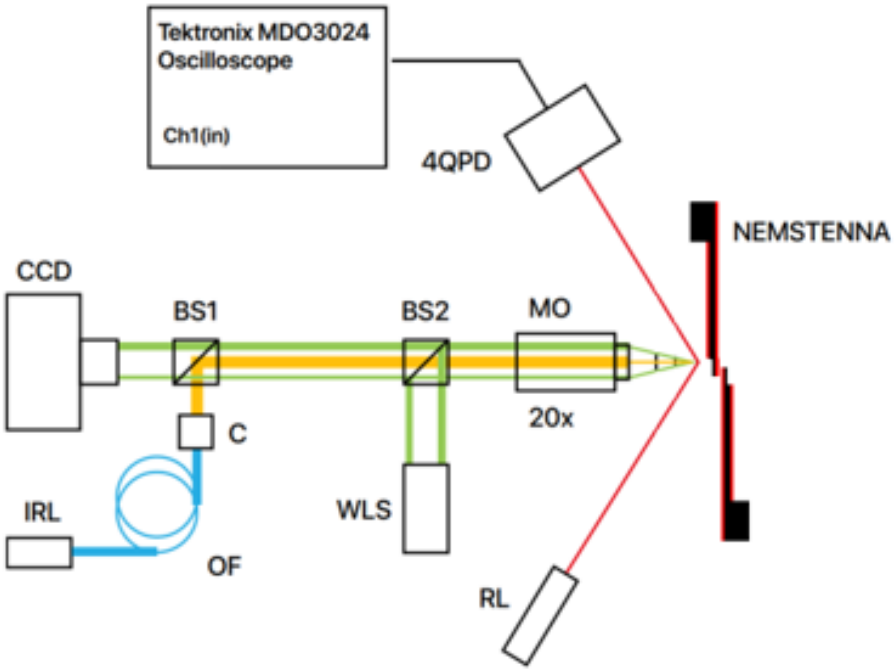

Figure D.1: Schematic of the NEMSTENNA characterization setup. Key components include infrared laser (IRL), 4-quadrant photodetector (4QPD), CCD camera (CCD), White light source (WLS), microscope objective (MO), red diode laser (RL), collimator (C), optical fiber, (OF), and beam splitters (BS1/BS2). The Tektronix MDO3024 oscilloscope handles analysis.

D.2 Experimental setup elements

Table D.1: Experimental setup elements used for NEMSTENNA characterization.

Element (acronym)	Model	Characteristic
Oscilloscope	Tektronix MDO3024	Monitors time-domain signals (e.g., displacement readouts).
Laser Controller	ITC 4001	Stabilizes and modulates the infrared laser power.
Infrared Laser (IRL)	Thorlabs SFL1550P	1.55 μm wavelength; excites NEMSTENNA cantilever.
Red diode laser (RL)	Thorlabs CPS11K-EC	673.8 nm diode laser; used for displacement detection.
Microscope Objective (MO)	Mitutoyo MPlanApoSL20X	Focuses IR and RL beams onto the NEMSTENNA.
Beam Splitters (BS1/BS2)	Thorlabs BS024/CM1-BS015	Direct IR laser beam and white light toward the NEMSTENNA.
4-Quadrant Photodetector (4QPD)	New Focus 2901	Detects cantilever displacements via reflected beam.
CCD Camera	DFK 72AUC02	Monitors alignment and cantilever position.
White Light Source (WLS)		Provides broadband illumination for CCD imaging.
Collimator (C)	Thorlabs TC12APC-1550	collimates IR laser beam.
Optical Fiber (OF)	Mode field diameter: 10.5±1.0 μm	Guides IR laser beam to the collimator.